OSU

The Ohio State University

A GTD ANALYSIS OF OGIVE PEDESTAL

By

Kin-Yue Albert Lai
W.D. Burnside

The Ohio State University

ElectroScience Laboratory

Department of Electrical Engineering
Columbus, Ohio 43212

Technical Report 716148-8
Contract NSG-1613
March 1986

National Aeronautics and Space Administration
Langley Research Center
Hampton, VA 23665

NOTICES

When Government drawings, specifications, or other data are used for any purpose other than in connection with a definitely related Government procurement operation, the United States Government thereby incurs no responsibility nor any obligation whatsoever, and the fact that the Government may have formulated, furnished, or in any way supplied the said drawings, specifications, or other data, is not to be regarded by implication or otherwise as in any manner licensing the holder or any other person or corporation, or conveying any rights or permission to manufacture, use, or sell any patented invention that may in any way be related thereto.

50272-101

REPORT DOCUMENTATION PAGE	1. REPORT NO. 716148-8	2.	3. Recipient's Accession No.

4. Title and Subtitle
A GTD Analysis of Ogive Pedestal

5. Report Date
March 1986

6.

7. Author(s)
Kin-Yue Albert Lai, W.D. Burnside

8. Performing Organization Rept. No.
716148-8

9. Performing Organization Name and Address
The ElectroScience Laboratory
The Ohio State University
1320 Kinnear Road
Columbus, Ohio 43212

10. Project/Task/Work Unit No.

11. Contract(C) or Grant(G) No.
(C) NSG-1613
(G)

12. Sponsoring Organization Name and Address
National Aeronautics and Space Administration
Langley Research Center
Hampton, Virginia

13. Type of Report & Period Covered
Technical

14.

15. Supplementary Notes

16. Abstract (Limit: 200 words)

The metal ogive pedestal is claimed to have low radar cross section and low observability features. This study uses the Geometric Theory of Diffraction (GTD) to analyze the pedestal scattering for three cases: direct backscattered field, backscattered field structure, and target/ pedestal multiple scattering. As a result, this study can be used to evaluated the various ways that the metal conical ogive pedestal can affect the performance of a high quality RCS measurement system.

17. Document Analysis a. Descriptors

b. Identifiers/Open-Ended Terms

c. COSATI Field/Group

18. Availability Statement	19. Security Class (This Report)	21. No. of Pages
APPROVED FOR PUBLIC RELEASE. DISTRIBUTION IS UNLIMITED.	UNCLASSIFIED	232
	20. Security Class (This Page) UNCLASSIFIED	22. Price

(See ANSI-Z39.18) See Instructions on Reverse OPTIONAL FORM 272 (4-77) (Formerly NTIS-35) Department of Commerce

TABLE OF CONTENTS

LIST OF TABLES

LIST OF FIGURES

CHAPTER I

INTRODUCTION

The ogival target-support pedestal as shown in Figure 1.1 is claimed to have a low radar cross section (RCS); yet, it can handle very large and heavy structures. This report attempts to find out whether this claim is true through an analysis using the Uniform Theory of Diffraction as well as actual measurements. The pedestal backscatter is just one aspect of this study. Another more serious issue is associated with the bistatic scattering by the pedestal which influences the target illumination.

The pedestal, as shown in Figure 1.1, is formed by fitting two conical pieces of metal together to make an ogive which is smaller at the top than the bottom. The whole pedestal is tilted forward to reduce the amount of scattering to the radar as will be discussed in Chapter III.

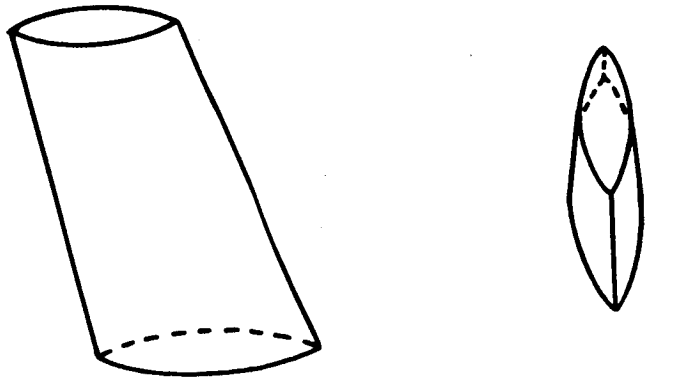

Figure 1.1. Ogive pedestal.

Inside the pedestal, a motor drives a shaft that sticks out of the top of the pedestal to support the target (as shown in Figure 1.2). Different lengths of shafts can be placed there depending on the type of measurement. Sometimes the shaft is simply a metal rod, but other times it might be a styrofoam rod or stand to make it more "invisible" to the radar.

The physical position of the pedestal for compact range applications is shown in Figure 1.3. The source is placed at the focus of the reflector so that a plane wave is formed which then strikes the pedestal and target.

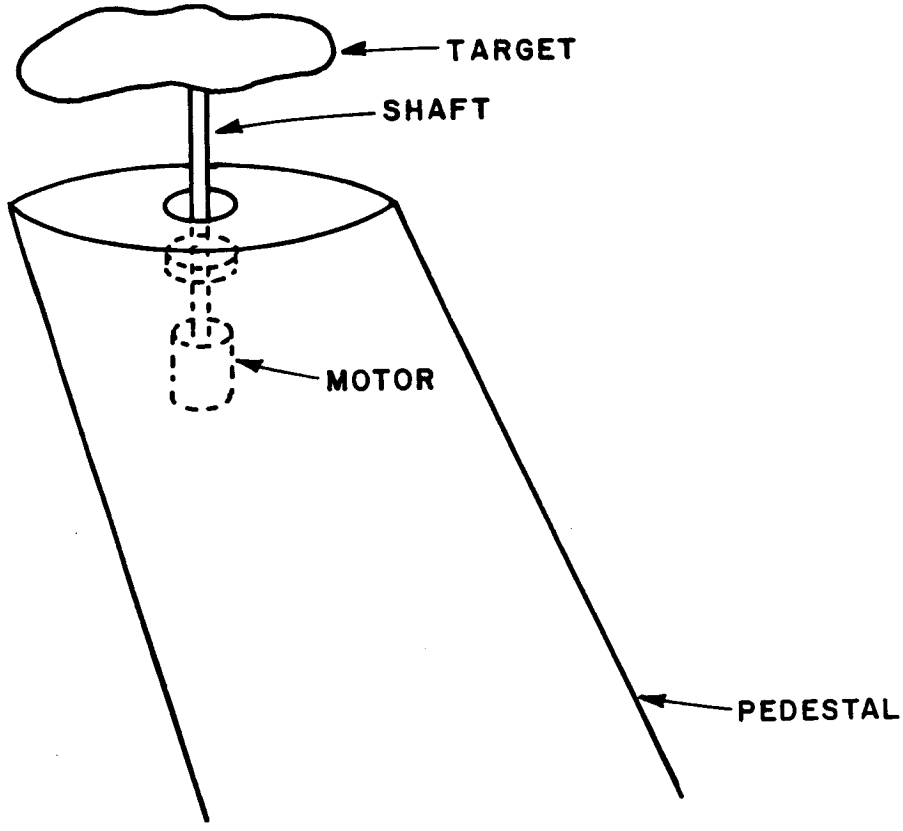

Figure 1.2. Target support system.

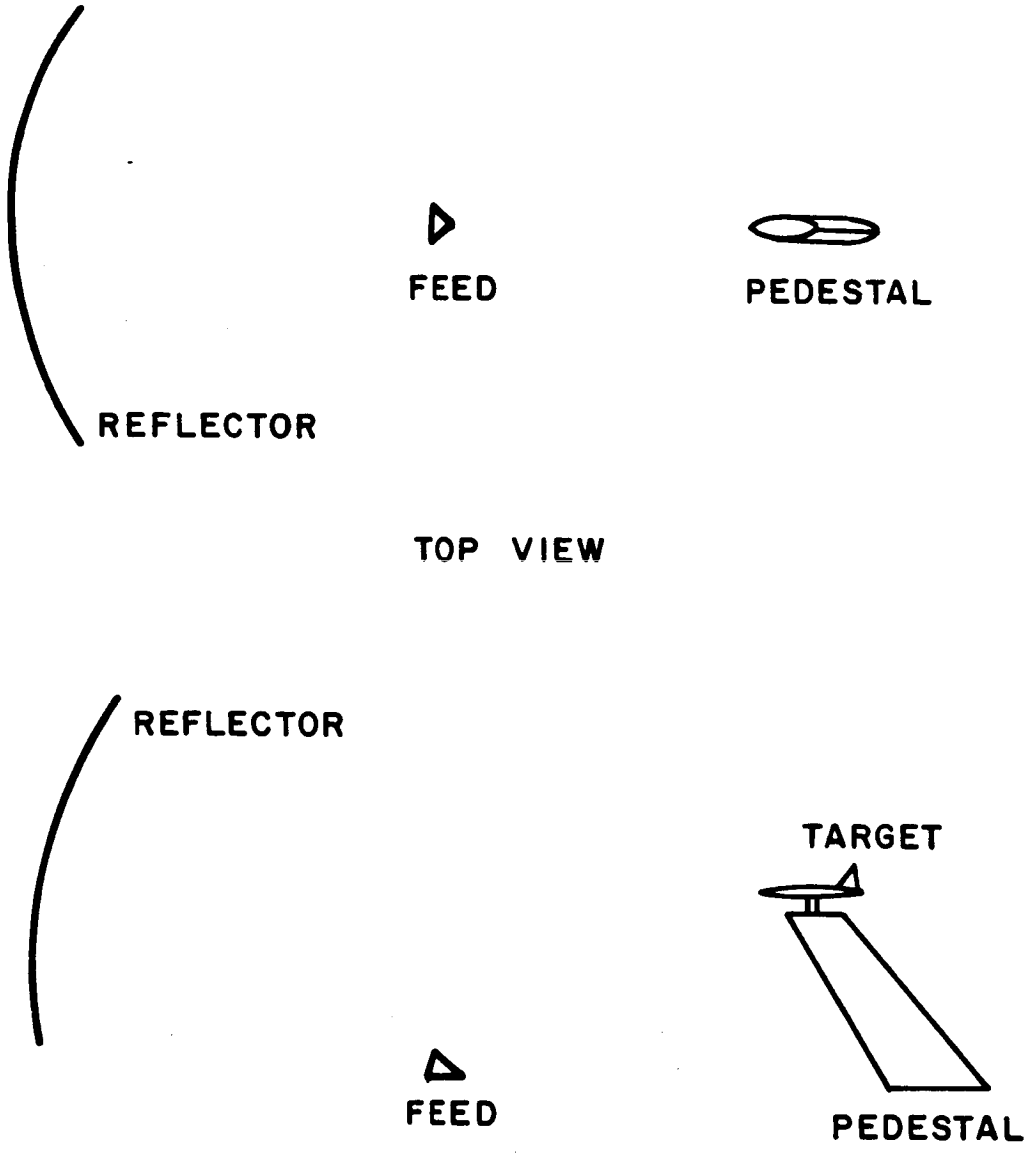

Figure 1.3. Compact range arrangement.

In a typical measurement sequence, one first records the return with the target on the pedestal, and then the return of the pedestal alone. These two responses are subtracted to obtain the target response. In doing so, one assumes at least three things: 1) the field above the pedestal is a uniform plane wave; i.e., it is not significantly perturbed by the pedestal; 2) there is no significant interaction between the target and pedestal; and 3) the pedestal was undisturbed by either adding or removing the target. The first assumption will be studied in Chapter V by calculating as well as measuring the field above the pedestal. The extent to which the second and third assumptions are correct depends on the target as well as the shape of the top of the pedestal.

After analyzing the present condition, one would like to know how to use the pedestal optimally. For example, if the two assumptions are not valid near the top of the pedestal, can one lift the target higher above the pedestal so that the field there is more like a plane wave which also reduces the target/pedestal interaction? And if that is possible, how high does one need to go? One can also find out certain limitations in using the pedestal. For example, are there certain regions behind the pedestal that one should not use because of the field structure there? If the field is not a perfect plane wave, what is the variation at different levels above the pedestal? Can one live with them?

All these assumptions, limitations and optimalizations can be analyzed using the Uniform theory of diffraction (UTD). The UTD is a

high frequency method which is used to calculate the edge diffracted, corner diffracted, reflected and creeping wave field components so that when they are added to the incident field, the total field is smooth and continuous. This method also allows one to single out different scattering mechanisms in order to evaluate the cause of certain problem areas.

Unfortunately there are regions where the UTD fails. One such region is called caustic as will be encountered in Chapter IV. Similarly, many secondary wave mechanisms, like double diffraction, creeping waves diffracted from edges, etc. do not have solutions yet. Luckily, most of these contributions are of rather small magnitude; i.e., including or excluding them does not cause too big a difference. Nevertheless,they will be pointed out as they are encountered.

Now that one has a basic concept of this study, let us examine the material in each chapter. In Chapter II a theoretical background of the UTD mechanisms is given in terms of reflection, edge diffraction, corner diffraction and creeping wave contributions. The RCS of the pedestal is calculated in Chapter III for two different ways of mounting: 1) mounting the target on a shaft well above the top of the pedestal, and 2) flush-mounting where the target just sits on top of the pedestal. The UTD is applied in Chapter IV to calculate the field around the pedestal. Each scattering mechanism is dealt with separately and then added up to form the total field. Measurements are compared with calculations in Chapter V for different levels around the pedestal. The last chapter concludes this report by coming back to the issues raised

in this chapter. Are the assumptions made in using this pedestal valid? Are those limitations in the use of this pedestal allowable? Has one optimized the use of this pedestal? And if not, what more can one do?

CHAPTER II

THEORETICAL BACKGROUND

A. INTRODUCTION

This chapter describes the theoretical background for this study. The Uniform Geometric Theory of Diffraction (UTD) is used to calculate the fields caused by edge diffraction, corner diffraction, surface reflection and creeping wave mechanisms on the pedestal, which is assumed to be perfectly conducting. The UTD is constructed such that the total field, which consists of the incident, reflected, and diffracted terms, is smooth and continuous throughout the whole pattern.

An exp(jwt) time dependence is assumed and will be suppressed in all field solutions.

B. CURVED SURFACE REFLECTION

The reflected field from a curved surface, as shown in Figure 2.1, is given by [1]

$$\vec{E}_{ref} = \vec{E}^{i}(Q_R) \cdot \overline{\overline{R}} \sqrt{\frac{\rho_1^{r}\,\rho_2^{r}}{(\rho_1^{r}+s)(\rho_2^{r}+s)}}\; e^{-jks} \tag{2.1}$$

where

$$\overline{\overline{R}} = R_s\, \hat{e}_{\perp}\, \hat{e}_{\perp} + R_h\, \hat{e}_{\parallel}^{i}\, \hat{e}_{\parallel}^{r} \tag{2.2}$$

$$R_{s,h} = -\sqrt{\frac{-4}{\xi^L}}\; e^{-j(\xi^L)^3/12} \left\{ \frac{e^{-j\pi/4}}{2\sqrt{\pi}\,\xi^L} [1-F(X^L)] + \hat{P}_{s,h}(\xi^L) \right\} \tag{2.3}$$

$$\xi^L = -2\, m(Q_R)\cos\theta^{i} \tag{2.4}$$

$$\cos\theta^{i} = \hat{n} \cdot \hat{s} \tag{2.5}$$

$$m(Q_R) = \left[\frac{k\, P_g(Q_R)}{2} \right]^{1/3} \tag{2.6}$$

$P_g(Q_R)$ = radius of curvature of the surface in the plane of incidence

$$= \frac{R}{\sin^2(\omega_r)} \quad \text{(for cylinder, also refer to Figure 2.2)} \tag{2.7}$$

$$\chi^L = 2\kappa L^L \cos^2\theta^i \tag{2.8}$$

$$L^L = \begin{cases} s' & , \text{ in the far zone} \\ \dfrac{ss'}{s+s'} & , \text{ in the near zone} \end{cases} \tag{2.9}$$

$\hat{n}$ = outward unit normal vector to the surface at Q_R.

$\hat{P}_{s,h}(\xi)$ = Pekeris' Caret functions

$$= \begin{Bmatrix} p^*(\xi) \\ -\dfrac{1}{2\sqrt{\pi\xi}} \\ q^*(\xi) \end{Bmatrix} e^{-j\pi/4} \tag{2.10}$$

$\left.\begin{matrix} p^*(\xi) \\ q^*(\xi) \end{matrix}\right\}$ = complex conjugate of the universal functions defined by Logan [2]

$$\hat{e}_\perp = \frac{\hat{n} \times \hat{s}}{|\hat{n} \times \hat{s}|} \tag{2.11}$$

$$\hat{e}^i_\parallel = \frac{\hat{I} \times \hat{e}_\perp}{|\hat{I} \times \hat{e}_\perp|} \tag{2.12}$$

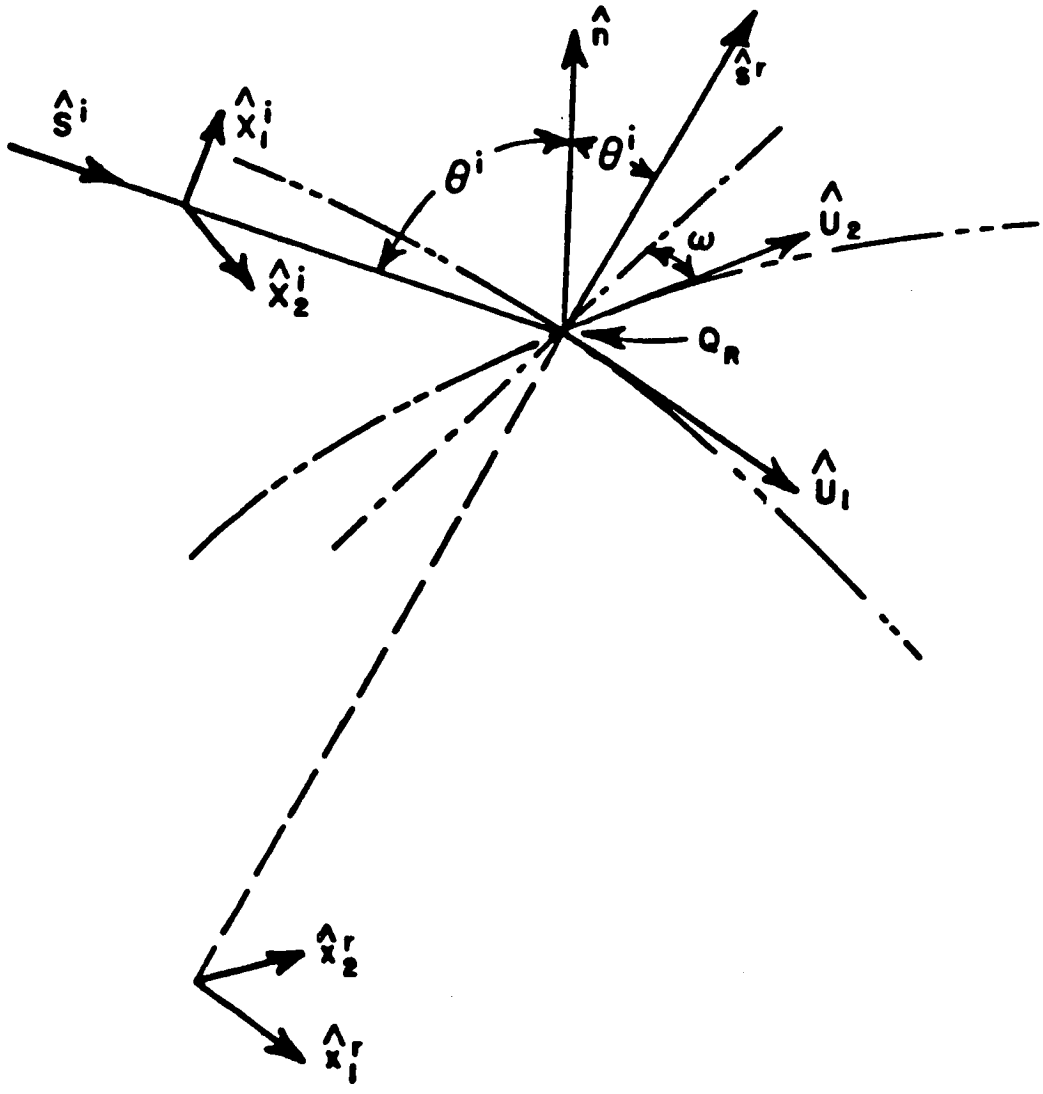

Figure 2.1. Geometry for the analysis of the reflected wavefront. The reflecting surface is S.

——— – – ——— Intersection of a principal plane of S at Q_R with S

——— – ——— Intersection of the plane of incidence with the plane tangent to S at Q_R.

– ——— – ——— – Extension of the reflected ray below S.

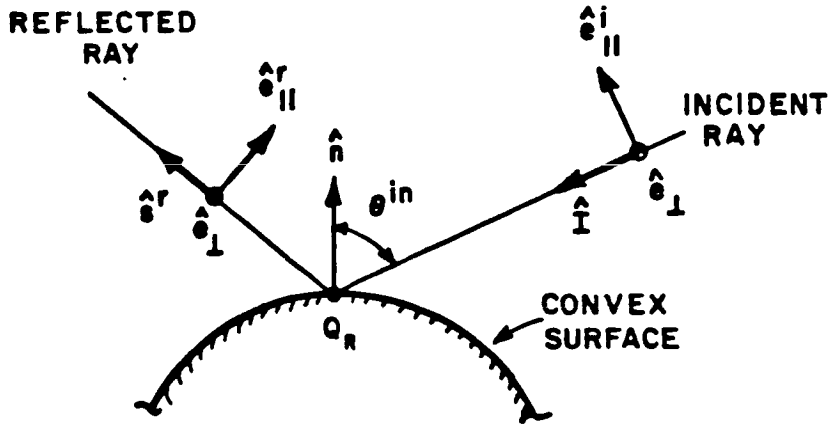

Figure 2.2. Cylinder reflected field geometry.

$$\hat{e}_{\parallel}^{i} = \frac{\hat{s} \times \hat{e}_{\perp}}{|\hat{s} \times \hat{e}_{\perp}|} \quad , \text{ and} \tag{2.13}$$

$\rho_{1,2}^{r}$ = principal radii of curvature of reflected wavefront [1]

The transition function [F(x)], as shown in Figure 2.3, provides continuity of the incident field across the shadow boundary and is given by

$$F(X) = 2J|\sqrt{x}|\, e^{jx} \int_{\sqrt{x}}^{\infty} e^{-jt^2} dt \tag{2.14}$$

$$= \begin{cases} \text{small argument region: } x < 0.3 \\ F(x) \approx [\sqrt{\pi x} - 2xe^{j\pi/4}]\, e^{j(\pi/4 + x)} \\ \text{linear interpolation region: } 0.3 < x < 5.5 \\ F(x) \approx F(x_n) + A_n(x - x_n) \quad \text{(refer to Table 2.1)} \\ \text{large argument region: } x > 5.5 \\ F(x) \approx 1 + \frac{j}{2x} - \frac{3}{4x^2} \end{cases} \tag{2.15}$$

(for $x < 0$. $F(x) = F^{*}(|x|)$)

Table 2.1

LINEAR INTERPOLATION DATA FOR F(x)

X_n	$F(X_n)$	A_n
0.3	0.5729 + j0.2677	0.0000 + j0.0000
0.5	0.6768 + j0.2682	0.5195 + j0.0025
0.7	0.7439 + j0.2549	0.3355 + j0.0665
1.0	0.8095 + j0.2322	0.2187 + j0.0757
1.5	0.8730 + j0.1982	0.1270 + j0.0680
2.3	0.9240 + j0.1577	0.0638 + j0.0506
4.0	0.9658 + j0.1073	0.0246 + j0.0296
5.5	0.9797 + j0.0828	0.0093 + j0.0163

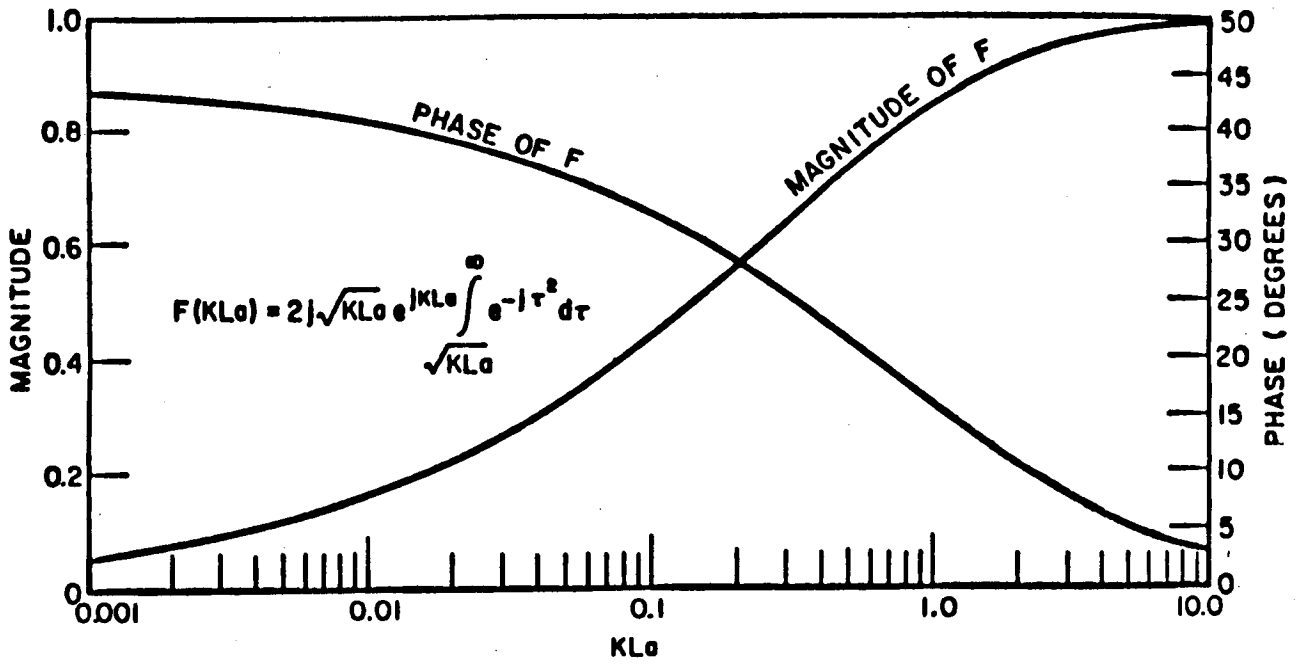

Figure 2.3. Transition function.

C. CURVED EDGE DIFFRACTION

The diffracted field from a curved surface with a curved edge, as shown in Figure 2.4, is given by [1]

$$\vec{E}^d = \vec{E}^i(Q_E) \cdot(-\hat{\beta}_o' \hat{\beta}_o D_s - \hat{\phi}'\hat{\phi} D_h) A(s,s')e^{-jks} \tag{2.16}$$

where

$$D_{s,h} = \frac{-e^{-j\pi/4}}{2n\sqrt{2\pi k}} \sin\beta_o \Bigg[\cot\left(\frac{\pi+(\phi-\phi')}{2n}\right) F(kL^i a^+(\phi-\phi'))$$

$$+ \cot\left(\frac{\pi-(\phi-\phi')}{2n}\right) F(kL^i a^-(\phi-\phi'))$$

$$\mp \cot\left(\frac{\pi+(\phi+\phi')}{2n}\right) F(kL^{rn} a^+(\phi-\phi'))$$

$$\mp \cot\left(\frac{\pi-(\phi+\phi')}{2n}\right) F(kL^{ro} a^-(\phi+\phi')) \Bigg] \tag{2.17}$$

The following parameters are used in this solution:

$$A(s,s') = \sqrt{\frac{\rho_c}{s(\rho_c+s)}} \tag{2.18}$$

$$\frac{1}{\rho_c} = \frac{1}{\rho_e^i} - \frac{\hat{n}_e\cdot(\hat{s}'-\hat{s})}{\rho_g \sin^2\beta_o'} \tag{2.19}$$

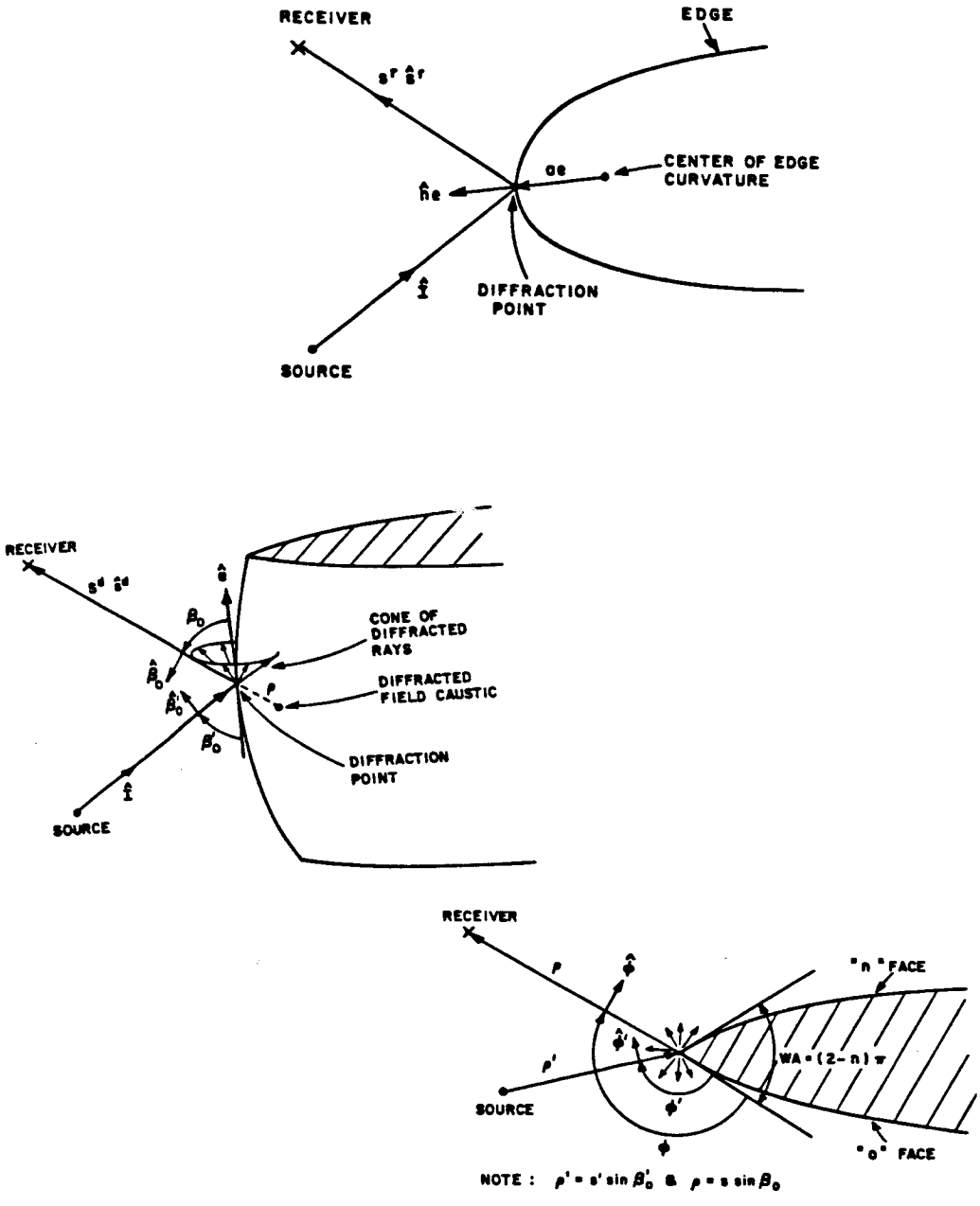

Figure 2.4. Geometry of curved wedge with curved edge.

ρ_e^i = radius of curvature of incidence wavefront in the edge-fixed plane of incidence which contains unit vectors s and e (infinite for plane, cylindrical, and conical waves; = s' for spherical waves).

ρ_g = radius of curvature of edge at diffraction point.

$\hat{n}_e$ = unit vector normal to edge at Q and directed away from the center of curvature.

$\hat{e}$ = unit vector tangent to edge at the point of diffraction.

$$L^i = \frac{s(\rho_e^i + s)\ \rho_1^i\ \rho_2^i}{\rho_e^i\ (\rho_1^i + s)(\rho_2^i + s)} \sin^2\beta_o \qquad (2.20)$$

$\rho_{1,2}^i$ = principal radii of curvature of the incident wavefront.

$$L^{r(n,o)} = \frac{s(\rho_e^r + s)\ \rho_1^r\ \rho_2^r}{\rho_e^r\ (\rho_1^r + s)(\rho_2^r + s)} \sin^2\beta_o \qquad (2.21)$$

(L^{rn} is L^r for "N" face, L^{ro} is L^r for "O" face)

ρ_e^r = reflected radius of curvature in the plane containing the reflected ray and edge ($\hat{e}$):

$$\frac{1}{\rho_e^r} = \frac{1}{\rho_e^i} - \frac{2(\hat{n}\cdot\hat{n}_e)(\hat{I}\cdot\hat{n})}{\rho_g \sin^2\beta_o} \qquad (2.22)$$

$\rho^r_{1,2}$ = principal radii of curvature of reflected wavefront [1].

$$a^{\pm}(\beta) = 2\cos\frac{2\ 2n\pi\ N^{\pm}-\beta}{2} \tag{2.23}$$

$N^{\pm}$ = integers which most satisfy the equations: $2\pi nN^{\pm}-\beta = \pm\pi$

$$\hat{\phi}' = \frac{\hat{I} \times \hat{e}}{|\hat{I} \times \hat{e}|} \tag{2.24}$$

$$\hat{\beta}' = \frac{\hat{I} \times \hat{\phi}}{|\hat{I} \times \hat{\phi}|} \tag{2.25}$$

$$\hat{\phi} = \frac{\hat{e} \times \hat{s}}{|\hat{e} \times \hat{s}|} \quad \text{, and} \tag{2.26}$$

$$\hat{\beta} = \frac{\hat{s} \times \hat{\phi}}{|\hat{s} \times \hat{\phi}|} \quad . \tag{2.27}$$

D. CORNER DIFFRACTION

The diffracted field from a corner, as shown in Figures 2.5 and 2.6 is the sum of contributions from each of the edges forming the corner. Each contribution is expressed as follows [3]:

$$\begin{bmatrix} E^c_{\beta o} \\ E^c_{\phi} \end{bmatrix} = \begin{bmatrix} -D^c_s & 0 \\ 0 & -D^c_h \end{bmatrix} \begin{bmatrix} E^i_{\beta' o} \\ E^i_{\phi'} \end{bmatrix} \sqrt{\frac{s'}{s''(s'+s'')}} \sqrt{\frac{s(s+s_c)}{sc}} \frac{e^{-jks}}{s} \tag{2.28}$$

where

$$D^c_{s,h} = \frac{e^{-j\pi/4}}{\sqrt{2\pi k}} C_{\substack{s \\ h}}(Q_E) \frac{\sqrt{\sin\beta_c \sin\beta_{oc}}}{\cos\beta_{oc} - \cos\beta_c} F(kL_c a(\pi+\beta_{oc}-\beta_c)) \tag{2.29}$$

$$C_{s_h} = \frac{-e^{-j\pi/4}}{2n\sqrt{2\pi\kappa}\,\sin\beta_o} \cdot$$

$$\cdot \left[\cot\left[\frac{\pi+(\phi-\phi')}{2n}\right] F(\kappa L^i a^+(\phi-\phi')) \left| F\left[\frac{L^i a^+(\beta^-)/\lambda}{\kappa L_c a(\pi+\beta_{oc}-\beta_c)}\right]\right| \right.$$

$$+ \cot\left[\frac{\pi-(\phi-\phi')}{2n}\right] F(\kappa L^i a^-(\phi-\phi')) \left| F\left[\frac{L^i a^-(\beta^-)/\lambda}{\kappa L_c a(\pi+\beta_{oc}-\beta_c)}\right]\right|$$

$$\mp \cot\left[\frac{\pi+(\phi+\phi')}{2n}\right] F(\kappa L^{rn} a^-(\phi+\phi')) \left| F\left[\frac{L^{rn} a^+(\beta^+)/\lambda}{\kappa L_c a(\pi+\beta_{oc}-\beta_c)}\right]\right|$$

$$\left. \mp \cot\left[\frac{\pi+(\phi+\phi')}{2n}\right] F(\kappa L^{ro} a^-(\phi+\phi')) \left| F\left[\frac{L^{ro} a^-(\beta^+)/\lambda}{\kappa L_c a(\pi+\beta_{oc}-\beta_c)}\right]\right| \right] \qquad (2.30)$$

$$L_C = \frac{\rho_C s}{\rho_C + s} \tag{2.31}$$

$$a(\psi) = 2\cos^2(\psi/2) \tag{2.32}$$

$$\beta^{\pm} = \phi \pm \phi' \tag{2.33}$$

and where ϕ, ϕ', L^i, L^{rn}, L^{ro}, $a^{\pm}(\beta)$ are defined in the previous edge diffraction section.

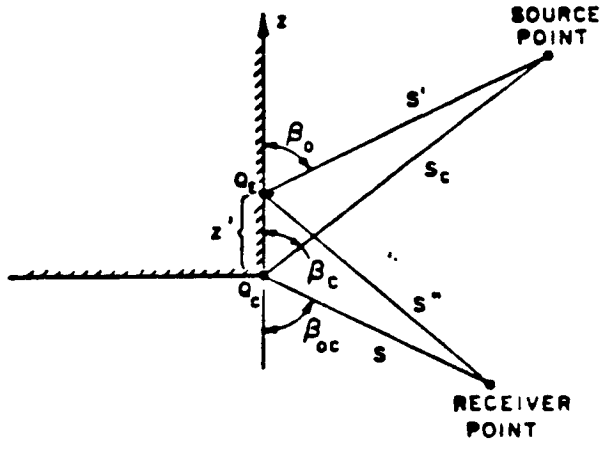

a) Corner in a planar surface.

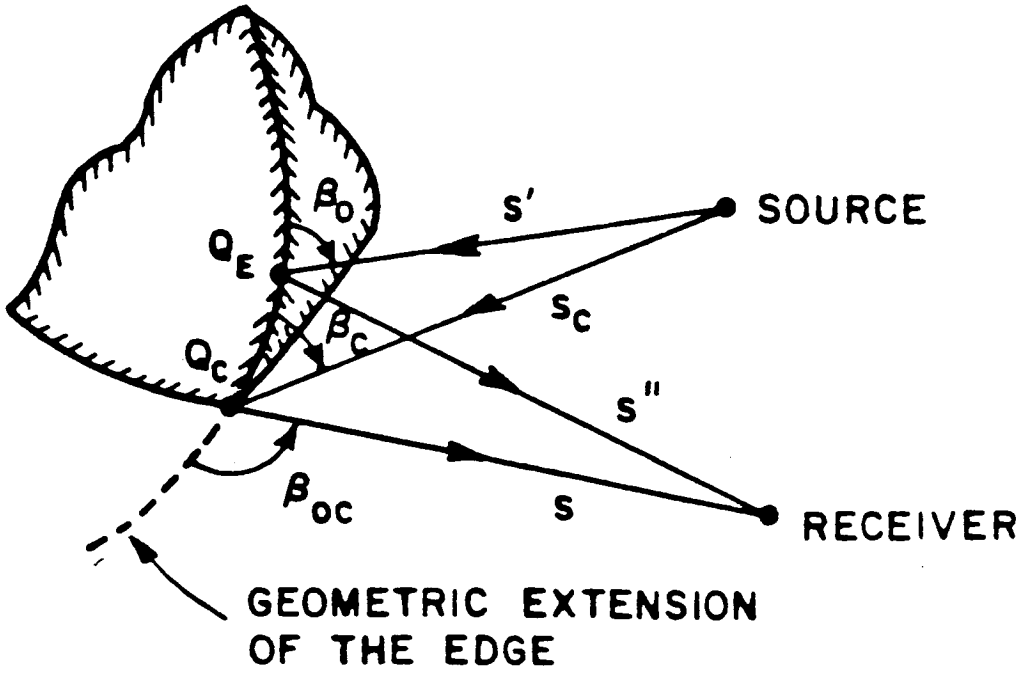

b) Corner in a non-planar surface.

Figure 2.5. Geometry for corner diffraction problem.

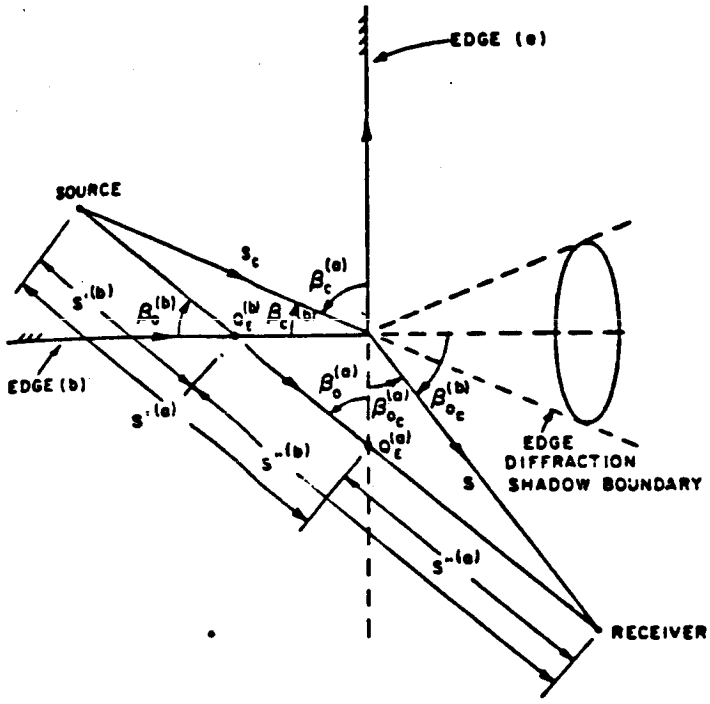

a) Case where only one edge diffracted field and both corner fields are received.

Figure 2.6. Various corner diffraction geometry.

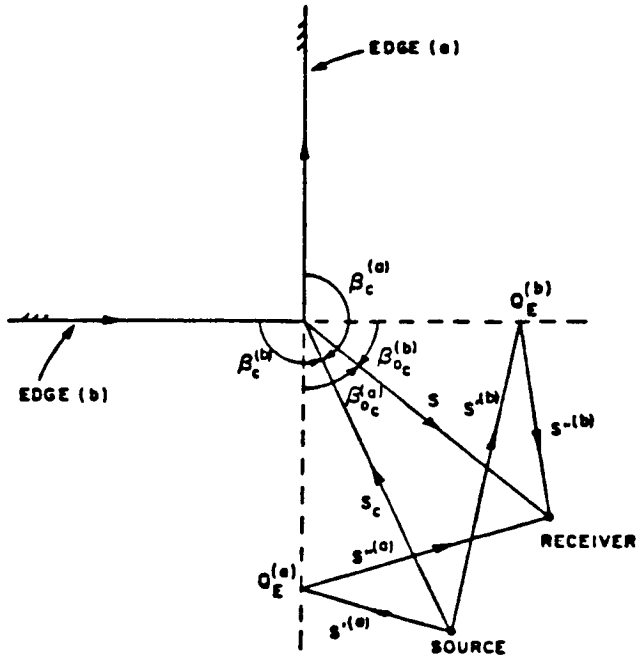

b) Case where only corner fields are received.

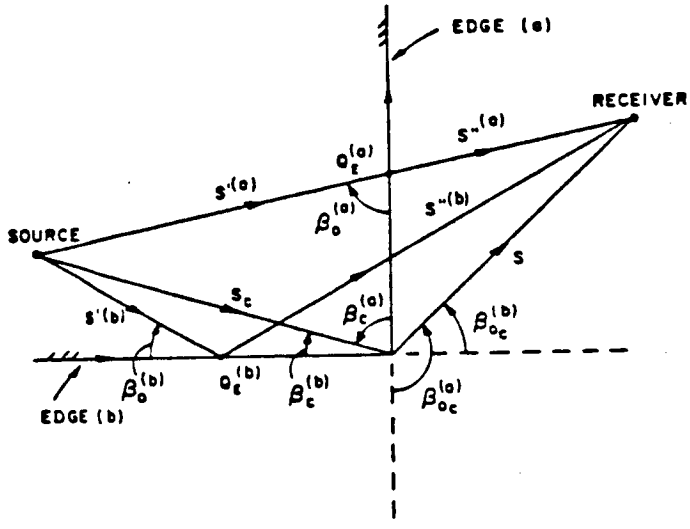

c) Case where all edge and corner diffracted fields are received.

Figure 2.6. Continued.

E. SURFACE CREEPING WAVE MECHANISM

The creeping wave on a curved surface, as shown in Figure 2.7, is given by [1]

$$\vec{E}_{creep} = \vec{E}^{i}(Q_1) \cdot \overline{\overline{T}} \sqrt{\frac{\rho_2^d}{s(\rho_2^d + s)}}\ e^{-jks} \tag{2.34}$$

where

$$\overline{\overline{T}} = T_s\ \hat{b}_1\ \hat{b}_2 + T_h\ \hat{n}_1\ \hat{n}_2 \tag{2.35}$$

$$T_{s,h} = -\sqrt{m(Q_1)m(Q_2)}\sqrt{\frac{2}{k}}\ \left\{ \frac{e^{-j\pi/4}}{2\sqrt{\pi}\xi^d}\ [1-F(x^d)] \right.$$

$$\left. + \hat{P}_{s,h}\ (\xi^d) \right\} \cdot \sqrt{\frac{dn(Q_1)}{dn(Q_2)}}\ e^{-jkt} \tag{2.36}$$

$$\xi^d = \int_{Q_1}^{Q_2} \frac{m(t')}{\rho g(t')}\, dt' \tag{2.37}$$

$$m(Q) = \left[\frac{k\ \rho_g(Q)}{2} \right]^{1/3} \tag{2.38}$$

$\rho_g(Q)$ = radius of curvature of the surface in the plane of incidence.

$$= \frac{R}{\sin^2(\omega_r)} \quad \text{for cylinder (refer to Figure 2.6).} \tag{2.39}$$

$$X^d = \frac{kL^d(\xi^d)^2}{2m(Q_1)m(Q_2)} \tag{2.40}$$

$$L^d = \begin{cases} s' \text{ , in the far zone} \\ \\ \dfrac{ss'}{s+s'} \text{ , in the near zone} \end{cases} \tag{2.41}$$

$\hat{n}_{1,2}$ = outward unit normal of surface.

$\hat{t}_{1,2}$ = unit tangent vector to the surface ray at $Q_{1,2}$

$$\hat{b}_{1,2} = \hat{t}_{1,2} \times \hat{n}_{1,2} \tag{2.42}$$

t = arc length of creeping wave.

$$\sqrt{\frac{dn(Q_1)}{dn(Q_2)}} = \sqrt{\frac{s'}{s'+t}} \tag{2.43}$$

ρ_2^d = caustic distance

$$= s'+t \tag{2.44}$$

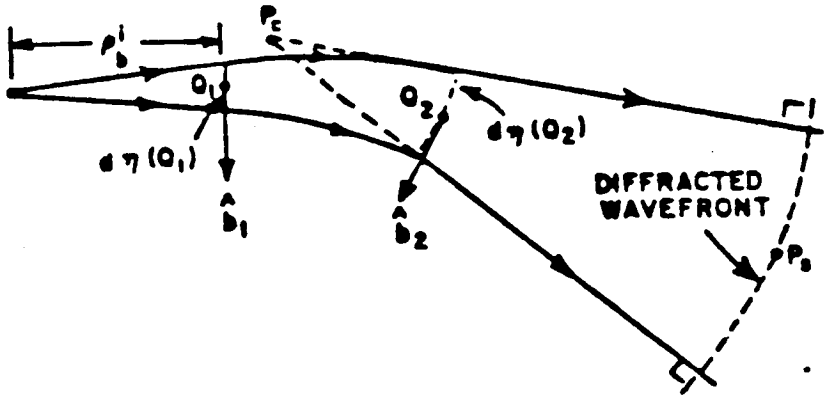

a) top view

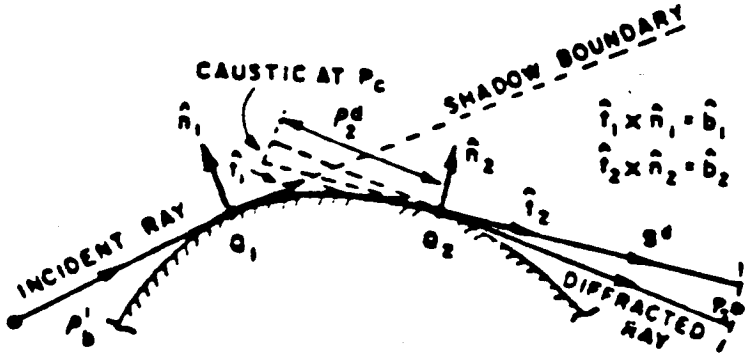

b) side view

Figure 2.7. Creeping wave geometry.

CHAPTER III

RADAR CROSS SECTION OF PEDESTAL

A. INTRODUCTION

The radar cross section (RCS) of the pedestal is calculated in this chapter with the target mounted in two ways: 1) the target is mounted with a shaft a certain height above the top of the pedestal as shown in Figure 3.1a, and 2) the target is flush-mounted on the top of the pedestal as shown in Figure 3.1b.

An analysis of how the RCS changes as a function of the angle of inclination of the pedestal as well as its shape is given. The idea is to show how one can effectively reduce the RCS of the target support without sacrificing the stability of the pedestal.

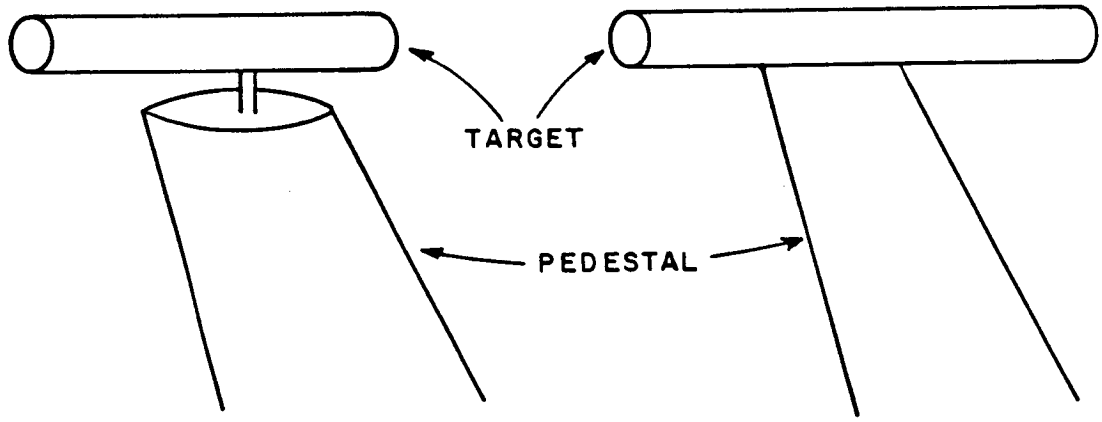

a) elevated-mounting b) flush-mounting

Figure 3.1. Two options of pedestal mounting.

B. THEORETICAL BACKGROUND

When the incident plane wave strikes the pedestal, there is the potential for a corner diffraction, an edge diffraction, reflection, and primary and secondary creeping wave mechanisms as illustrated in Figure 3.2. However, the shape of the pedestal directs most of the scattering mechanisms away from the backscatter direction. For example, since the pedestal is inclined with respect to the vertical, the incident wave is diffracted downward by the front edge. Since the pedestal side is illuminated near grazing incidence the incident wave is reflected back toward the chamber back wall. Since the upper edges curve backward, the incident wave is diffracted to the rear. Hence, the only mechanisms that can cause a significant backscatter are corner diffraction and secondary creeping wave mechanisms. Since there is no known solution for the secondary creeping wave mechanism, it is ignored; however, as will be seen from the results, it is not essential here. Although the corner diffraction from the front apex is composed of the contributions from each of the three edges forming the corner, the upper two edges are ignored since their major contributions as shown in Figure 3.2 are rather far away from the backscatter direction. Thus, the only contribution to backscatter considered here is the corner diffraction caused by the front edge.

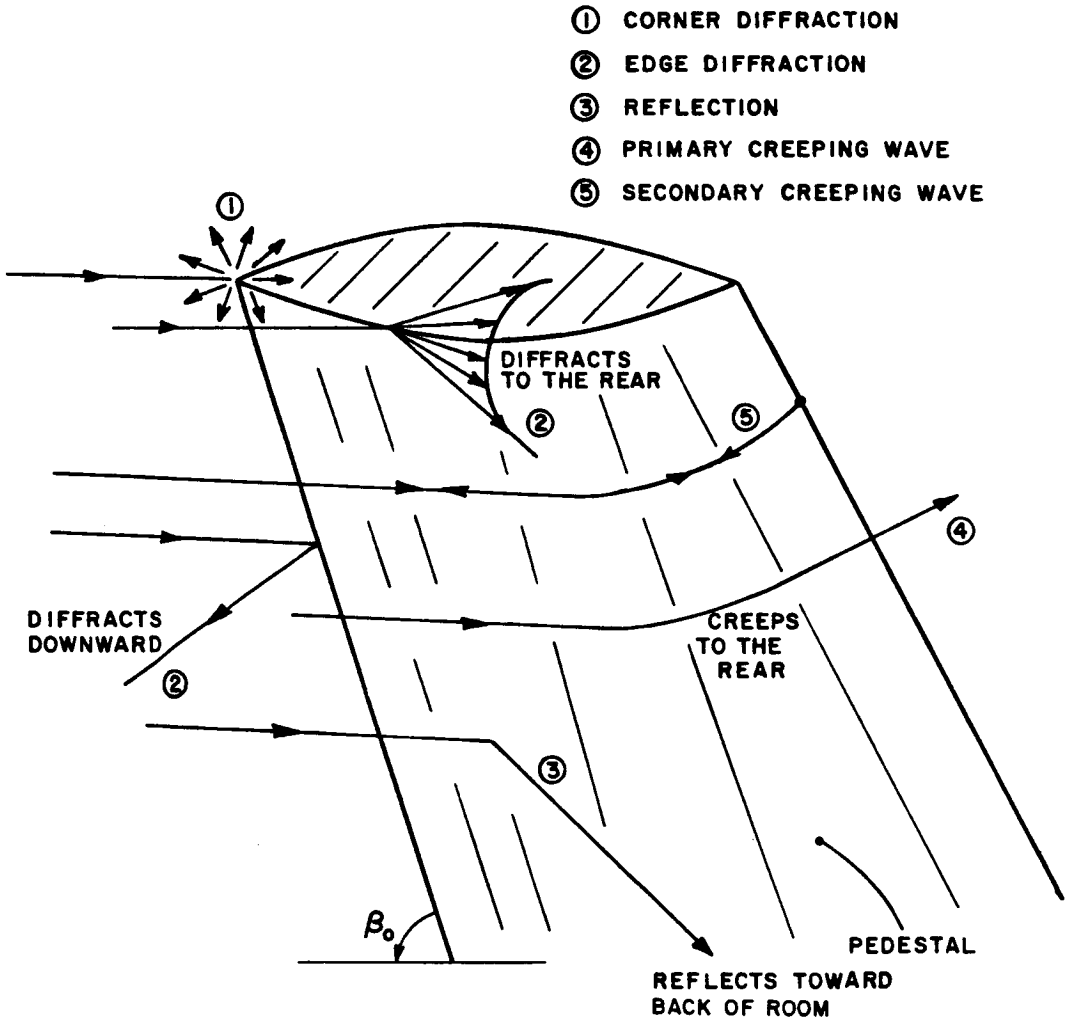

Figure 3.2. Various scattering mechanisms from the pedestal.

The corner diffracted field from the termination of the leading edge is simply an application of Equation (2.15) and is given by

$$\begin{bmatrix} E^c_{\beta o} \\ E^c_{\beta} \end{bmatrix} = \begin{bmatrix} -D^c_s & 0 \\ 0 & -D^c_h \end{bmatrix} \begin{bmatrix} E^i_{\beta o'} \\ E^i_{\phi'} \end{bmatrix} \sqrt{\frac{s'}{s''(s'+s'')}} \sqrt{\frac{s(s+s_c)}{s_c}} \frac{e^{-jks}}{s} \tag{3.1}$$

For the contribution from front edge as illustrated in Figure 3.3, distance parameters are specifically defined by

$$L^i = s \sin^2\beta_o \tag{3.2}$$

$$L^{rn} = L^{ro} = \frac{s \cdot \bar{R}}{(s+R)} \sin^2\beta_o \quad , \text{ and} \tag{3.3}$$

$$L_c = \frac{\rho_c s}{\rho_c} \tag{3.4}$$

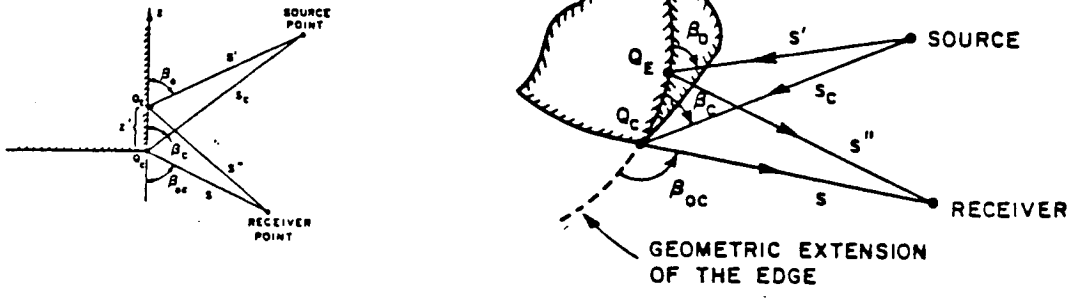

a) Corner in a planar surface b) Corner in a non-planar surface

Figure 3.3. Corner diffraction geometry.

C. ELEVATED-MOUNTING PEDESTAL

The elevated-mounting pedestal is modeled by a simple slanted ogive as shown in Figure 3.4. To support the validity of this UTD result, the RCS of our pedestal was measured and is shown in Figure 3.5. Note the good agreement between measured and calculated result. In order to illustrate how the RCS of the pedestal varies relative to its design parameters, Figure 3.6 illustrates the RCS for several pedestal designs. In each case, the RCS decreases as the inclination angle (β_0) is decreased. The most pronounced decrease occurs between 89° and 75°, where it drops about 25 dbsm. After that it decreases steadily at about 3 dbsm per 10°. As one increases frequency, the RCS decreases. For example, at a 60° angle of inclination, the RCS drops about 6 dbsm going from 1 to 2 Ghz. Changing the wedge angle also affects the RCS. From Figures 3.6a through c, it is shown that the RCS increases with increasing wedge angle. This result compares well with a previous analysis of the front edge of the pedestal by Rudduck et al. [5].

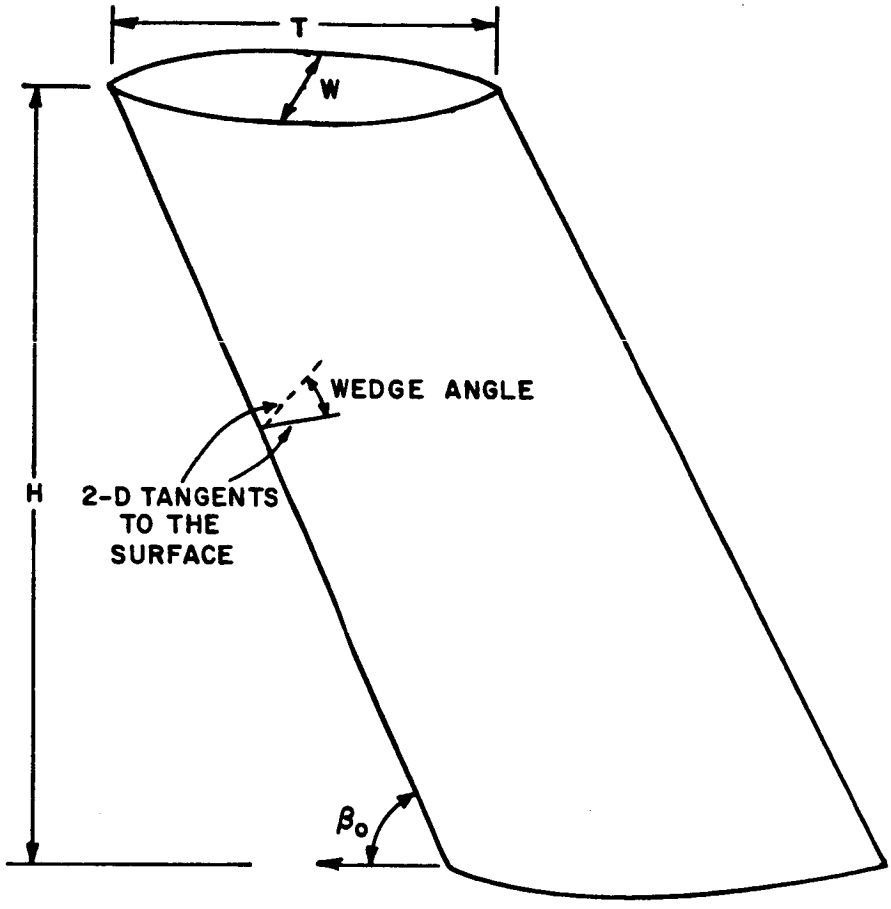

Figure 3.4. Elevated-mounting pedestal model.

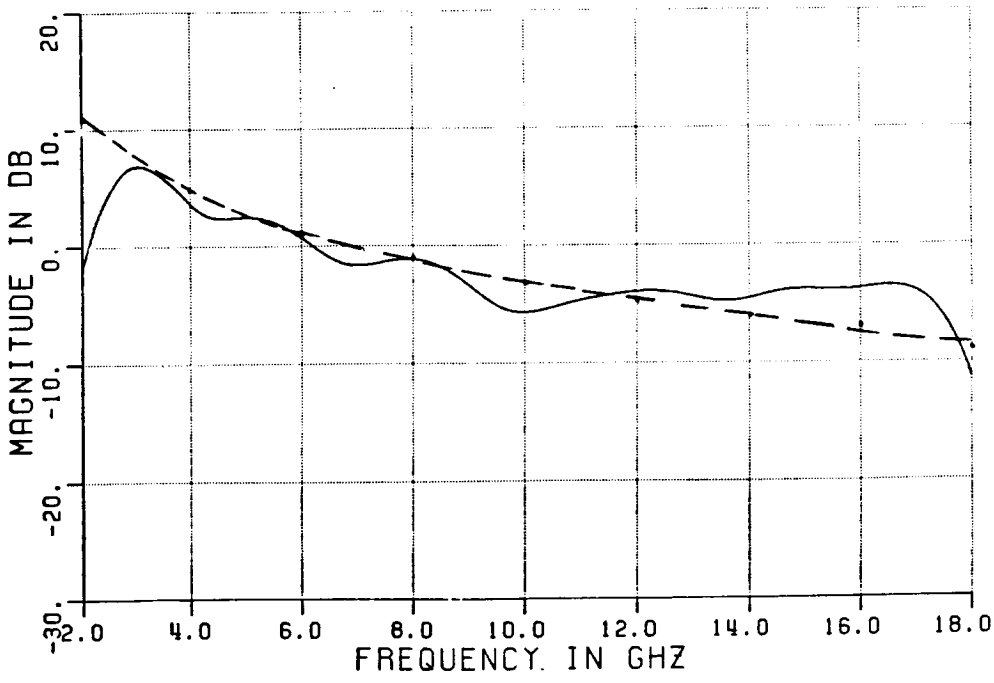

a) vertical polarization

_____ measured result
_ _ _ _ _ _ _ _ calculated result

Figure 3.5. Measured RCS of pedestal at various frequencies with T=14", W=4", β_0=75°.

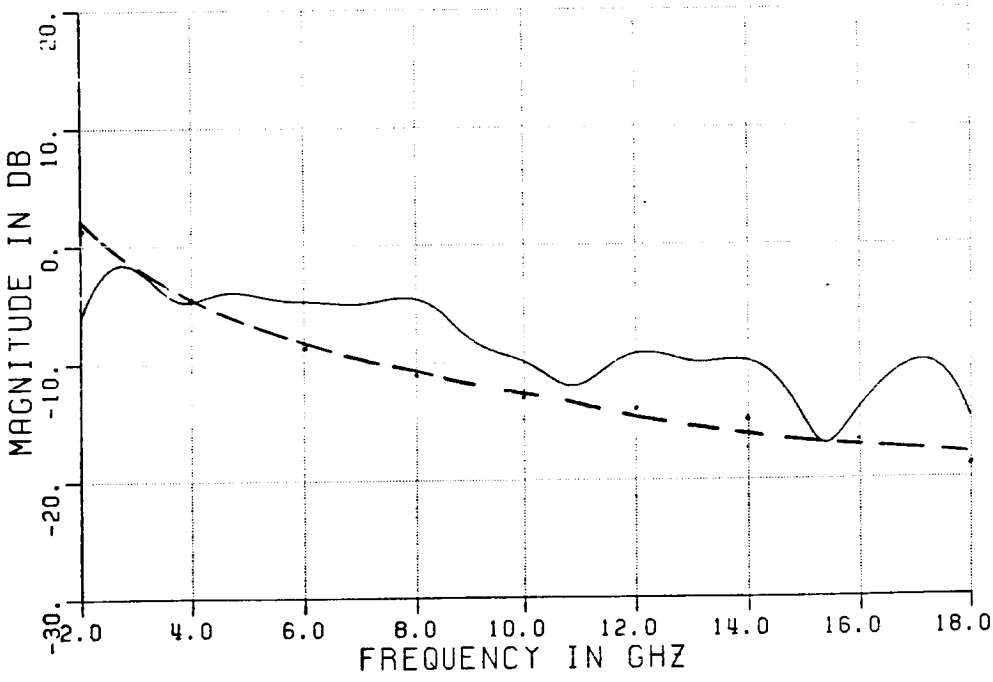

b) horizontal polarization

_____ measured result
_ _ _ _ _ _ _ _ calculated result

Figure 3.5. Continued.

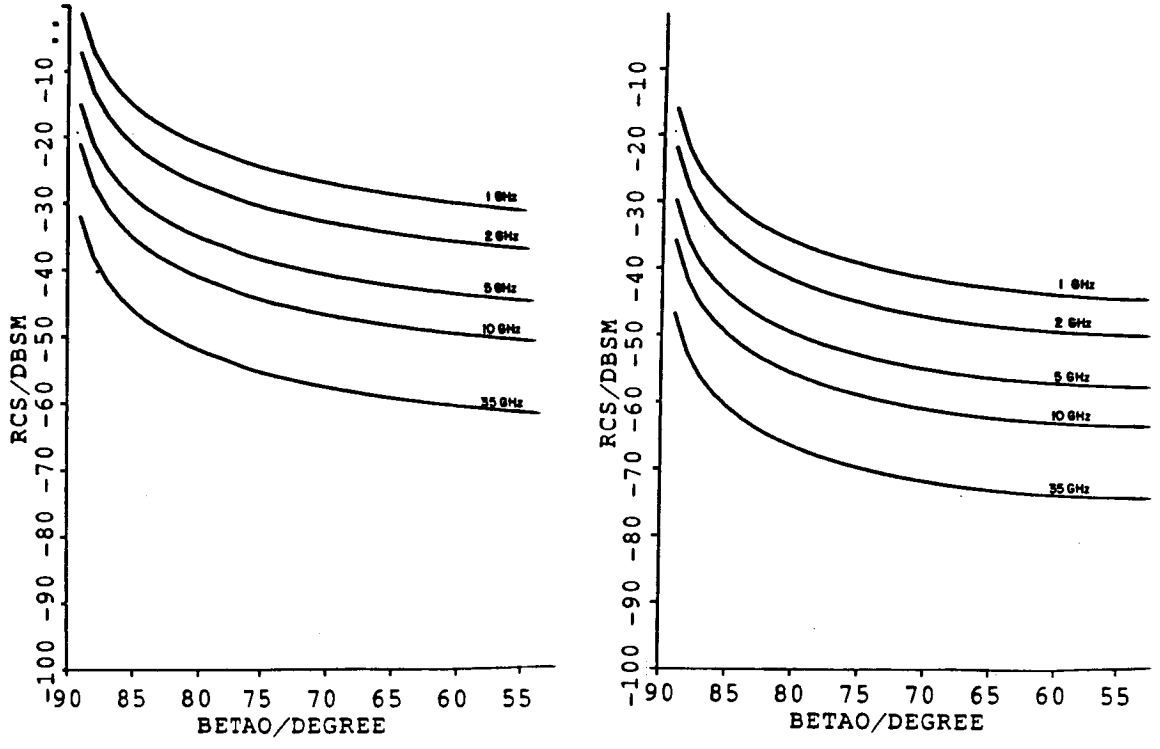

vertical polarization

horizontal polarization

a) wedge angle = 37.86°
T=0.6 meters; W=0.1 meters.

Figure 3.6. RCS of elevated-mounting pedestal.

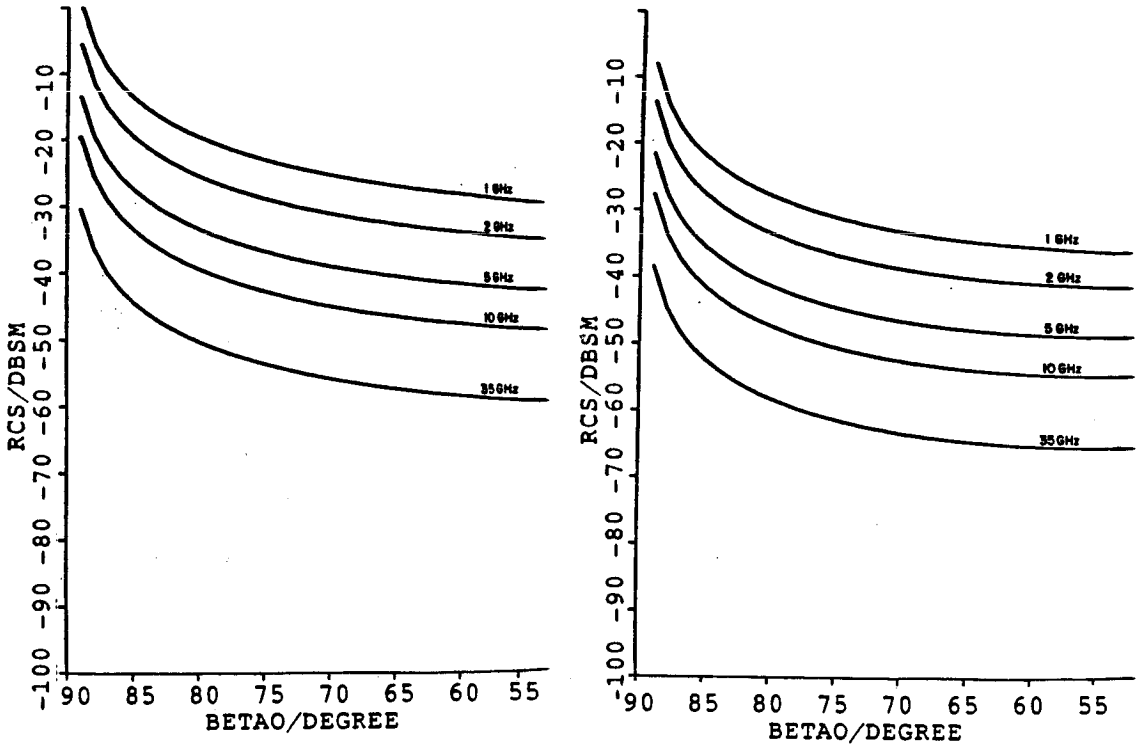

vertical polarization horizontal polarization

b) wedge angle = 73.75°
T=0.6 meters; W=0.2 meters

Figure 3.6. Continued.

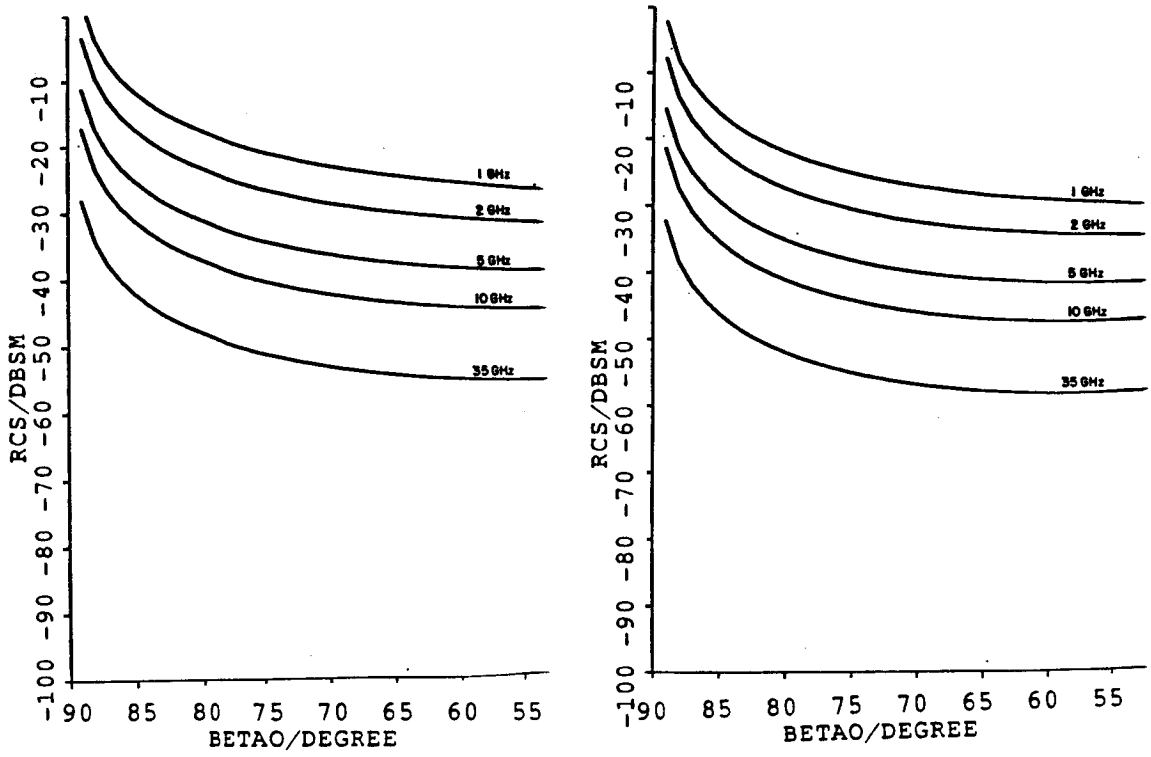

vertical polarization

horizontal polarization

c) wedge angle = 106.27°
T=0.6 meters, W=0.3 meters

Fig 3.6. Continued.

D. FLUSH-MOUNTING PEDESTAL

The flush-mounting pedestal is modeled by a simple slanted ogive with an infinite ground plane flush mounted to the top which simulates the target that would normally be mounted there (see Figure 3.7). Using image theory, the ground plane is replaced by a mirror image of the ogive as shown in Figure 3.8. The RCS is then calculated using the equivalent structure which contains the original pedestal and its image. Before the true pedestal and image geometry are calculated it is instructive to examine the RCS as the angle of the image pedestal is rotated relative to the true pedestal. This is useful in terms of understanding how the RCS changes with the image structure present. For example, one might expect that the pedestal return is smaller for the flush mounted case since the pedestal terminates into the target. This is not the case.

To show why the RCS is larger for this case, one needs to grasp how the image affects the results. So the original pedestal is fixed at an angle of inclination of 60 degrees, and the "image" pedestal is varied from $\phi = 180°$ to 110° as shown in Figure 3.9. The angle between the front edge of the original and the image pedestal is ϕ. The reason for fixing the observation point with respect to one edge and varying the other edge is to see how the RCS changes as one moves the observation point from the lit region (see Figure 3.10a) to the shadow region (see Figure 3.10c) of the front edge of the pedestal (in this case, the image pedestal). On each curve, the RCS first increases, becomes infinite, and then decreases as the β_0 angle decreases. The RCS becomes infinite

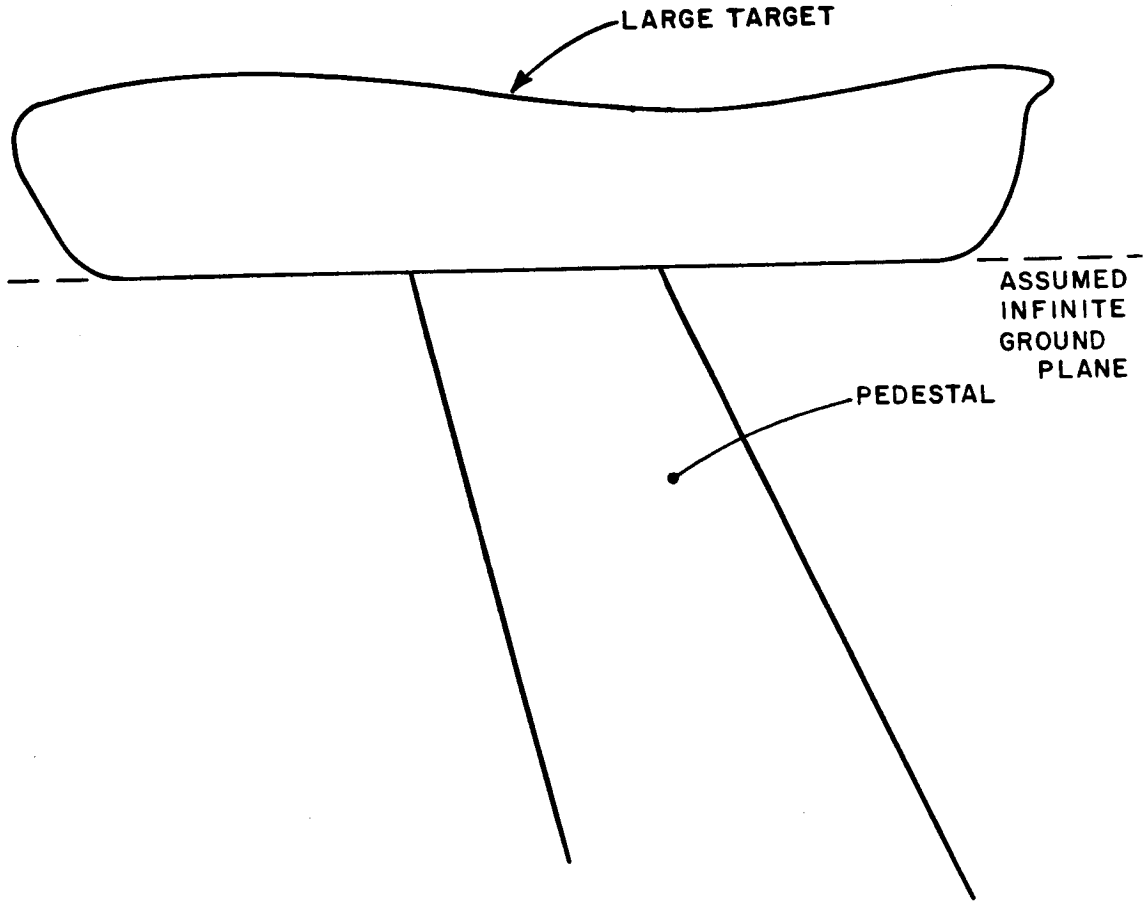

Figure 3.7. Flush-mounting pedestal.

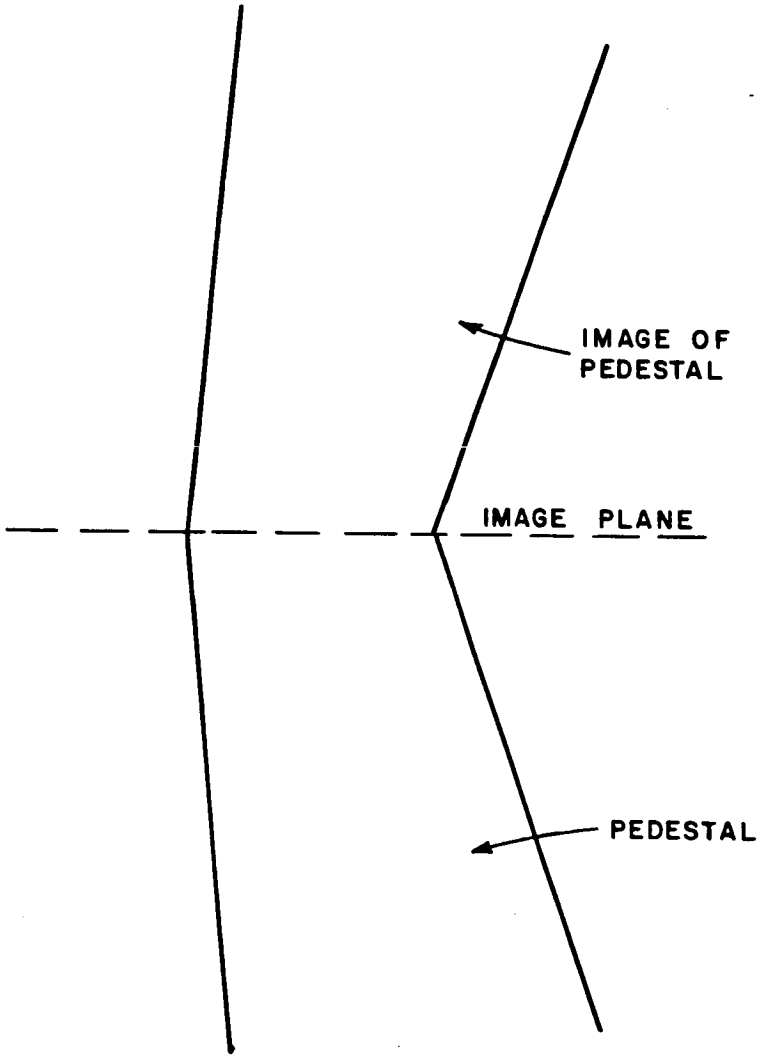

Figure 3.8. Image equivalent of flush-mounting pedestal.

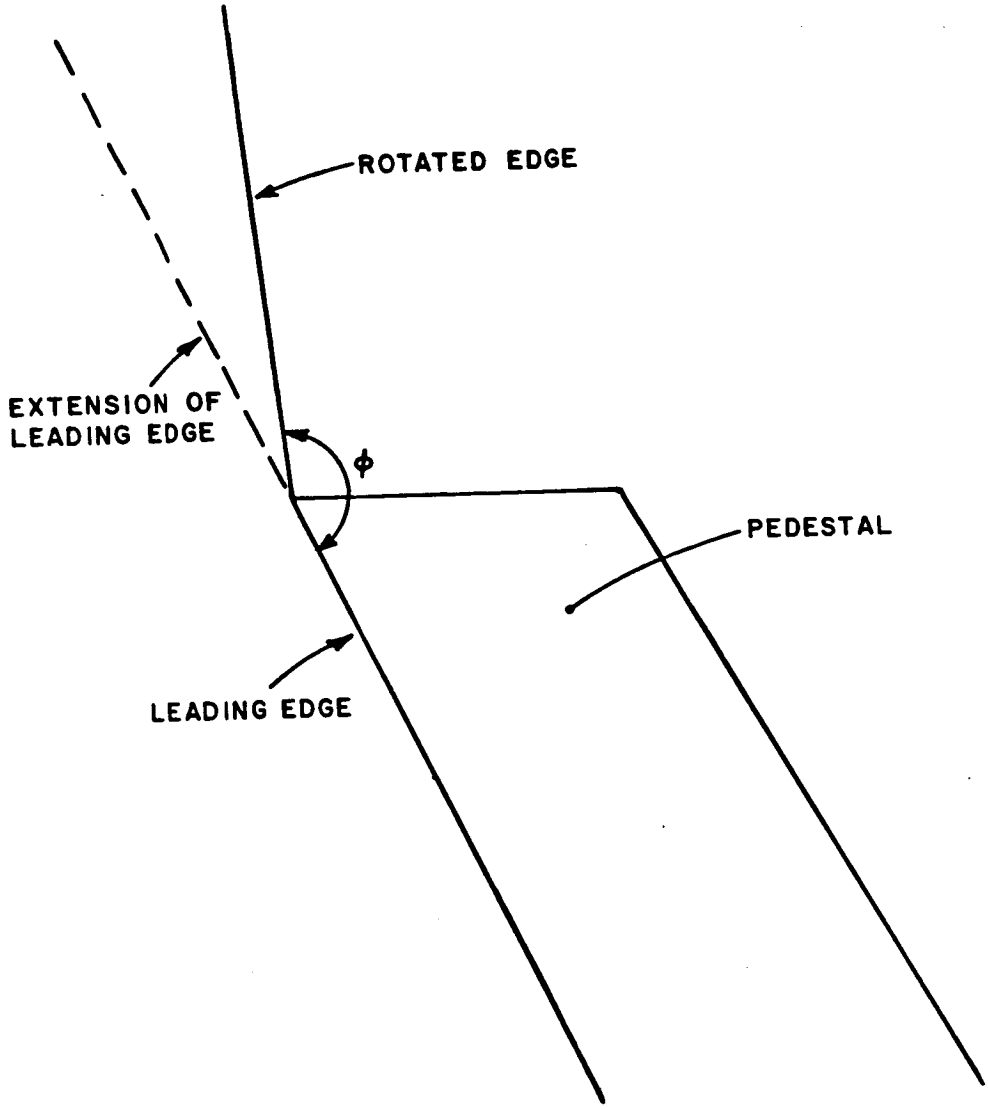

Figure 3.9. Geometry of RCS calculation of flush-mounting pedestal.

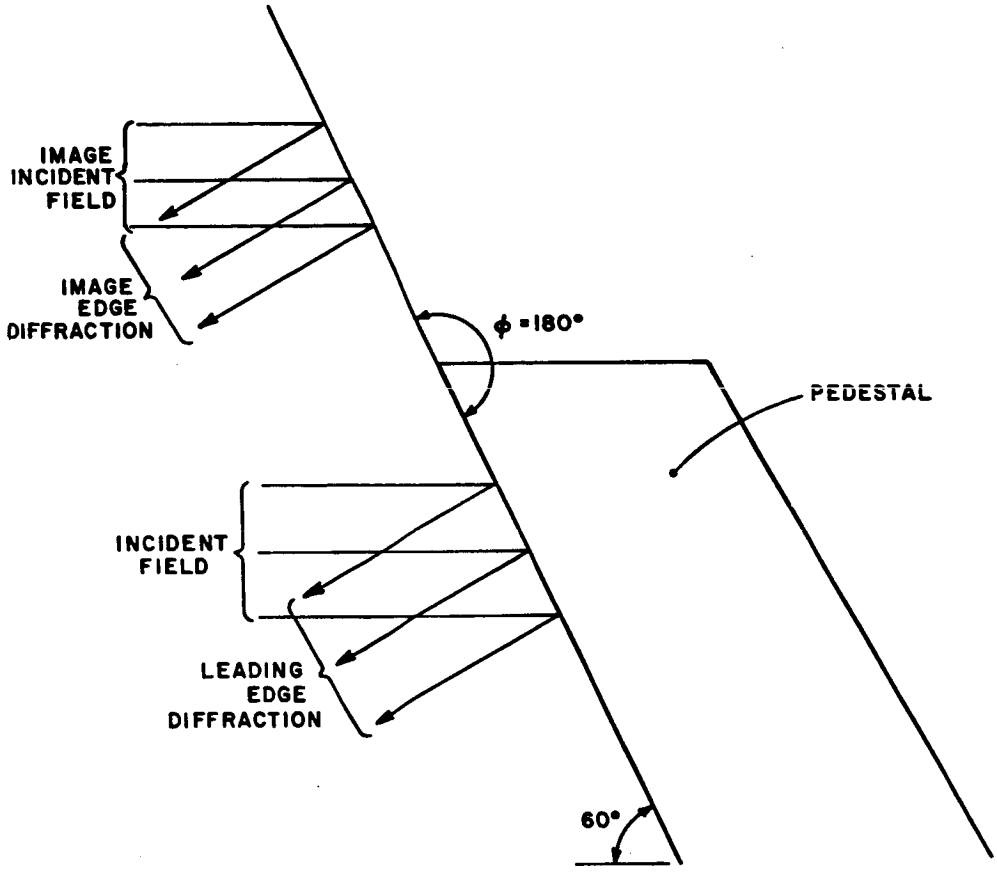

a) The observation point in the lit region

Figure 3.10. The effect of rotating the upper edge.

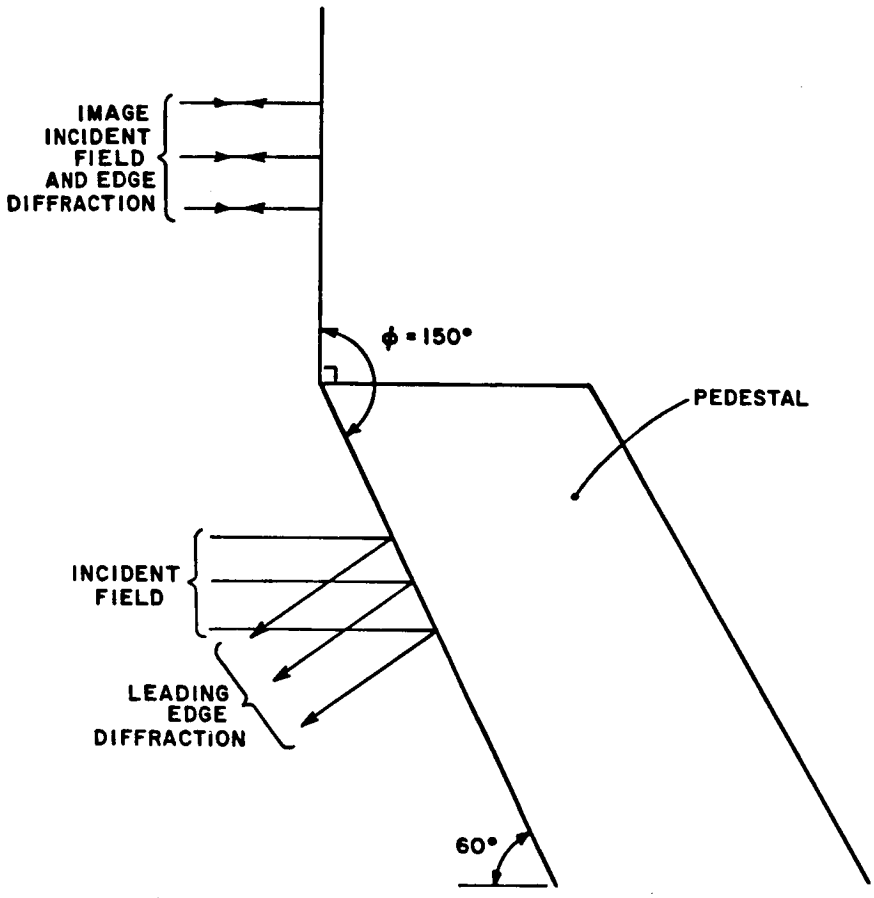

b) The observation point on the shadow boundary of the upper edge

Figure 3.10. Continued.

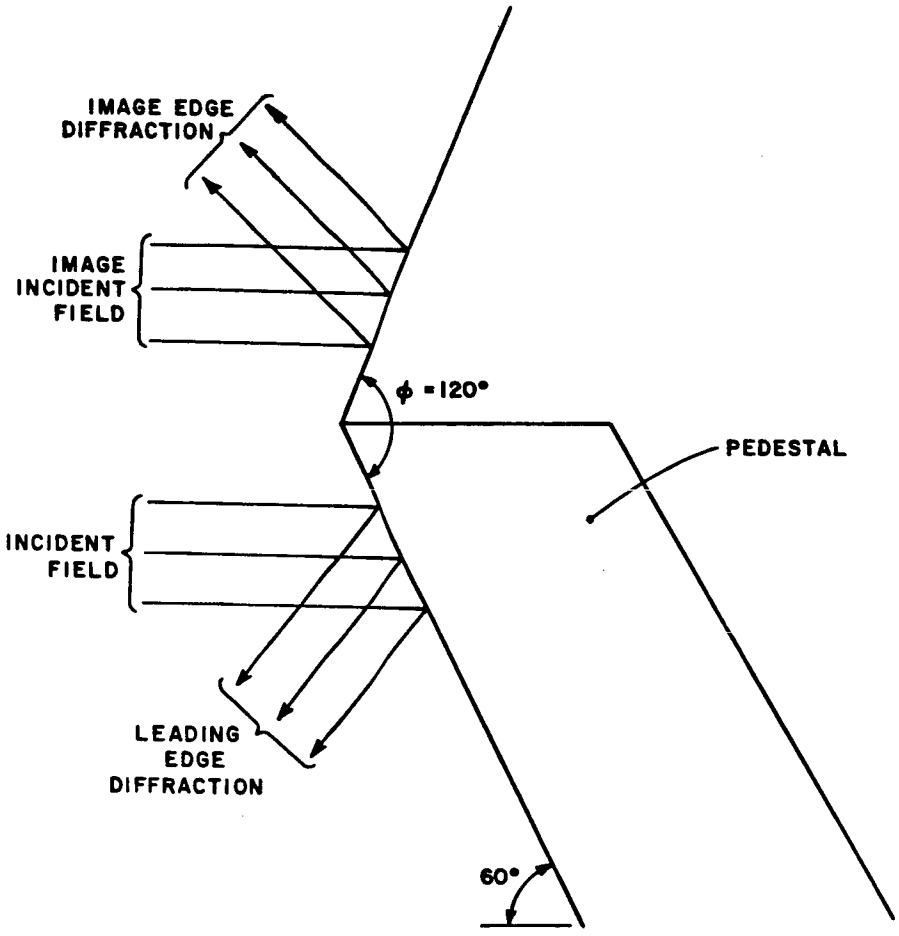

c) The observation point in the shadow region of the upper edge

Figure 3.10. Continued.

because at that angle the upper part is perpendicular to the incoming wave so that the observation point is in the caustic region (see Figure 3.10b).

The RCS of the flush-mounting pedestal is shown in Figure 3.11. As the frequency increases, the RCS decreases. For example, at a 60° angle of inclination, the RCS decreases by 6 dbsm going from 1 GHz to 2 GHz.

As before, changing the wedge angle affects the RCS of the pedestal. The trend is similar for the same reasons stated before and can be observed by comparing Figures 3.11a, b, and c.

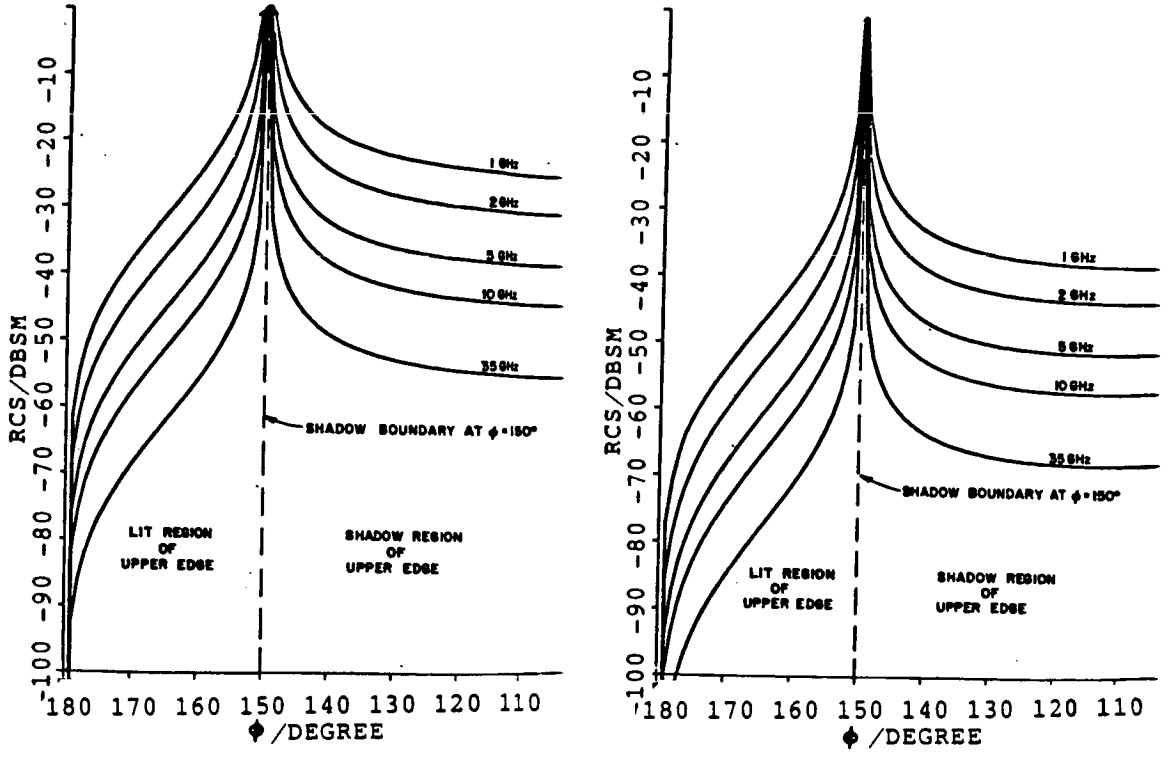

Vertical polarization horizontal polarization

a) wedge angle = 37.86°
T=0.6 meters; W=0.1 meters

Figure 3.11. RCS of flush-mounting pedestal.

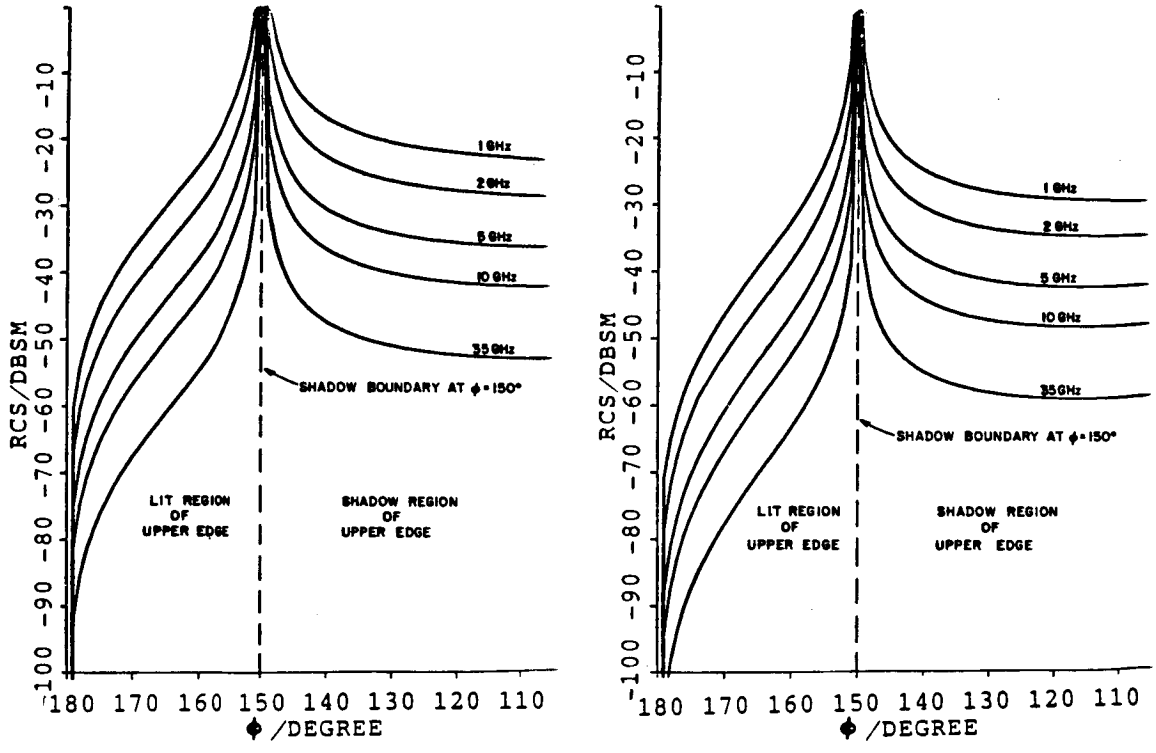

Vertical polarization horizontal polarization

b) wedge angle = 73.75°
T=0.6 meters; W=0.2 meters

Figure 3.11. Continued.

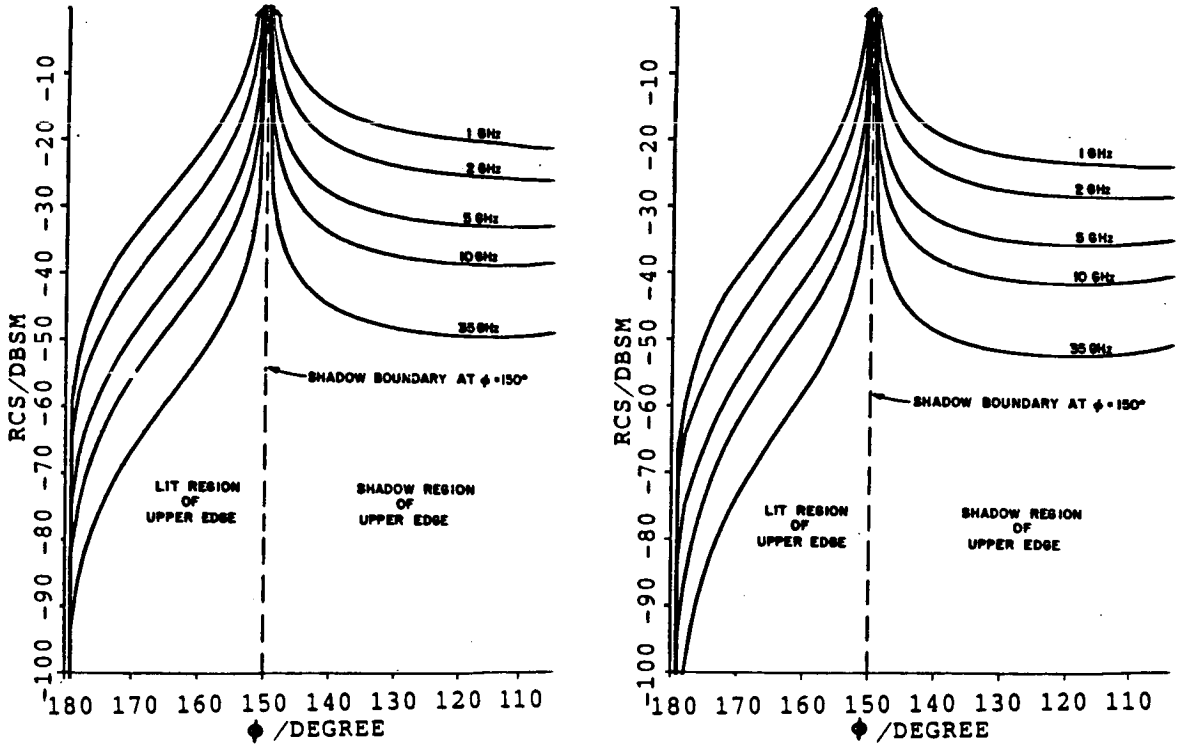

Vertical polarization

horizontal polarization

c) wedge angle = 106.27°
T=0.6 meters; W=0.3 meters

Figure 3.11. Continued.

E. CONCLUSION

In this chapter, it was observed how changing the type of mounting, the angle of inclination and the incident wave frequency affected the RCS of the pedestal. A judicious choice must be made by the pedestal design engineer in choosing which combination would suit his needs best in getting the lowest RCS results using small inclination angles (β_0) and small edge angles. These requirements are obviously counter to handling large and heavy targets.

The flush-mounting pedestal has a higher RCS than the elevated-mounting pedestal. This can be seen by comparing Figure 3.6 and 3.11. For example, at a 60° angle of inclination and 1 GHz, the RCS of the elevated-mounting pedestal is -30 dbsm for vertical polarization while the RCS of the flush-mounting pedestal is -24 dbsm. The RCS decreases rapidly when one decreases the angle of inclination to about 75°. After that, the decrease is steady at about 3 dbsm per 10°. This angle cannot be too small because the stability of the pedestal would be threatened depending on the shape and material of the pedestal and a compromise must then be made. As the frequency increases, the RCS of the pedestal decreases by λ^2, where λ is the wavelength. This is obviously the most flexible variable affecting the RCS of the pedestal: a well-equipped laboratory could set up a 35 GHz system which would drive the RCS down to -50 dbsm easily. By decreasing the wedge angle, one can also decrease the RCS as observed by comparing Figures 3.6a, b, and c, or by comparing Figures 3.11 a, b, and c.

CHAPTER IV

BISTATIC SCATTERING BY TARGET PEDESTAL

A. INTRODUCTION

The bistatic scattering of the target pedestal is analyzed in this chapter to illustrate the field structure surrounding the pedestal. In particular, an analysis of the field quality around but well below the top of the pedestal is presented to illustrate how the lower body of the pedestal perturbs the field. The space around and above the top of the pedestal where the target would be placed is addressed next.

The type of contributions included are the incident, edge diffracted, corner diffracted, surface reflected and creeping wave fields. These contribute in various regions (refer to Figure 4.1) as follows:

$$E = \begin{cases} \vec{E}^{i} + \vec{E}^{d} + \vec{E}^{d}_{c} & \text{region I} \\ \vec{E}^{i} + \vec{E}^{d} + \vec{E}^{d}_{c} + \vec{E}^{ref} & \text{region II} \\ \vec{E}^{i} + \vec{E}^{ref} & \text{region III} \\ \vec{E}^{creep} & \text{region IV} \end{cases}$$

where

$\vec{E}^{i}$ = incident field

$\vec{E}^{d}$ = edge diffracted field

$\vec{E}_{c}^{d}$ = corner diffracted field

$\vec{E}^{ref}$ = reflected field, and

$\vec{E}^{creep}$ = creeping field .

Since the major scattering occurs around the top of the pedestal, the flaring of the pedestal from top to bottom is not significant. Thus, one can use an ogival cylinder that has a constant diameter from top to bottom as shown in Figure 4.2 to simulate the pedestal scattering.

In order to illustrate the field quality near the top of the pedestal, one needs to use various pattern cuts as illustrated in Figure 4.3. An azimuth cut is shown in Figure 4.3a and represents horizontal circles centered along the mounting shaft axis. A roll plane cut is shown in Figure 4.3b and represents vertical circular cuts going from left to right with the center along the longitudinal axis of the top of the pedestal. The final one, as shown in Figure 4.3c, is an elevation cut where the observation circle wraps around the pedestal vertically from front to back with the center being along the lateral axis of the pedestal.

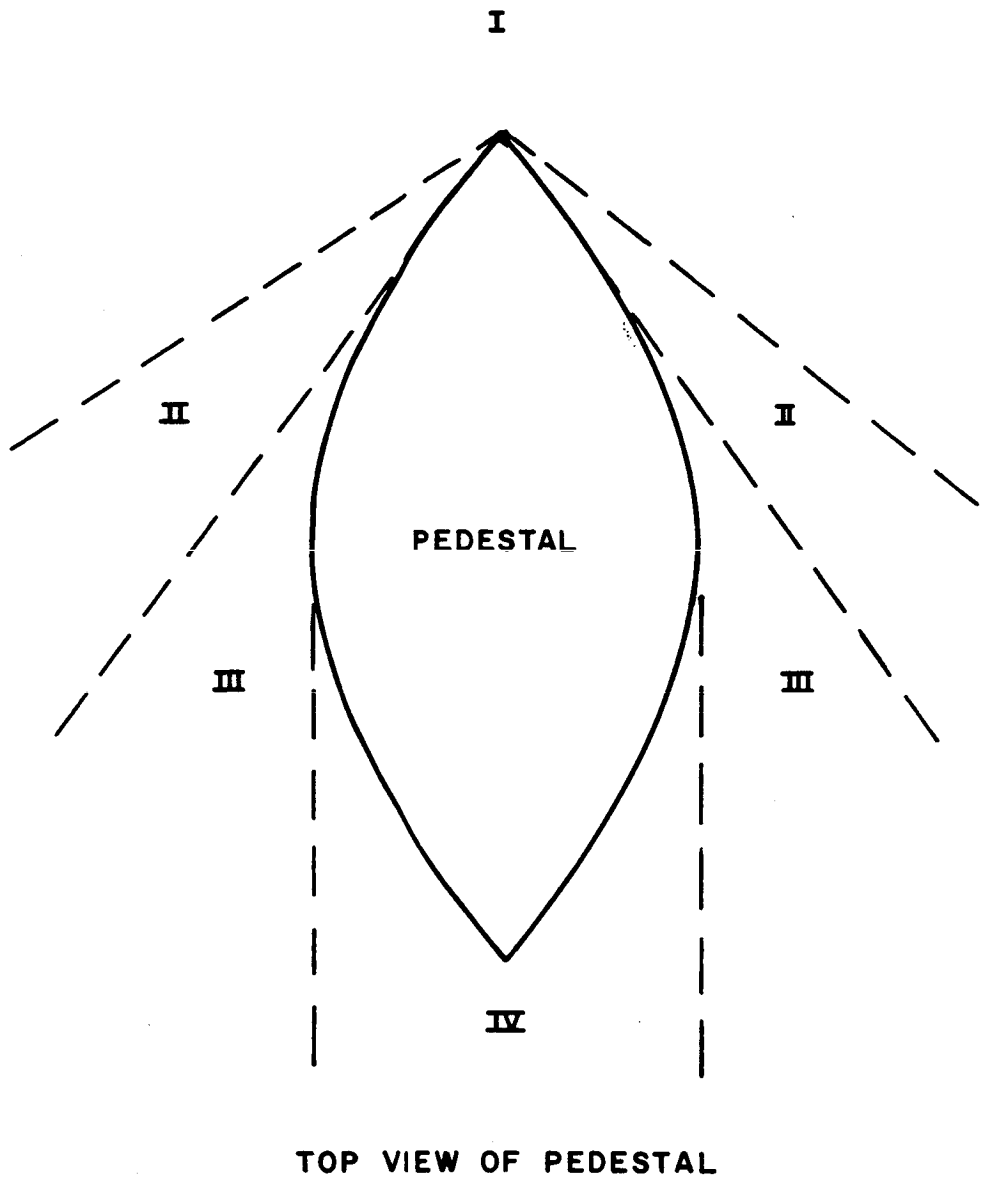

Figure 4.1. Regions of interest.

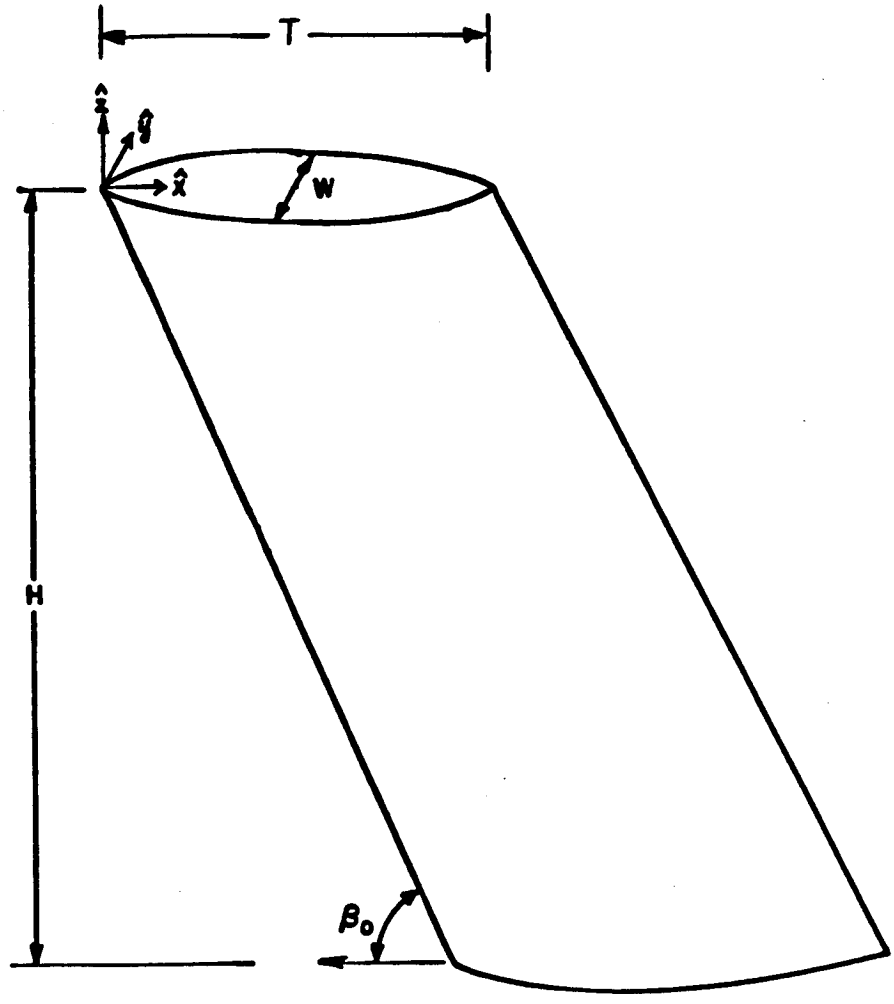

Figure 4.2. Model of pedestal in the UTD calculation.

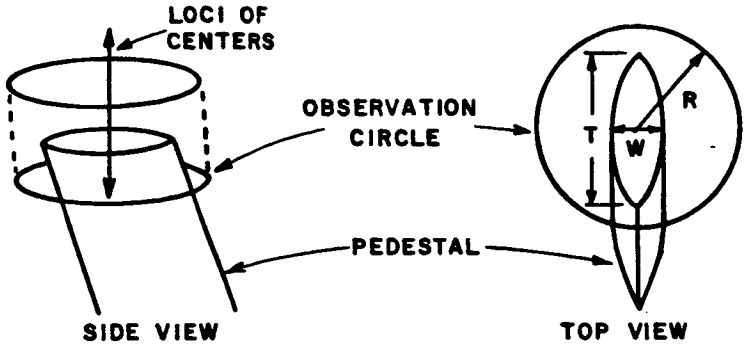

a) azimuth cut

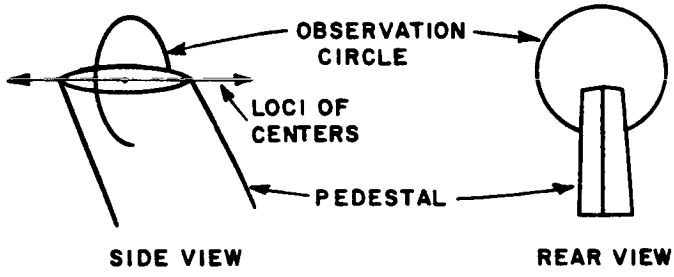

b) roll plane cut

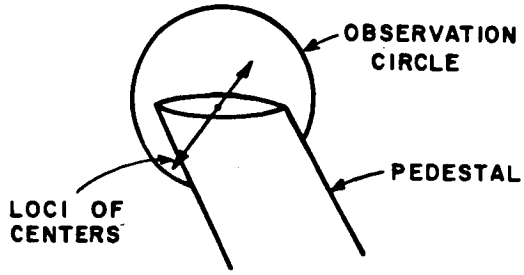

c) elevation cut

Figure 4.3. Field plotting geometry.

An example of a plot is shown in Figure 4.4. Note that all the relevant data are shown on the plot. For example, the length, width, height, and inclination angle of the pedestal are shown at the top of the figure along with the height and radius of the observation circle. The frequency and polarization of the source are also indicated. The circular plot is a db plot with the maximum db shown at the right upper corner of the plot, and the scale is always 10 dB per division. The type of field plotted is indicated below the plot.

B. BISTATIC SCATTERING AROUND PEDESTAL BELOW THE TOP

B.1. Incident Field

The incident field, as plotted in Figure 4.5, is given by:

$$E = \begin{cases} \hat{z}\, e^{-j\kappa x} & \text{not shadowed, and} \\ 0 & \text{shadowed by pedestal} \end{cases} \qquad (4.1)$$

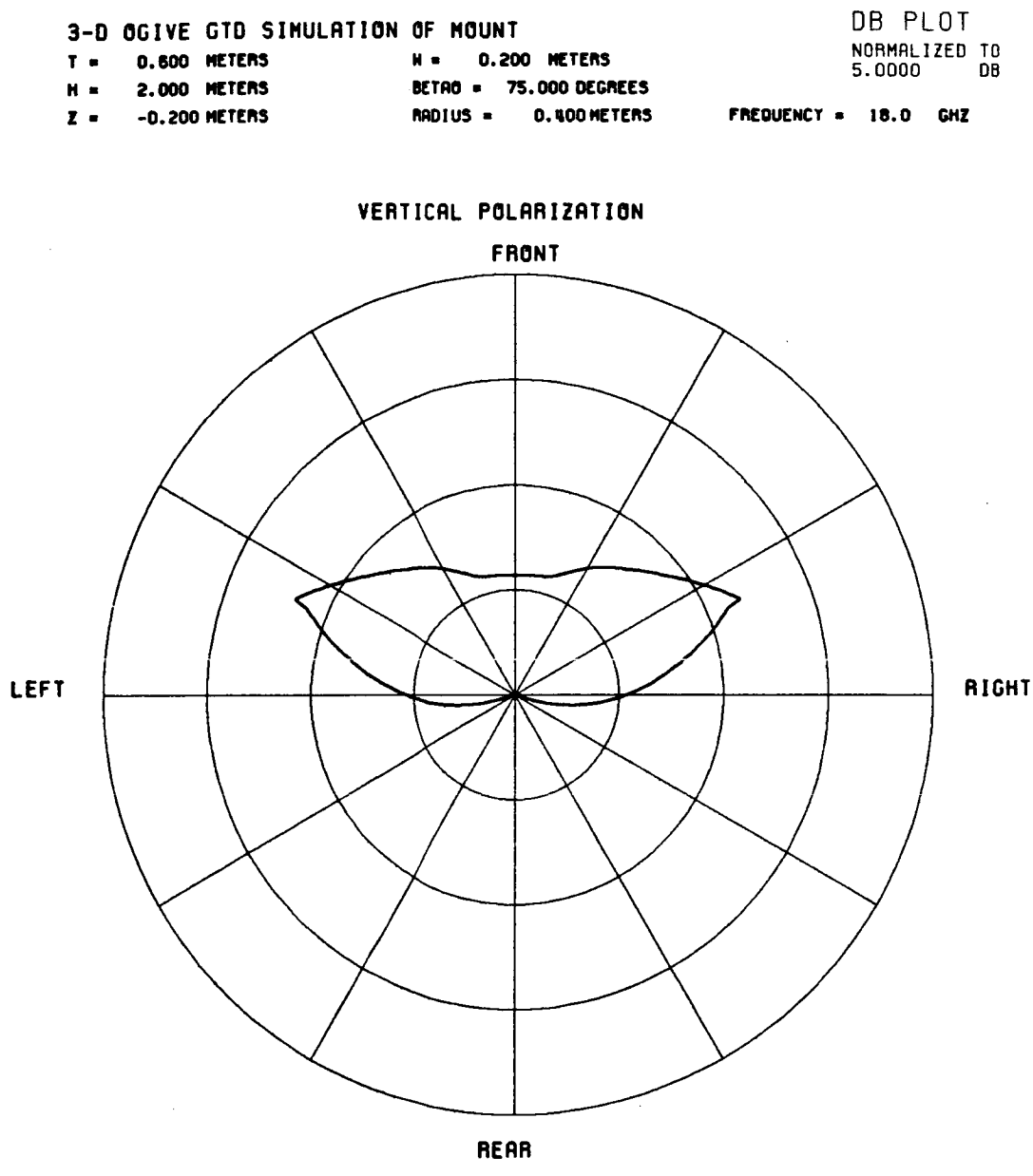

Figure 4.4. Example of a plot.

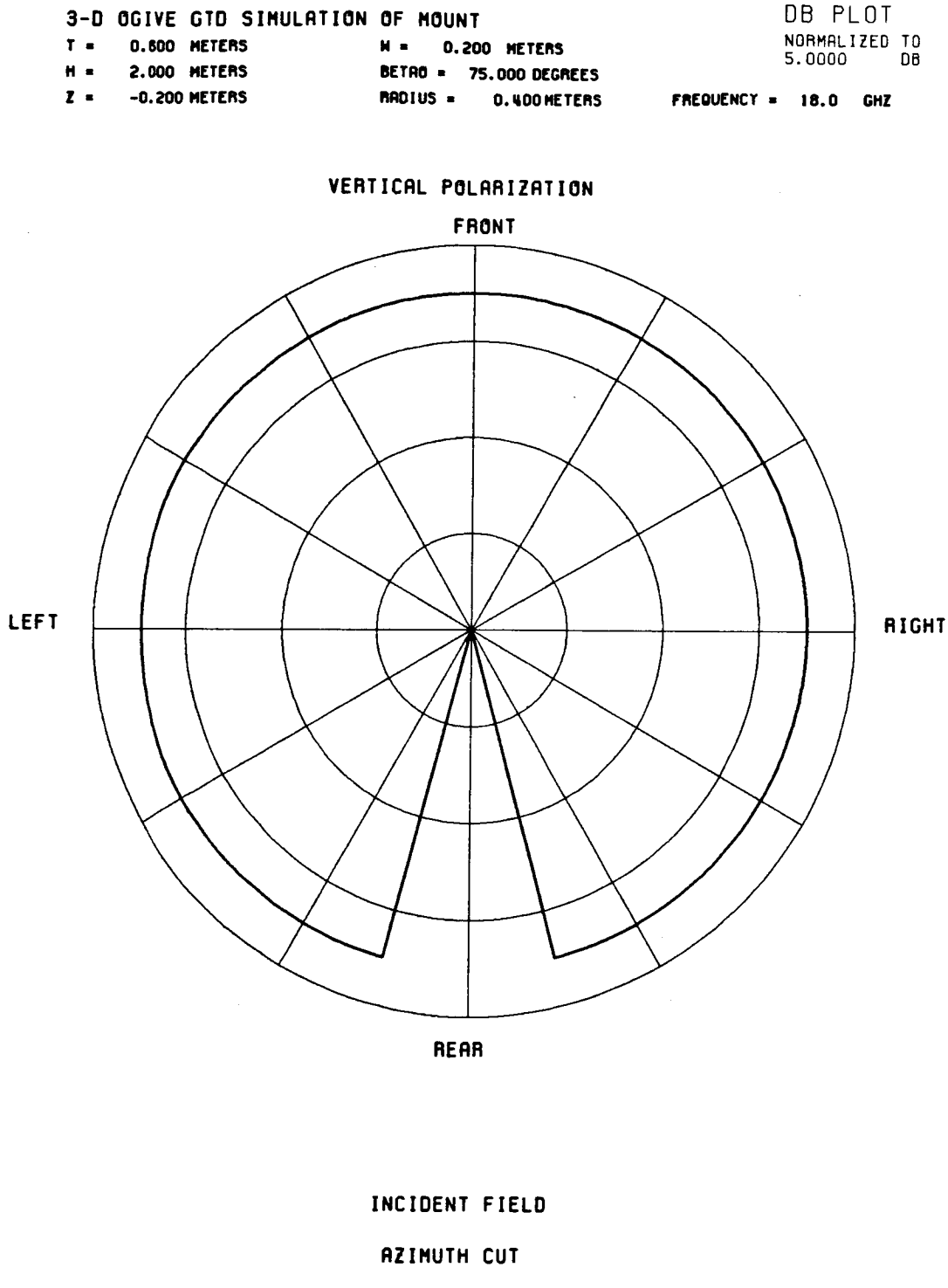

Figure 4.5. Incident field.

B.2. Front Edge Diffracted Field

The front edge diffracted field, as shown in Figure 4.6, is given using Equation (2.14) by

$$\vec{E}^d = \vec{E}^i(Q_E)(-\hat{\beta}_o'\hat{\beta}_o D_s - \hat{\phi}'\hat{\phi} D_n)\sqrt{\frac{\rho_c}{s(\rho_c+s)}}\; e^{-jks} \quad . \tag{4.2}$$

Since a plane wave field is incident on the edge,

$$\rho_e^i = \infty \quad . \tag{4.3}$$

and with the edge being straight,

$$\rho_g = \infty \quad . \tag{4.4}$$

Therefore, one obtains

$$\rho_c = \rho_e^r = \rho_1^i = \rho_2^i = \infty \quad . \tag{4.5}$$

Hence, the distance parameters are given by

$$L^i = s \sin^2\beta_o \tag{4.6}$$

$$\rho_1^r = \rho_2^r = R \text{ , and} \tag{4.7}$$

$$L^{rn} = L^{ro} = \frac{s \times R}{(s+R)} \sin^2\beta_o \quad . \tag{4.8}$$

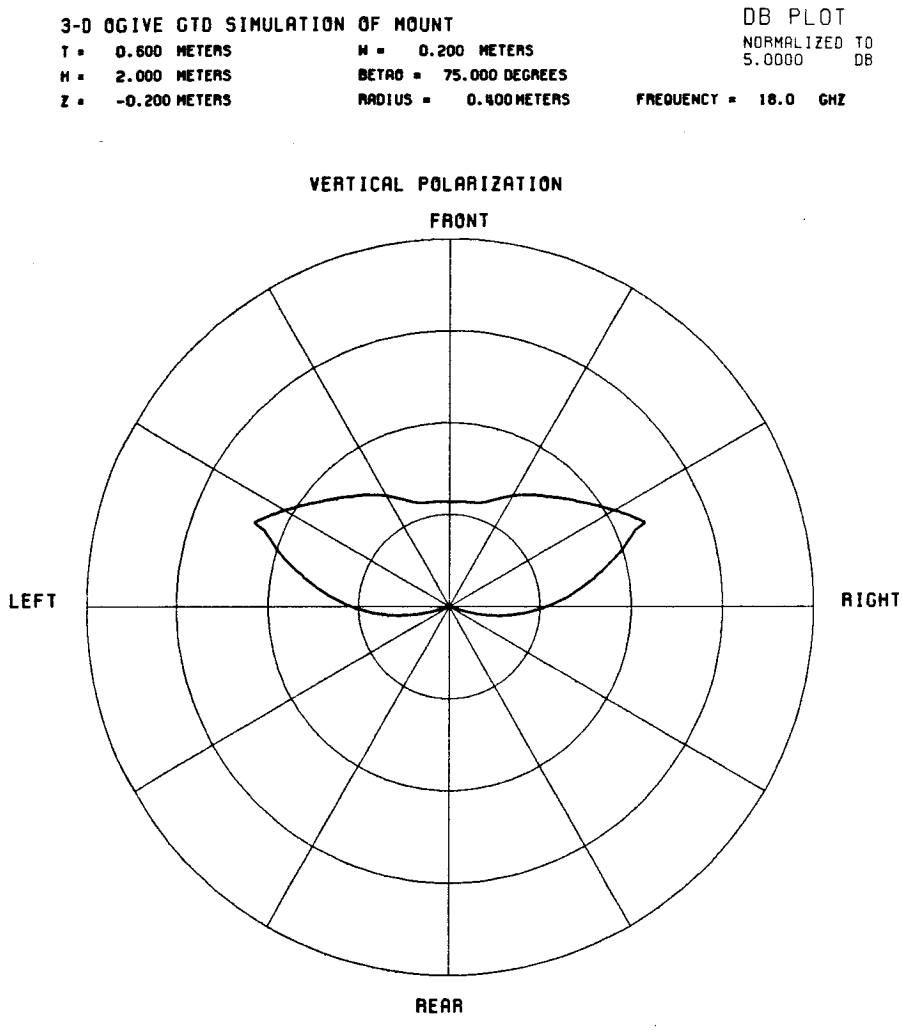

Figure 4.6. Front edge diffracted field.

B.3. Corner Diffracted Field

The corner diffracted field is the sum of contributions from the three edges forming the corner. The contribution from each edge is given using Equation (2.28) by

$$\begin{bmatrix} E^c_{\beta o} \\ E^c_{\phi} \end{bmatrix} = \begin{bmatrix} -D^c_s & 0 \\ 0 & -D^c_h \end{bmatrix} \begin{bmatrix} E^{\bar{c}}_{\beta o'} \\ E^i_{\phi'} \end{bmatrix} \sqrt{\frac{s'}{s''(s'+s'')}} \sqrt{\frac{s(s+s_c)}{s_c}} \frac{e^{-jks}}{s} \, . \tag{4.9}$$

For the contribution from the front edge, the distance parameters were defined in the previous section:

$$L^i = S \sin^2\beta_o \tag{4.10}$$

$$L^{rn} = L^{ro} = \frac{sR}{(s+R)} \sin^2\beta_o \, , \text{ and} \tag{4.11}$$

$$L_c = s \, . \tag{4.12}$$

For the contribution from the two upper edges, the arguments are different because the edge is curved such that the following result:

$$\rho^i_e = \infty \tag{4.13}$$

ρ_g = radius of curvature of ellipse

$$\frac{1}{\rho_c} = \frac{-\hat{n}_e \cdot (\hat{s}_c - \hat{s})}{\rho_g \sin\beta_c \sin\beta_{oc}} \tag{4.14}$$

$$L^i = s \cdot \sin^2\beta_o \tag{4.15}$$

$$L^{rn} = \frac{s''(\rho_e^r + s'')\rho_1^r \sin^2\beta_o}{\rho_e^r (\rho_1^r + s'')} \tag{4.16}$$

$$L^{ro} = s \times \sin^2\beta_o \quad , \text{ and} \tag{4.17}$$

$$L_c = \frac{\rho_c s}{\rho_c + s} \, . \tag{4.18}$$

An example of this contribution is given in Figure 4.7.

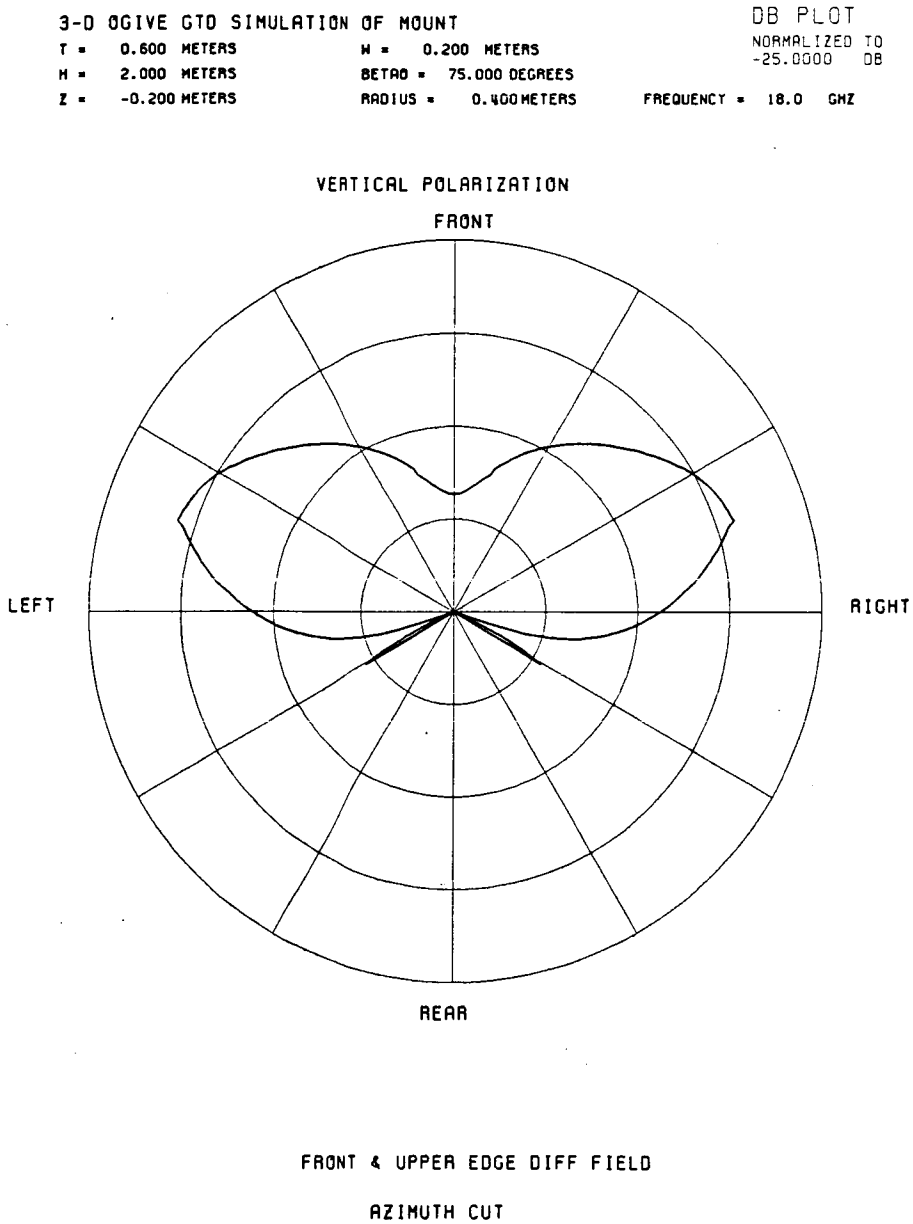

Figure 4.7. Corner diffracted field.

B.4. Reflected Field

The reflected field, an example of which is shown in Figure 4.8, is given using Equation (2.1) by

$$\vec{E}^{ref} = \vec{E}^{i}(Q_R) \cdot \overline{\overline{R}} \sqrt{\frac{\rho_1^r \rho_2^r}{(\rho_1^r+s)(\rho_2^r+s)}}\, e^{-jks} \tag{4.19}$$

where

$$m(Q) = \left[\frac{\kappa\rho_g}{2}\right]^{1/3} \tag{4.20}$$

$$\rho_g = \frac{R}{\sin^2\omega_r} \tag{4.21}$$

$$L^L = s \tag{4.22}$$

$$X^L = 2\kappa L^L \cos^2\theta^i \quad , \text{ and} \tag{4.23}$$

$$\xi^L = -2m(Q_R)\cos\theta^i \ . \tag{4.24}$$

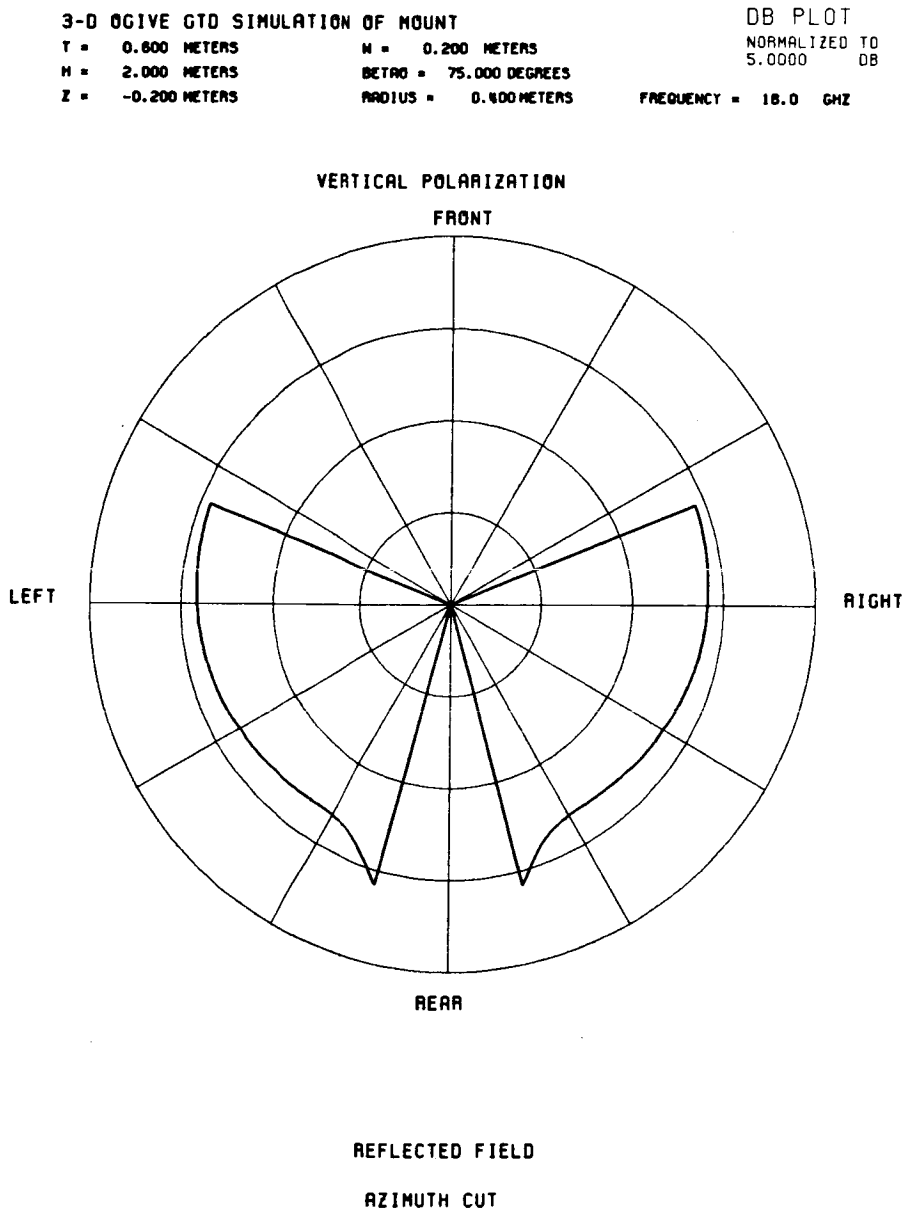

Figure 4.8. Reflected field.

B.5. Creeping Wave Field

The creeping wave, an example of which is shown in Figure 4.9, is given using Equation (2.34) by

$$\vec{E}^{creep} = \vec{E}^{i}(Q_1) \cdot \overline{\overline{T}} \quad \frac{\rho_2^d}{s(\rho_2^d+s)} \quad e^{-jks} \tag{4.25}$$

where

$$m(0) = \left(\frac{k\rho_g}{2}\right)^{1/3} \tag{4.26}$$

$$\rho_g = \frac{R}{\sin^2\omega_r} \tag{4.27}$$

$$\xi^d = \int_{Q_1}^{Q_2} \frac{m(t')}{\rho_g(t')}\, dt' = \frac{m}{\rho_g}\, t \tag{4.28}$$

t = arc length of creeping wave path

$s' \to \infty$, and (4.29)

$L^d = s$. (4.30)

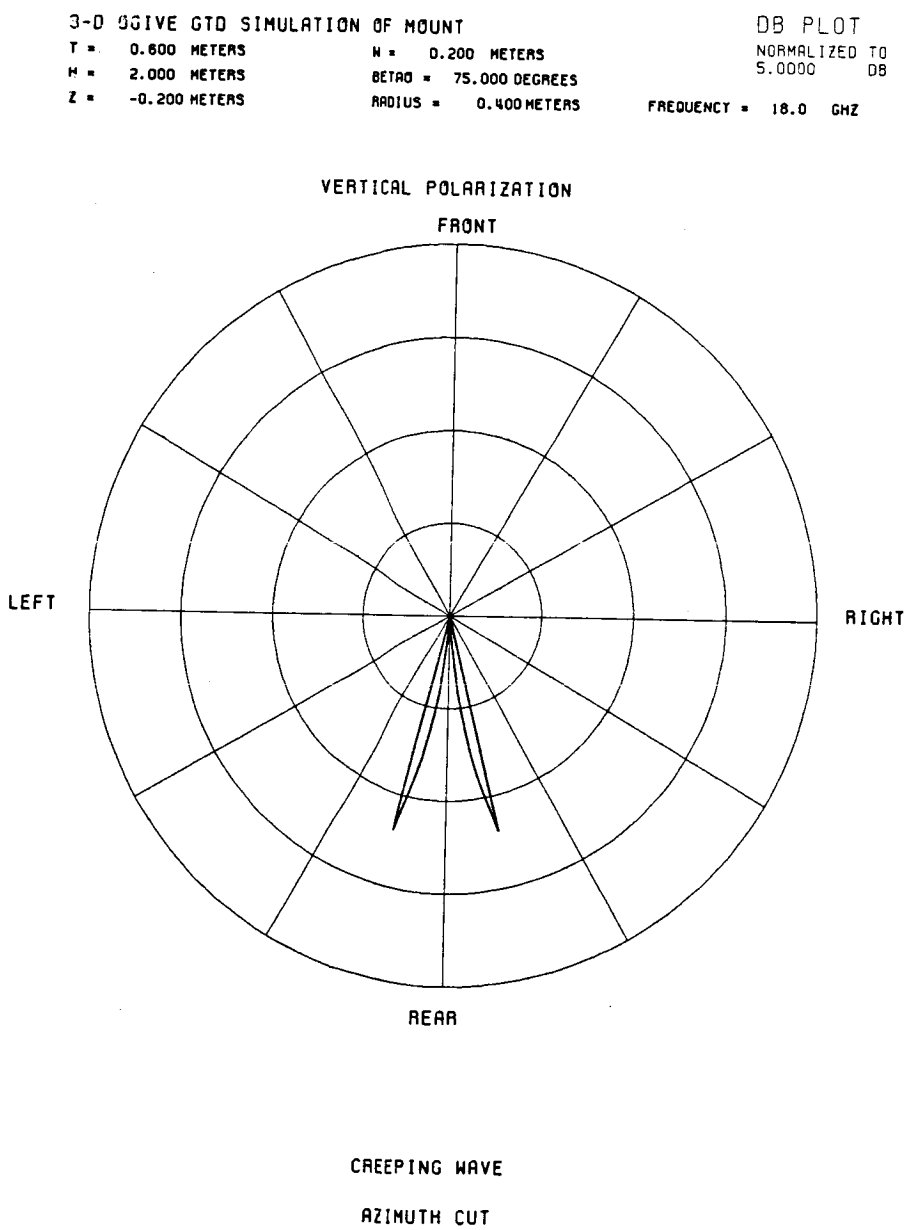

Figure 4.9. Creeping wave field.

B.6. Combination of Field Components

In this section, various field terms are added to show their effect on the resulting field patterns. First, let us examine the effect of the front edge diffraction in relation to the reflection shadow boundary of the pedestal surface. The reflected field of the pedestal is shown in Figure 4.10. From the plot, there are two reflection shadow boundaries: one associated with the termination at the front edge and the other caused by the curvature of the pedestal as illustrated in Figure 4.11. For the time being let us only concentrate on the first boundary, i.e., 1 as shown in Figures 4.10 and 4.11. The front edge diffracted field, as shown in Figure 4.12, should compensate for this field boundary. This is indeed true as one can see when they are added together as illustrated in Figure 4.13.

Next let us concentrate on the boundary 2 as illustrated in Figures 4.10 and 4.11. This reflection shadow boundary, which is caused by the curvature of the pedestal, is also the incident shadow boundary of the pedestal. The reflected field plus incident field is shown in Figure 4.14. The discontinuity at the rear of the pedestal is still present and should be compensated for by a creeping wave, which is illustrated by the results shown in Figure 4.15. The sum of these mechanisms is shown in Figure 4.16 and seen to be smooth and continuous around this boundary.

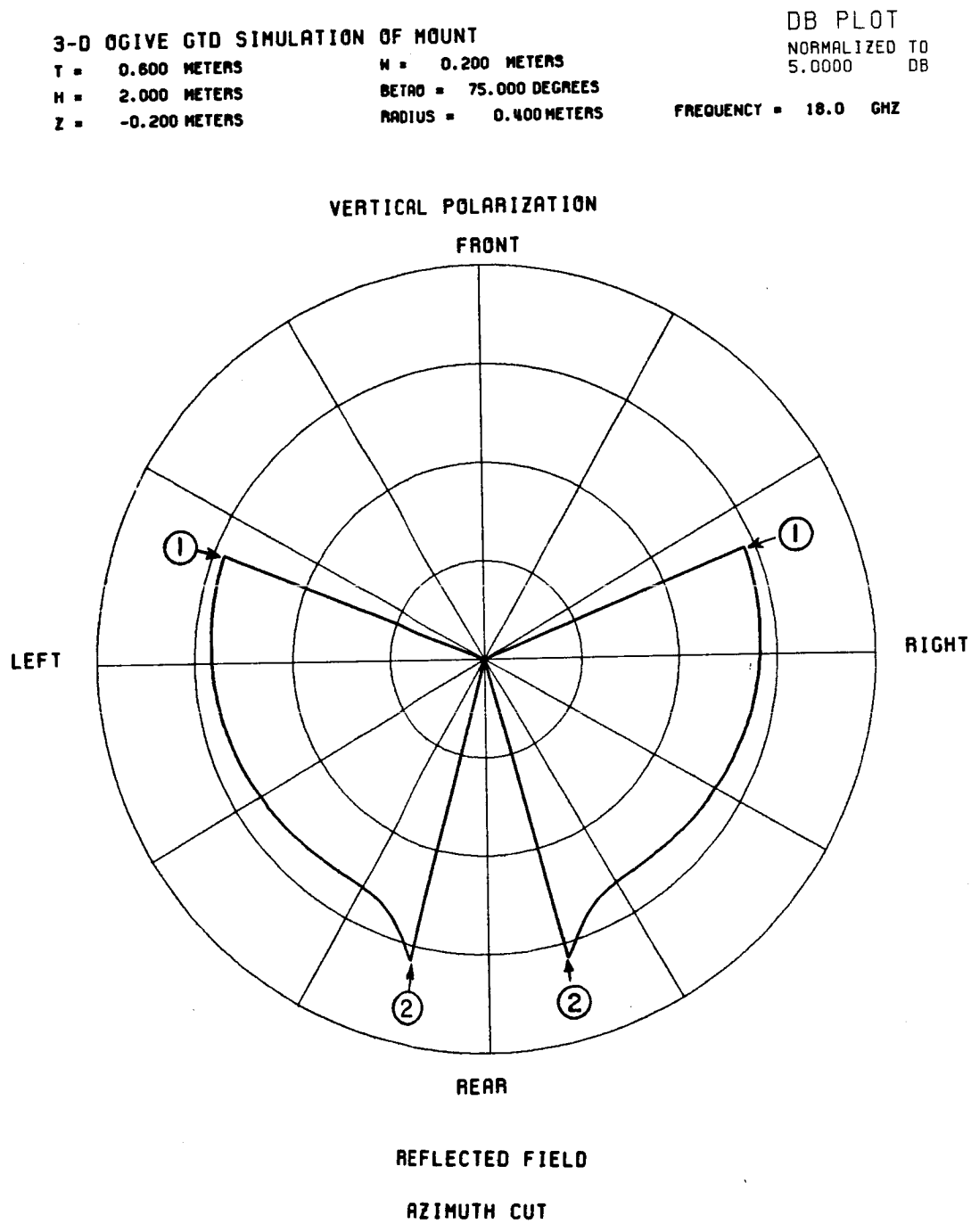

Figure 4.10. Reflected field.

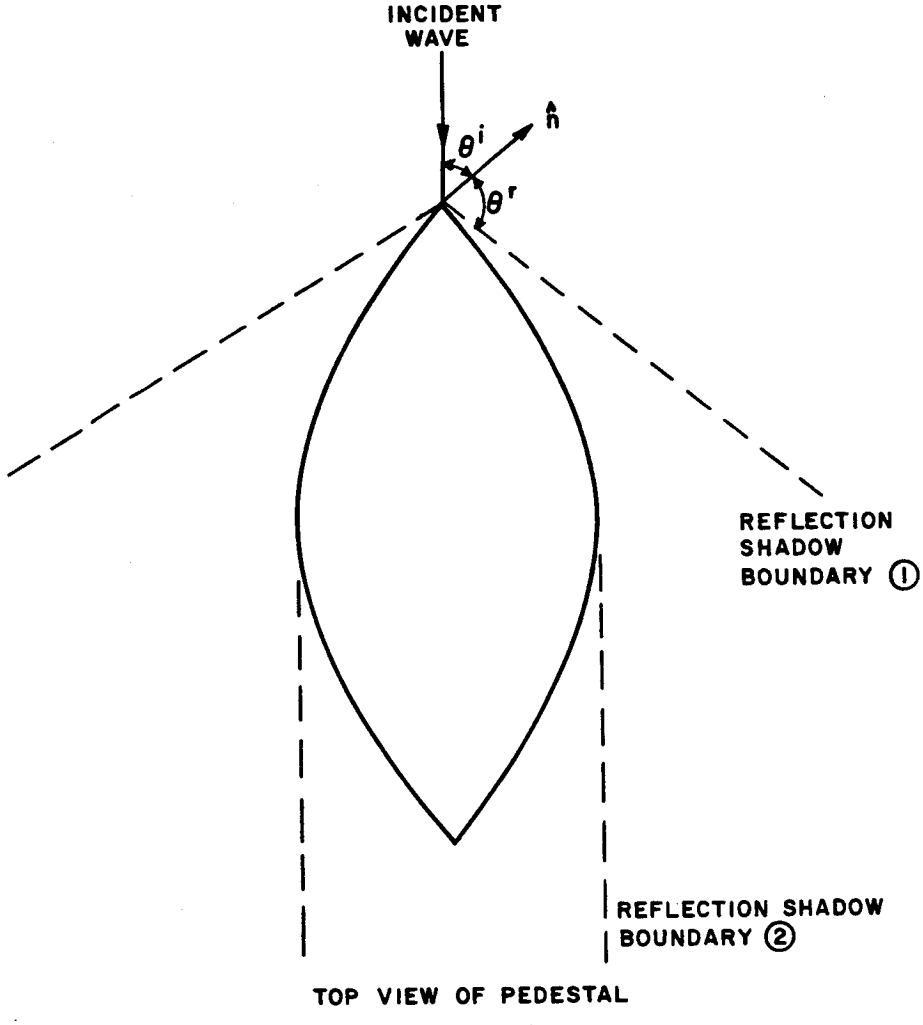

Figure 4.11. Reflection shadow boundaries.

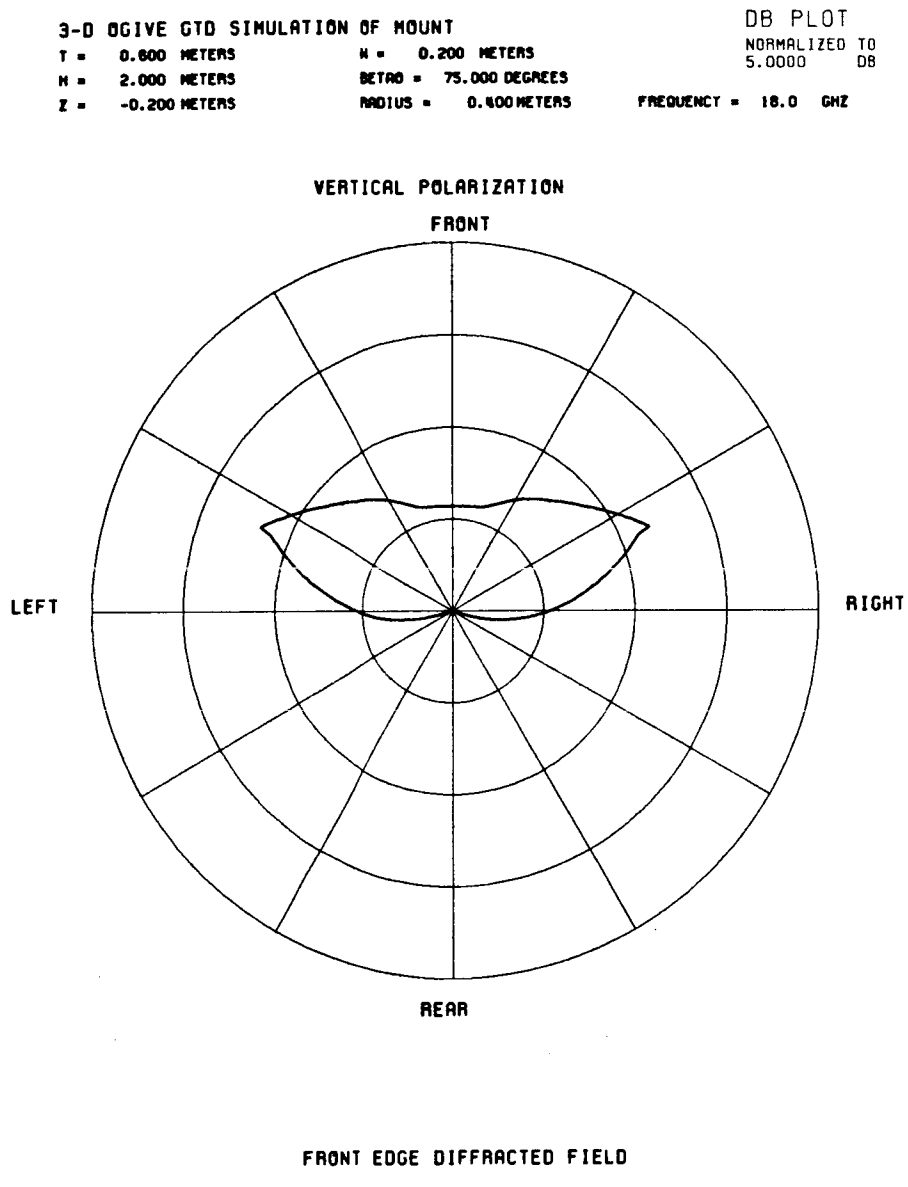

Figure 4.12. Front edge diffracted field.

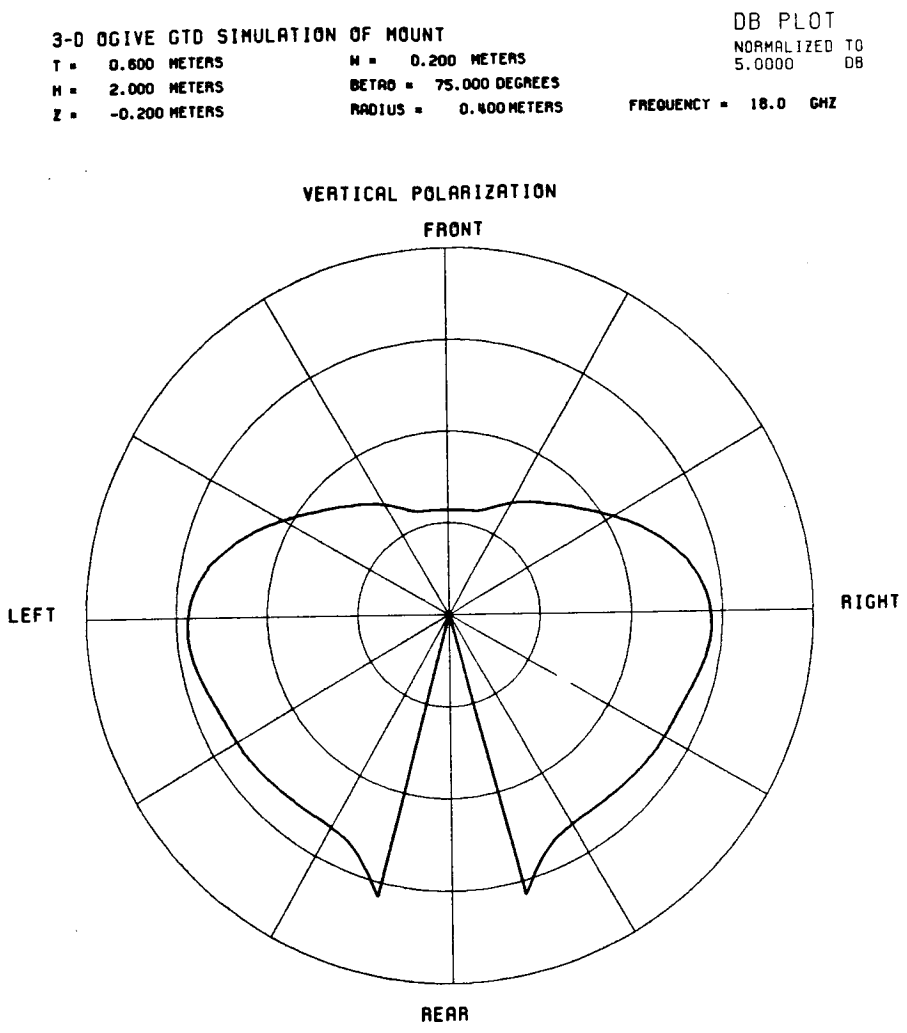

Figure 4.13. Sum of reflected field and front edge diffracted field.

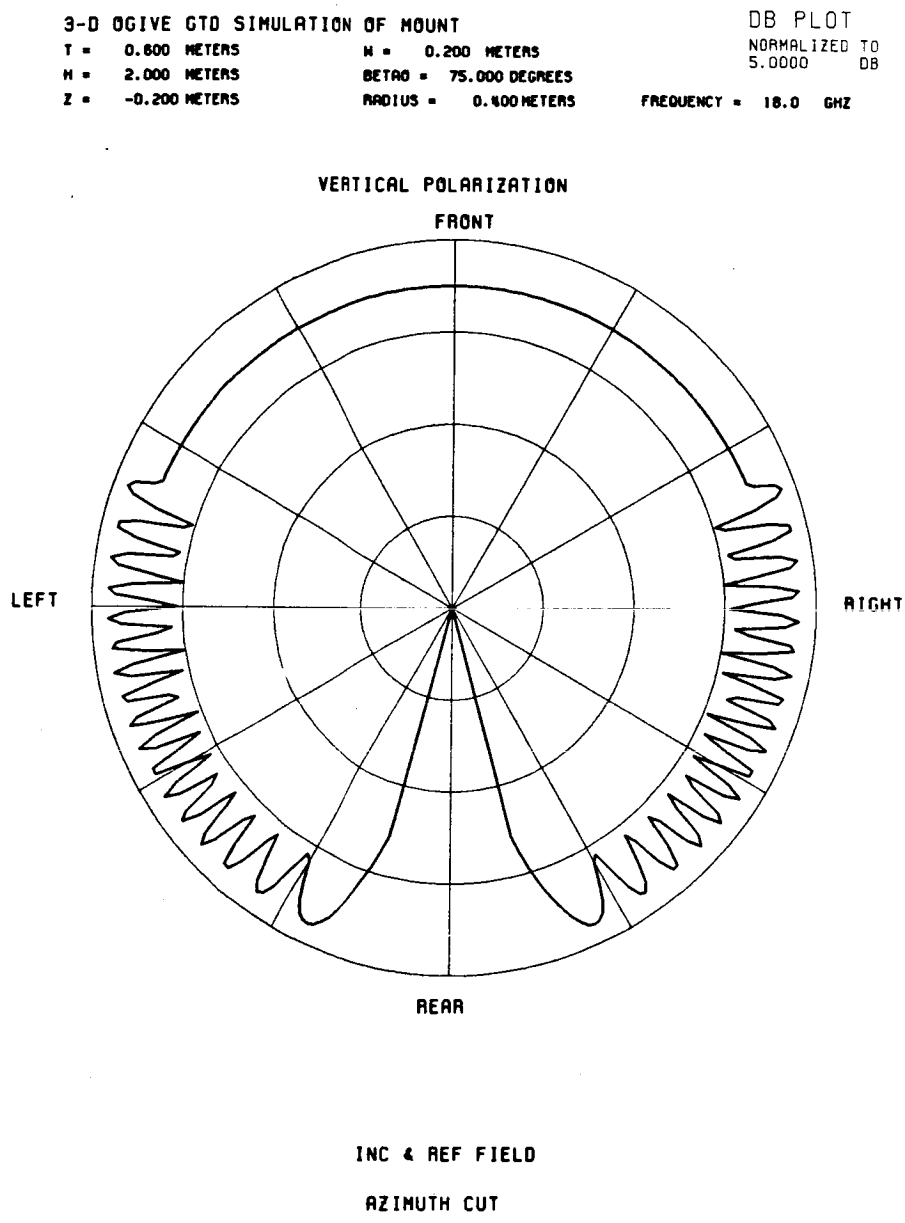

Figure 4.14. Reflected plus incident field.

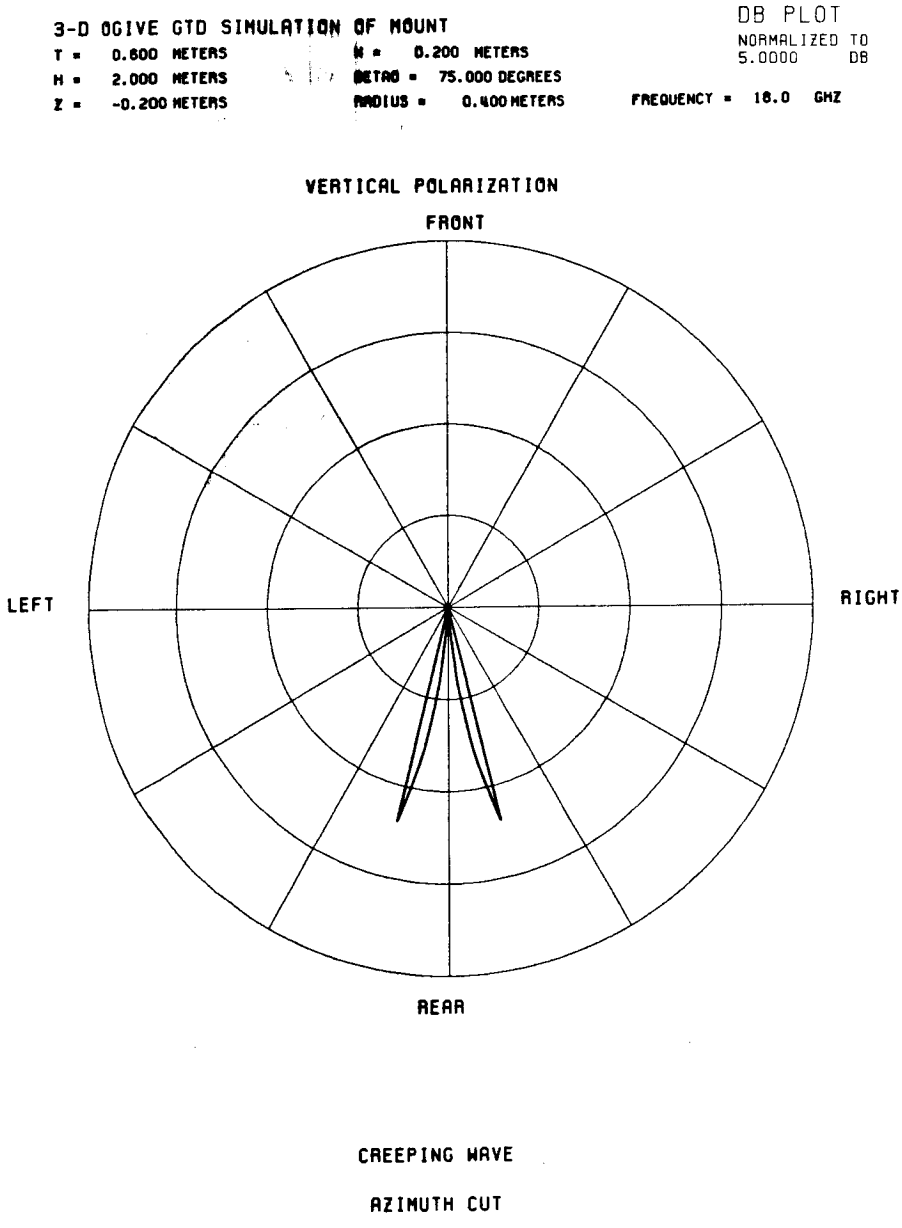

Figure 4.15. Creeping wave.

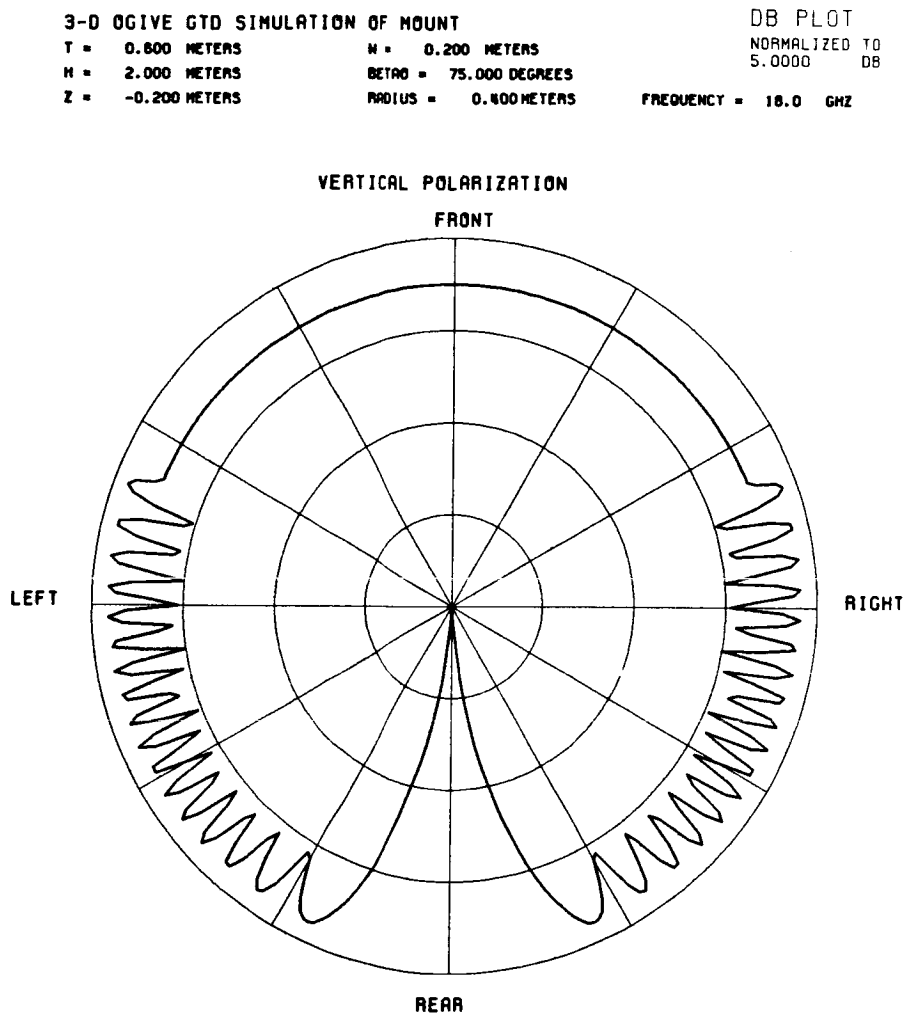

Figure 4.16. Reflected, incident, plus creeping wave fields.

B.7. Conclusion

After looking at the specific performance of UTD, let us now look at the total field. The contributions in various regions are (refer to Figure 4.1) as follows:

$$E = \begin{cases} \vec{E}^i + \vec{E}^d + \vec{E}^d_c & \text{region I} \\ \vec{E}^i + \vec{E}^d + \vec{E}^d_c + \vec{E}^{ref} & \text{region II} \\ \vec{E}^i + \vec{E}^{ref} & \text{region III} \\ \vec{E}^{creep} & \text{region IV} \end{cases}$$

The total field is plotted in Figure 4.17 and is seen to be smooth and continuous throughout for the case treated in the previous section.

So far our concentration has been on the analysis and verifying its expected behavior. Now that our results appear correct, let us study the significance of our findings. First, it is clear that the pedestal greatly distorts the incident plane wave. There is a strong reflection off to the sides of the pedestal and a deep null behind it. It is obvious from these results that the target cannot have significant scattering centers either off to the sides or aft of the pedestal below the top. If it does, the target illumination is far from the desired plane wave and large errors will result.

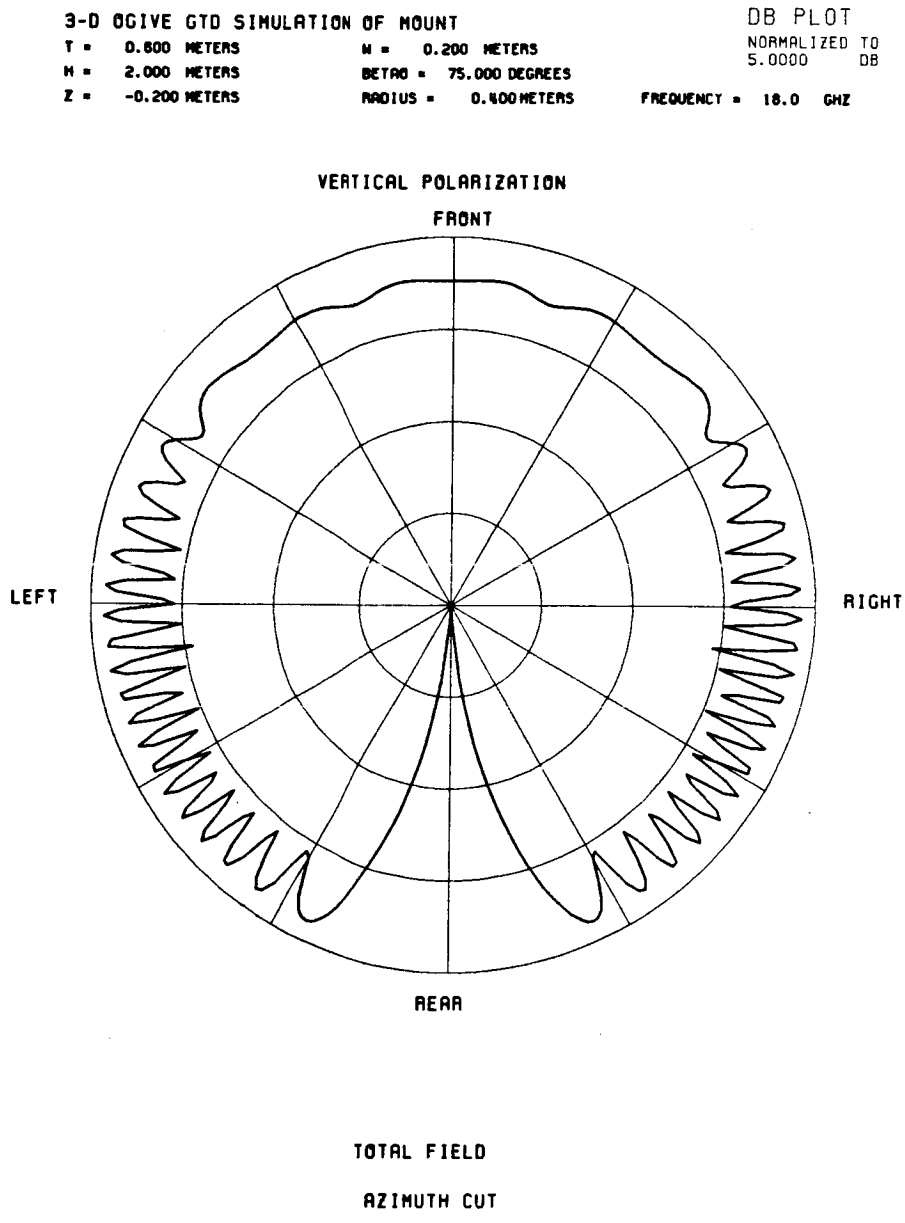

Figure 4.17. Total field.

C. BISTATIC SCATTERING ABOVE THE TOP OF THE PEDESTAL

This section presents a UTD near field analysis of the bistatic scattering around and above the top of the pedestal where the target is placed. Note that the target is somehow embedded within this field structure. If the field structure is modified relative to the incident plane wave, the target illumination will be corrupted. Therefore how the total field fluctuates is of particular concern in this region. The incident, edge diffracted, corner diffracted and edge creeping fields are present as shown in Figure 4.18. Since there is no closed form solution for an edge diffracted, creeping wave field, it is ignored here. The remaining contributions give a fairly accurate result except when the field point is near the rear tip of the top of the pedestal. Thus, the total field is approximately given by

$$\vec{E} = \vec{E}^{i} + \vec{E}^{d} + \vec{E}^{d}_{c}$$

where $\vec{E}^{i}$ = incident field

$\vec{E}^{d}$ = edge diffracted field, and

$\vec{E}^{d}_{c}$ = corner diffracted field.

C.1. Incident Field

The incident field, as plotted in Figure 4.20, is:

$$\vec{E}^{i} = \hat{z}\, e^{-jkx} \quad . \tag{4.31}$$

Note that it is never shadowed by the pedestal.

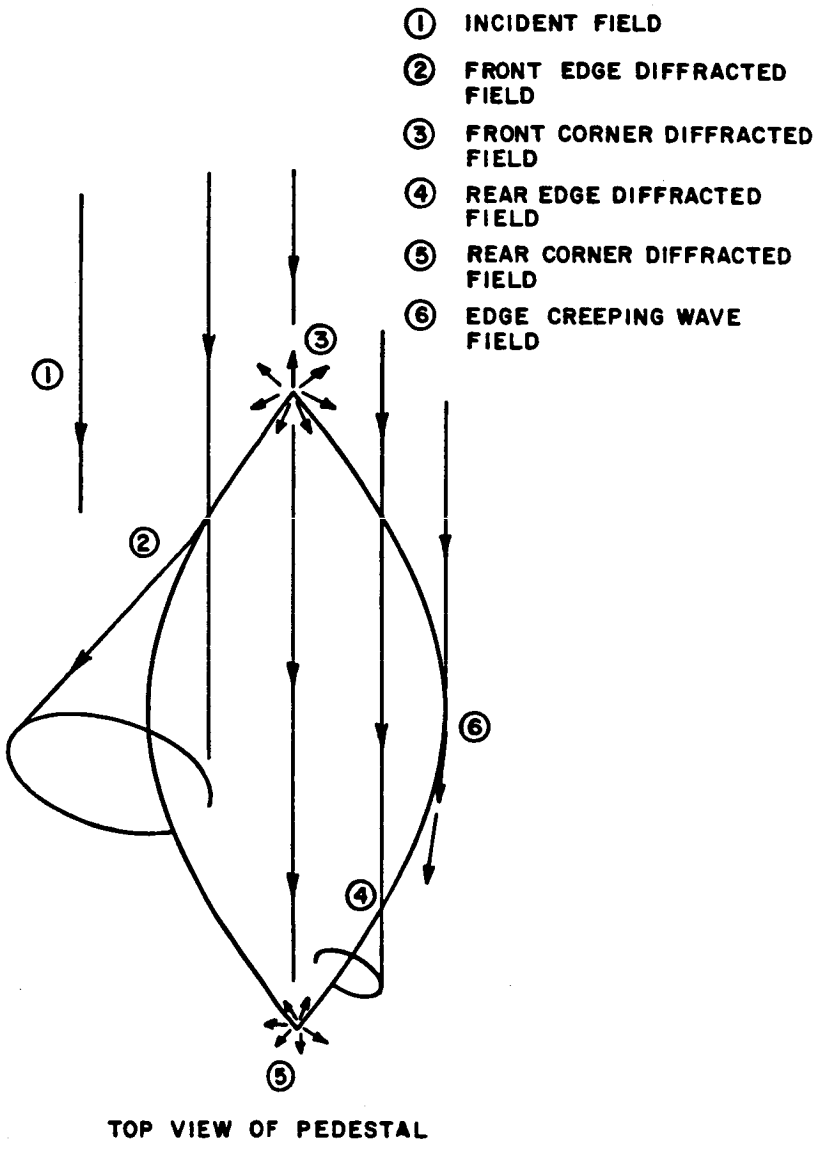

Figure 4.18. Various contributions to total field.

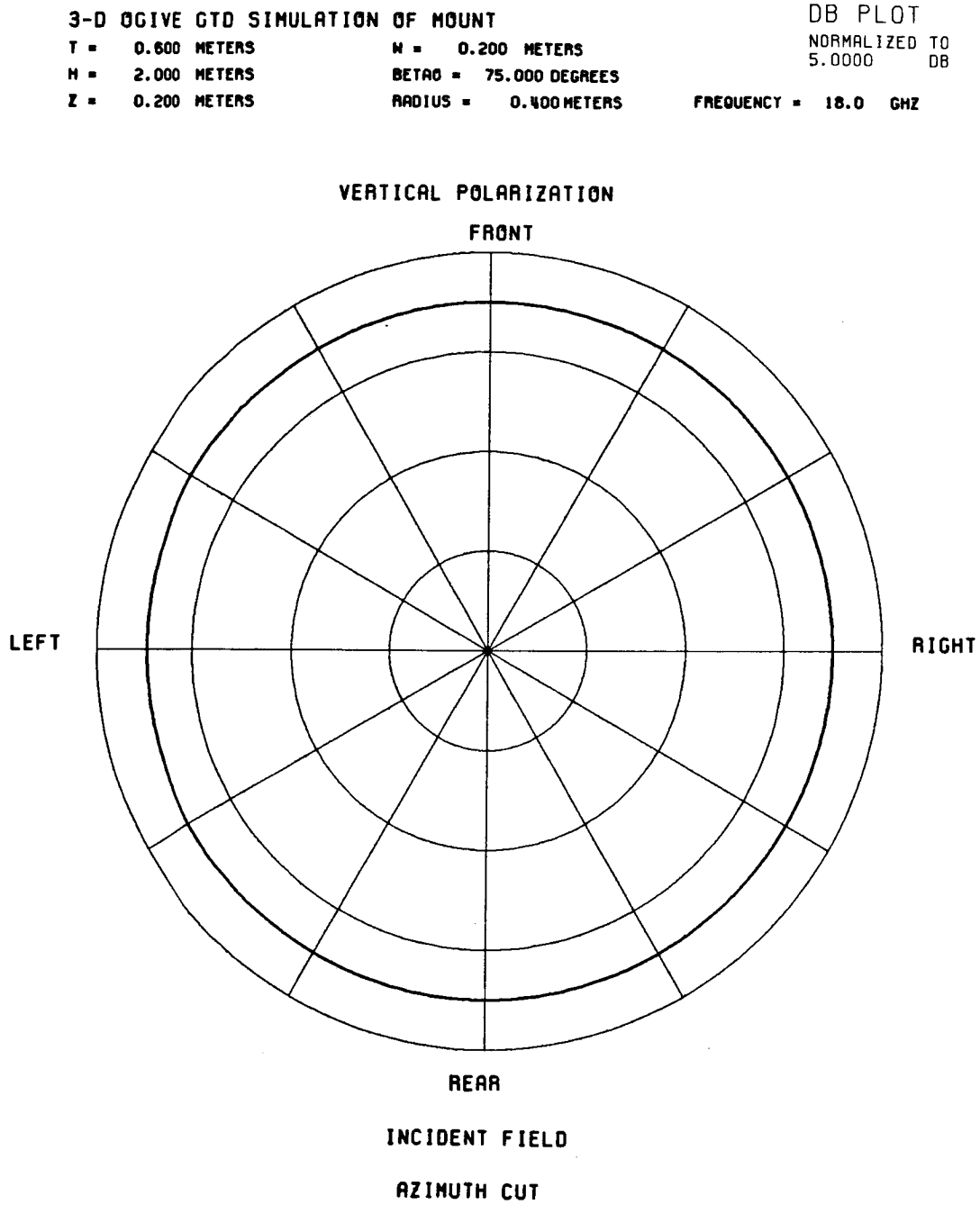

Figure 4.19. Incident field.

C.2. Edge Diffracted Field from Front Upper Edge

The edge diffracted field is given using Equation (2.14) by

$$\vec{E}^d = \vec{E}^i(Q_E)(-\hat{\beta}_o'\hat{\beta}_o D_s - \hat{\phi}'\hat{\phi} D_h)\sqrt{\frac{\rho_c}{s(\rho_c+s)}}\, e^{-jks} \quad . \tag{4.32}$$

In this case a plane wave is incident so $\rho_e^i = \infty$.

If the ellipse at the top of the pedestal has a radius of curvature given by ρ_g; then, one obtains that

$$\frac{1}{\rho_c} = \frac{-\hat{n}_e(\hat{s}'-\hat{s})}{\rho_g \sin^2\beta_o} \quad . \tag{4.33}$$

The distance parameters are also given by

$$L^i = s\,\sin^2\beta_o \tag{4.34}$$

$$\frac{1}{\rho_c} = \frac{-2(\hat{n}\cdot\hat{n}_e)(\hat{I}\cdot\hat{n})}{\rho_g \sin^2\beta_o} \tag{4.35}$$

$$\frac{1}{\rho_1^r} = \frac{2\,\sin^2\theta_2}{R\cos\theta^i} \quad , \text{ and} \tag{4.36}$$

$$L^{rn} = \frac{s(\rho_e^r+s)\rho_1^r\,\sin^2\beta_o}{\rho_e^r(\rho_1^r+s)} \quad . \tag{4.37}$$

A result associated with this contribution is shown in Figure 4.20.

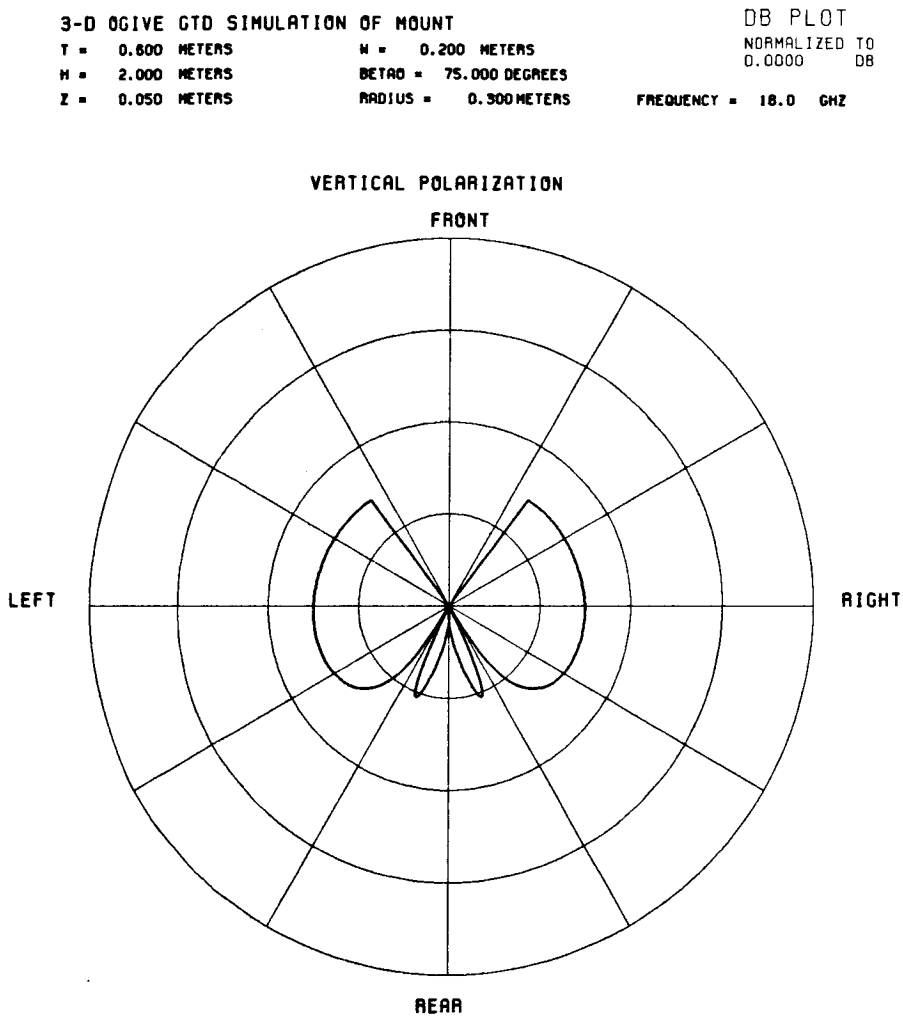

Figure 4.20. Front upper edge diffracted field.

C.3. Edge Diffracted Field from Rear Upper Edge

The rear edges at the top of the pedestal diffract in terms of a double diffraction problem: the incident field first strikes the front upper edge, then it diffracts and grazes along the upper surface until it strikes the rear edge where it again diffracts. Since an exact solution to this form of double diffraction does not exist, let us make an appropriate approximation. First by continuity of the electric field it is well known that the grazing field that strikes the rear upper edge should approximate a plane wave. Next, since this edge is along the shadow boundary, the incident field is one half that of the original plane wave. An example of this result is shown in Figure 4.22.

One thing one needs to be aware of is the incompleteness of this approach. It does not address edge creeping wave which should compensate for the apparent discontinuity of the diffraction points on the rim of the top of the pedestal. Also note that at the rear of the pedestal, a spike appears in the results. This is due to the fact that the diffraction points of the sides of the rear edge coincide for that observation point. There is no need to worry because the corner diffraction term will correct this problem, as will be seen later.

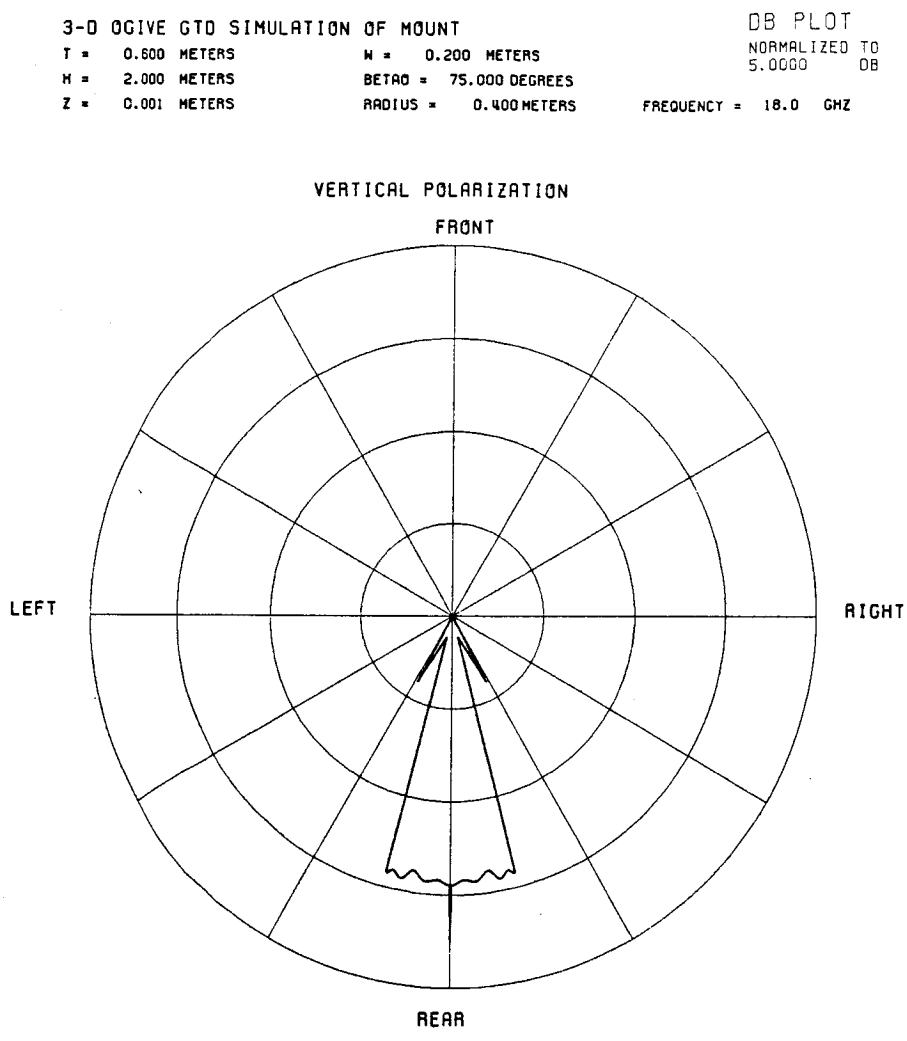

Figure 4.21. Rear upper edge diffracted field.

C.4. Corner Diffracted Field from Front Apex

The corner diffracted field is the sum of contributions from the three edges forming the corner as shown in Figure 4.22. The contribution from each edge is given by:

$$\begin{bmatrix} E^c_{\beta o} \\ E^c_{\phi} \end{bmatrix} = \begin{bmatrix} -D^c_s & 0 \\ 0 & -D^c_h \end{bmatrix} \begin{bmatrix} E^i_{\beta o'} \\ E^i_{\phi'} \end{bmatrix} \sqrt{\frac{s'}{s''(s'+s'')}} \sqrt{\frac{s(s+s_c)}{s_c}} \frac{e^{-jks}}{s} \cdot \tag{4.38}$$

For the contribution from the front edge, the distance parameters are the same as those for the front edge diffraction and are as follows

$$L^i = s \sin^2\beta_o \tag{4.39}$$

$$L^{rn} = L^{ro} = \frac{sR}{s+R} \sin^2\beta_o \text{ , and} \tag{4.40}$$

$$L_c = S \text{ .} \tag{4.41}$$

For the contribution from the two upper edges, the arguments are different because the edge is curved such that

$$\rho^i_e = \infty \tag{4.42}$$

ρ_g = radius of curvature of ellipse

$$\frac{1}{\rho_c} = \frac{-\hat{n}_e \cdot (\hat{s}_c - \hat{s})}{\rho_g \sin\beta_c \sin\beta_{oc}} \tag{4.43}$$

$$L^i = s \sin^2\beta_o \tag{4.44}$$

$$L^{rn} = \frac{s''(\rho_e^r + s'')\rho_1^r \sin^2\beta_o}{\rho_e^r (\rho_1^r + s'')} \tag{4.45}$$

$$L^{ro} = s \sin^2\beta_o \text{ , and} \tag{4.46}$$

$$L_c = \frac{\rho_c s}{\rho_c + s} \text{ .} \tag{4.47}$$

An example of this contribution is given in Figure 4.23. Also the superposition of this corner field and front edge diffracted field is given in Figure 4.24.

c-2

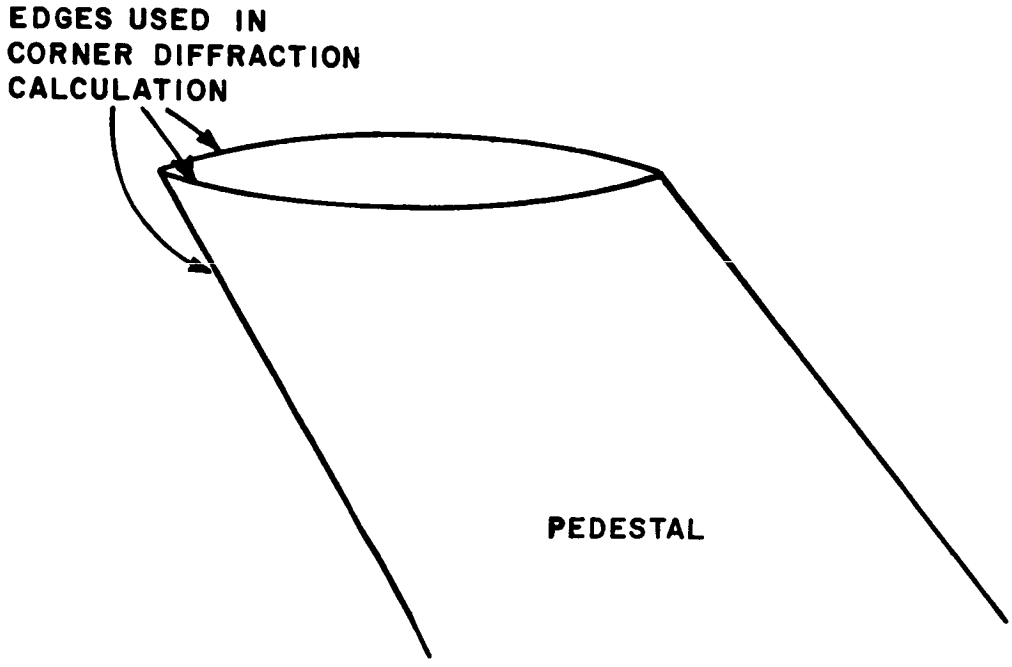

Figure 4.22. Front corner diffraction mechanism.

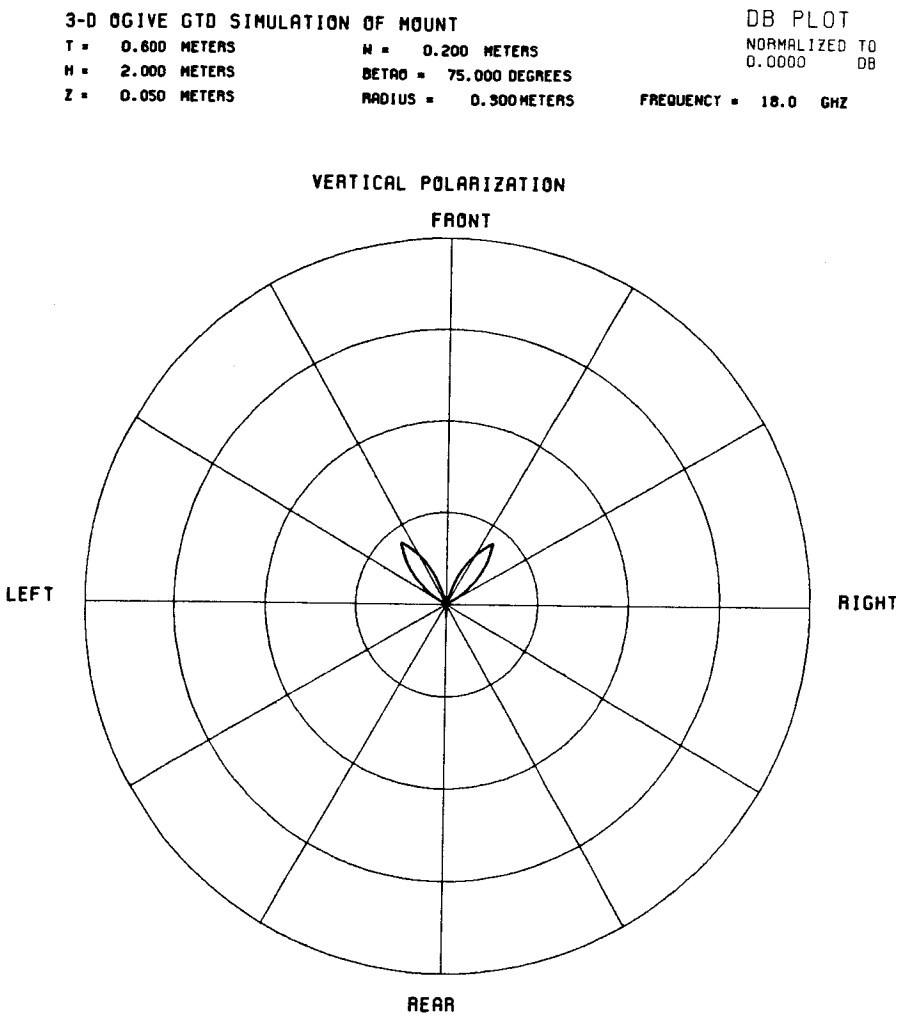

Figure 4.23. Front corner diffracted field.

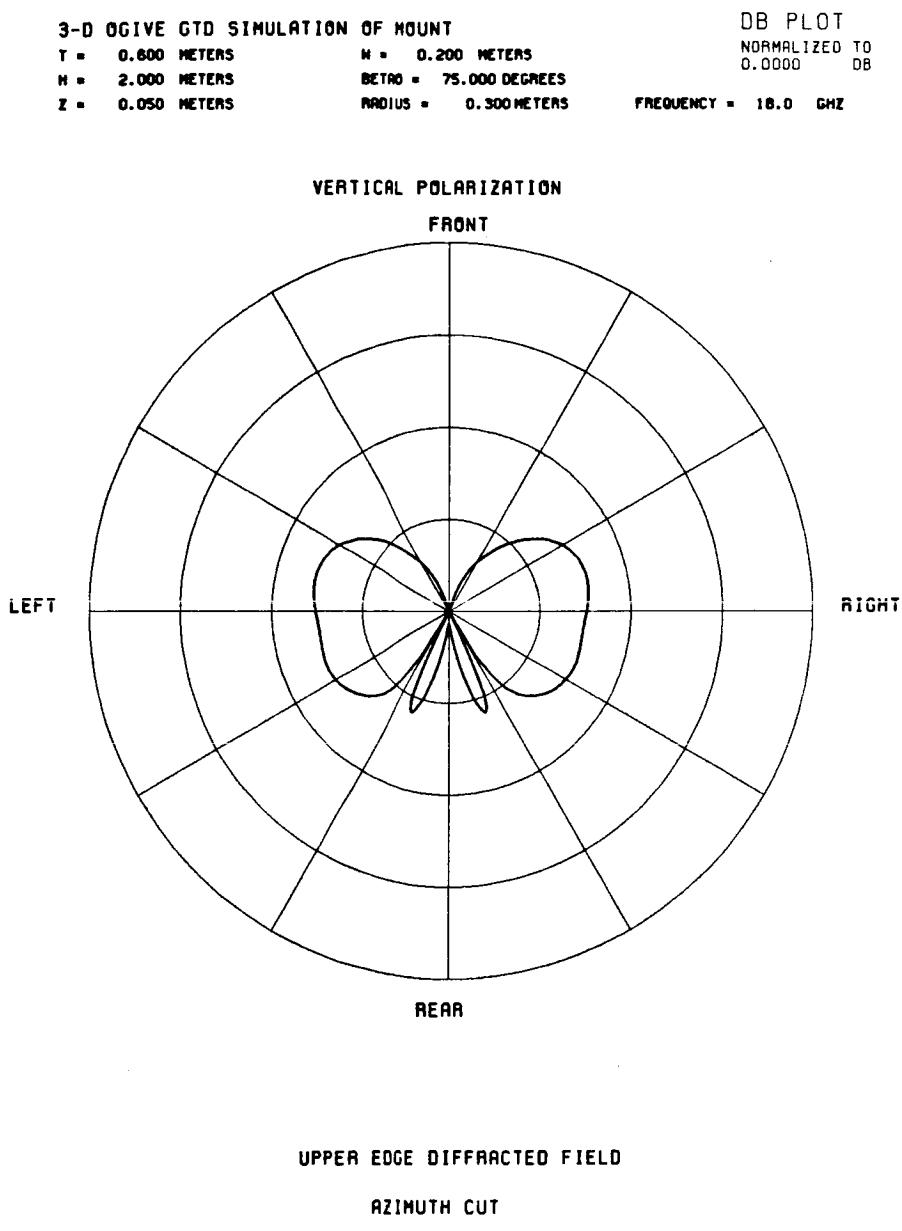

Figure 4.24. Front corner plus front edge diffracted field.

C.5. Corner Diffracted Field From Rear Apex

Following the same argument as in Section C.3, the incident field striking the rear apex is approximately a plane wave with half the amplitude of the original source. An example of this contribution is shown in Figure 4.25. As was seen earlier, this corner diffracted field should compensate for the spike at the rear of the pedestal. This is indeed so, as can be seen in Figure 4.26 where the corner diffracted field is added to the edge diffracted field.

C.6. Combinations of Fields

In this section, various fields are combined to check the accuracy of the solution. First, the edge diffracted field is added to the incident and reflected field to test its validity; second, the corner diffracted field is added to edge diffracted field to see whether it produces a smooth and continuous field at the termination of the edge.

A roll plane cut is displayed for the reflected field as shown in Figure 4.27. The discontinuity near the bottom is caused by moving the observation point inside the pedestal, so it is not important. The upper discontinuity is important because it is the reflection shadow boundary of the pedestal at the upper edge. To see whether our edge diffracted field is working correctly, it is shown in Figure 4.28 and added to the reflected field in Figure 4.29. Indeed the two add up to form a smooth and continuous field.

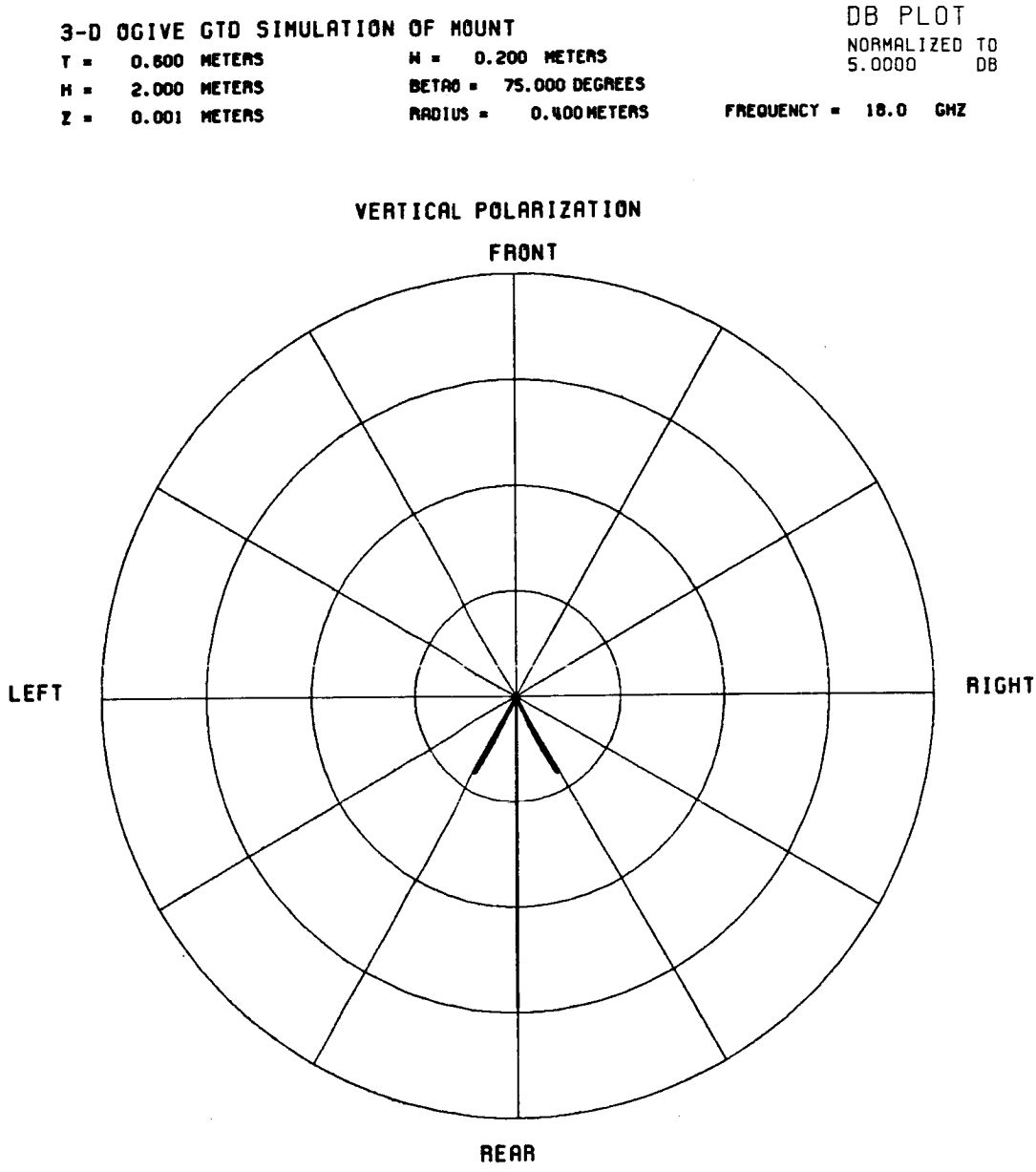

Figure 4.25. Rear corner diffracted field.

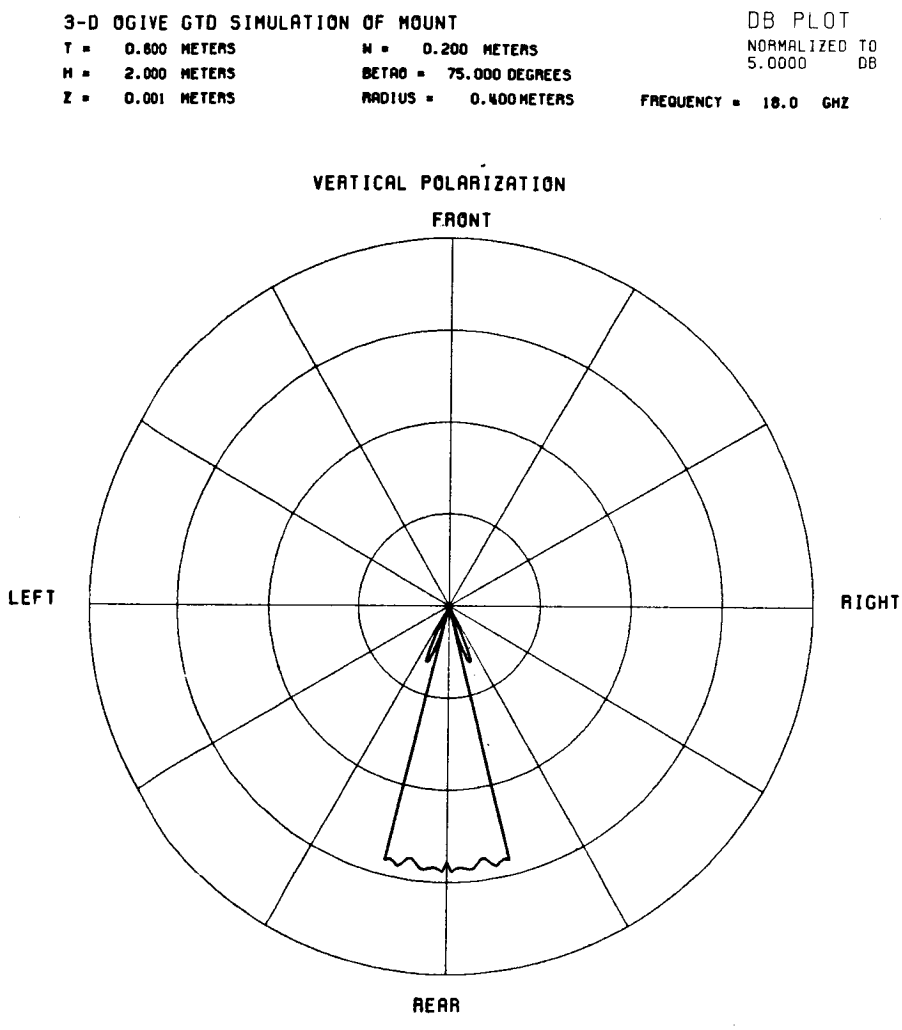

Figure 4.26. Rear corner and edge diffracted field.

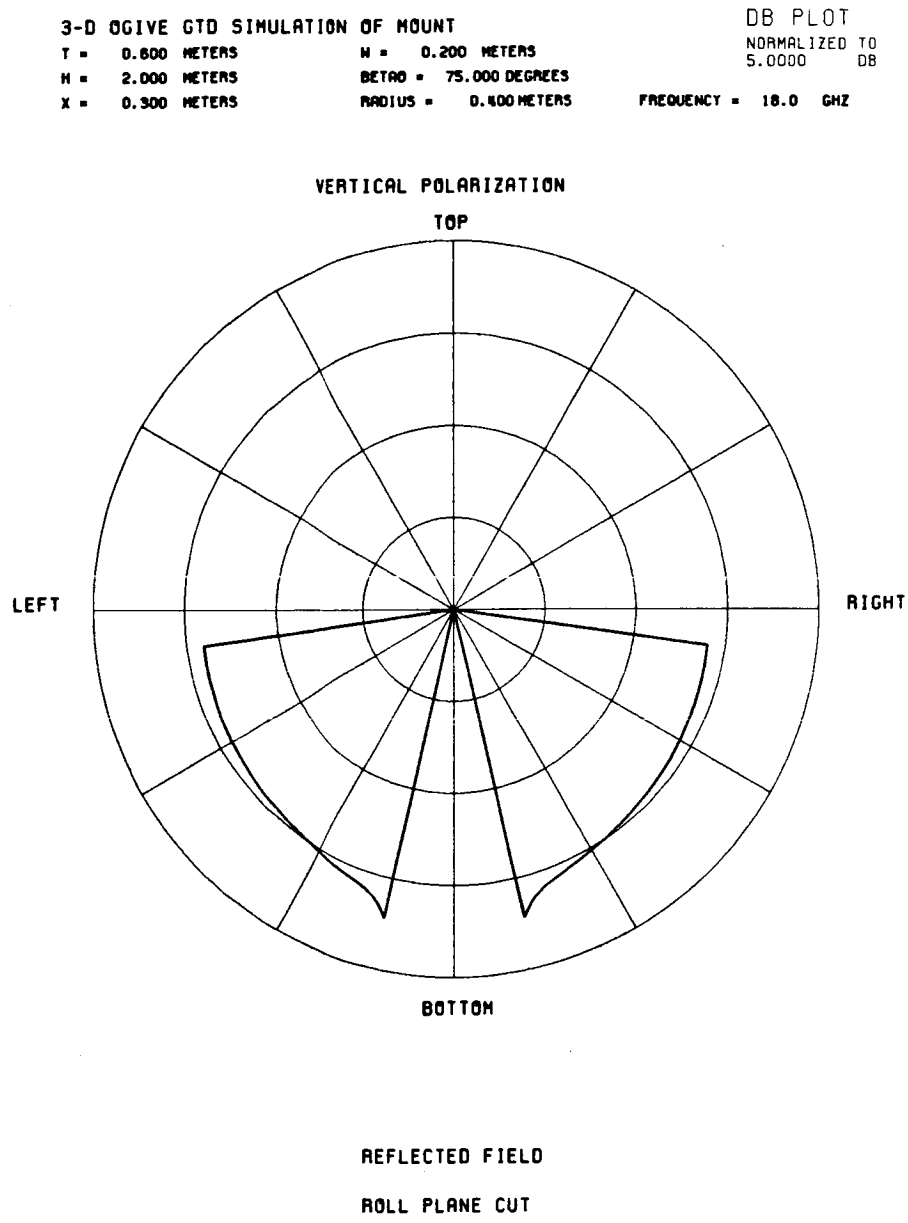

Figure 4.27. Reflected field.

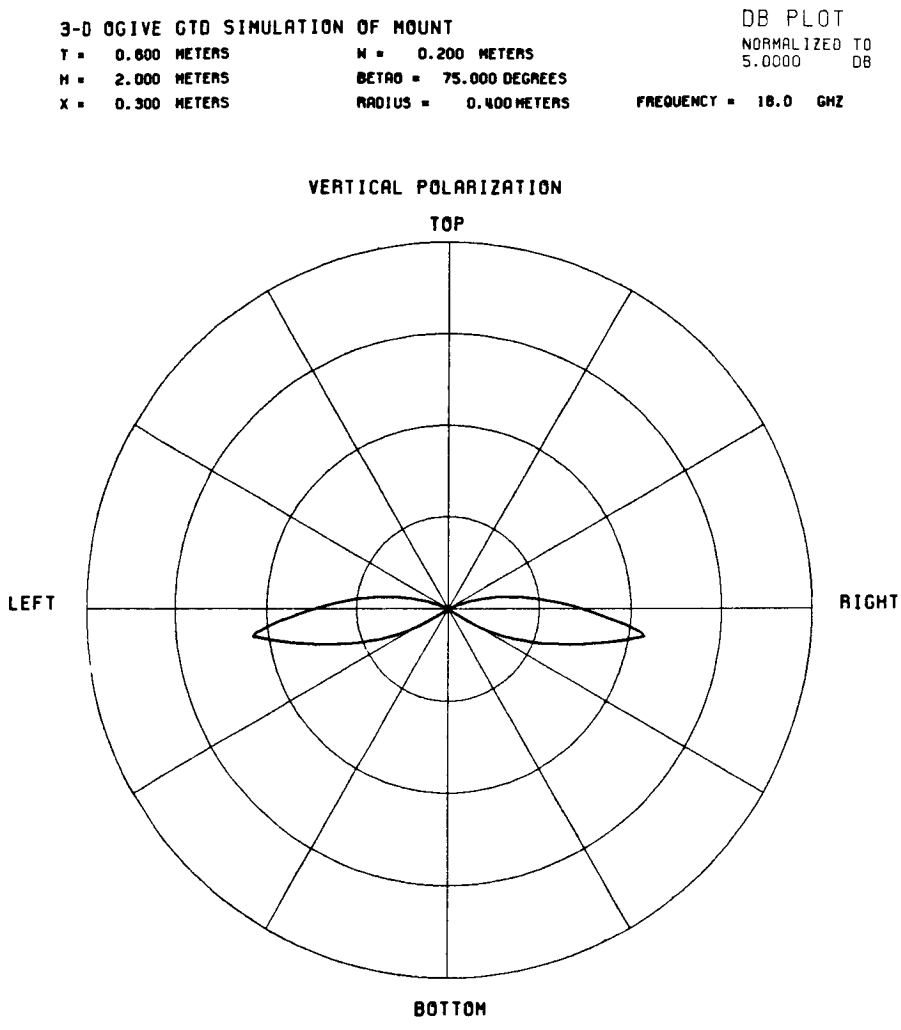

Figure 4.28. Front upper edge diffracted field.

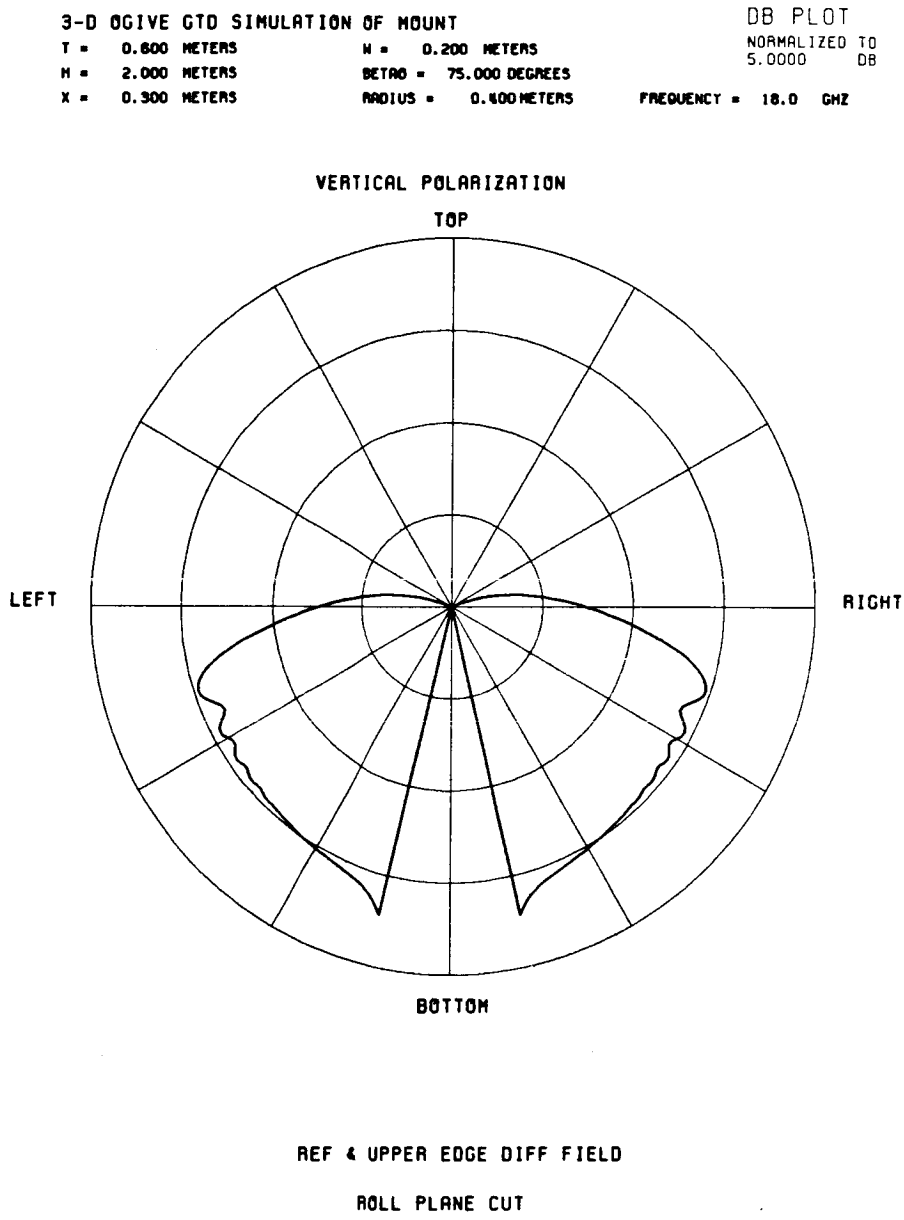

Figure 4.29. Sum of reflected and edge diffracted fields.

Next let us examine the effect of corner diffraction. Figure 4.30 is an elevation cut display of the front edge diffracted field. The discontinuity at the top is due to the termination of the leading edge of the pedestal. The corner diffraction, as shown in Figure 4.31, compensates for this discontinuity and produces a smooth pattern as shown in Figure 4.32.

C.7. Conclusion

Finally the total field is given as the sum of these terms such that

$$\vec{E} = \vec{E}^{i} + \vec{E}^{d} + \vec{E}^{d}_{c} \ . \tag{4.48}$$

An example of the total field calculation is shown in Figure 4.33 for an azimuth pattern cut. Note that due to the lack of a solution for the edge creeping wave and a proper double diffraction solution, the field is basically an approximation and is not completely smooth near the rear of the pedestal. In order to see how the field varies with position above the pedestal, various azimuth cuts are shown in Figures 4.34 and 4.35. One can see there is an equivalent scattering mechanism that comes in and out of phase with the incident wave. As one goes higher and higher relative to the top of the pedestal, this effect gradually disappears and a reasonable plane wave is obtained.

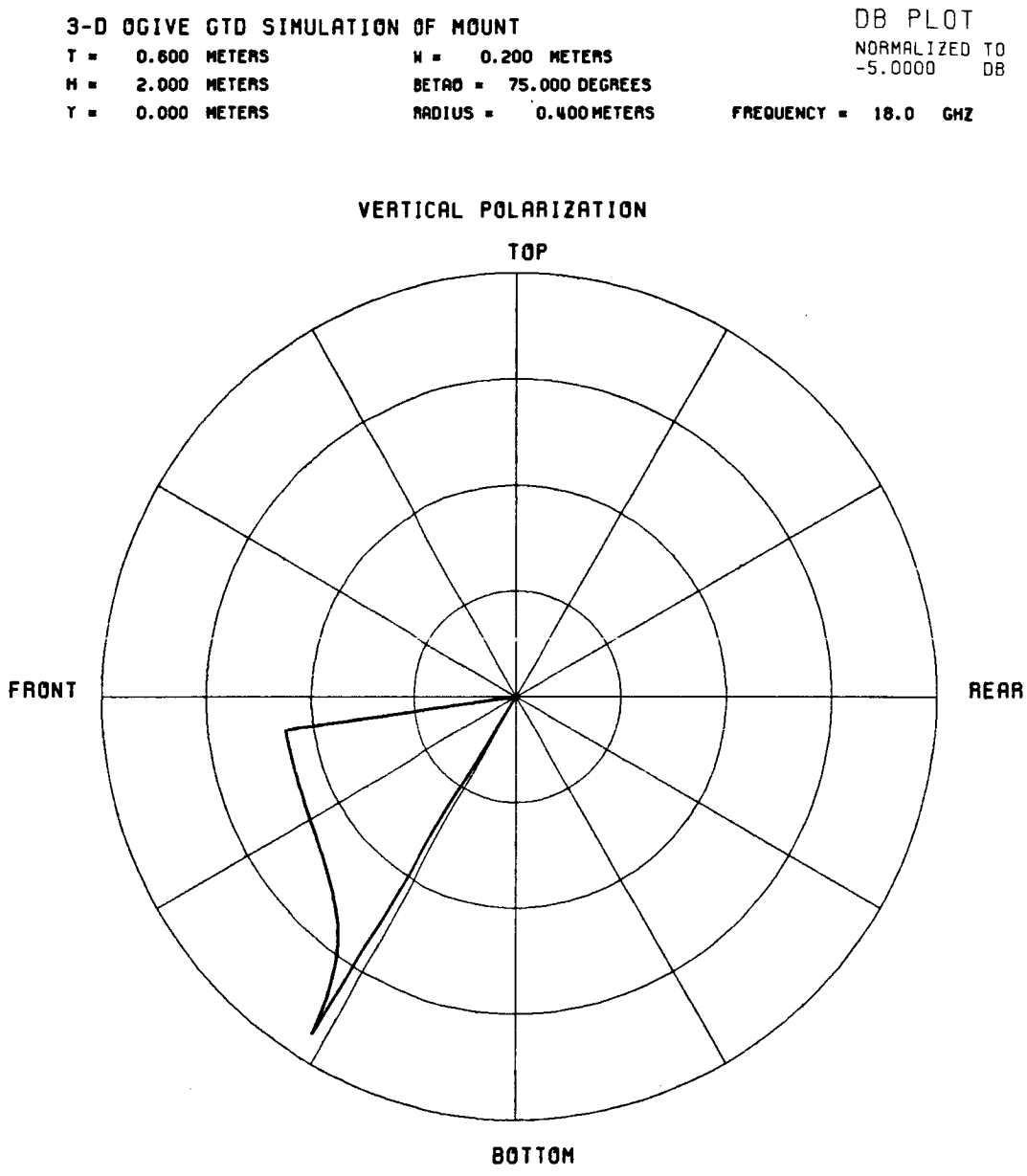

Figure 4.30. Front edge diffracted field.

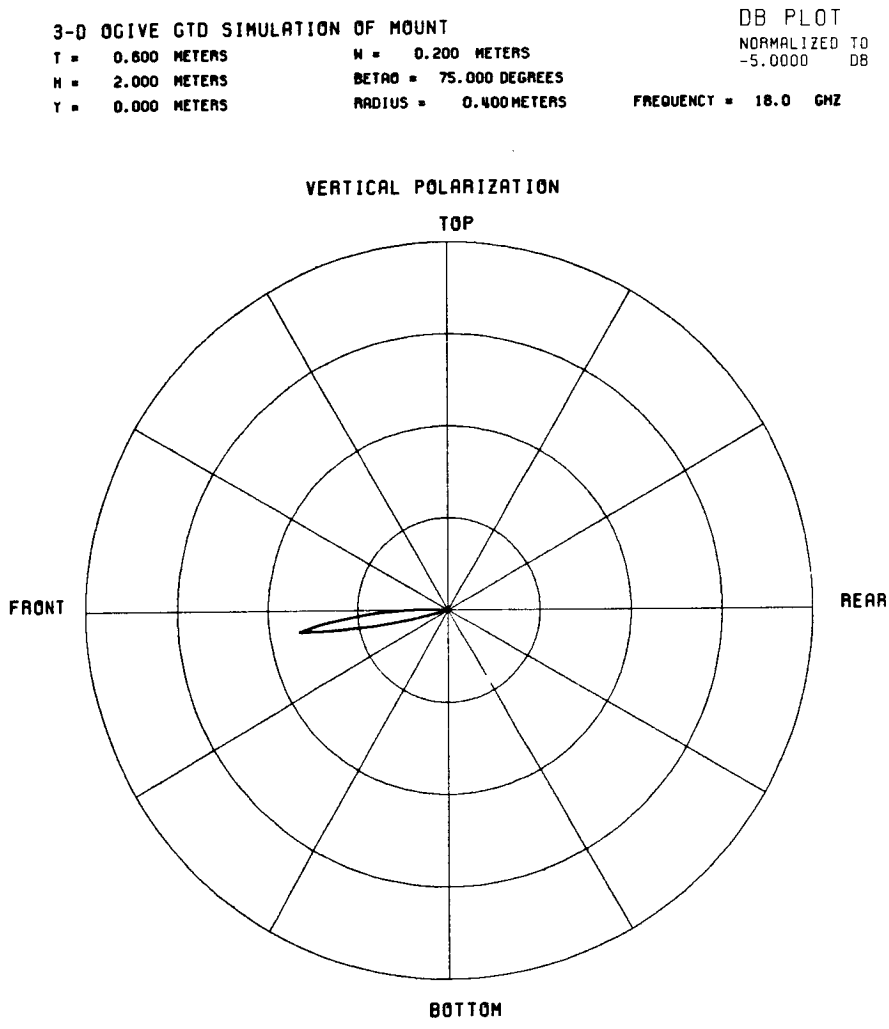

Figure 4.31. Front corner diffraction.

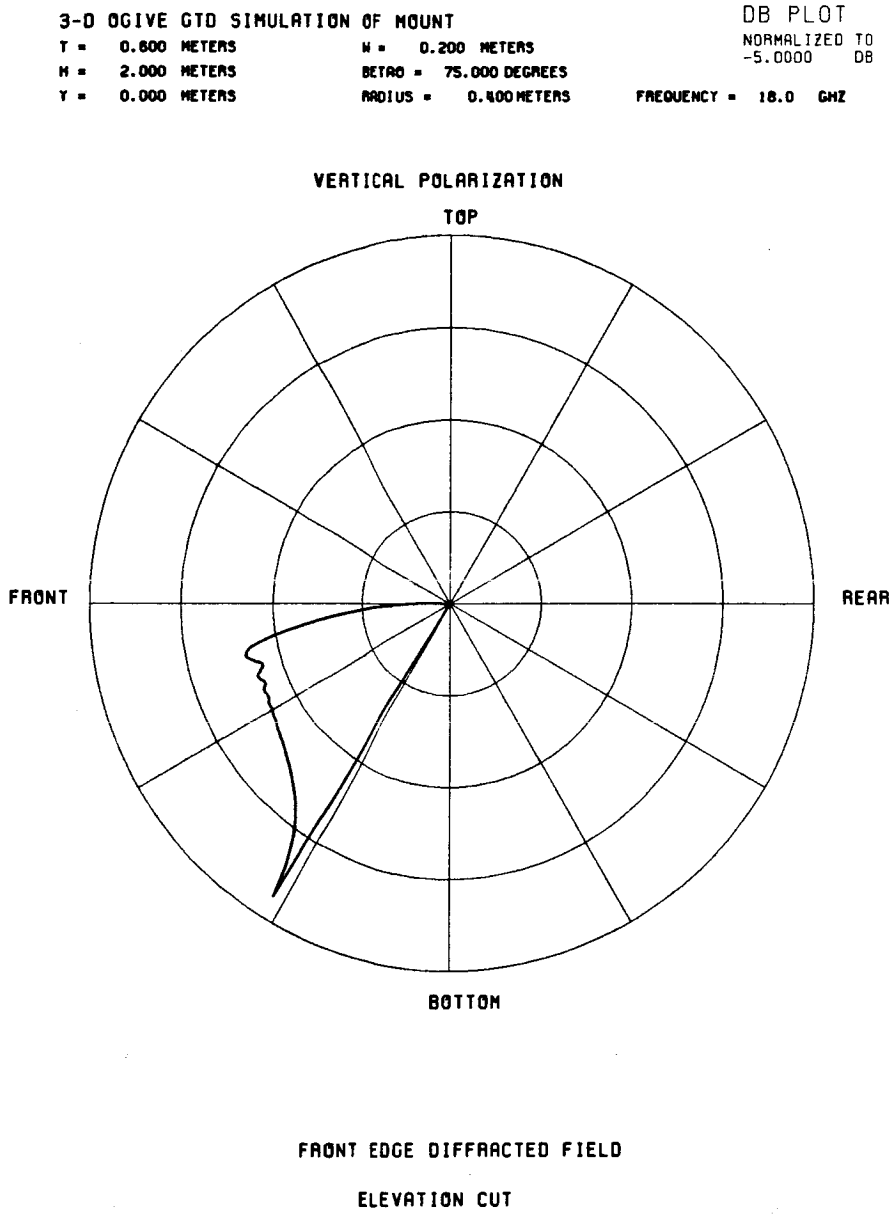

Figure 4.32. Sum of front edge and front corner diffracted field.

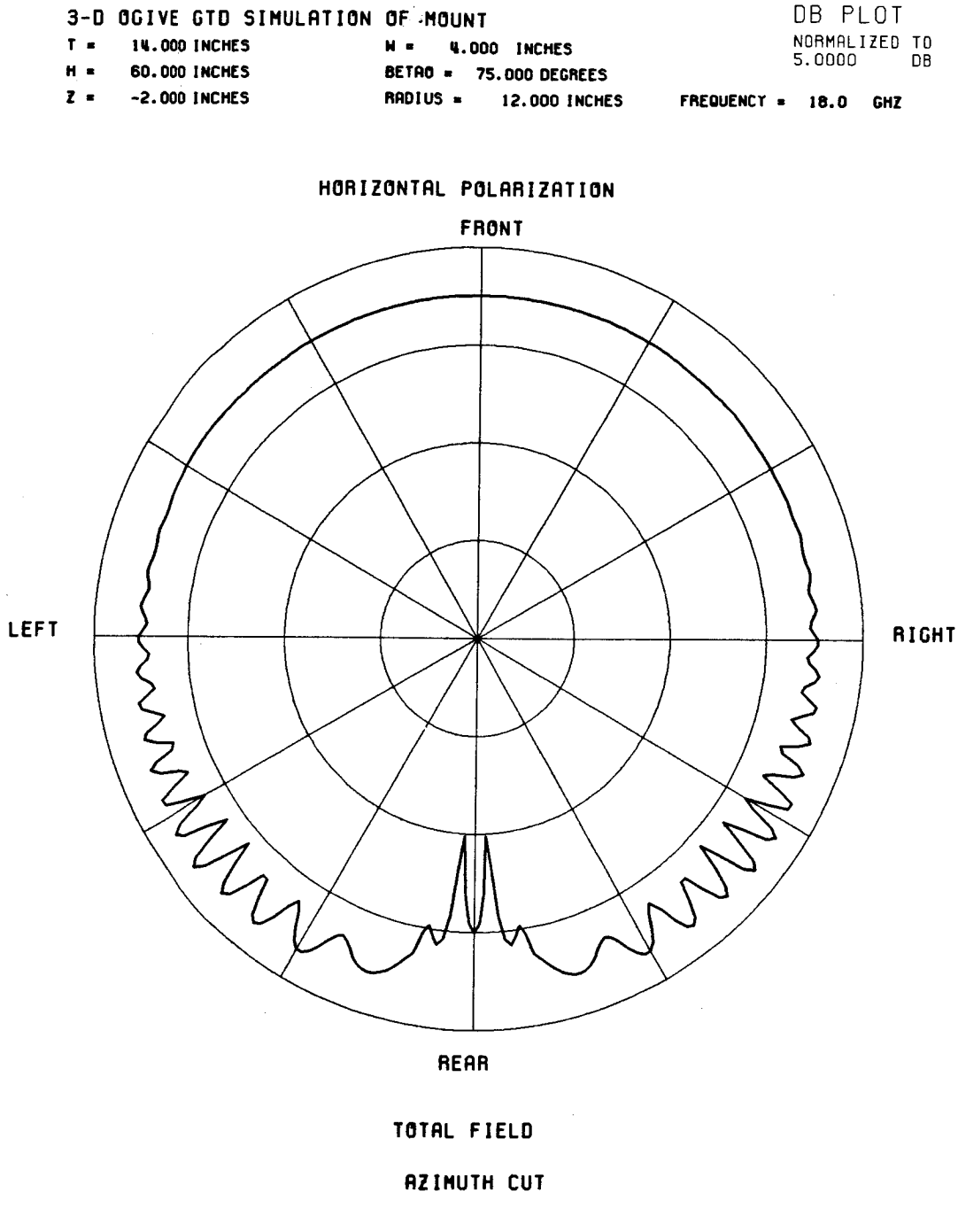

Figure 4.33. Total field.

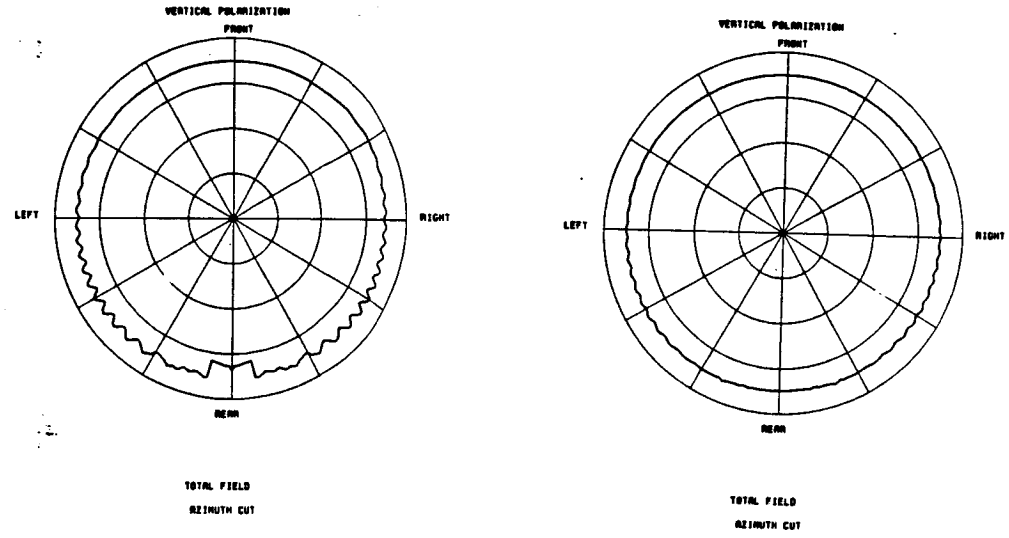

(a) Z=0.5"

(b) Z=3.0"

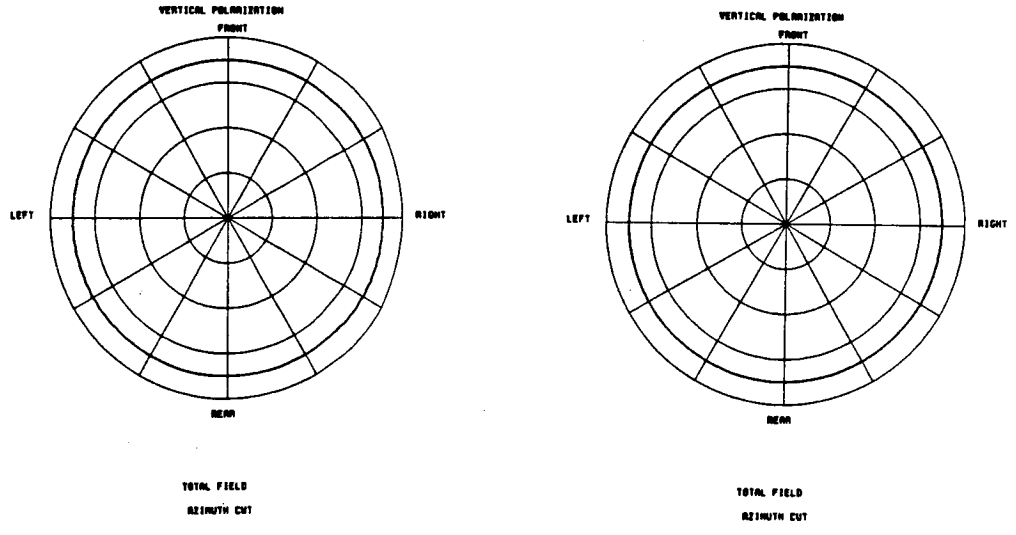

(c) Z=6.0"

(d) Z=9.0"

Figure 4.34. Total field (vertical polarization) at various levels where T=14", W=4", β_0=75°, R=12", F= 18 GHz.

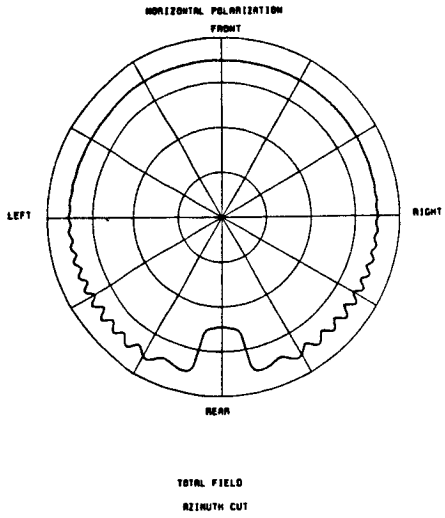

(a) Z=0.5"

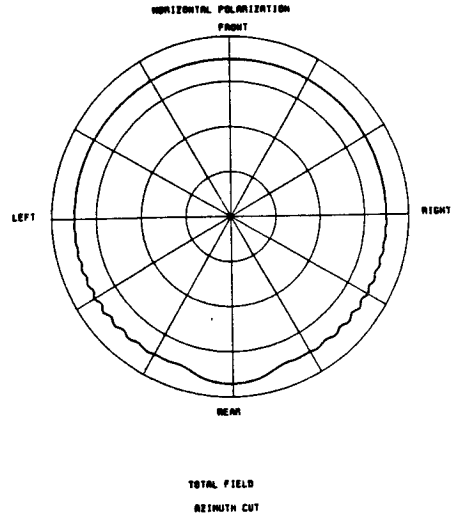

(b) Z=3"

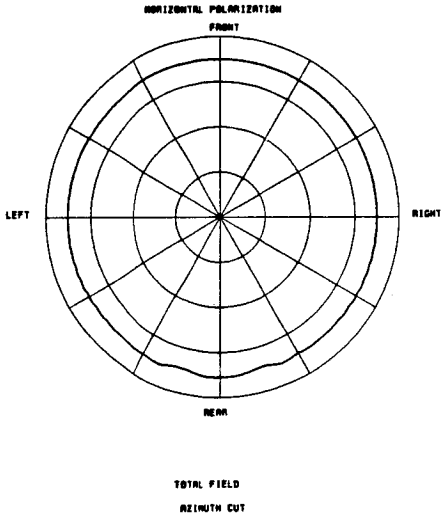

(c) Z=6"

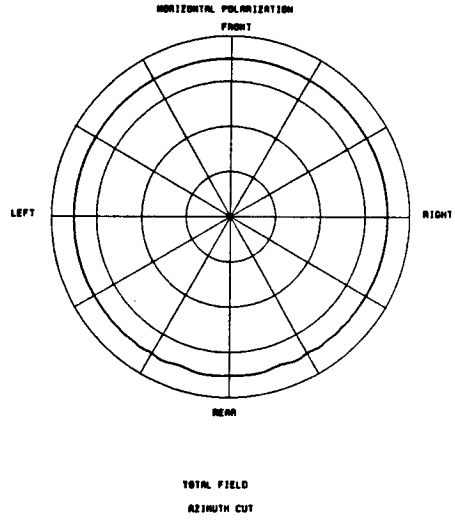

(d) Z=9"

Figure 4.35. Total field (horizontal polarization) at various levels where T=14", W=4", β_0=75°, R=12", F=18 GHz.

CHAPTER V

COMPARISON BETWEEN MEASUREMENT AND CALCULATION

A. INTRODUCTION

This chapter presents a comparison of measured and calculated results for the backscatter from a test sphere at various positions around the pedestal. From this comparison, UTD is shown to be sufficiently accurate to predict the field structure in the space above the pedestal. UTD solution is than used to determine what areas around the pedestal are sufficiently free of pedestal clutter to allow for reasonable measurement accuracy.

B. EXPERIMENTAL SET-UP

A 3.187 inches sphere was used to probe the field around the pedestal. The sphere was held in place using four strings and manipulated to various positions by adjusting the strings as shown in Figure 5.1. A total of 21 positions were used, 16 of which were above the top of the pedestal, and 5 below. For each position, both vertical and horizontal polarized fields were used to illuminate the test sphere and pedestal. Refer to Figure 5.2 for a complete list of the various coordinate locations used for this study.

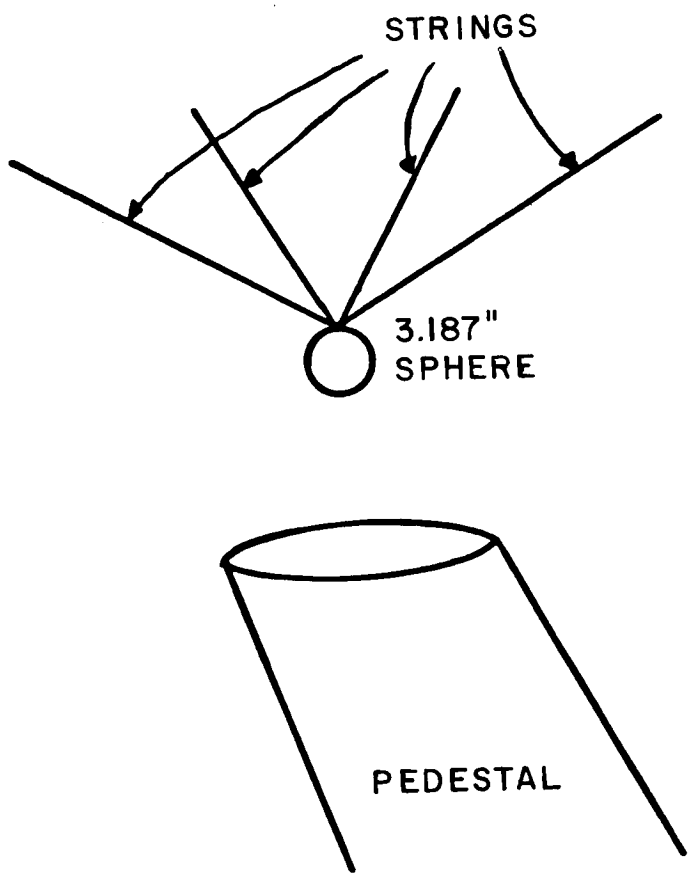

Figure 5.1. Test sphere set-up.

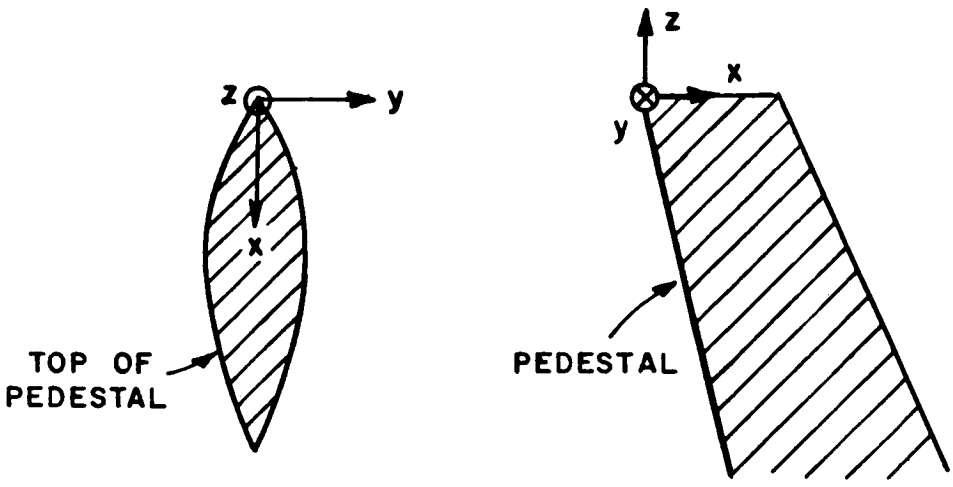

TOP VIEW SIDE VIEW

CONFIGURATION	X/INCHES	Y/INCHES
CONF1*	2	0
CONF2*	7	0
CONF3*	12	0
CONF4*	7	-7
CONF5*	15	0
CONF6*	15	-3
CONF7*	15	-6
CONF8*	15	-9

*	VP	HP
Z=3"	A	C
Z=6"	B	D

CONF9@	-3	0
CONF10@	2	-7
CONF11@	7	-7
CONF12@	12	-7
CONF13@	17	0

@	VP	HP
Z=-2"	E	F

Figure 5.2. Coordinates of various sphere positions relative to pedestal.

C. THEORETICAL BACKGROUND

The backscatter of a small test sphere contains five main components as described below:

1) Direct reflection: when the incident ray stikes the sphere, it is specularly reflected back by the sphere as shown in Figure 5.3a.

2) Creeping wave: when the incident ray strikes the side of the sphere, it creeps around half the circumference and radiates back as shown in Figure 5.3b. Note that there are an infinite number of possible paths so that an eigenfunction solution is used as opposed to UTD.

3) Interaction between sphere and top of pedestal: when the sphere is above the top of the pedestal, the incoming ray may reflect down off the sphere, reflect off the top of the pedestal, reflect off the sphere a second time and return back to the radar. Or, it may reflect down, strike an edge of the pedestal, reflect off the sphere a second time and return to the radar as shown in Figure 5.3c.

4) Primary interaction between pedestal and sphere: when the ray diffracts off an edge or reflects off the side of the pedestal, it may strike the sphere and

reflect back to the radar as shown in Figure 5.3d. Note that by reciprocity, a ray can travel in the reverse direction which doubles the magnitude of this contribution.

5) Secondary interaction between pedestal and sphere: when the ray diffracts off an edge, reflects off the side or creeps on and launches from the surface, it may strike the sphere and reflects back to the pedestal and subsequently back to the radar as shown in Figure 5.3e.

In all cases of reflection from the sphere, Equation (5.1) is used as follows:

$$\vec{E}^{ref} = - \vec{E}^{i} \sqrt{\frac{\rho_1^r \, \rho_2^r}{(\rho_1^r+s)(\rho_2^r+s)}} \, e^{-jks}$$

where

$$\frac{1}{\rho_1^r} = \frac{1}{s'} + \frac{2\cos\theta^i}{R}$$

$$\frac{1}{\rho_2^r} = \frac{1}{s'} + \frac{2}{R\cos\theta^i}$$

and s is the distance from the sphere to the observation point.

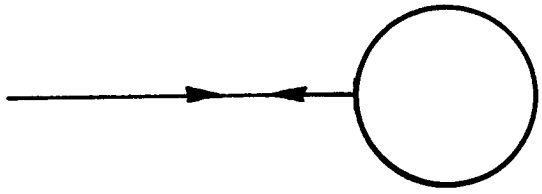

a) direct reflection

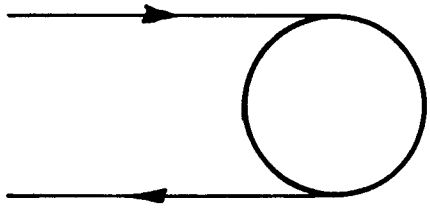

b) creeping wave

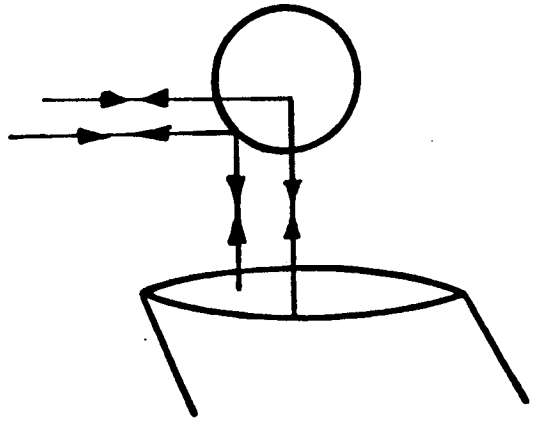

c) interaction between sphere and top of pedestal

Figure 5.3. Five main components associated with pedestal/sphere backscattered field.

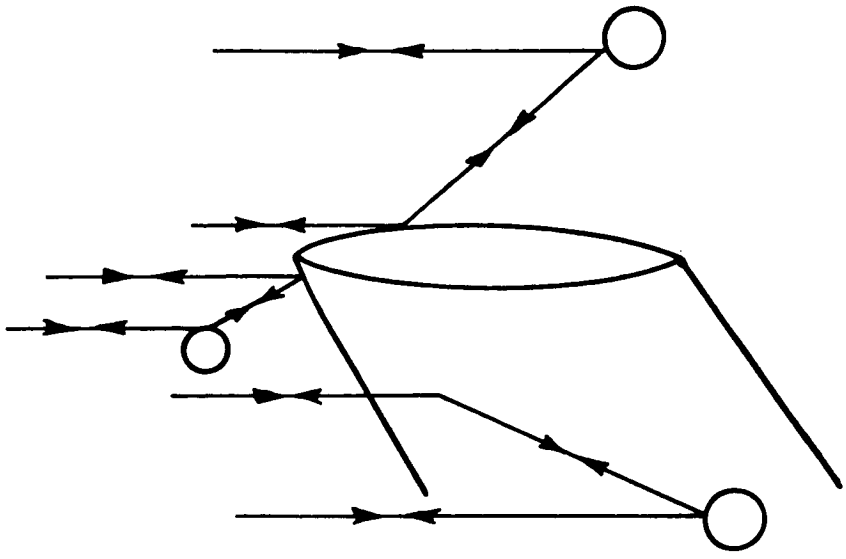

d) primary interaction between pedestal and sphere

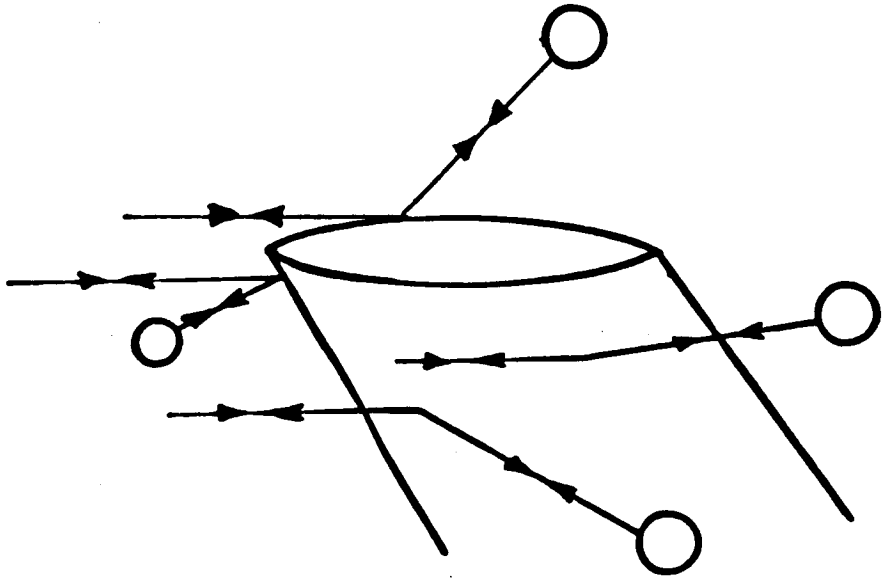

e) secondary interaction between pedestal and sphere

Figure 5.3. Continued.

D. COMPARISON OF RESULTS

The backscattered field of the test sphere at each position around the pedestal is plotted in both the time and frequency domains. In each domain, the measured response is compared to the calculated response. Moreover in the frequency domain, the difference between the magnitude of the exact sphere response and the calculated or measured results is presented. So on each frequency domain plot, one can evaluate 1) either the measured or the calculated response, 2) the exact sphere response, and 3) the magnitude difference between 1) and 2). An example is shown in Figures 5.7 and 5.8.

There are a few points one needs to be aware of:

1) The exact sphere response, as shown in Figure 5.4a, has two major components. The first one, which has an RCS magnitude of 0.012 square meters, is the direct reflection term from the test sphere. The second and much smaller components is the creeping wave term. All the calculations are basically similar to the exact sphere result with additional terms due to multiple scattering involving the pedestal. The sphere return will appear at various times on these plots because it is being moved to various locations within the test volume around the pedestal.

2) The calculation of the vertically polarized response is not as accurate as that of the horizontally polarization one because of two problems. First, UTD fails in the region behind the pedestal for vertical polarization as explained in Chapter IV; thus, there is an inherent problem in the calculation. Second, the test sphere is hung up using four strings taped to its top so that the major creeping wave term for vertical polarization will strike it, causing a set of string/sphere scattering terms, as shown in Figure 5.5a. This problem is not as significant for horizontal polarization (see Figure 5.5b) because the major creeping wave passes along the side of the test sphere, not its top. Hence there is a problem due to the experimental set-up.

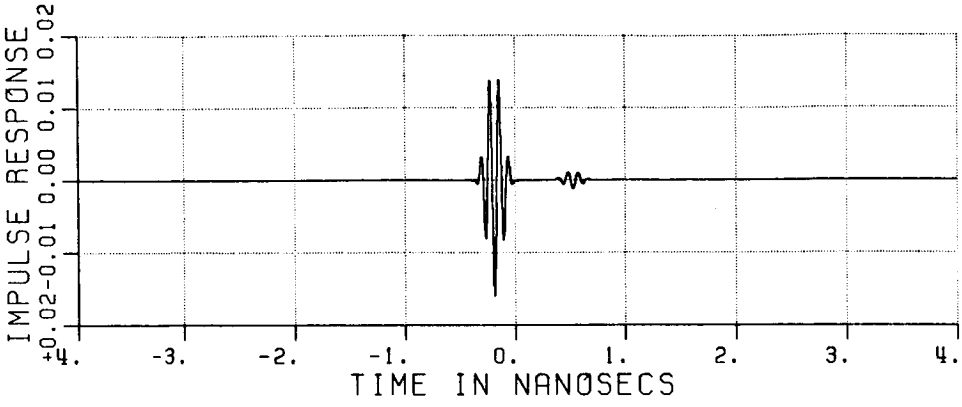

a) time domain

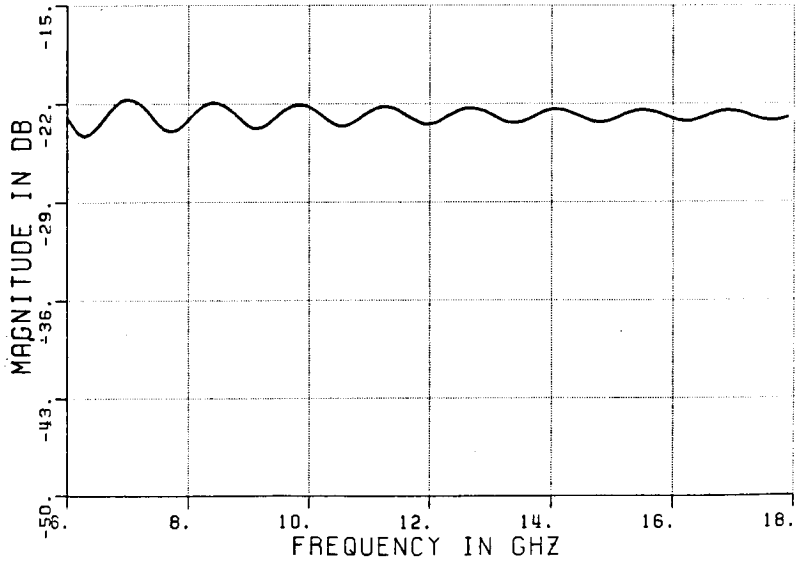

b) frequency domain

Figure 5.4. Exact sphere response.

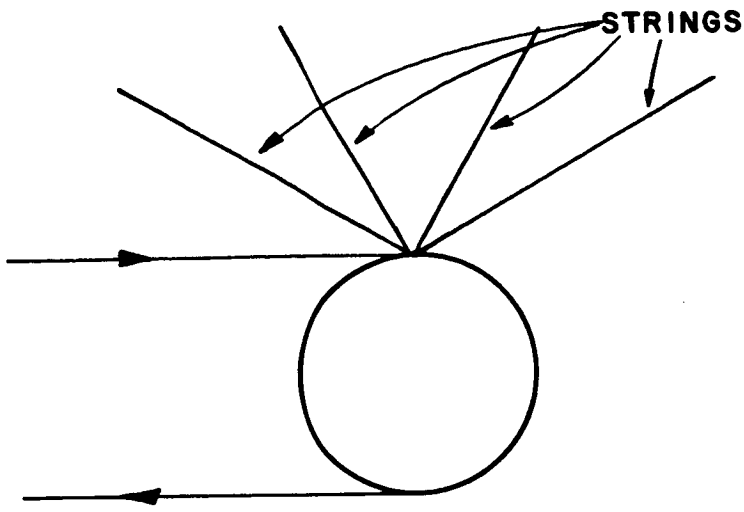

a) vertical polarization

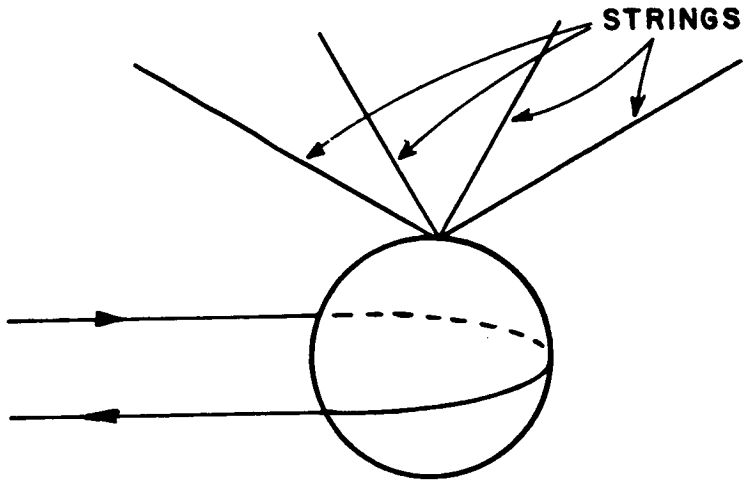

b) horizontal polarization

Figure 5.5. Major creeping wave paths for vertically and horizontally polarizated signals.

Because all the data associated with the sphere/pedestal scattering is basically the same, let us examine one test case, and then the reader can evaluate the others using the same approach. For example, let us study "CONF3C" as shown in Figures 5.6 to 5.8. Note that "CONF3C" as defined in Figure 5.2 is positioned at X=12", Y=0", and Z=3". The major ray components as shown in Figure 5.6 are 1) the direct reflected ray, 2) primary pedestal-sphere interaction, 3) sphere-pedestal top interaction, and 4) creeping wave. On the time domain plots of Figure 5.7, one should notice three distinct terms. The first and longest one is the direct reflection term closely followed by the primary pedestal-sphere interaction, the second one is the sphere-pedestal top interaction, and the third one is the creeping wave term.

From the timing information of Figure 5.6, the direct reflection path takes 1.76 ns. to travel from the reference line at the pedestal tip to the sphere and back. The primary diffracted ray takes about 1.93 ns., the sphere-pedestal top interaction takes 2.16 ns., and the creeping wave term takes 2.46 ns. From this time information, one immediately recognizes why the calculation looks like it does. The direct reflection and primary interaction are so close that they come in and out of phase to produce rather large fluctuations by comparing Figure 5.7 with the exact sphere as shown in Figure 5.4. Then after a delay of 2.16-1.93 = 0.23 ns., one observes the sphere-pedestal top reflection term. Finally, after another delay of 2.46-2.16 = 0.3 ns., one notices the creeping wave. Comparing measured and calculated results, one observes very good agreement except for a slight magnitude difference which is within experimental error limits. The frequency

domain data for "CONF3C" is shown in Figure 5.8 where the measured data is plotted on top, and the calculated one on the bottom. On each plot the bold curve is either the measured or calculated response, the curve with long dash lines is the exact sphere response, and the curve with short dash lines is the difference between the two. The exact sphere response is the desired response, i.e., if the pedestal is perfect, it would be invisible to the radar and not affect the target response. However, since the pedestal is not perfect, these results are used to illustrate the significance of the error. One can also compare the measured data to the calculated data to see how well UTD works in each situation.

Similar results for the various sphere locations defined in Figure 5.2 are shown in Figures 5.9 to 5.92. Note that one has to move about 6" above the pedestal before the target/sphere interaction is acceptable. Further, very large errors occur as the target extends below the top of the pedestal. This becomes very serious as the sphere moves behind the pedestal. Absorber could be used to reduce the sphere/pedestal interaction for sphere location off to the side of the pedestal; however, the addition of the absorber will create more blockage as the sphere is moved behind the pedestal. The reflection from the pedestal is so serious that one must use some absorber at least near the top of the pedestal. The pedestal or pedestal/absorber blockage issue must be faced in either case. Nevertheless, one is forewarned of this potential serious problem. In any event, it is suggested that one evaluate how severe the problem is by probing the area areound their pedestal as done here.

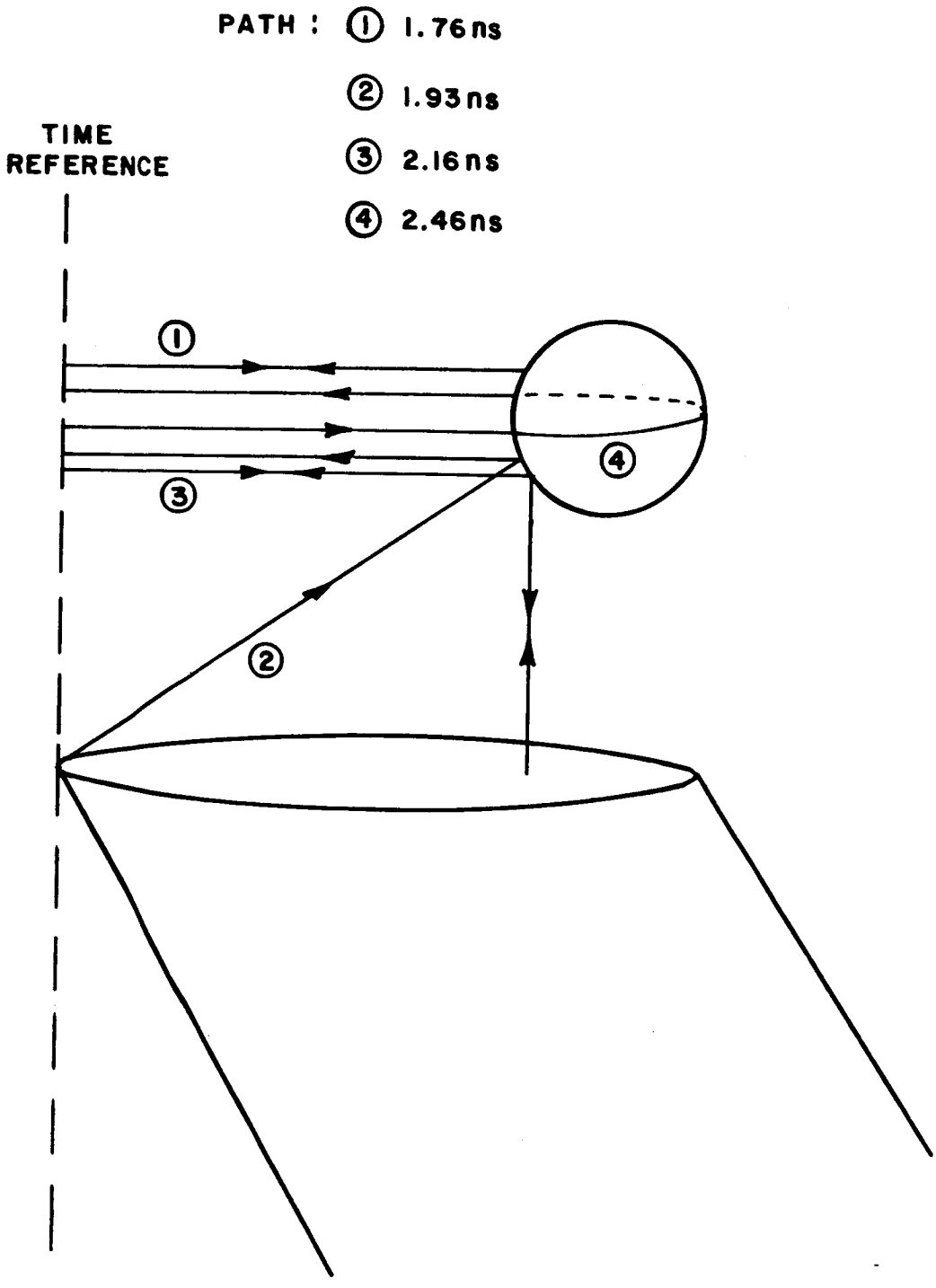

Figure 5.6. Ray tracing of CONF3C.

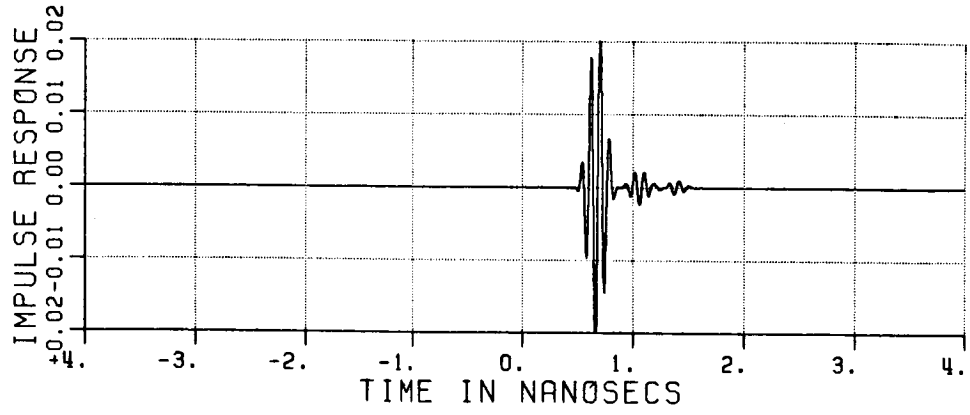

a) Calculated result

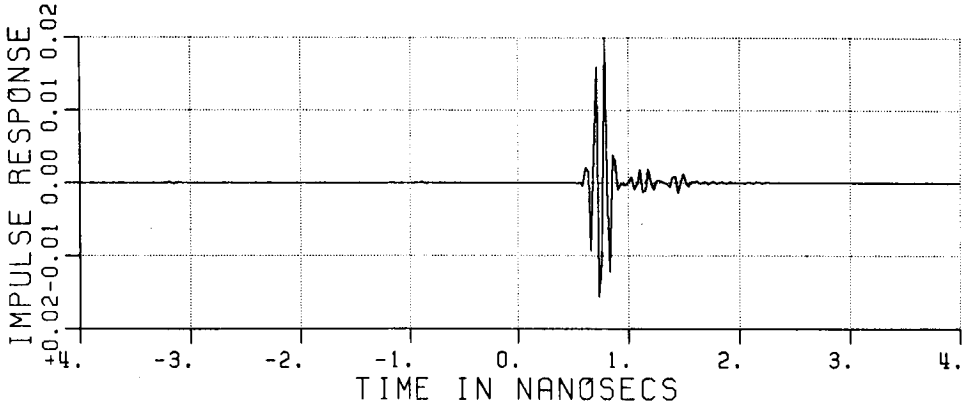

b) Measured result

Figure 5.7. Time domain plots of CONF3C: X=12",Y=0",Z=3"; HP.

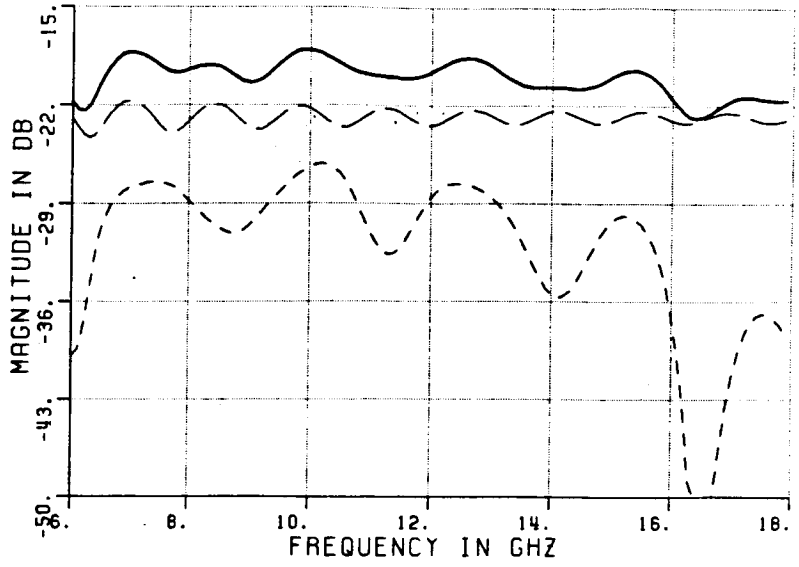

a) calculated result

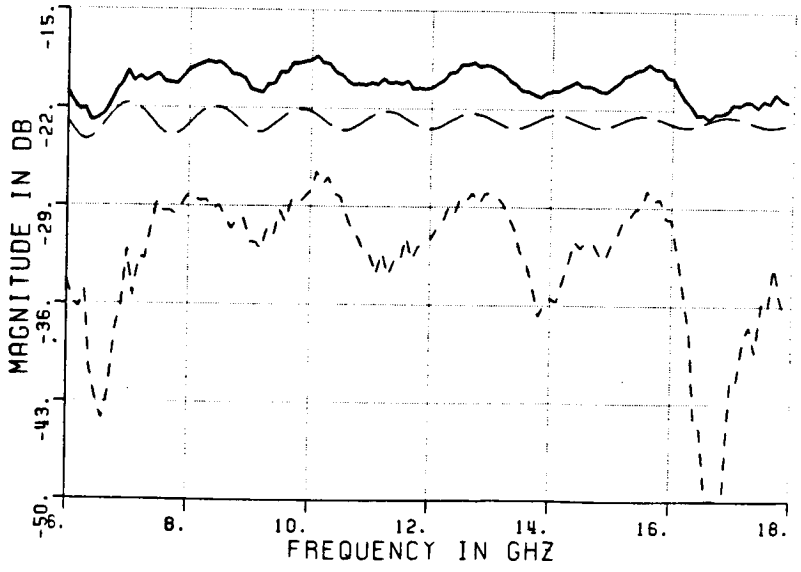

b) measured result

Figure 5.8. Frequency domain plots of CONF3C: X=12",Y=0",Z=3"; HP.

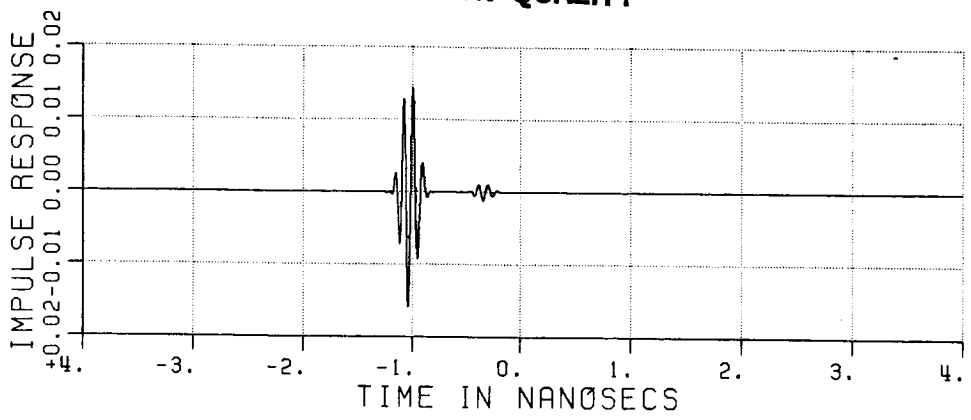

a) Exact sphere

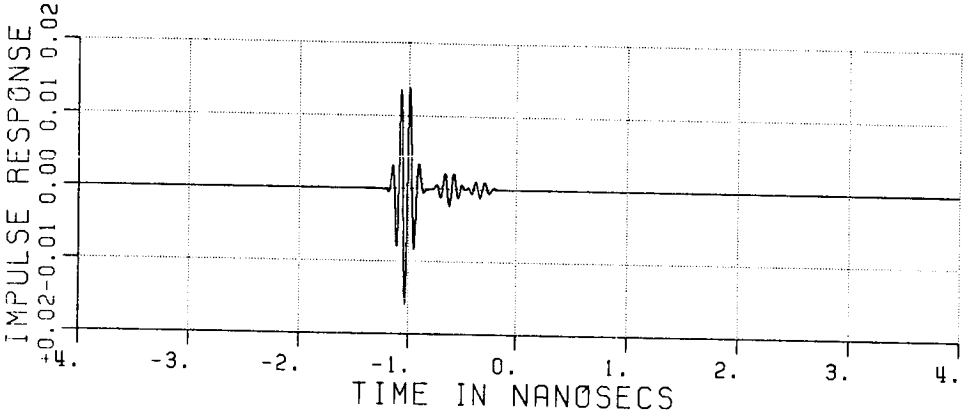

b) Calculated result

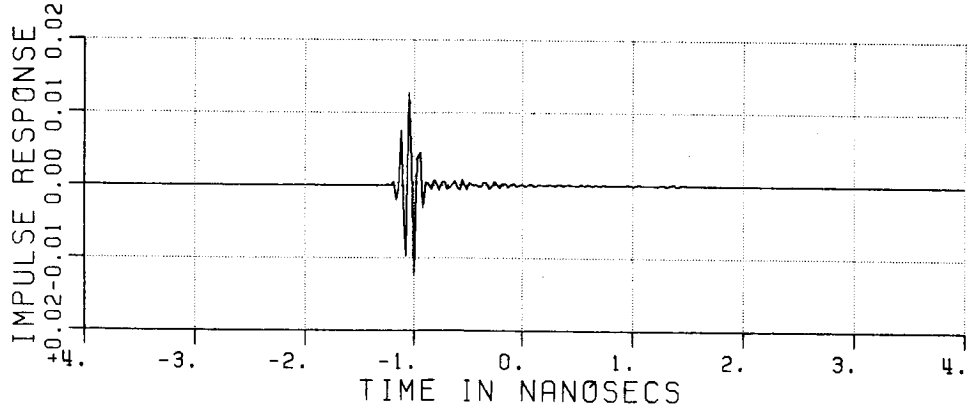

c) Measured result

Figure 5.9. Time domain plots of CONF1A: X=2",Y=0",Z=3"; VP.

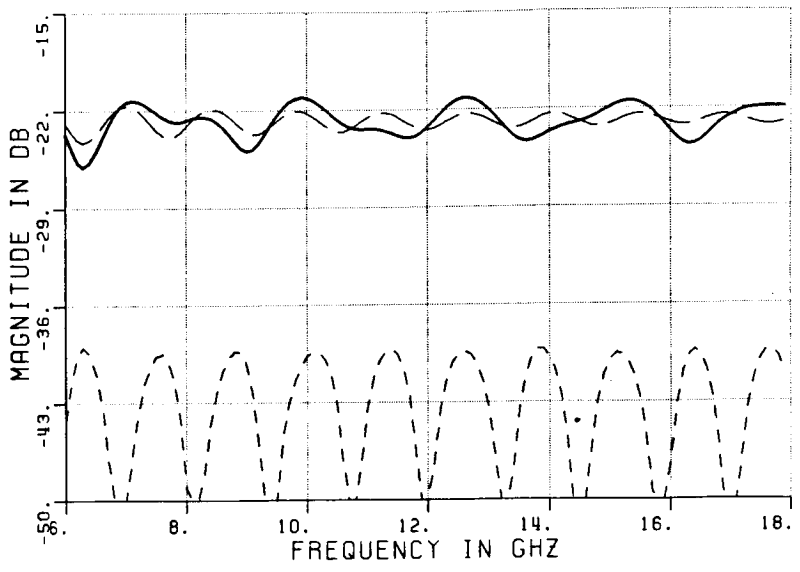

a) calculated result

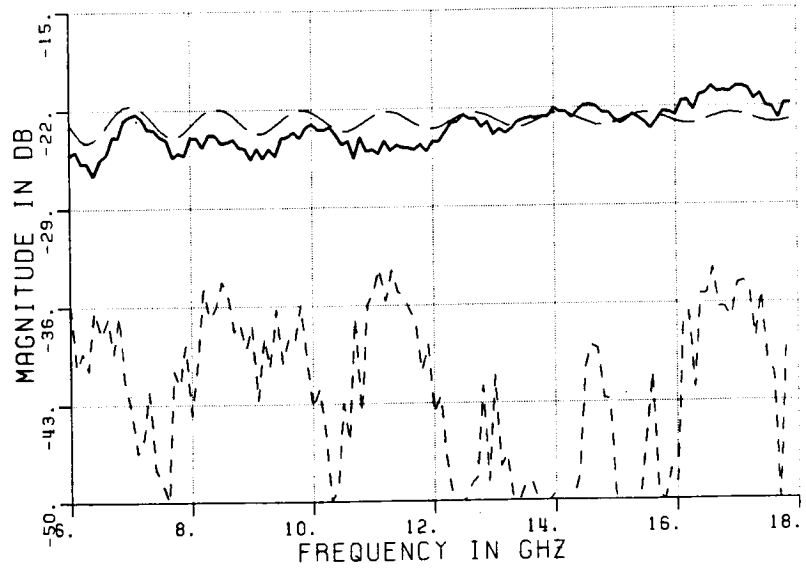

b) measured result

Figure 5.10. Frequency domain plots of CONF1A: X=2",Y=0",Z=3"; VP.

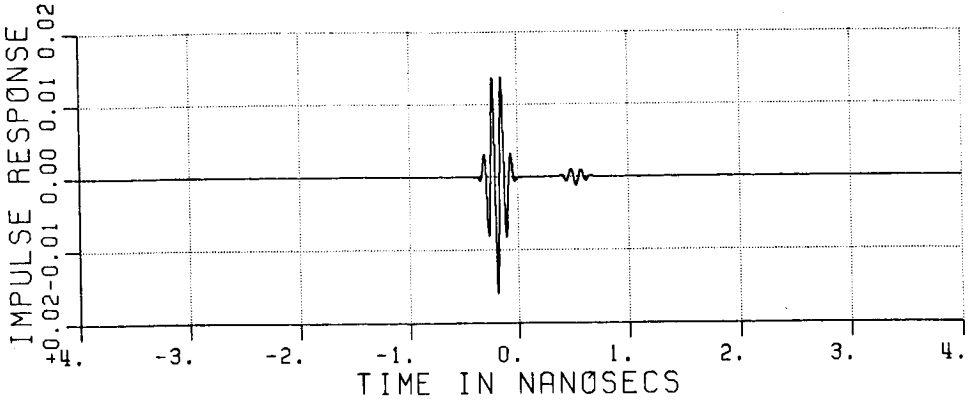

a) Exact sphere

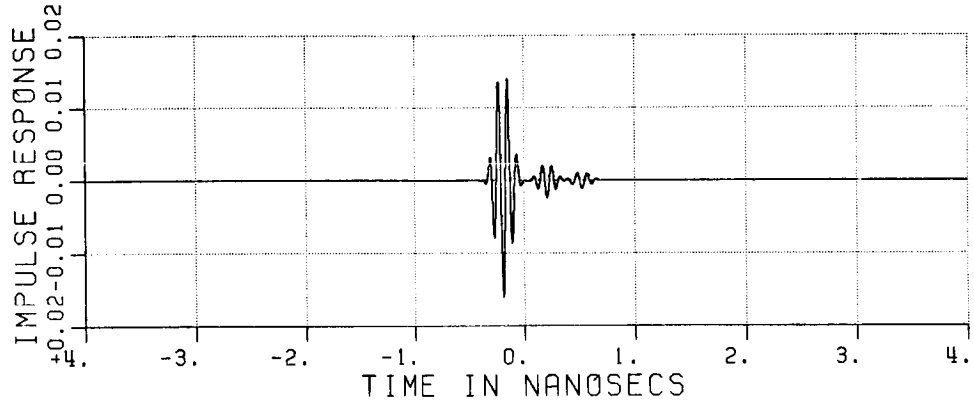

b) Calculated result

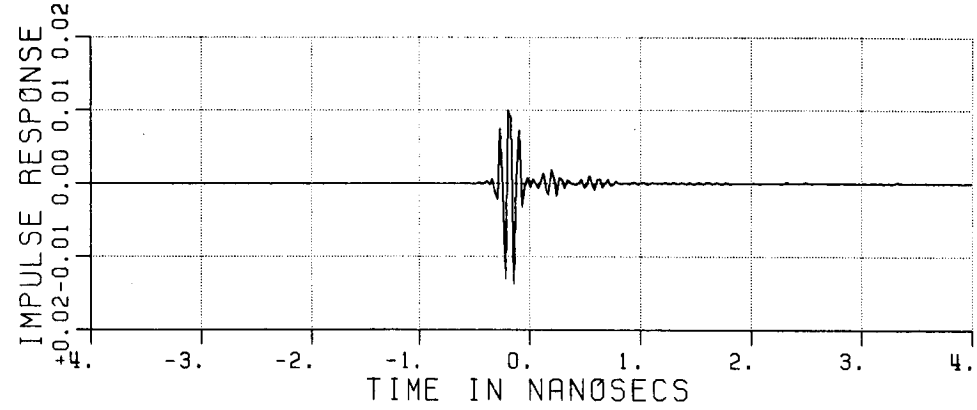

c) Measured result

Figure 5.11. Time domain plots of CONF2A: X=7",Y=0",Z=3"; VP.

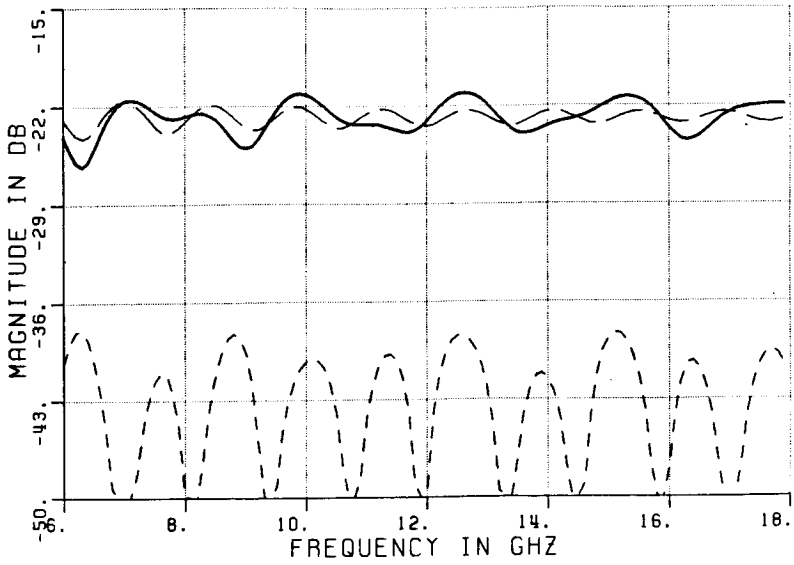

a) calculated result

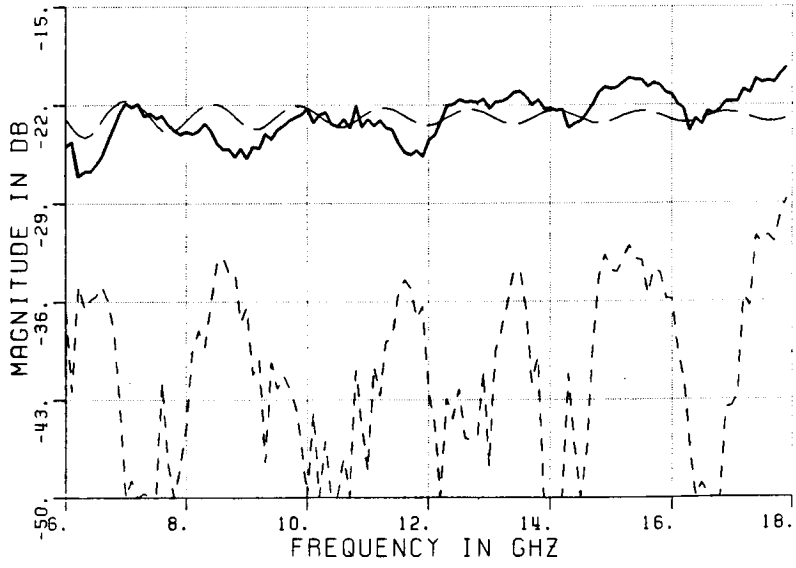

b) measured result

Figure 5.12. Frequency domain plots of CONF2A: X=7",Y=0",Z=3"; VP.

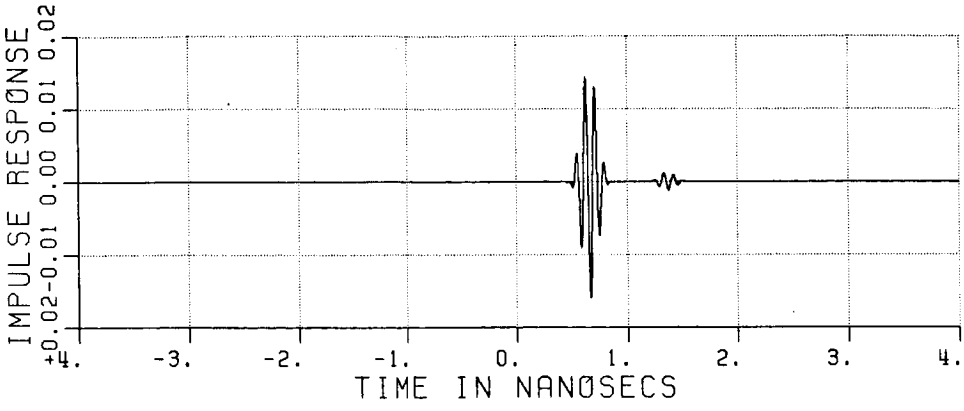

a) Exact sphere

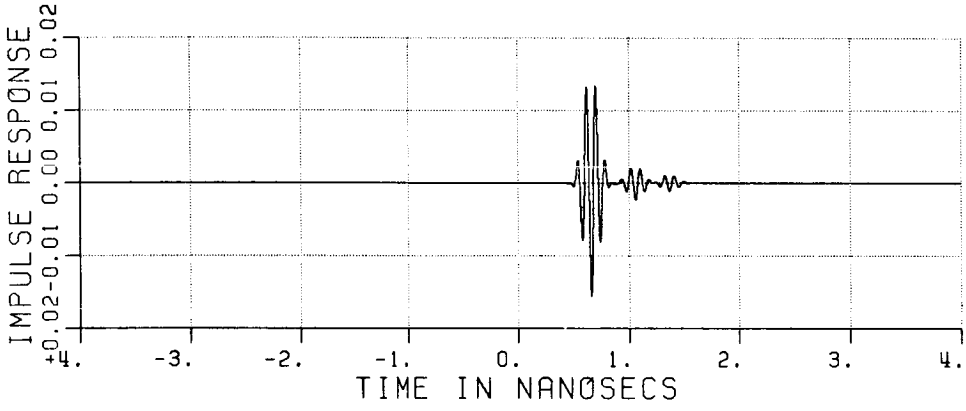

b) Calculated result

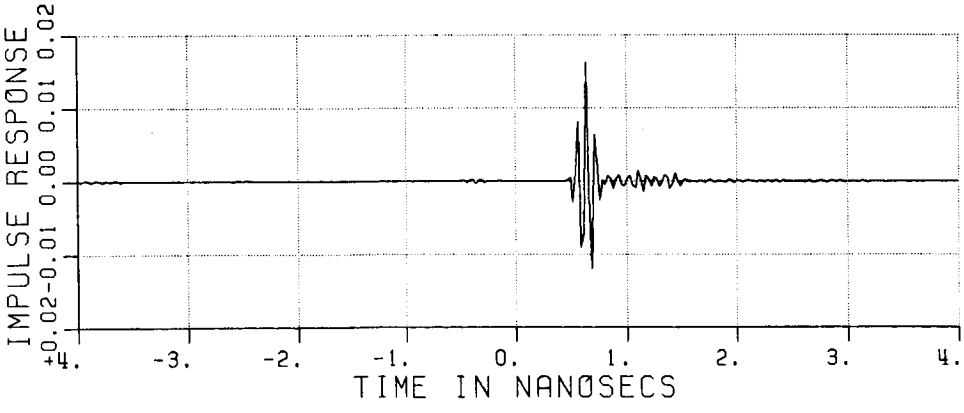

c) Measured result

Figure 5.13. Time domain plots of CONF3A: X=12",Y=0",Z=3"; VP.

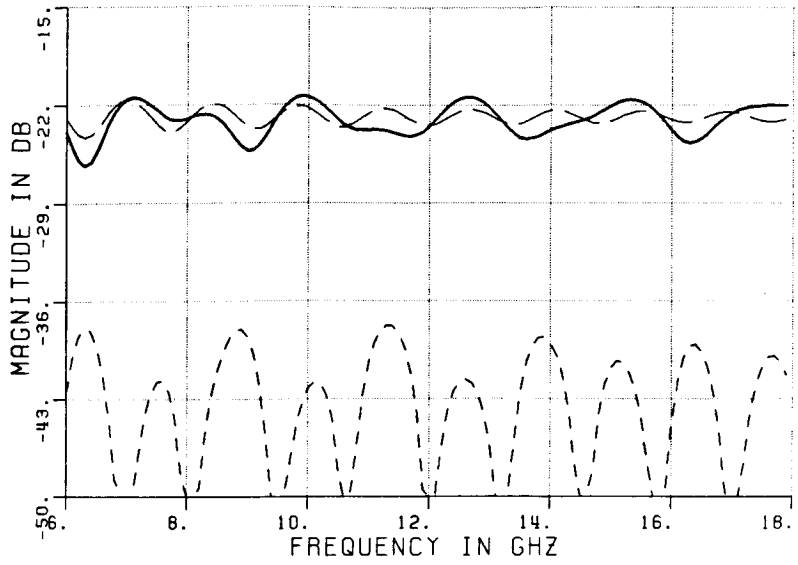

a) calculated result

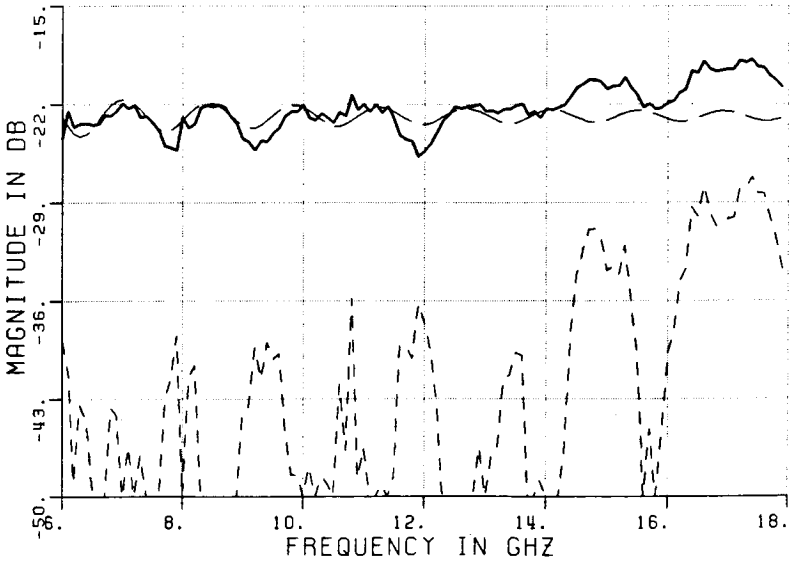

b) measured result

Figure 5.14. Frequency domain plots of CONF3A: X=12",Y=0",Z=3"; VP.

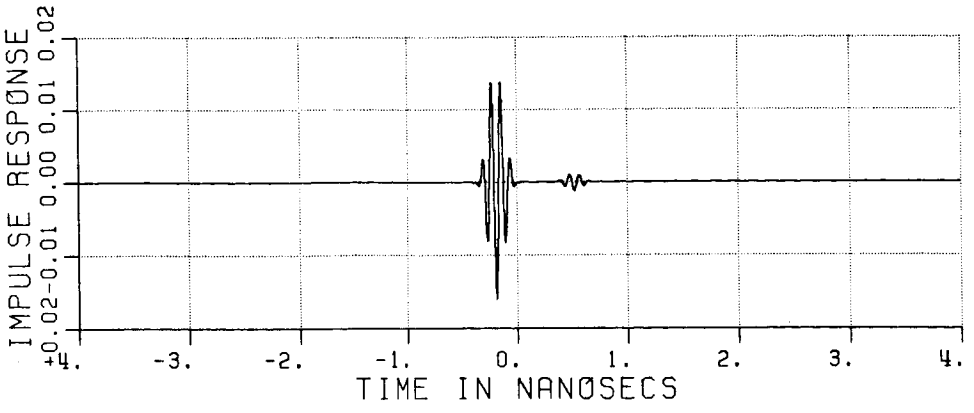

a) Exact sphere

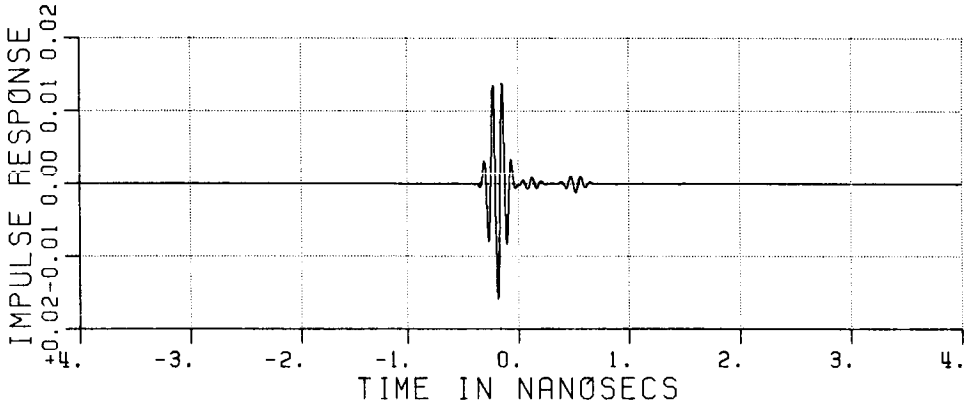

b) Calculated result

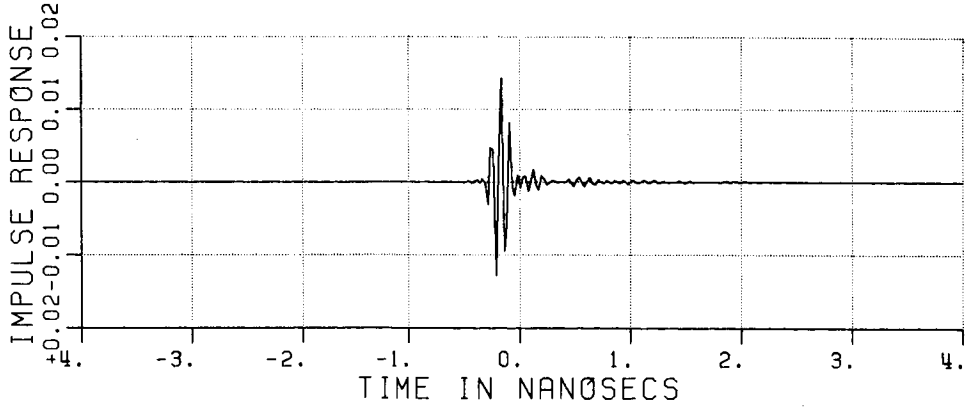

c) Measured result

Figure 5.15. Time domain plots of CONF4A: X=7",Y=-7",Z=3"; VP.

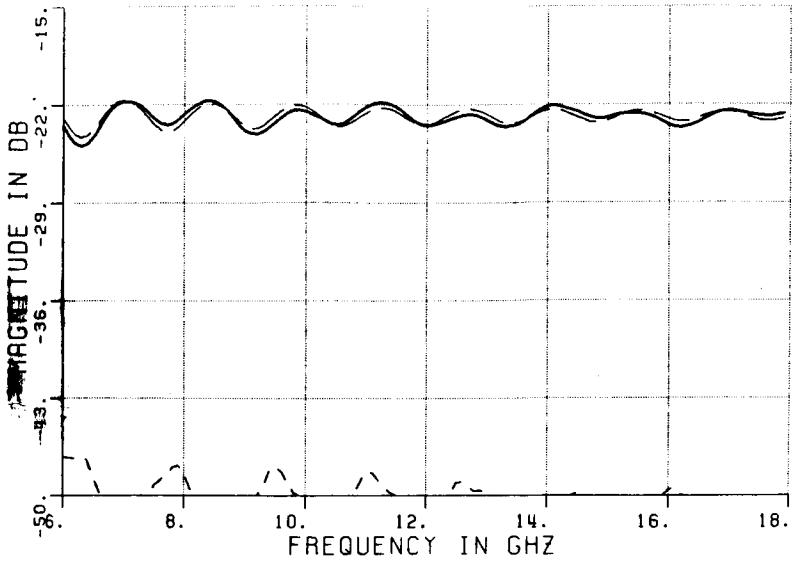

a) calculated result

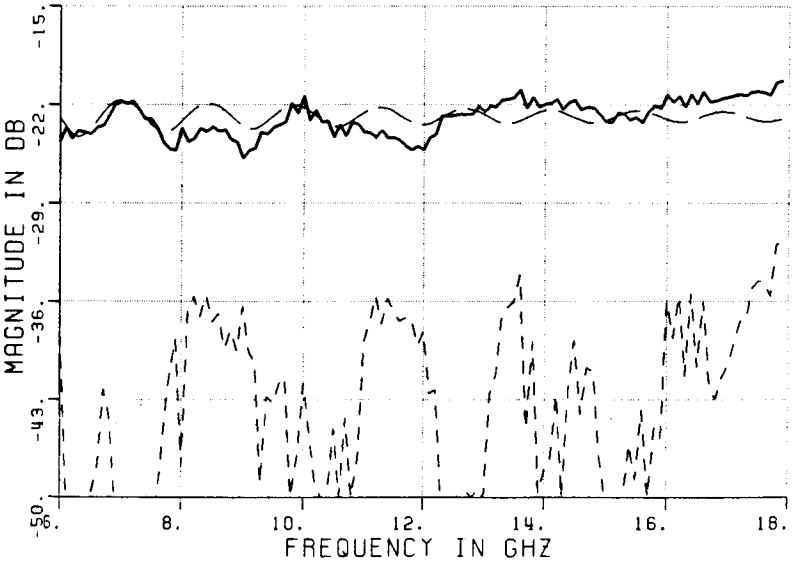

b) measured result

Figure 5.16. Frequency domain plots of CONF4A: X=7",Y=-7",Z=3"; VP.

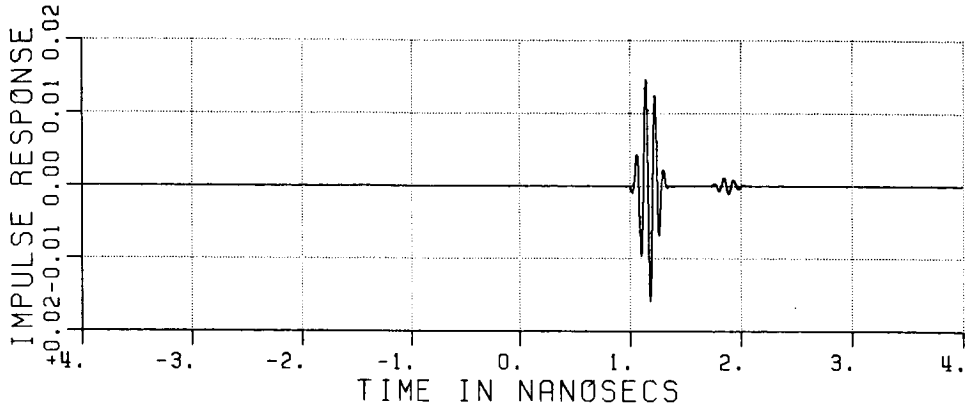

a) Exact sphere

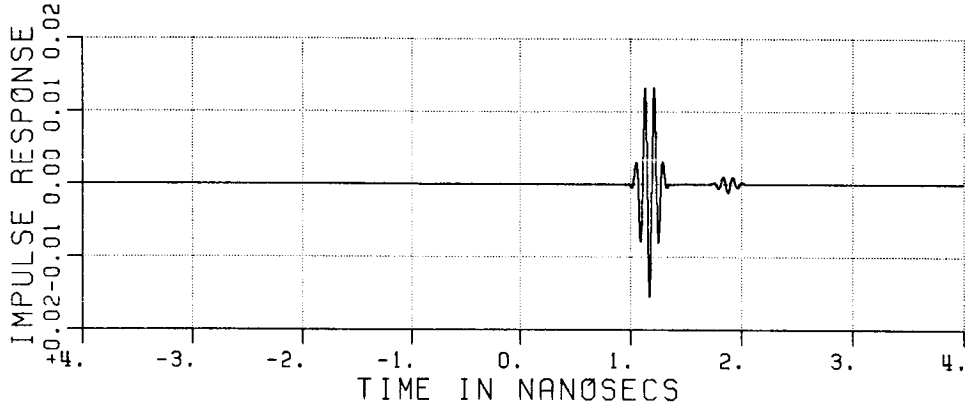

b) Calculated result

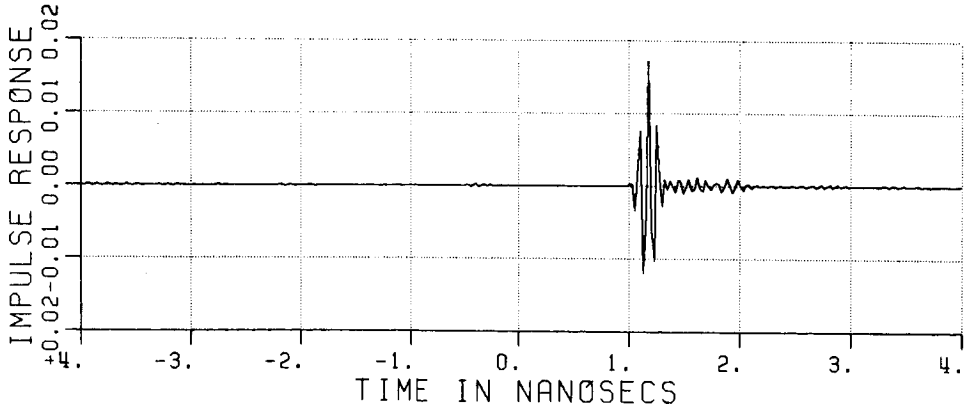

c) Measured result

Figure 5.17. Time domain plots of CONF5A: X=15",Y=0",Z=3"; VP.

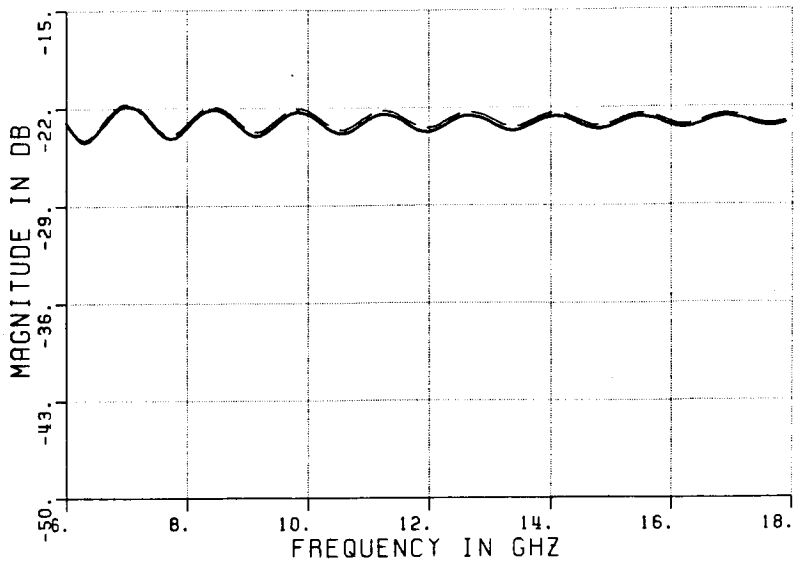

a) calculated result

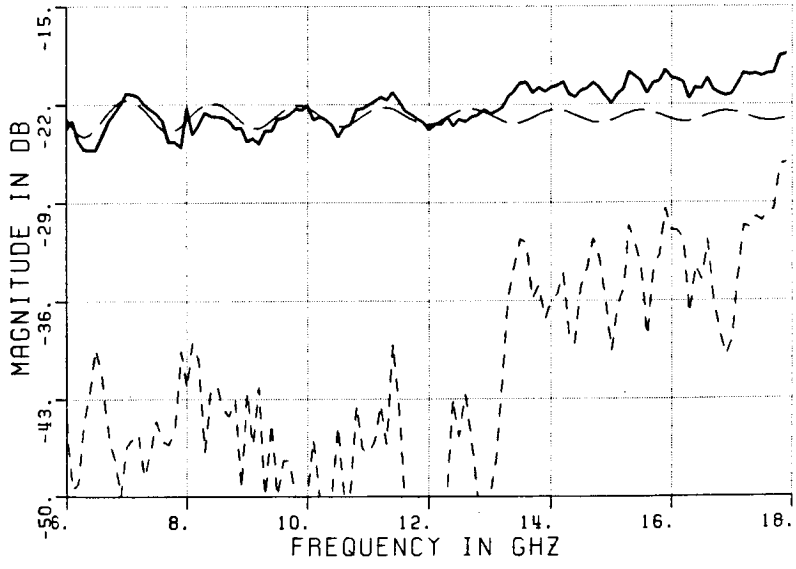

b) measured result

Figure 5.18. Frequency domain plots of CONF5A: X=15",Y=0",Z=3"; VP.

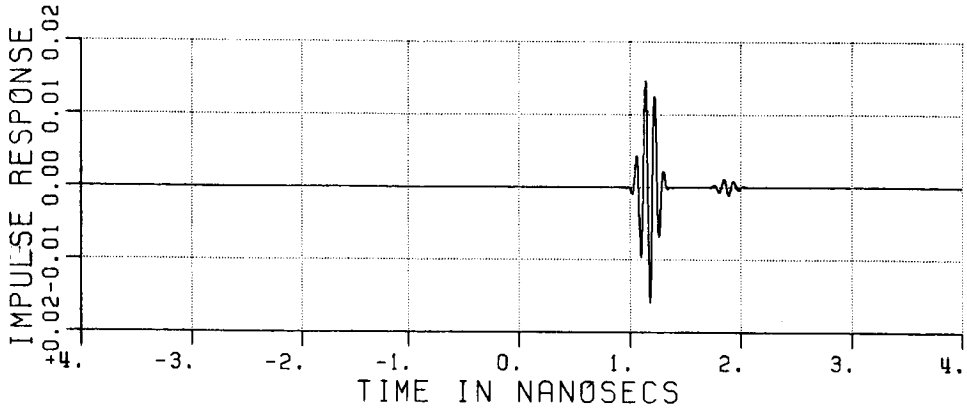

a) Exact sphere

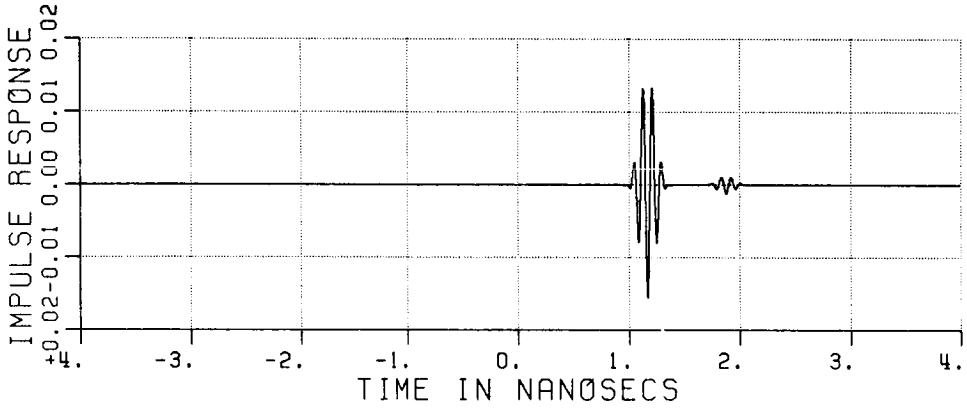

b) Calculated result

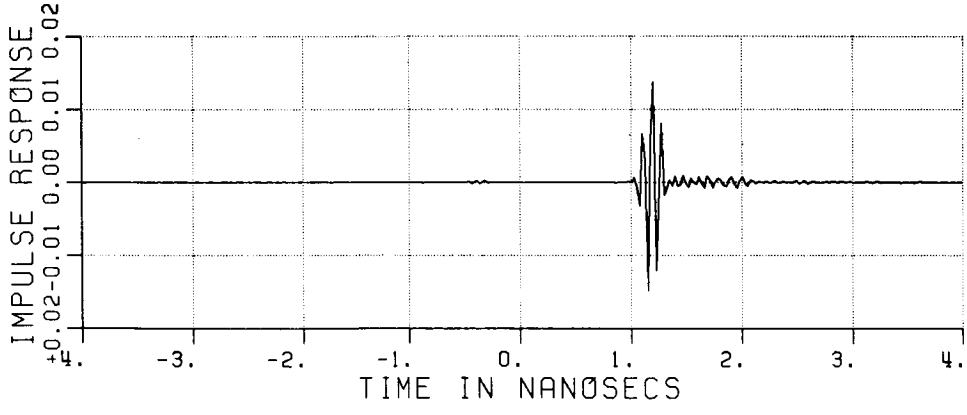

c) Measured result

Figure 5.19. Time domain plots of CONF6A: X=15",Y=-3",Z=3"; VP.

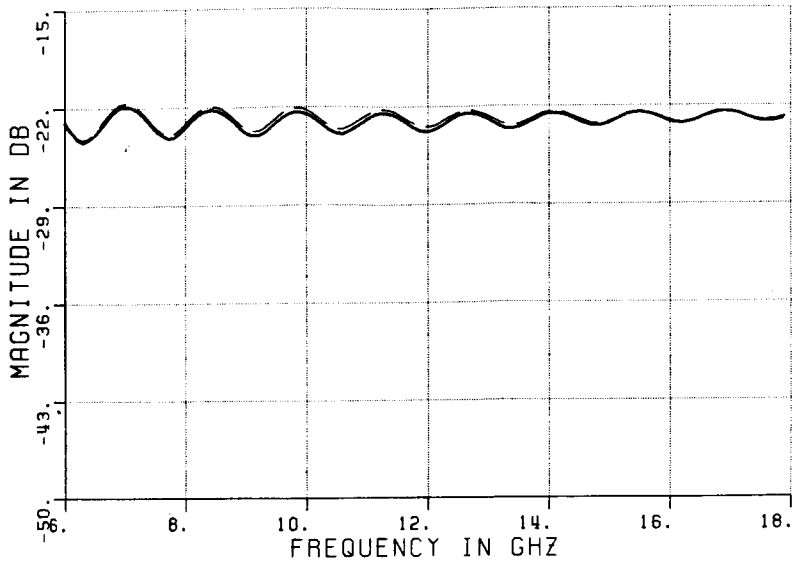

a) calculated result

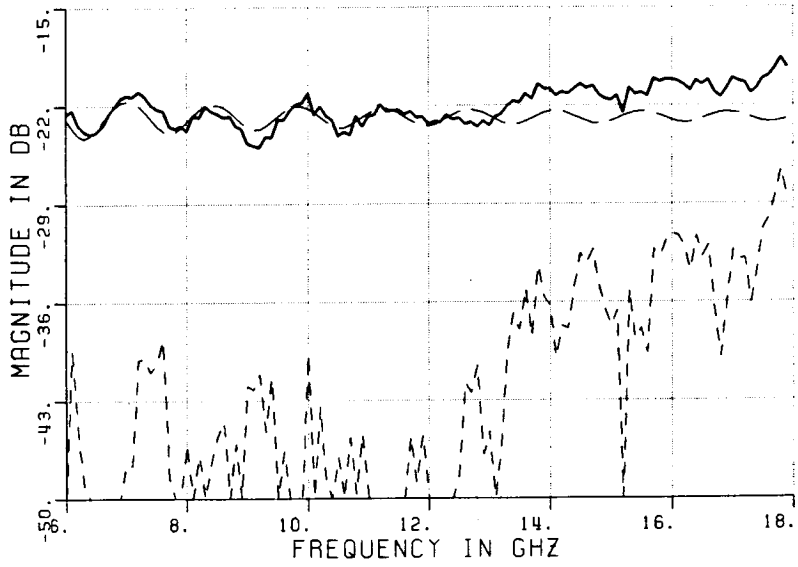

b) measured result

Figure 5.20. Frequency domain plots of CONF6A: X=15",Y=-3",Z=3"; VP.

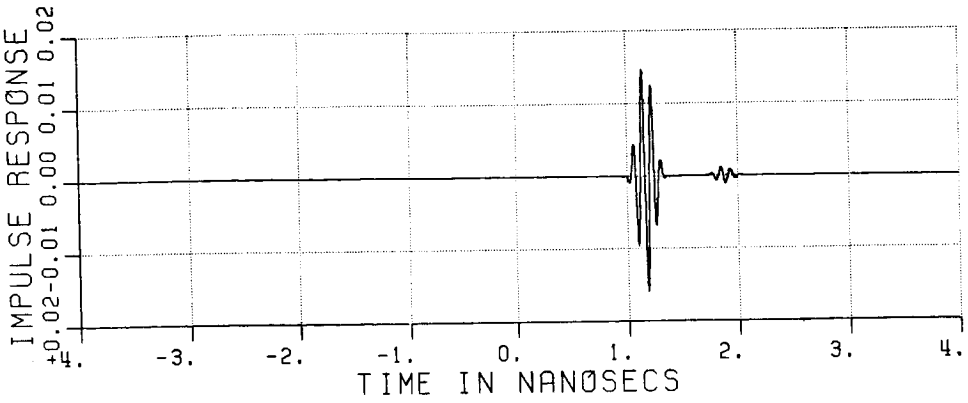

a) Exact sphere

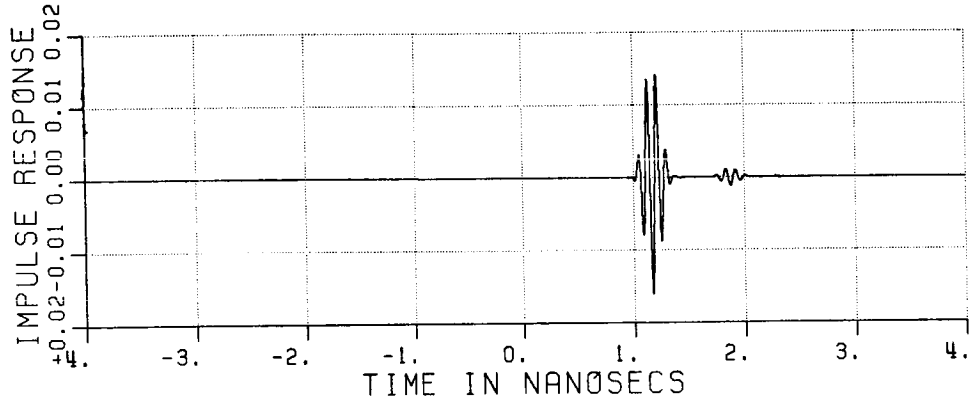

b) Calculated result

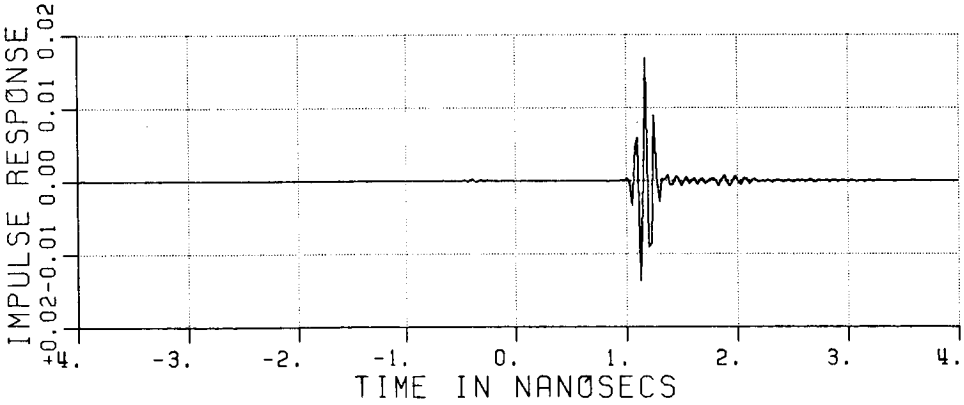

c) Measured result

Figure 5.21. Time domain plots of CONF7A: X=15",Y=-6",Z=3"; VP.

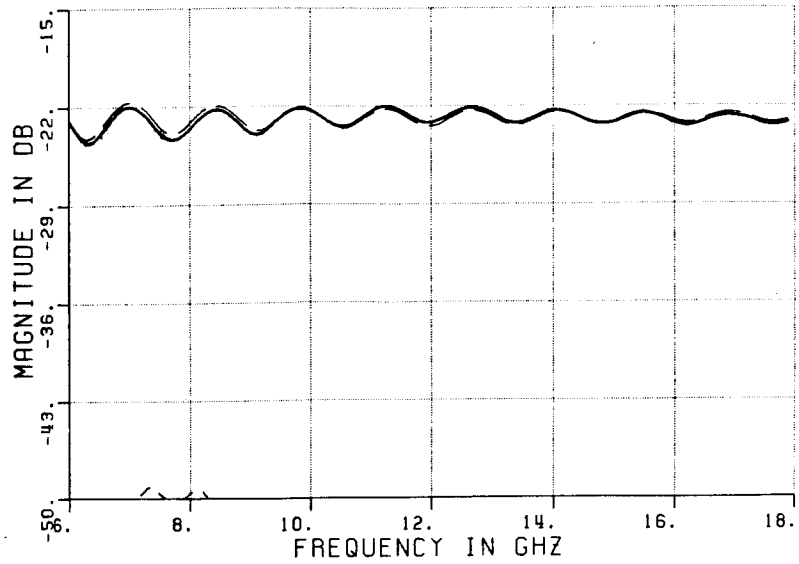

a) calculated result

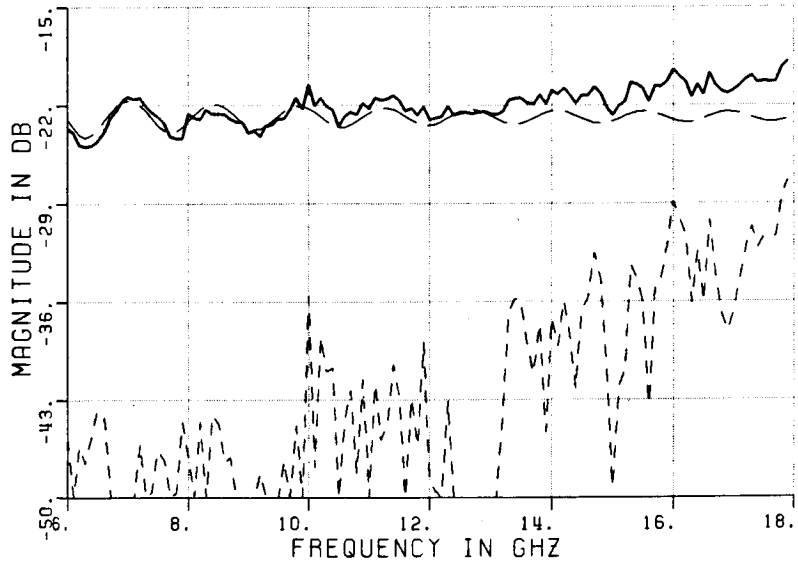

b) measured result

Figure 5.22. Frequency domain plots of CONF7A: X=15",Y=-6",Z=3"; VP.

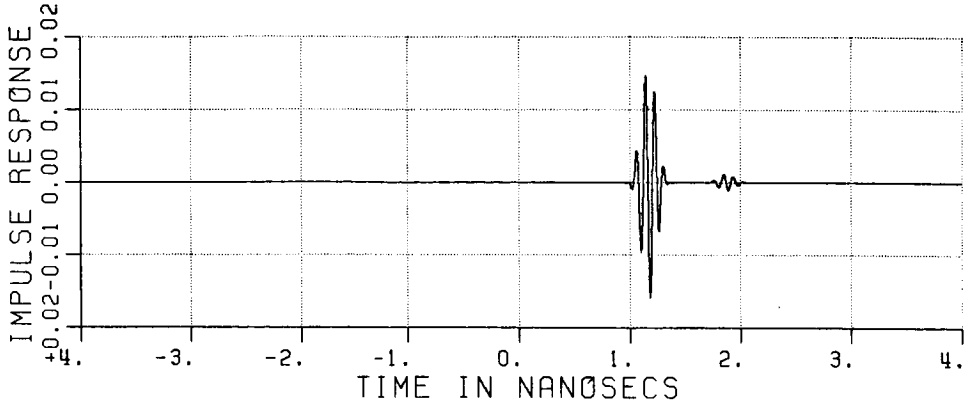

a) Exact sphere

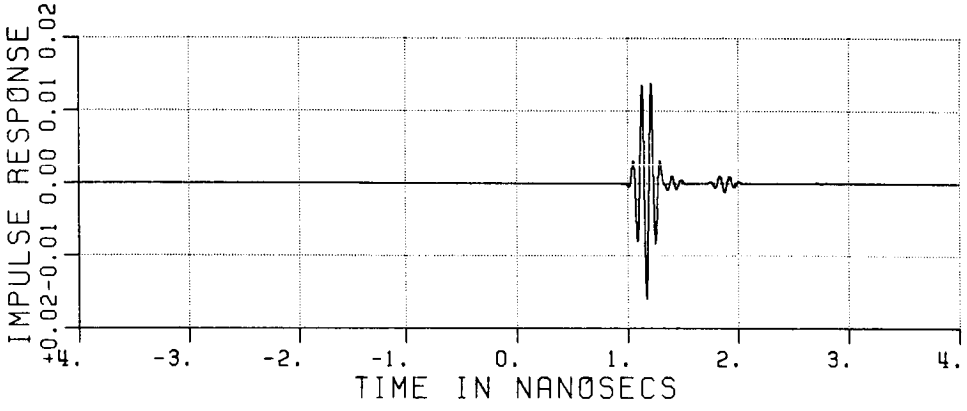

b) Calculated result

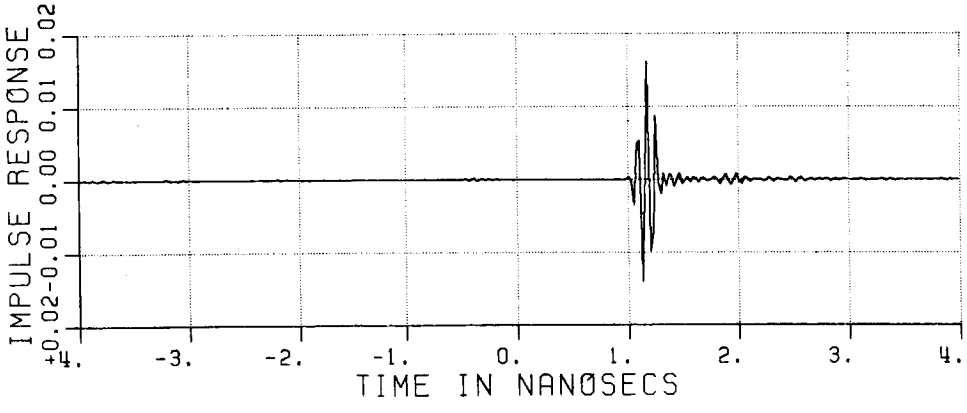

c) Measured result

Figure 5.23. Time domain plots of CONF8A: X=15",Y=-9",Z=3"; VP.

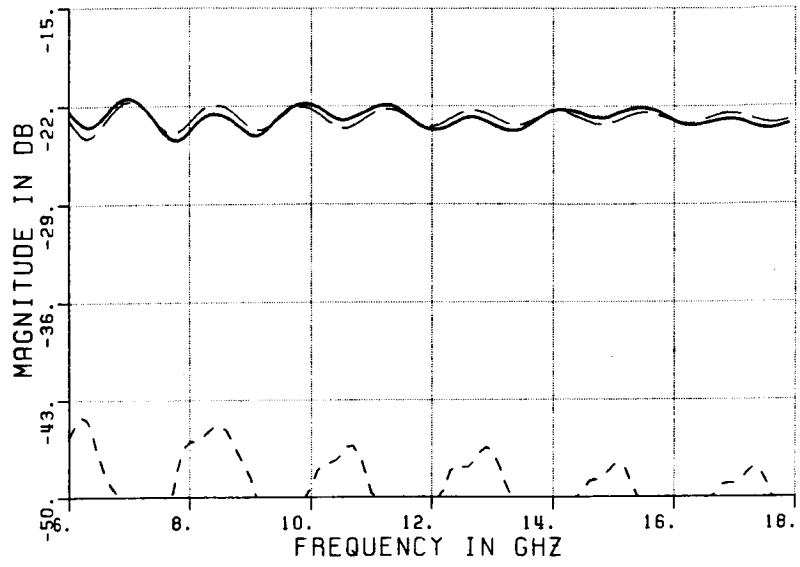

a) calculated result

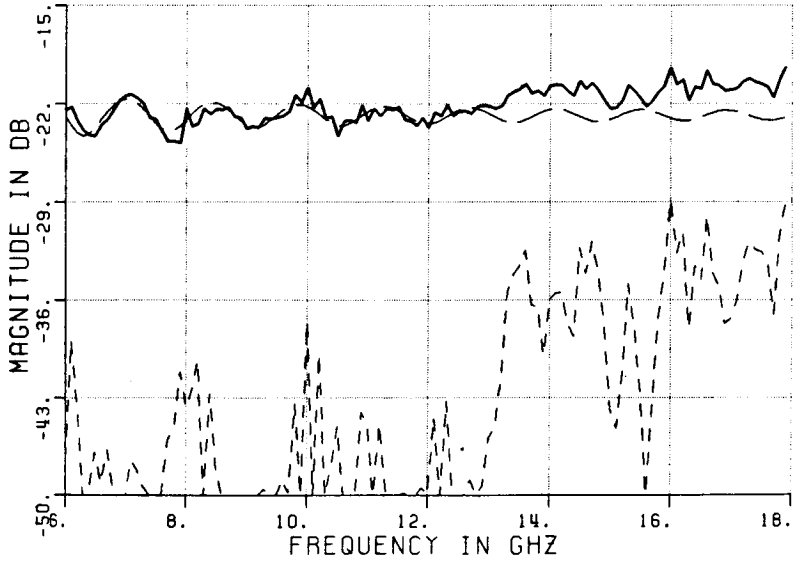

b) measured result

Figure 5.24. Frequency domain plots of CONF8A: X=15",Y=-9",Z=3"; VP.

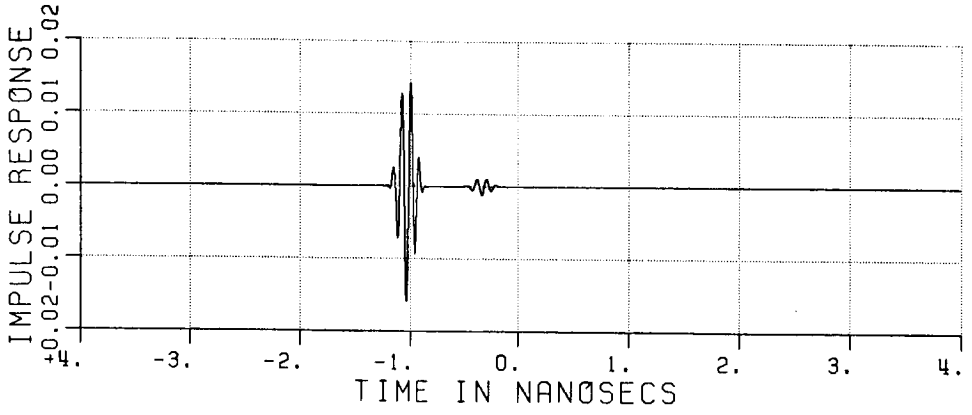

a) Exact sphere

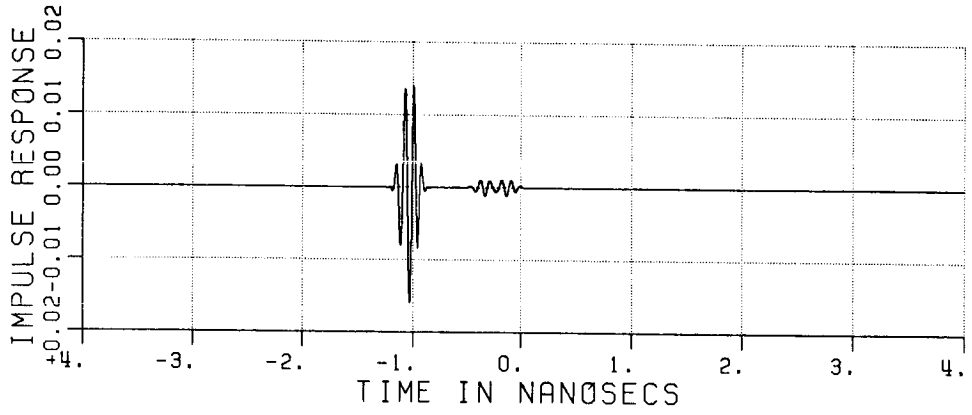

b) Calculated result

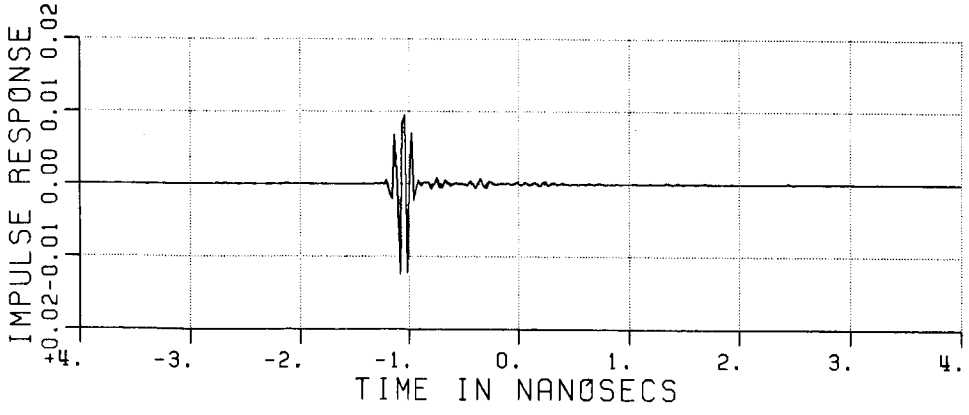

c) Measured result

Figure 5.25. Time domain plots of CONF1B: X=2",Y=0",Z=6"; VP.

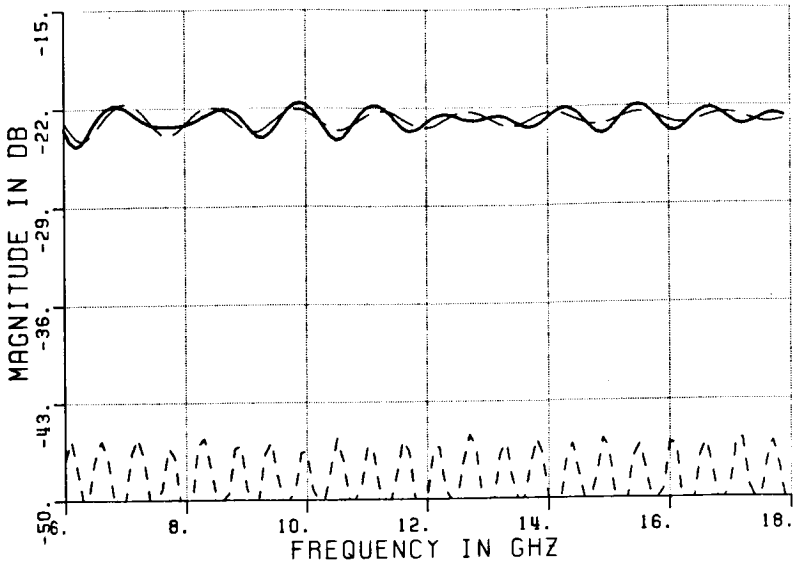

a) calculated result

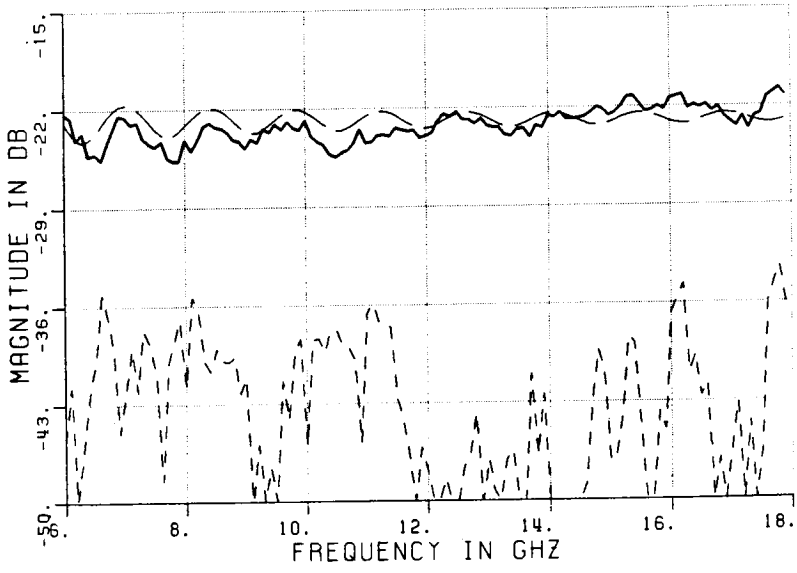

b) measured result

Figure 5.26. Frequency domain plots of CONF1B: X=2",Y=0",Z=6"; VP.

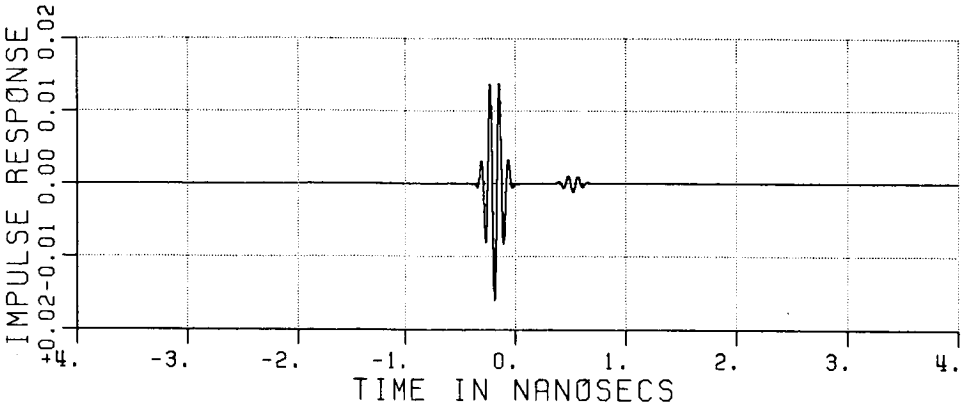

a) Exact sphere

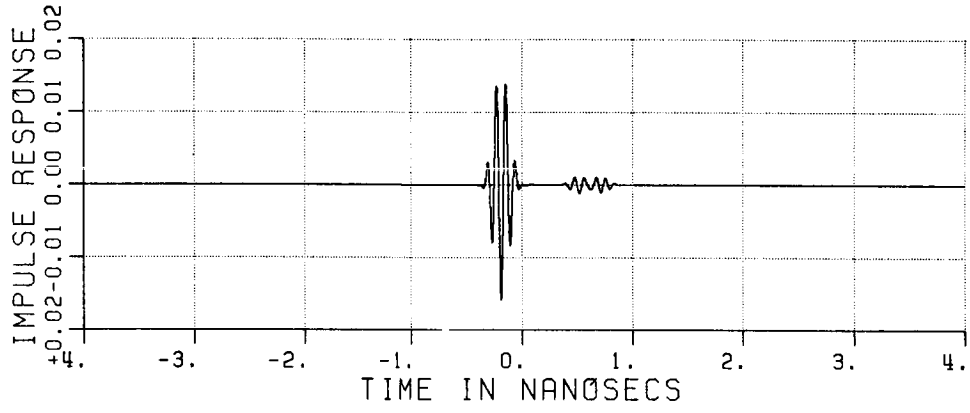

b) Calculated result

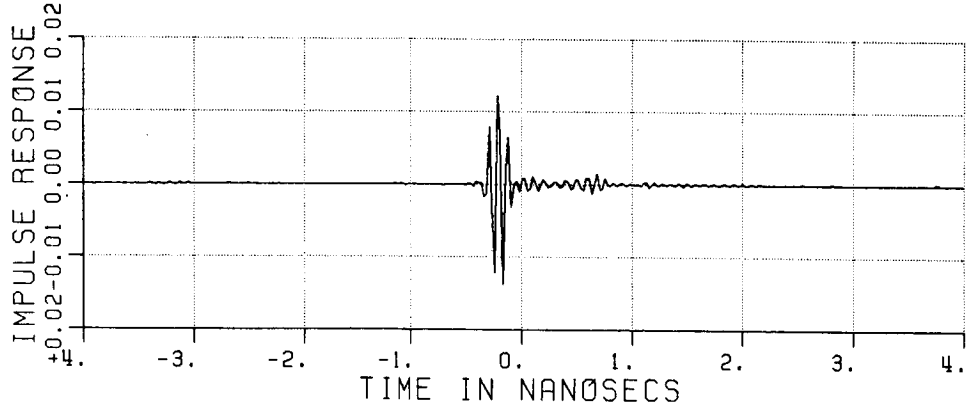

c) Measured result

Figure 5.27. Time domain plots of CONF2B: X=7",Y=0",Z=6"; VP.

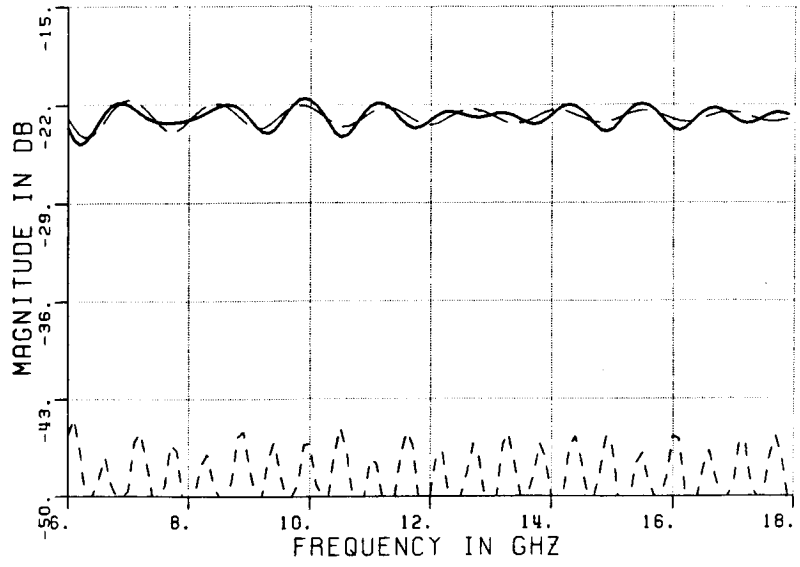

a) calculated result

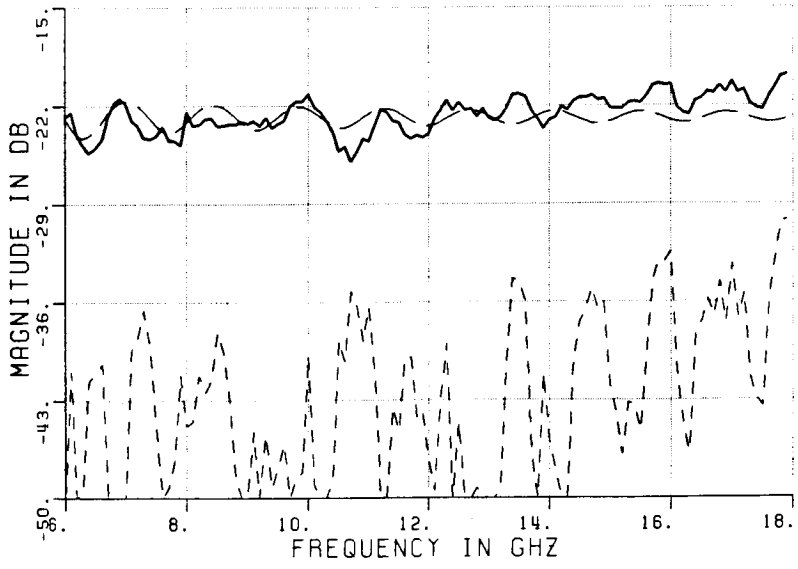

b) measured result

Figure 5.28. Frequency domain plots of CONF2B: X=7",Y=0",Z=6"; VP.

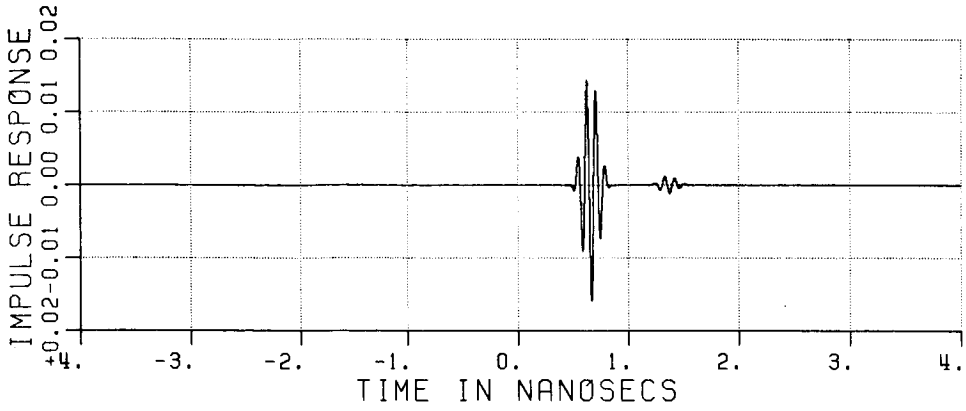

a) Exact sphere

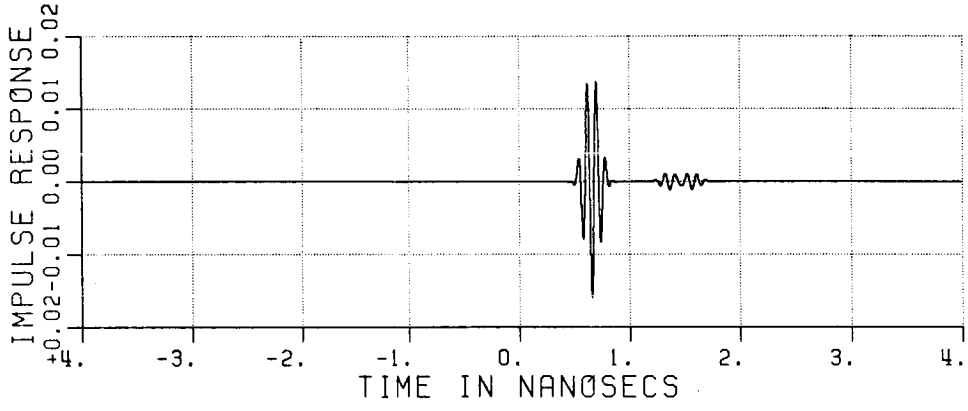

b) Calculated result

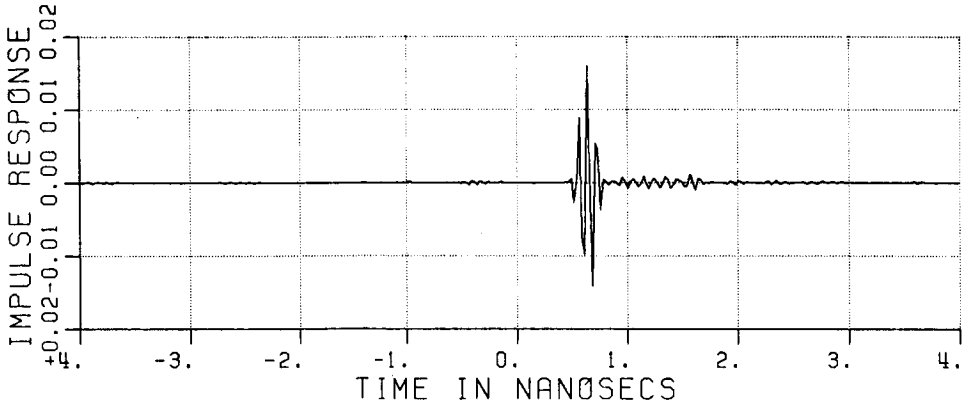

c) Measured result

Figure 5.29. Time domain plots of CONF3B: X=12",Y=0",Z=6"; VP.

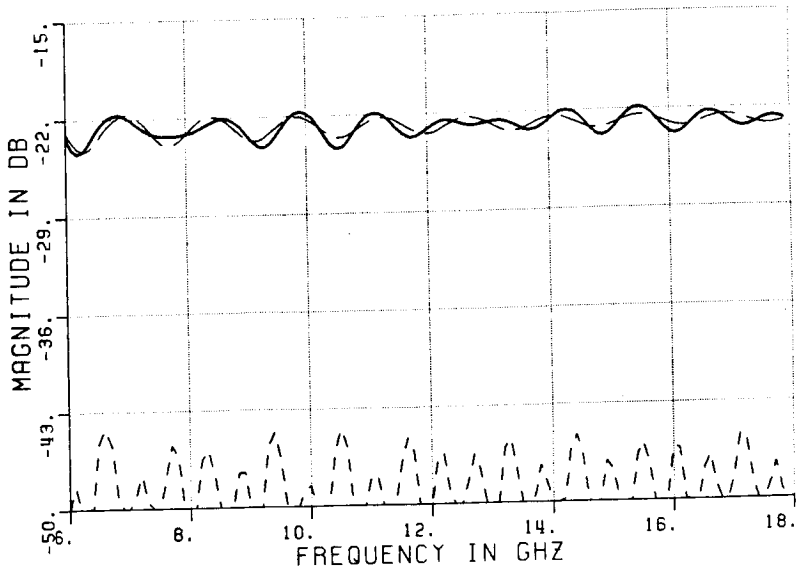

a) calculated result

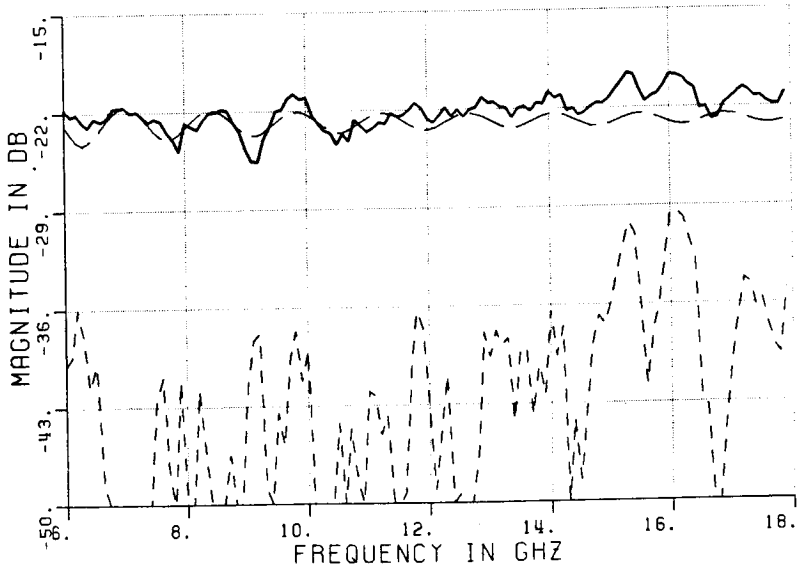

b) measured result

Figure 5.30. Frequency domain plots of CONF3B: X=12",Y=0",Z=6"; VP.

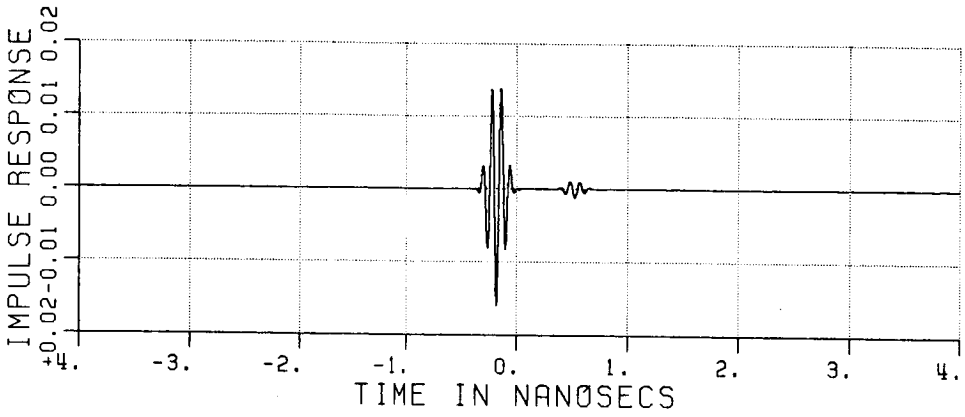

a) Exact sphere

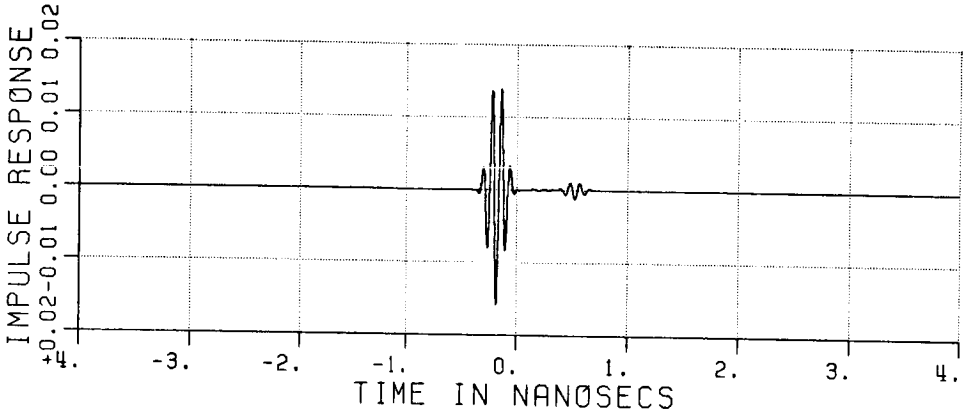

b) Calculated result

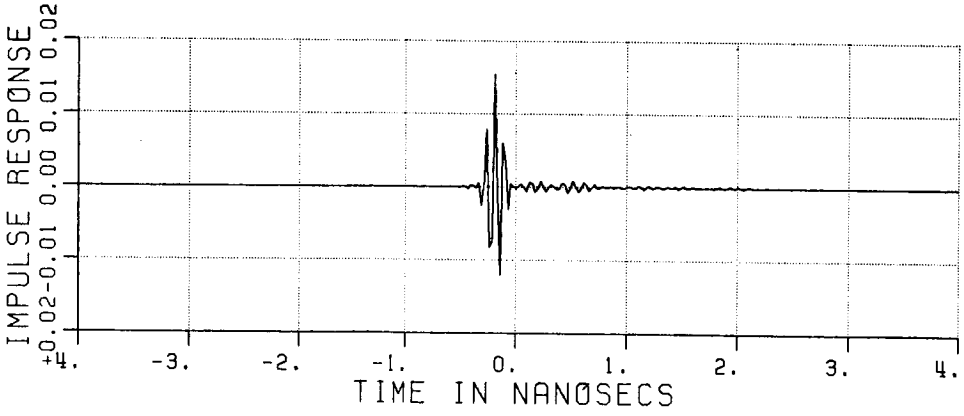

c) Measured result

Figure 5.31. Time domain plots of CONF4B: X=7",Y=-7",Z=6"; VP.

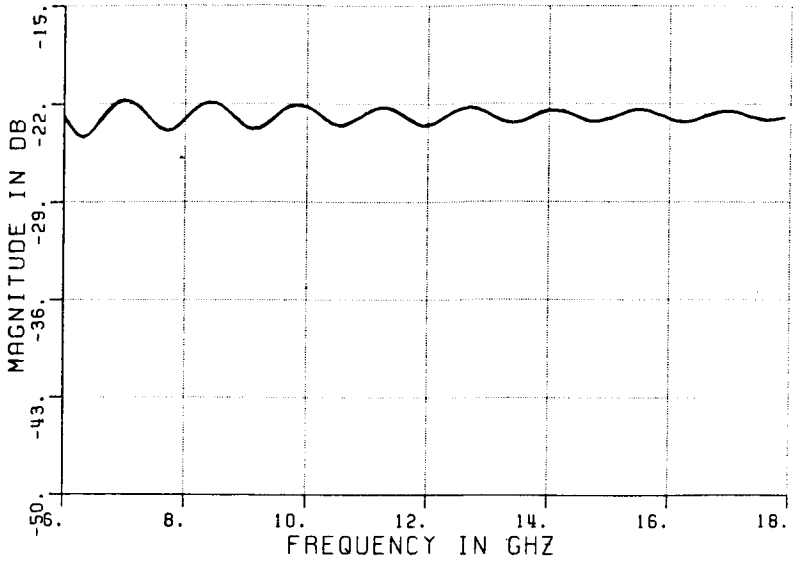

a) calculated result

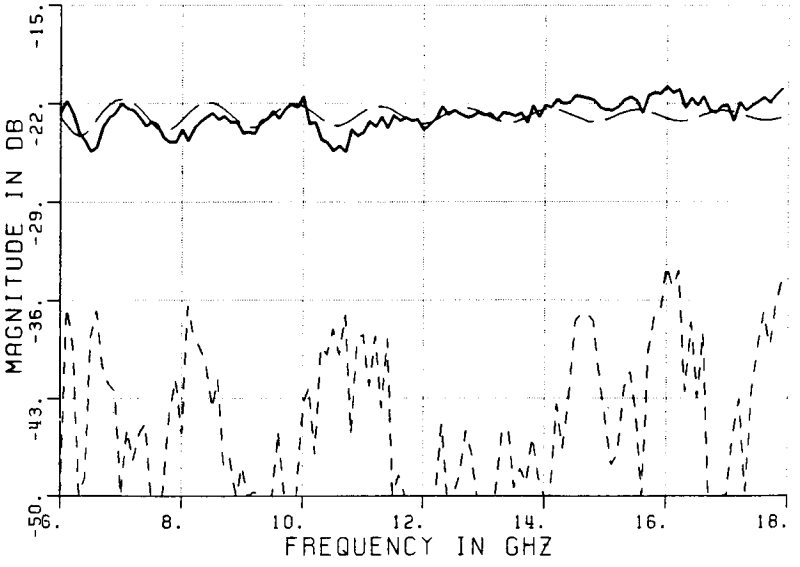

b) measured result

Figure 5.32. Frequency domain plots of CONF4B: X=7",Y=-7",Z=6"; VP.

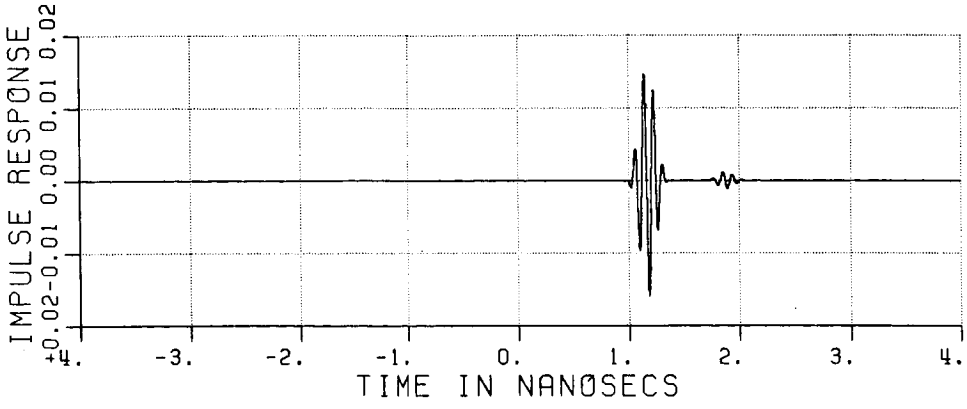

a) Exact sphere

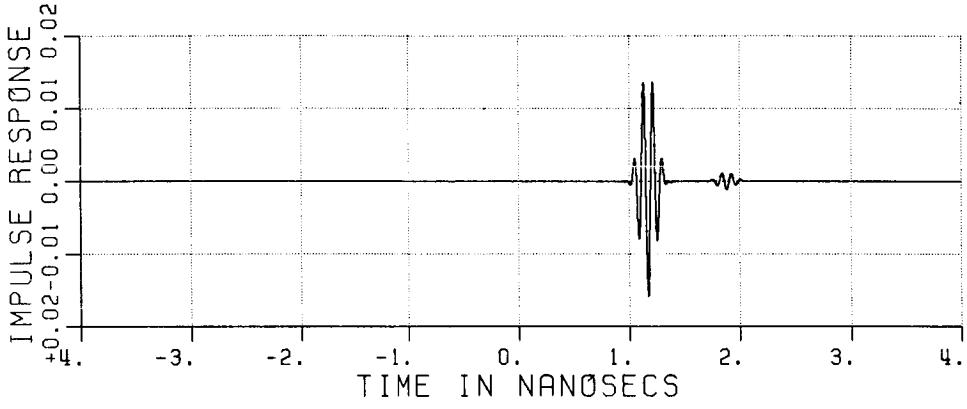

b) Calculated result

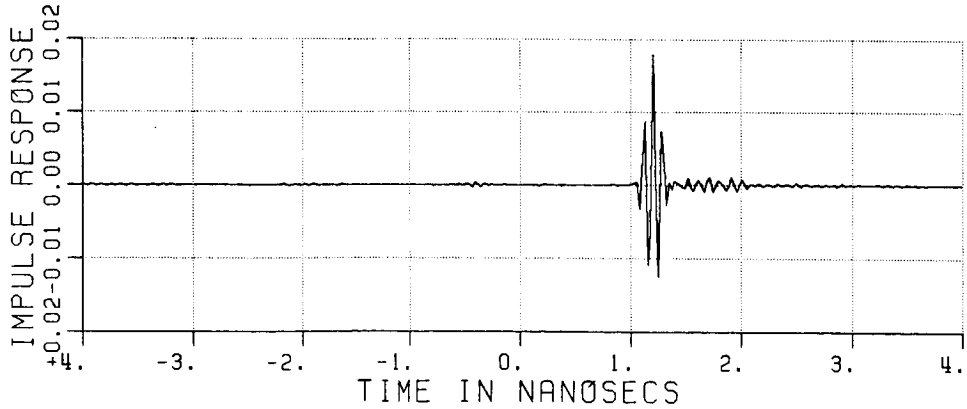

c) Measured result

Figure 5.33. Time domain plots of CONF5B: X=15",Y=0",Z=6"; VP.

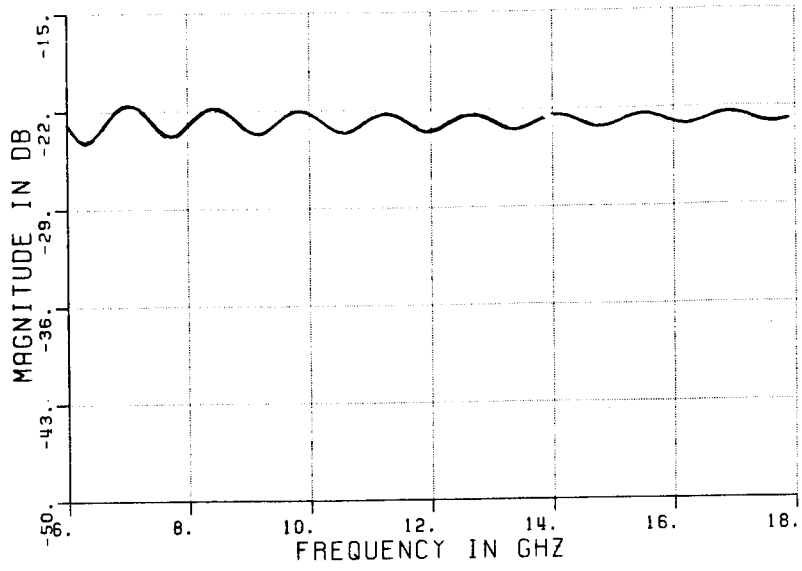

a) calculated result

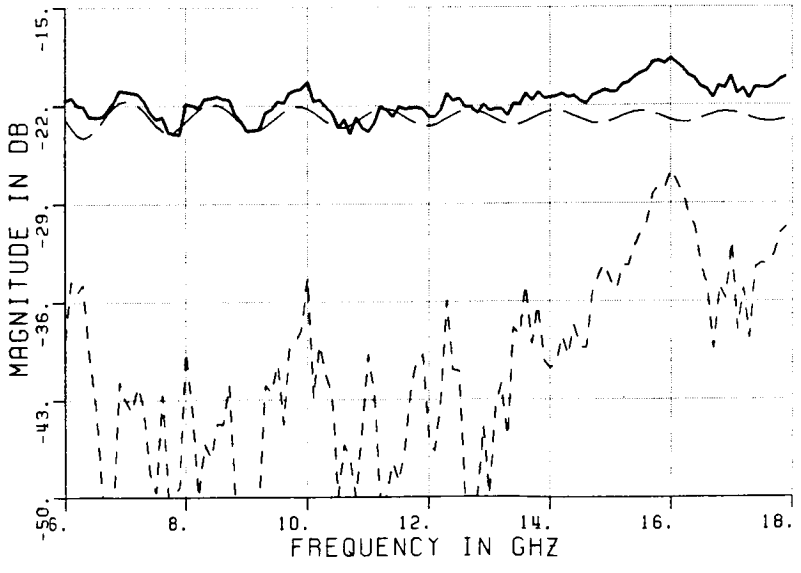

b) measured result

Figure 5.34. Frequency domain plots of CONF5B: X=15",Y=0",Z=6"; VP.

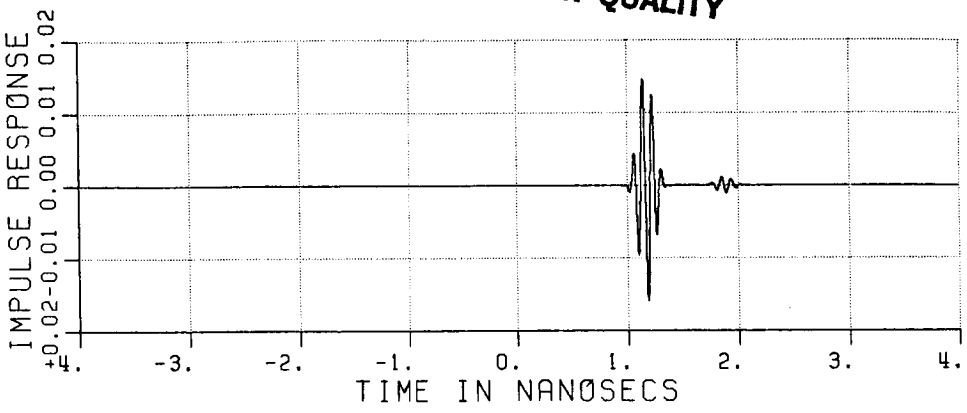

a) Exact sphere

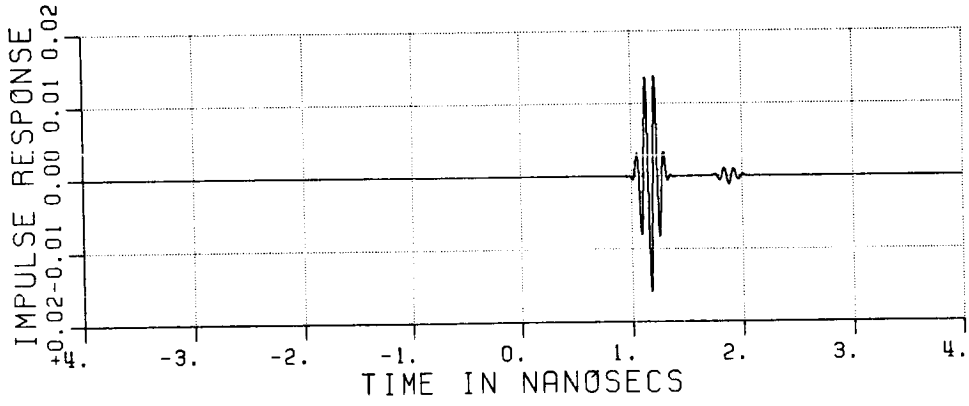

b) Calculated result

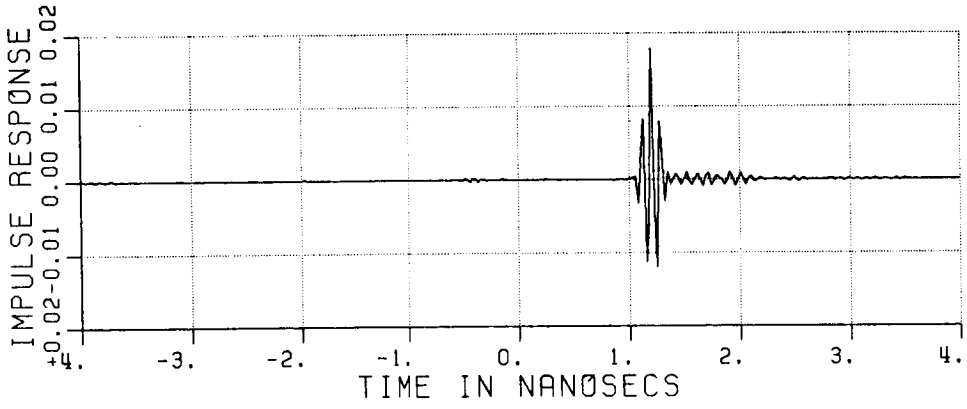

c) Measured result

Figure 5.35. Time domain plots of CONF6B: X=15",Y=-3",Z=6"; VP.

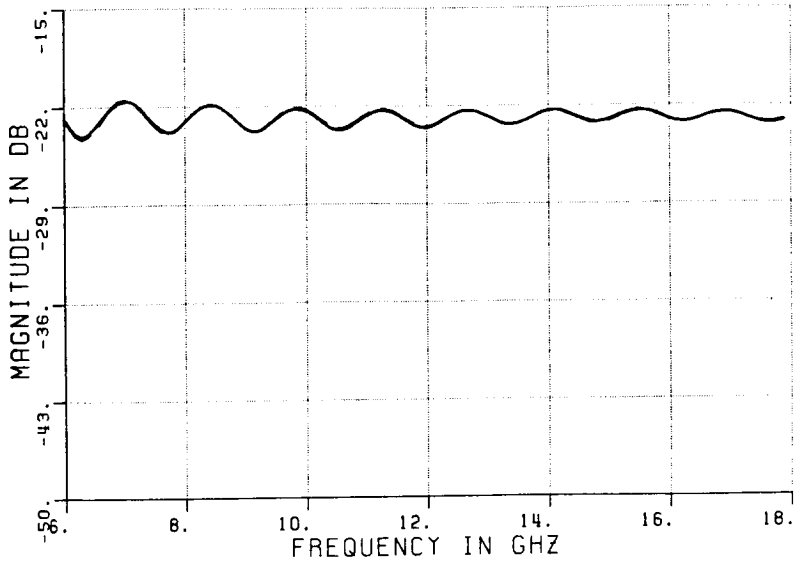

a) calculated result

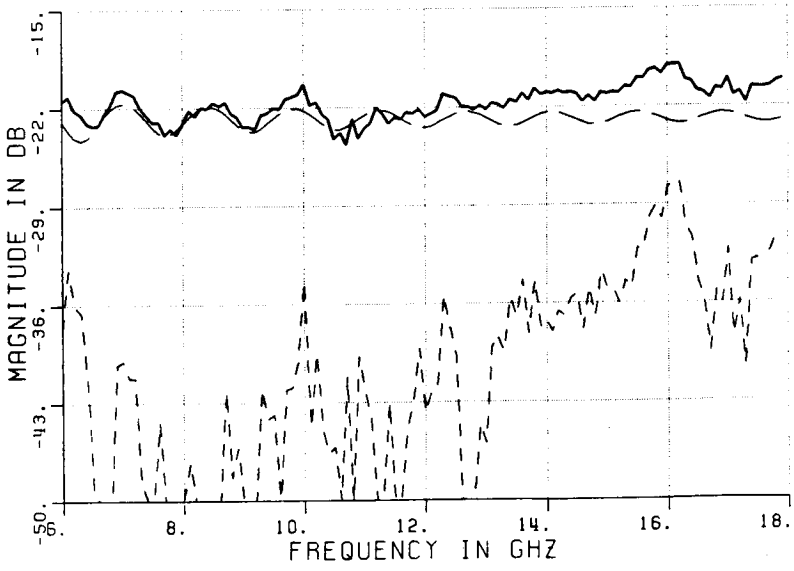

b) measured result

Figure 5.36. Frequency domain plots of CONF6B: X=15",Y=-3",Z=6"; VP.

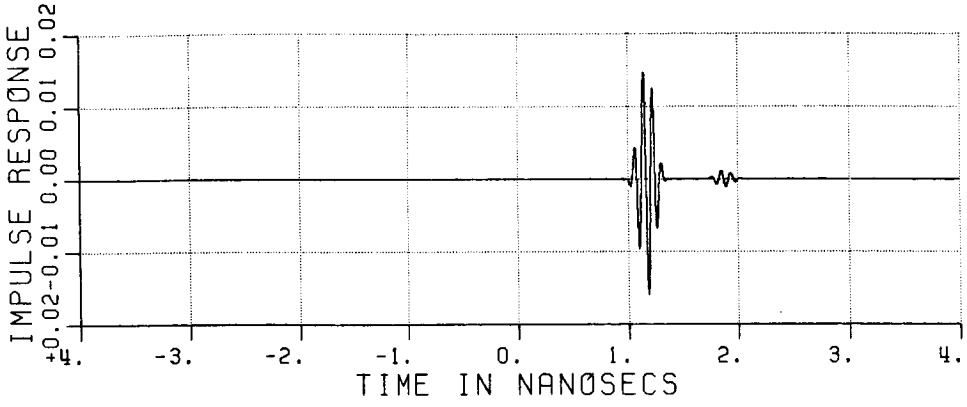

a) Exact sphere

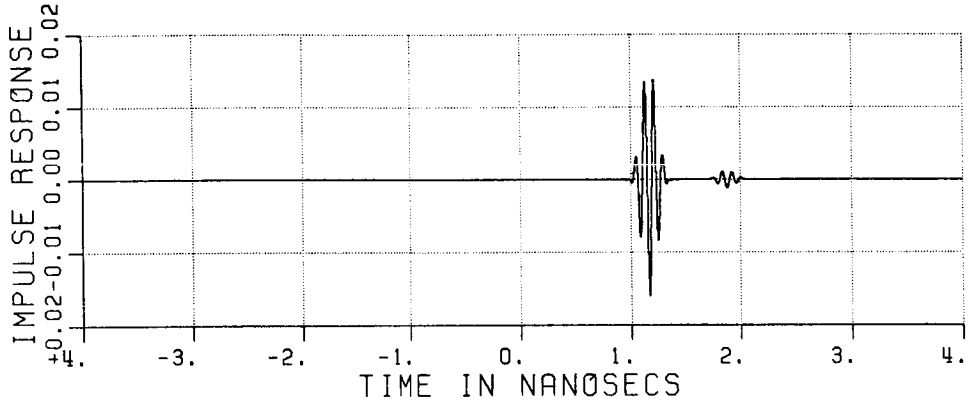

b) Calculated result

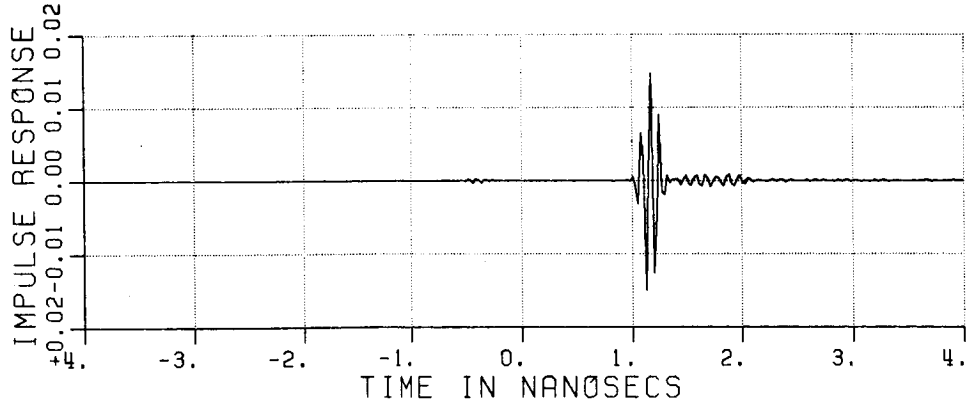

c) Measured result

Figure 5.37. Time domain plots of CONF7B: X=15",Y=-6",Z=6"; VP.

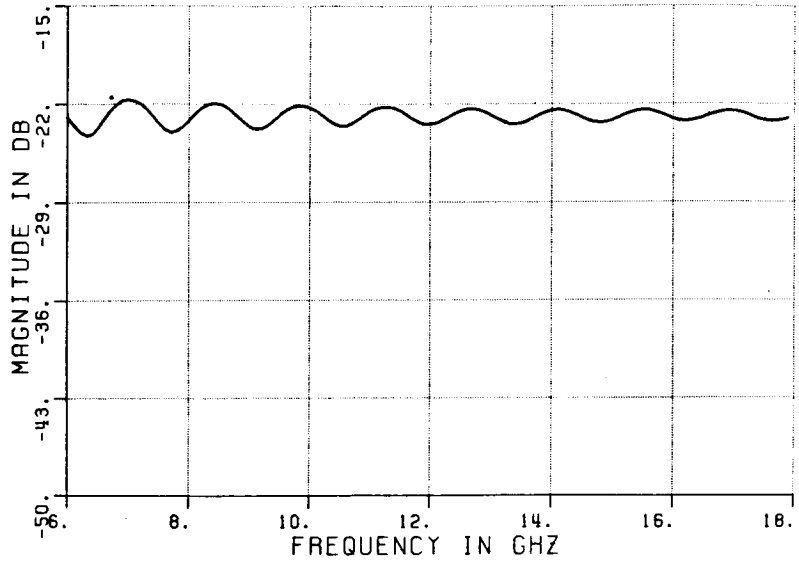

a) calculated result

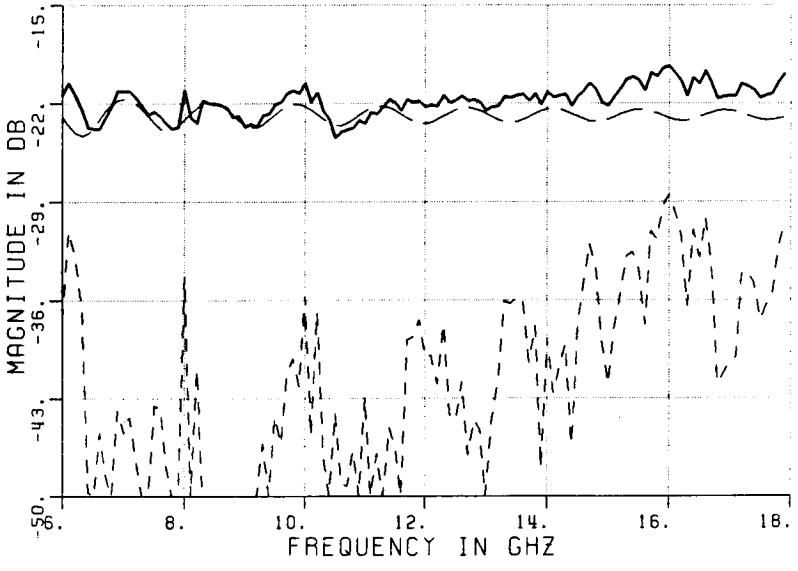

b) measured result

Figure 5.38. Frequency domain plots of CONF7B: X=15",Y=-6",Z=6"; VP.

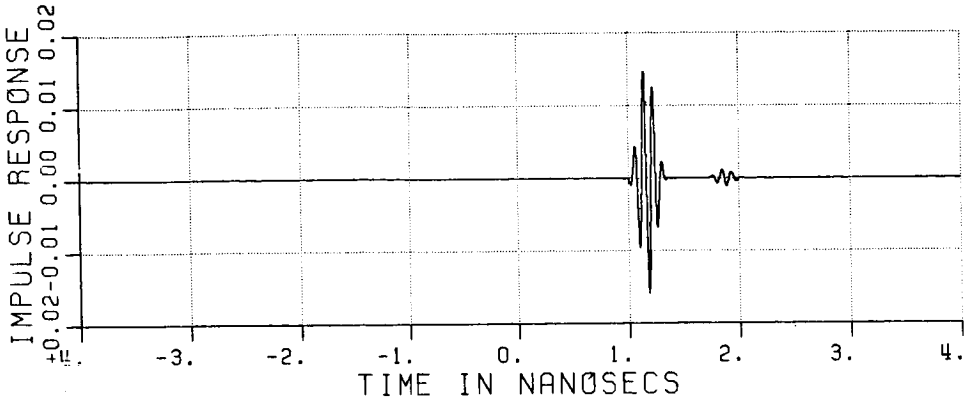

a) Exact sphere

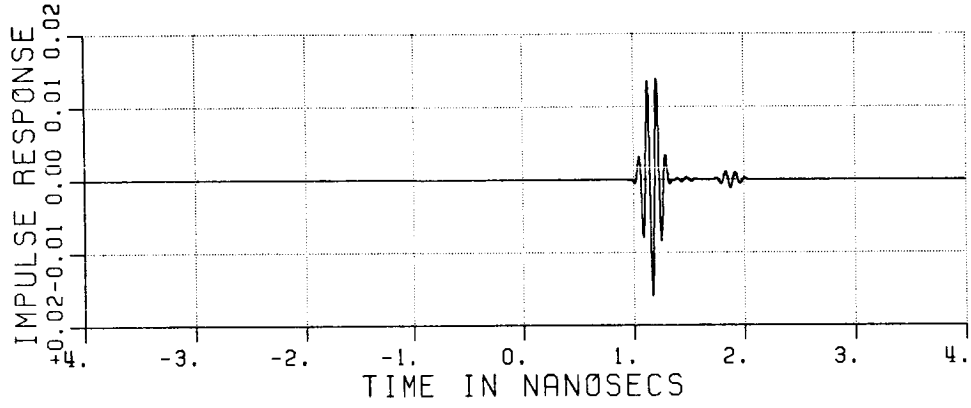

b) Calculated result

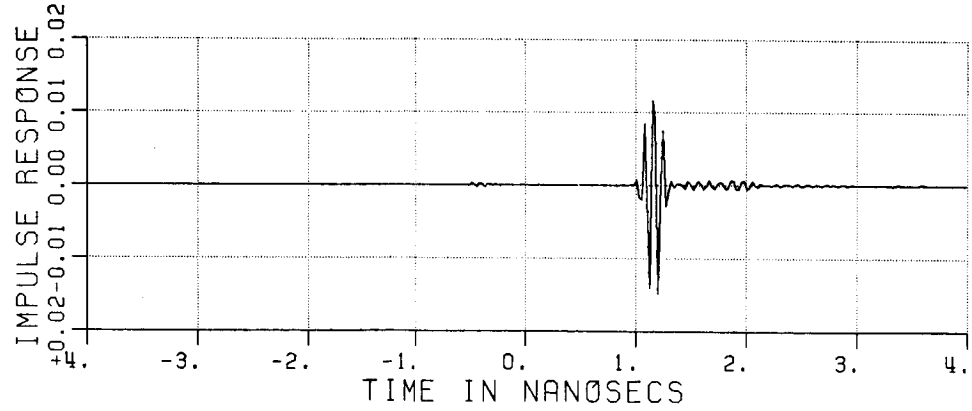

c) Measured result

Figure 5.39. Time domain plots of CONF8B: X=15",Y=-9",Z=6"; VP.

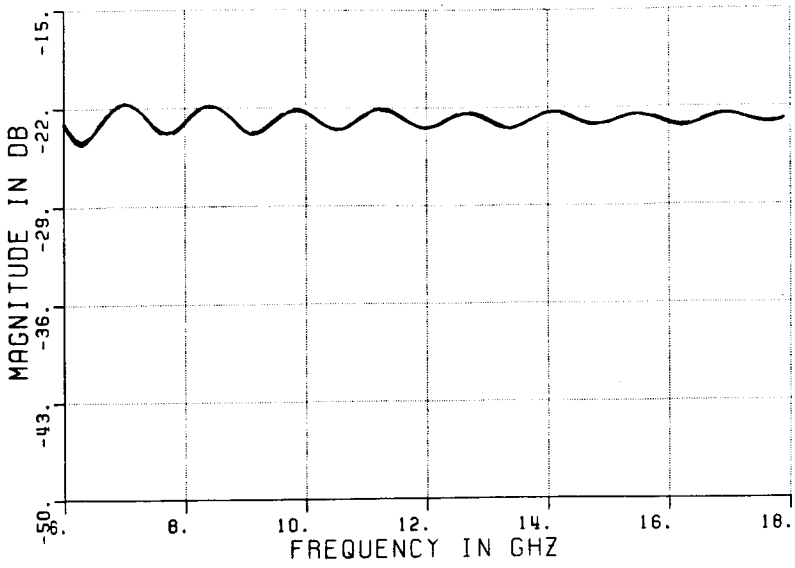

a) calculated result

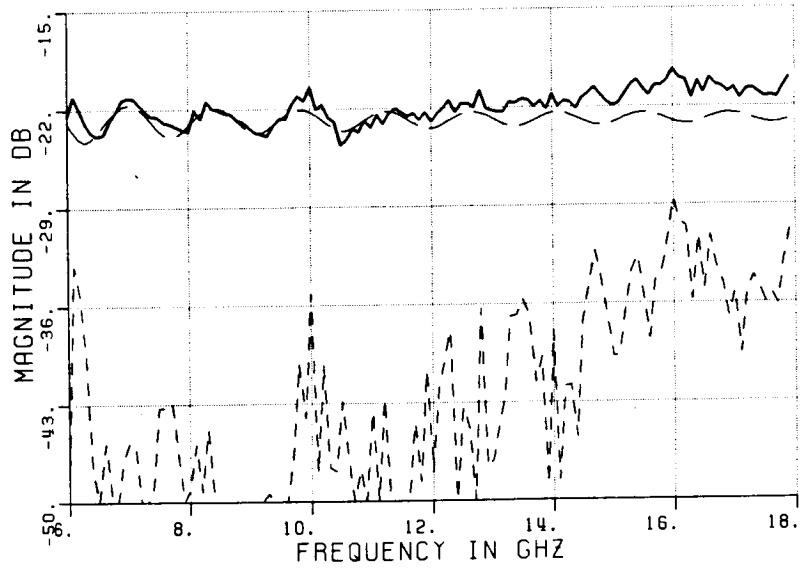

b) measured result

Figure 5.40. Frequency domain plots of CONF8B: X=15",Y=-9",Z=6"; VP.

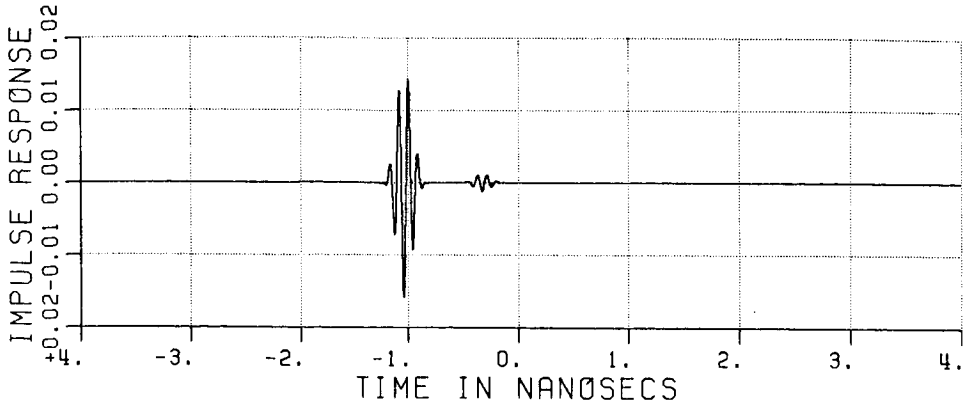

a) Exact sphere

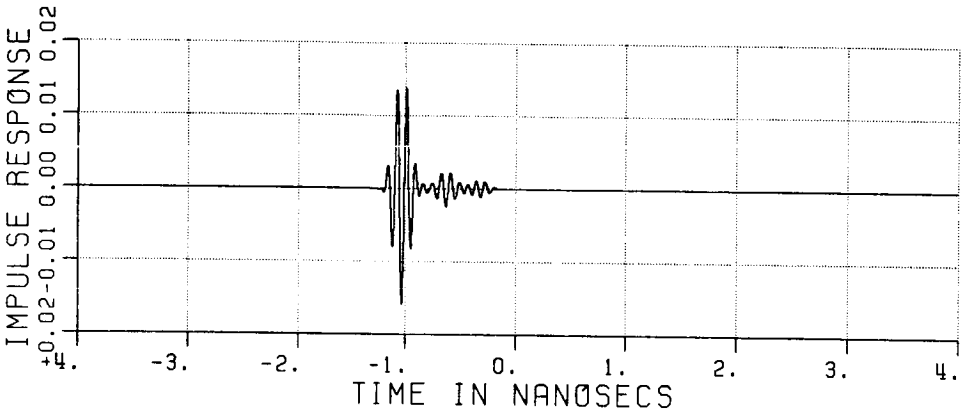

b) Calculated result

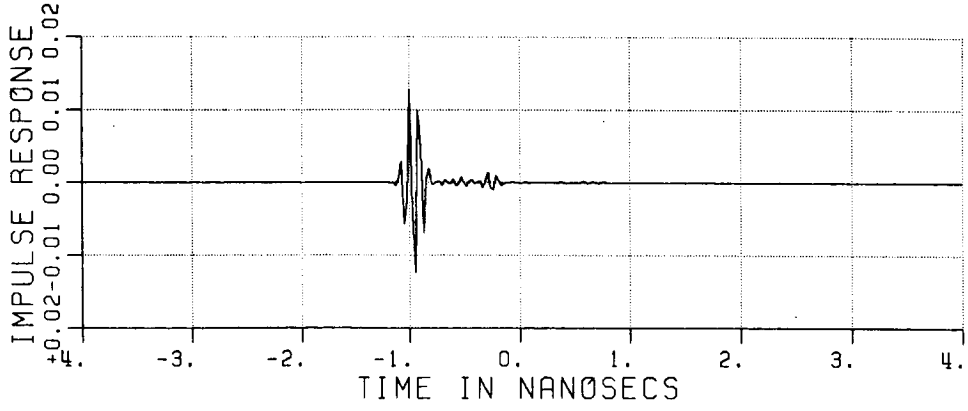

c) Measured result

Figure 5.41. Time domain plots of CONF1C: X=2",Y=0",Z=3"; HP.

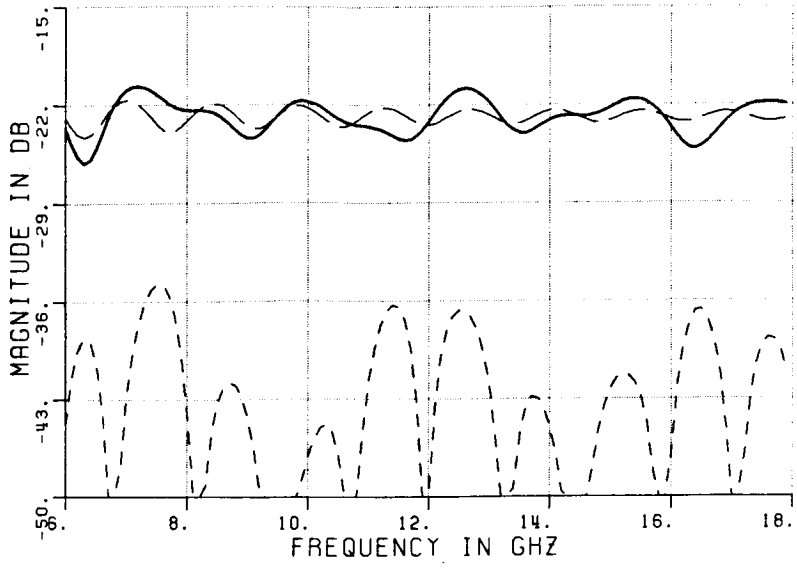

a) calculated result

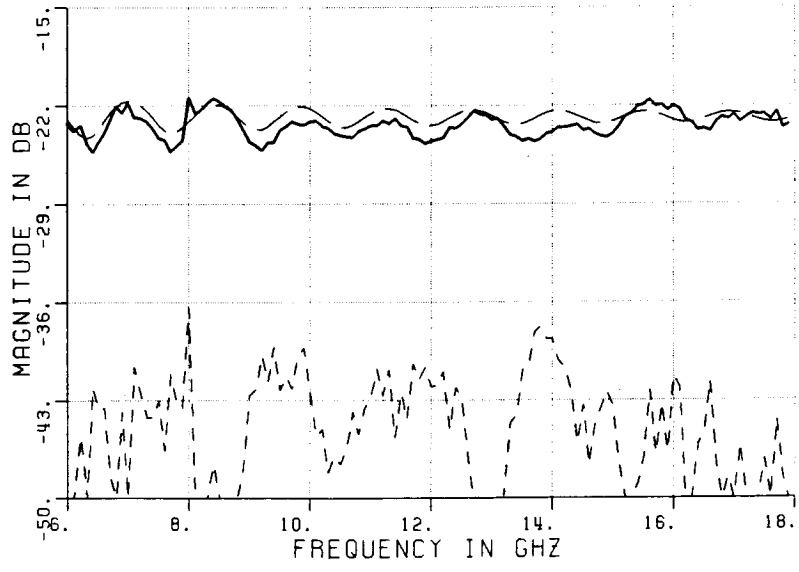

b) measured result

Figure 5.42. Frequency domain plots of CONF1C: X=2",Y=0",Z=3"; HP.

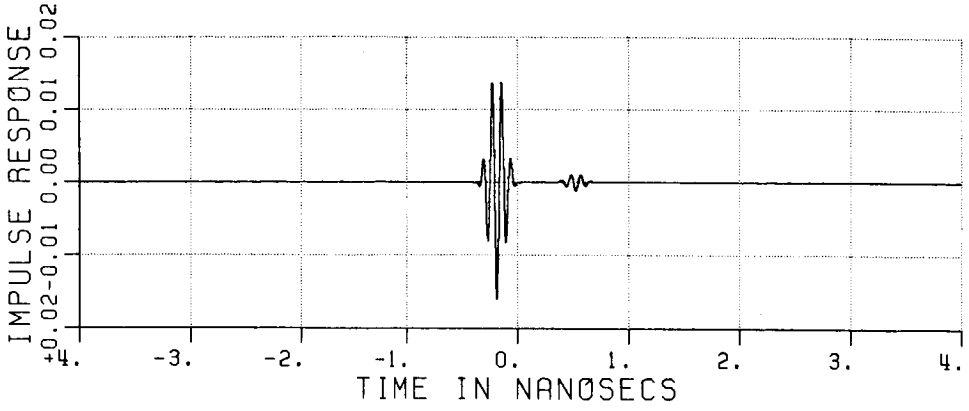

a) Exact sphere

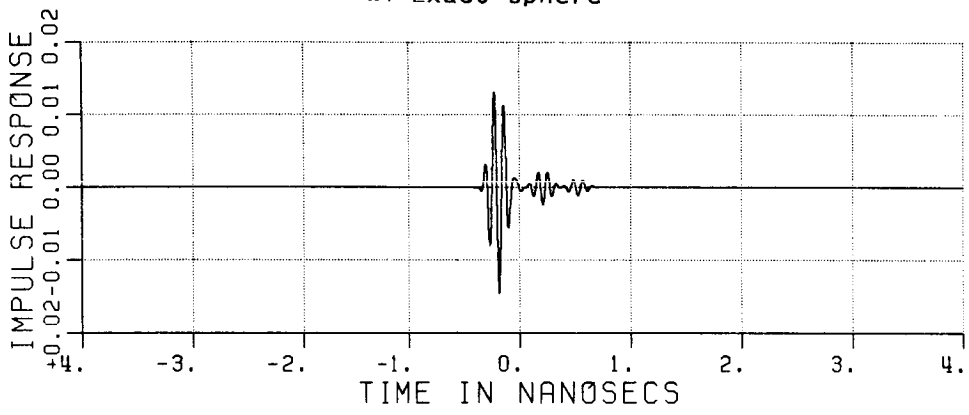

b) Calculated result

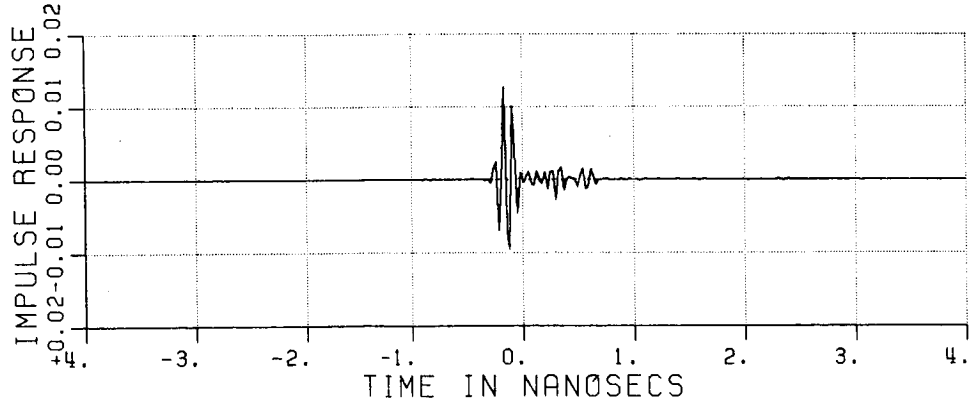

c) Measured result

Figure 5.43. Time domain plots of CONF2C: X=7",Y=0",Z=3"; HP.

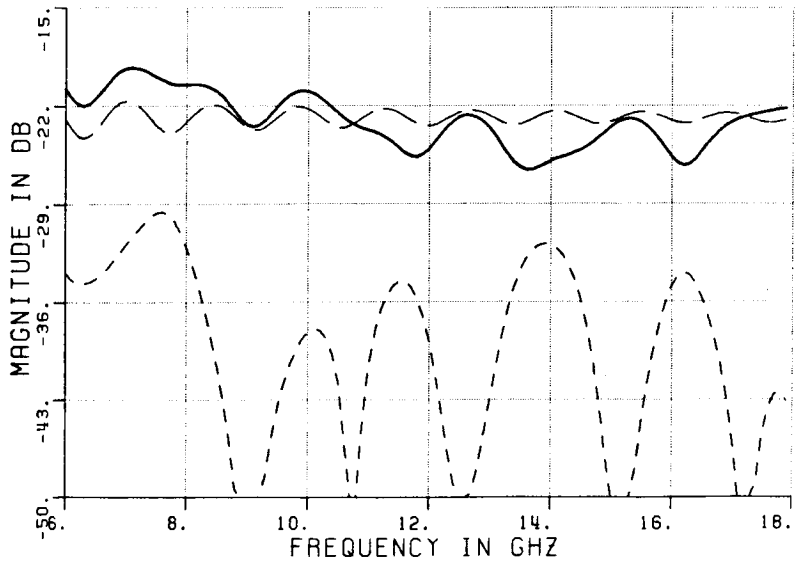

a) calculated result

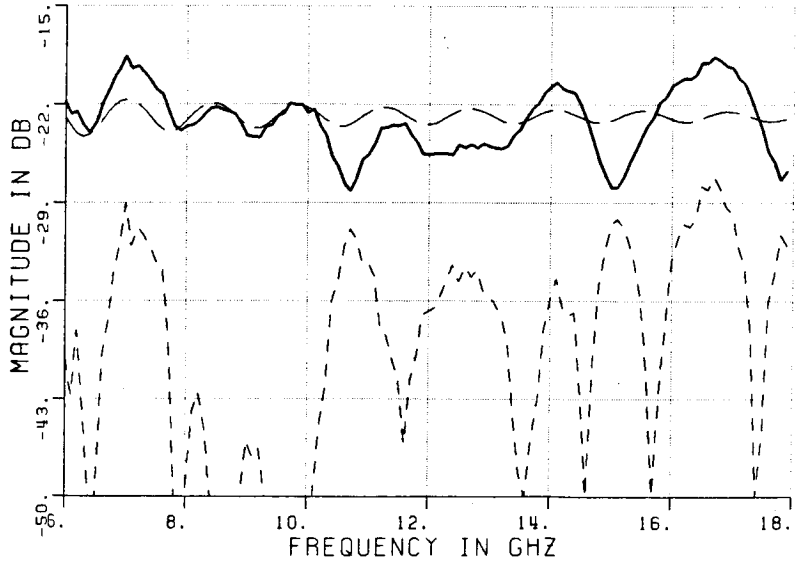

b) measured result

Figure 5.44. Frequency domain plots of CONF2C: X=7",Y=0",Z=3"; HP.

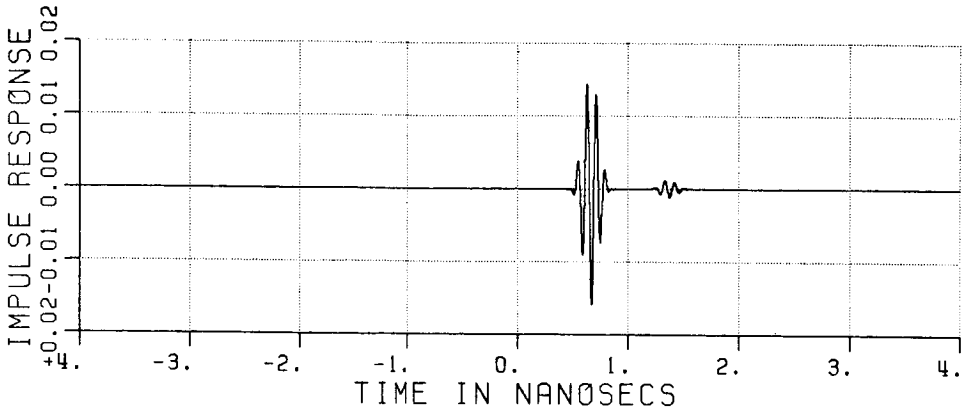

a) Exact sphere

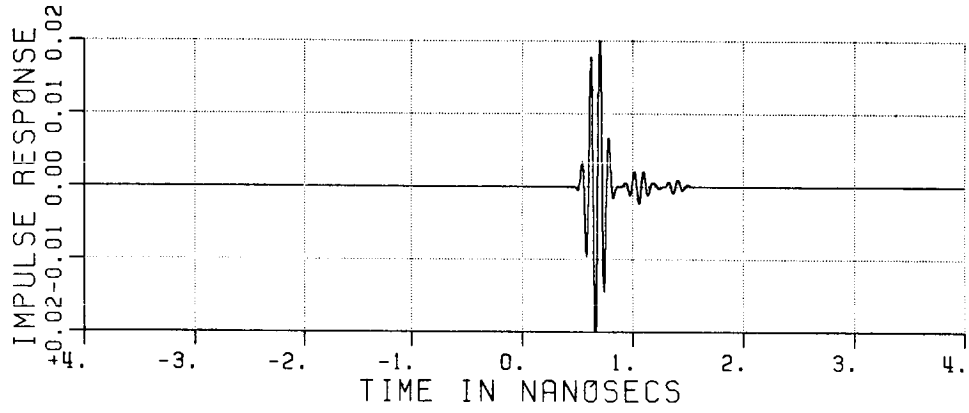

b) Calculated result

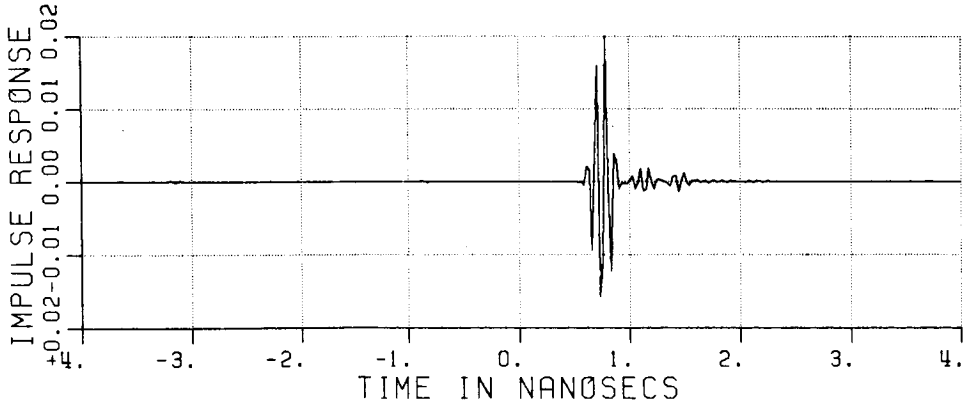

c) Measured result

Figure 5.45. Time domain plots of CONF3C: X=12",Y=0",Z=3"; HP.

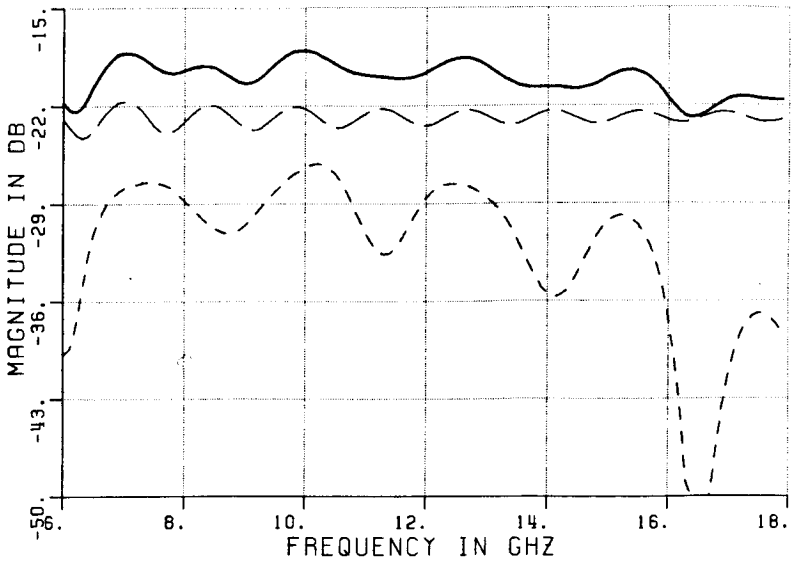

a) calculated result

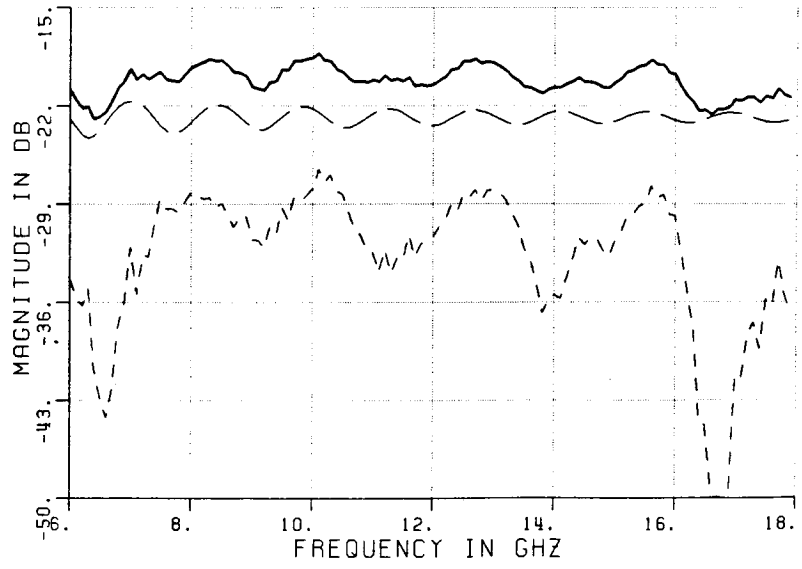

b) measured result

Figure 5.46. Frequency domain plots of CONF3C: X=12",Y=0",Z=3"; HP.

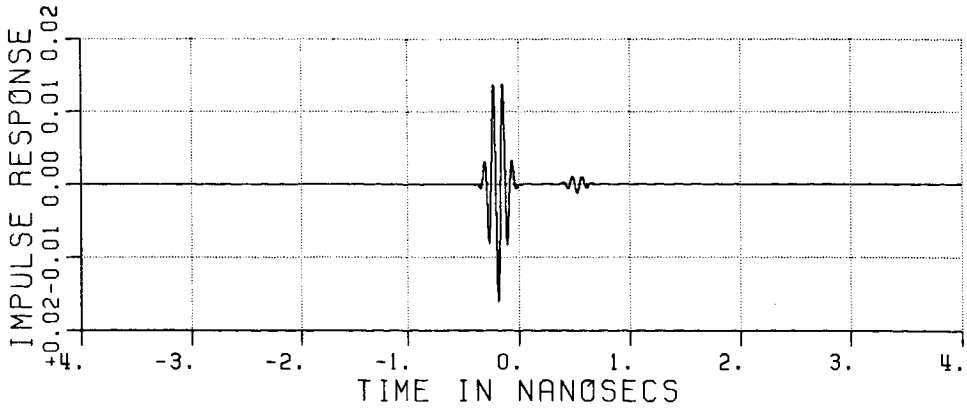

a) Exact sphere

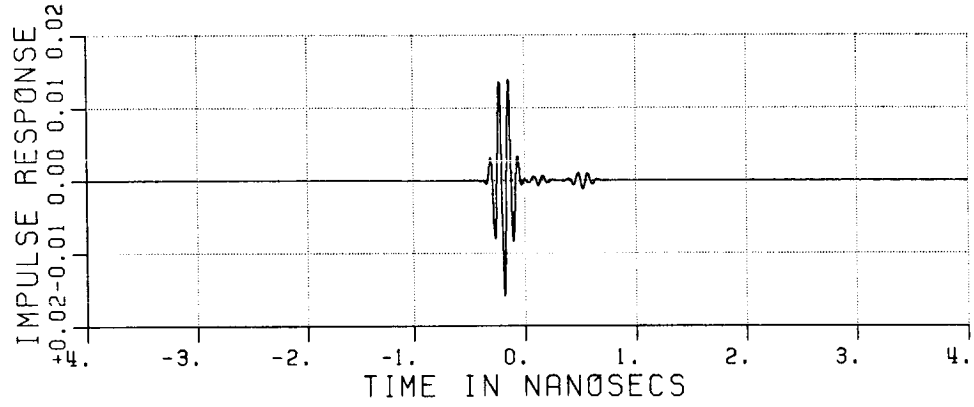

b) Calculated result

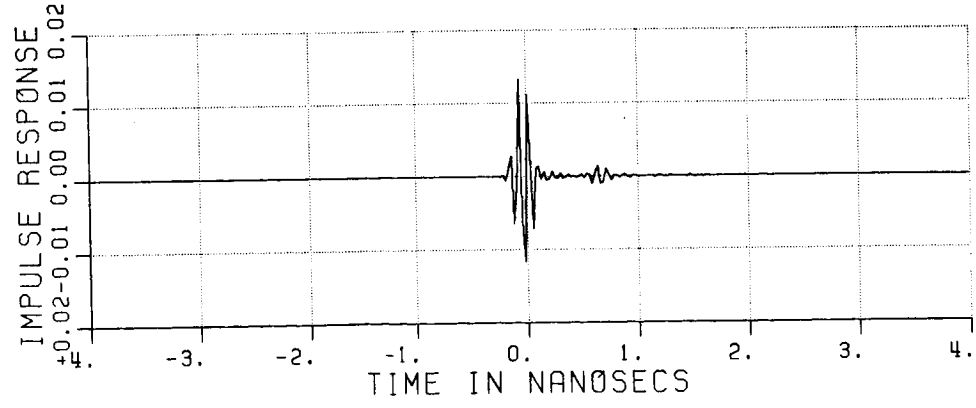

c) Measured result

Figure 5.47. Time domain plots of CONF4C: X=7",Y=-7",Z=3"; HP.

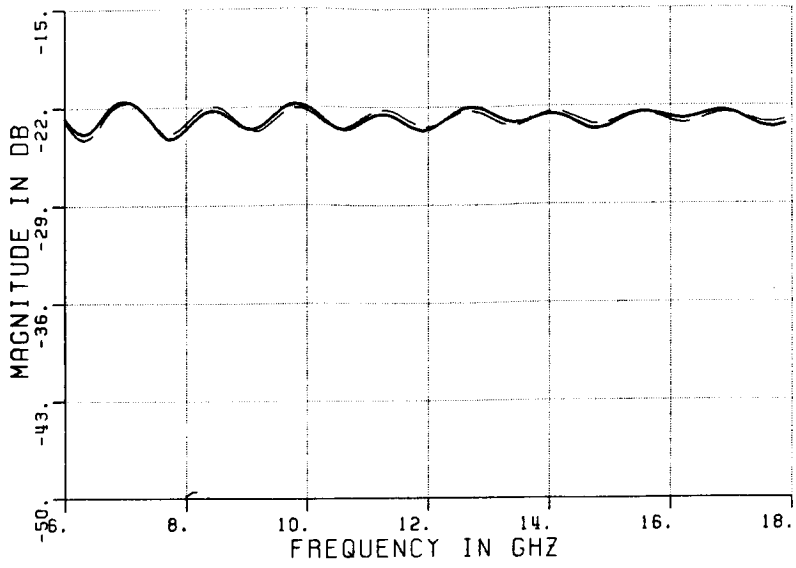

a) calculated result

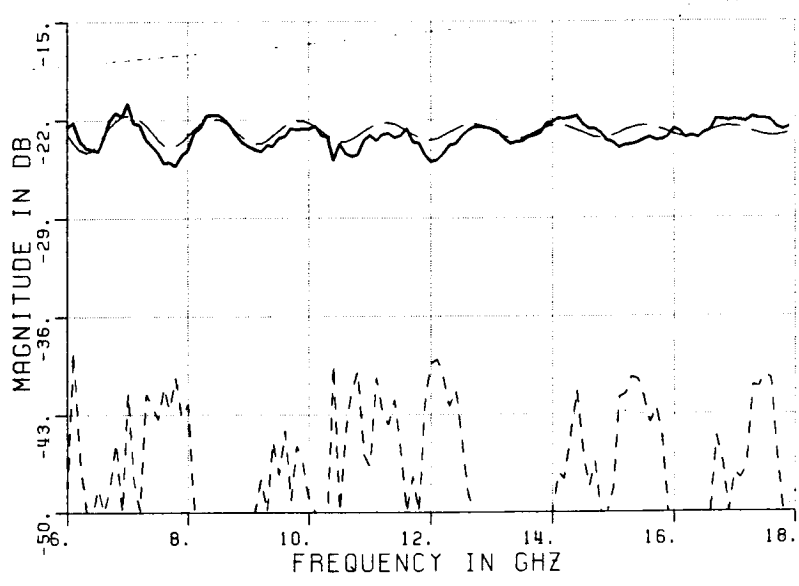

b) measured result

Figure 5.48. Frequency domain plots of CONF4C: X=7",Y=-7",Z=3"; HP.

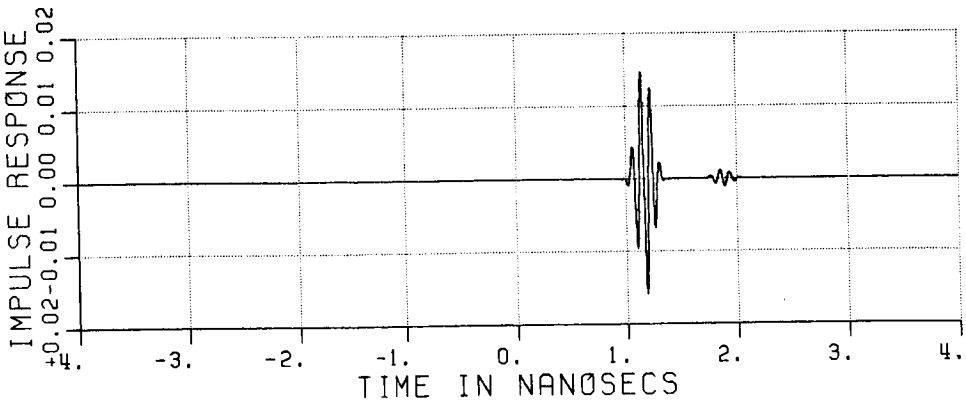

a) Exact sphere

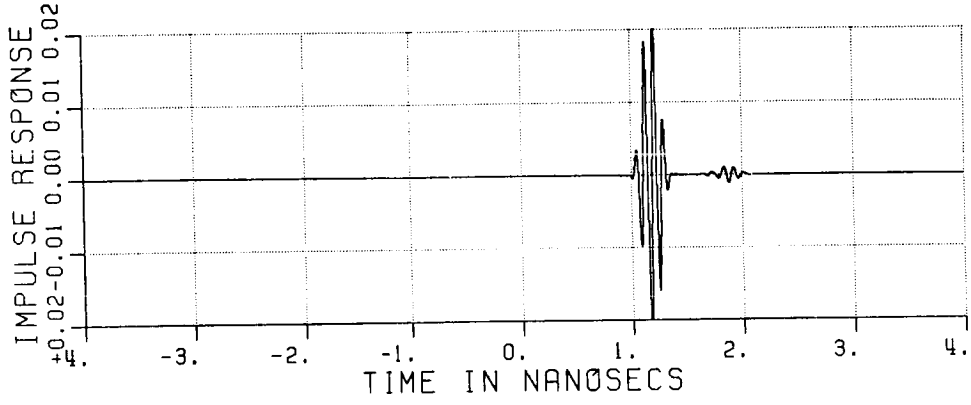

b) Calculated result

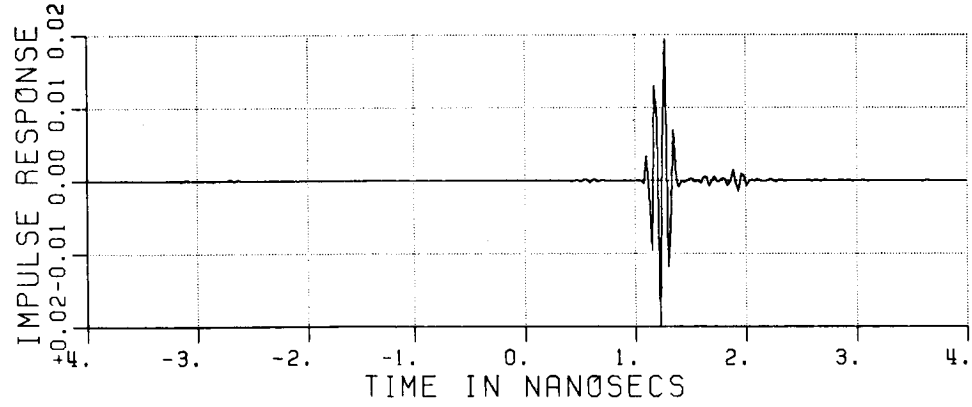

c) Measured result

Figure 5.49. Time domain plots of CONF5C: X=15",Y=0",Z=3"; HP.

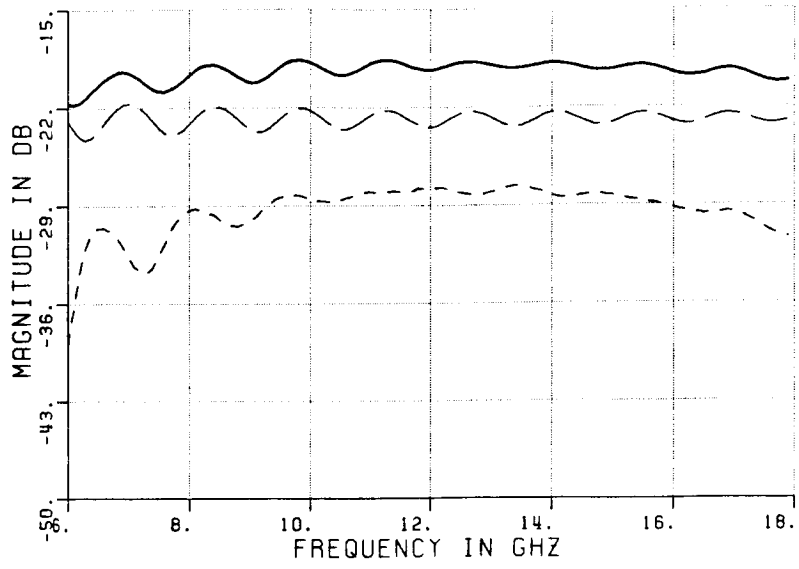

a) calculated result

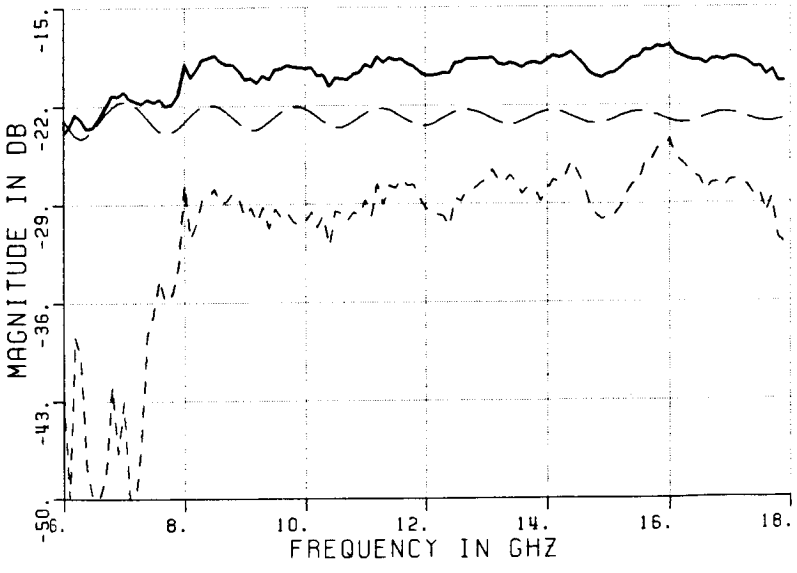

b) measured result

Figure 5.50. Frequency domain plots of CONF5C: X=15",Y=0",Z=3"; HP.

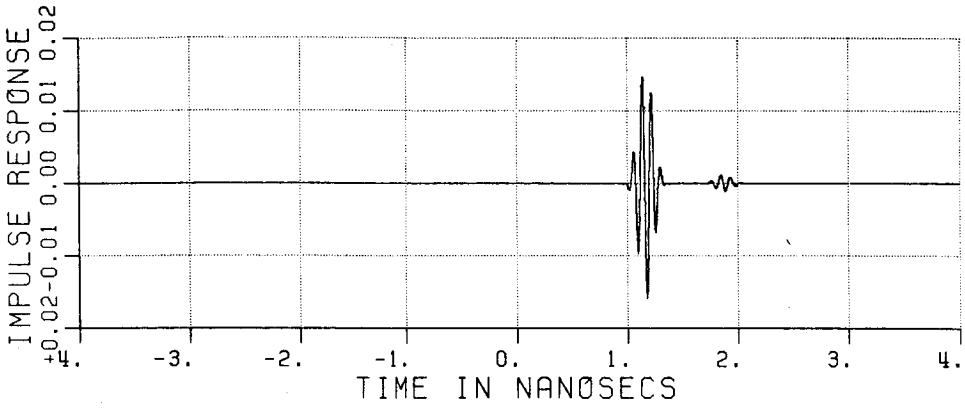

a) Exact sphere

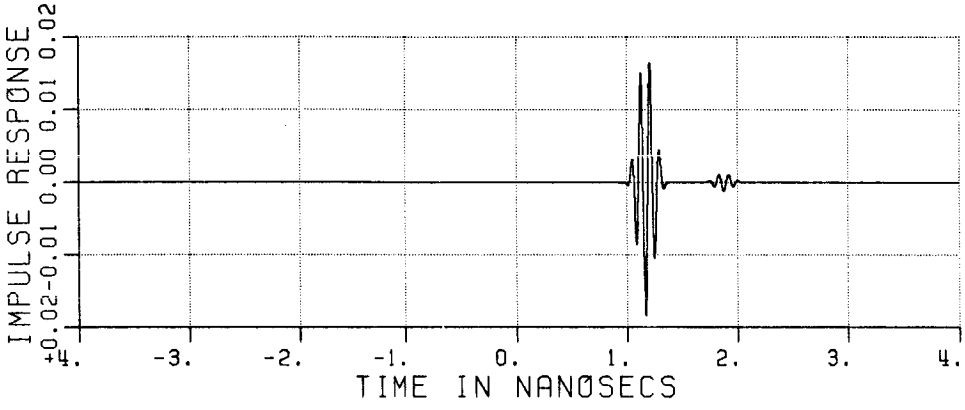

b) Calculated result

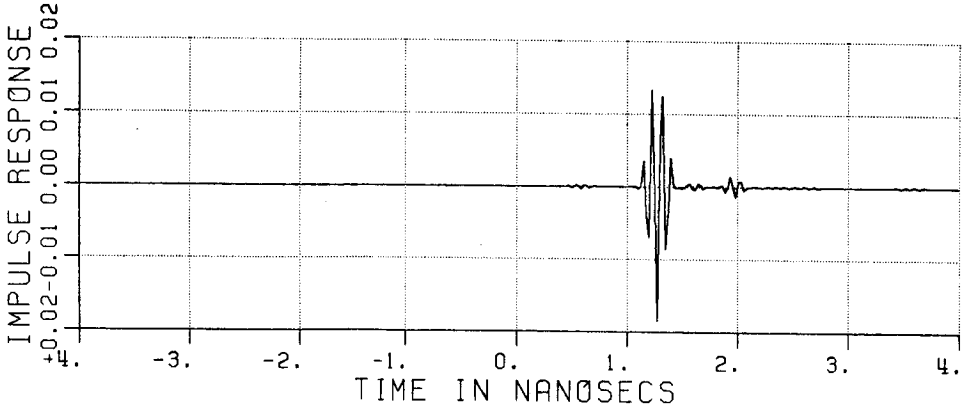

c) Measured result

Figure 5.51. Time domain plots of CONF6C: X=15",Y=-3",Z=3"; HP.

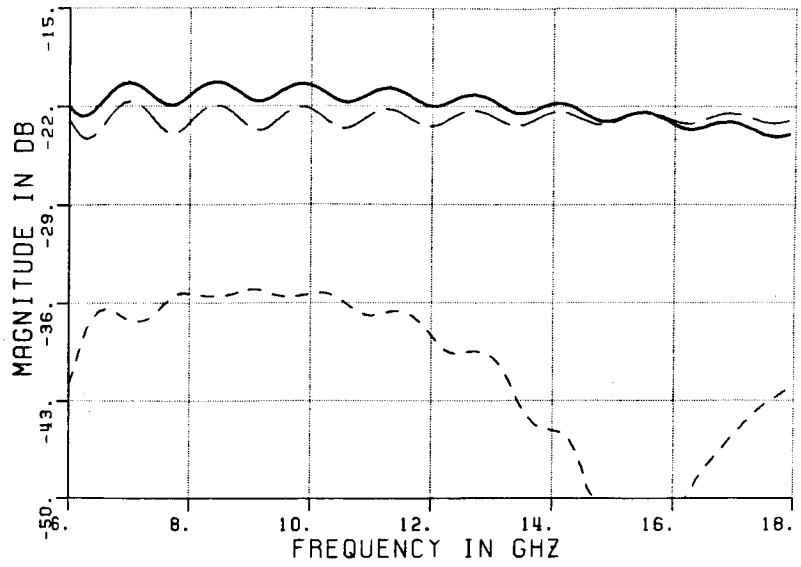

a) calculated result

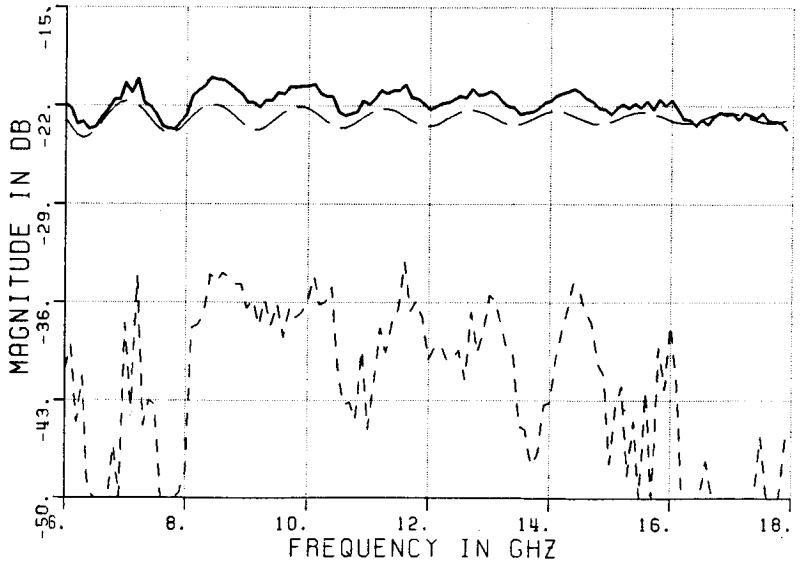

b) measured result

Figure 5.52. Frequency domain plots of CONF6C: X=15",Y=-3",Z=3"; HP.

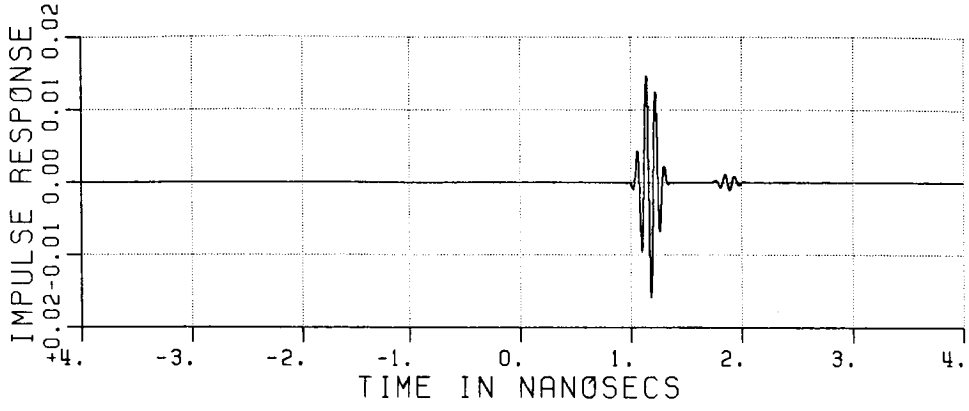

a) Exact sphere

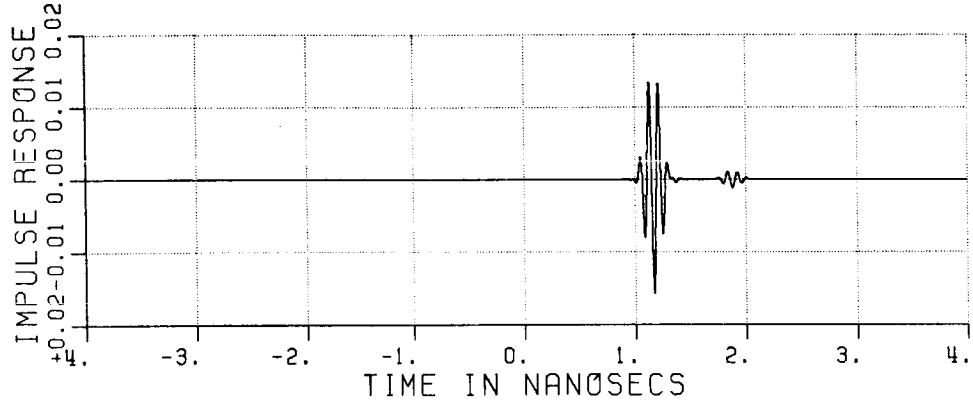

b) Calculated result

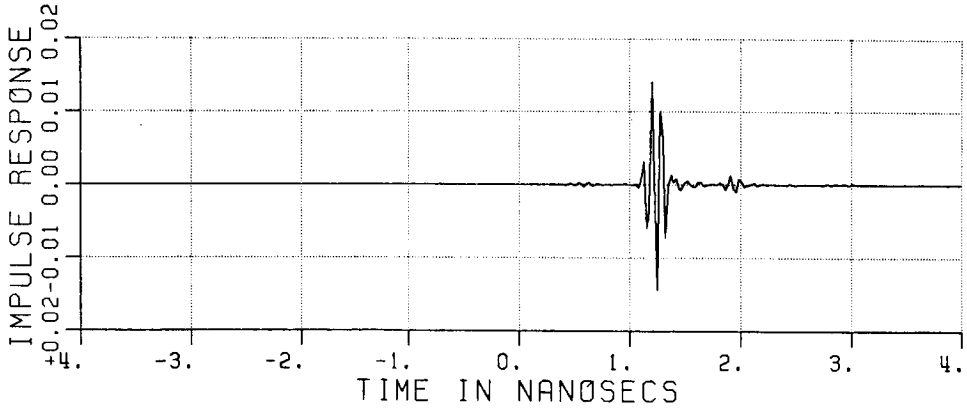

c) Measured result

Figure 5.53. Time domain plots of CONF7C: X=15",Y=-6",Z=3"; HP.

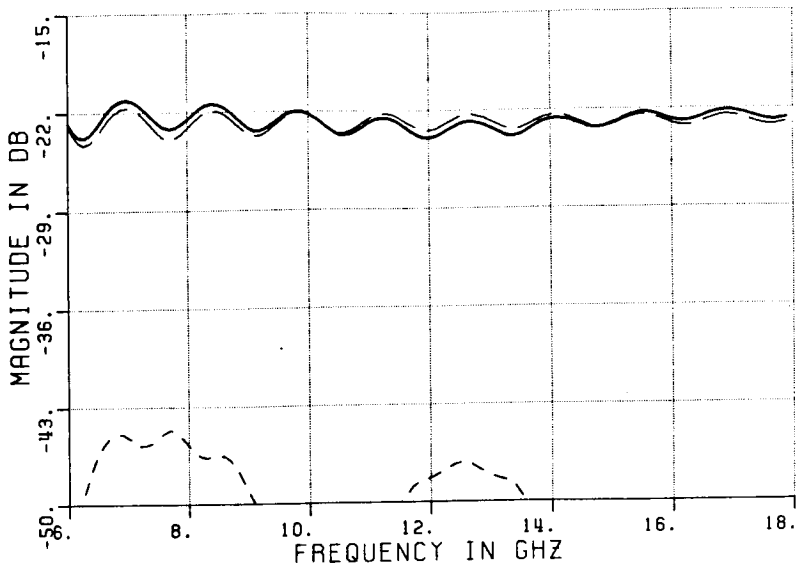

a) calculated result

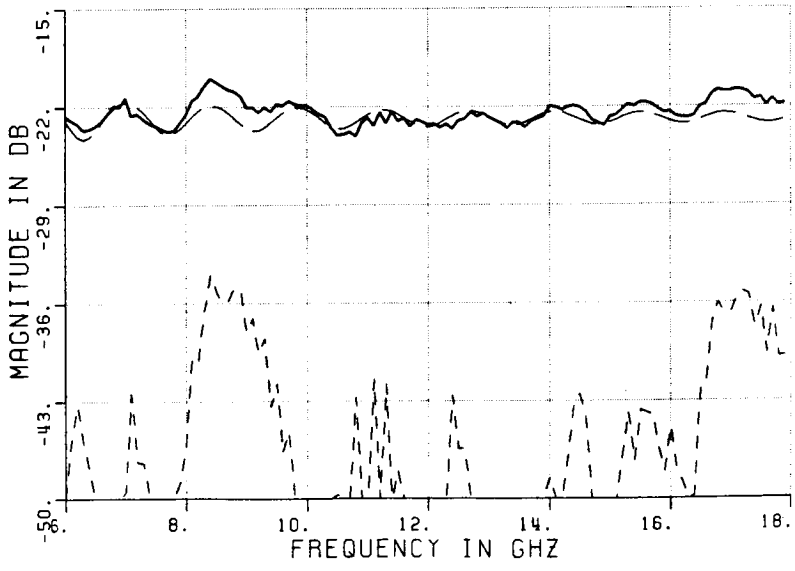

b) measured result

Figure 5.54. Frequency domain plots of CONF7C: X=15",Y=-6",Z=3"; HP.

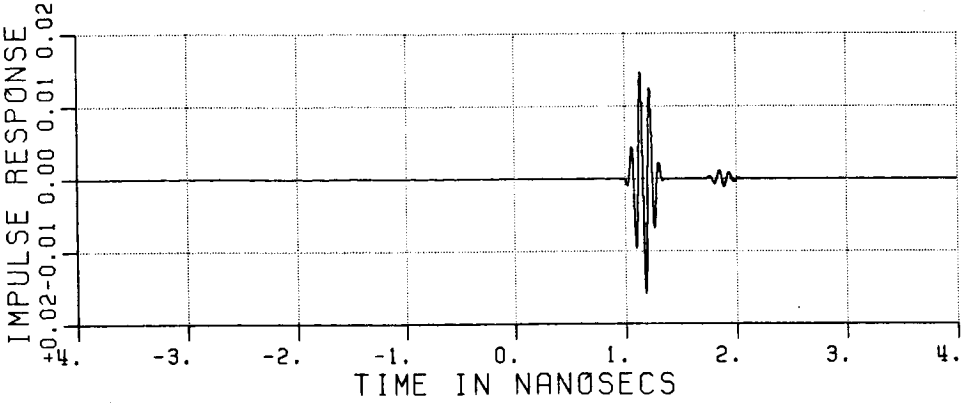

a) Exact sphere

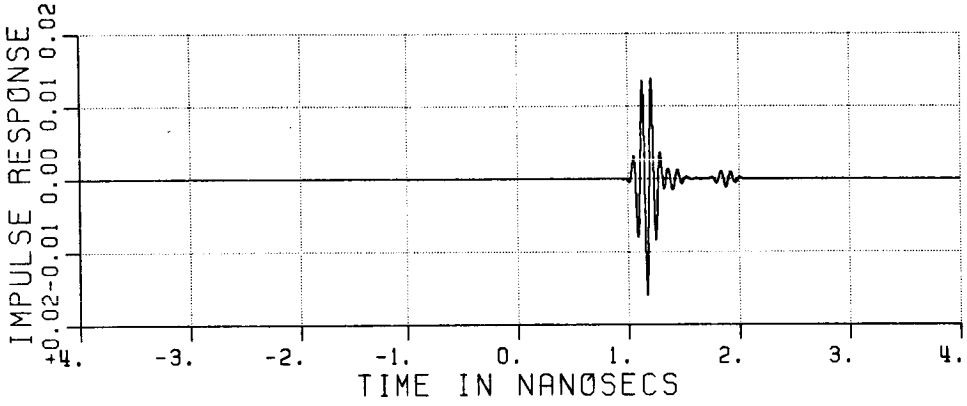

b) Calculated result

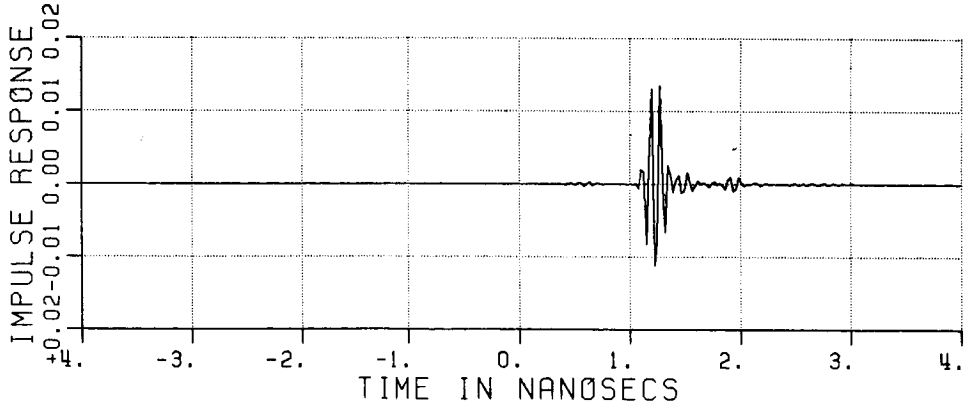

c) Measured result

Figure 5.55. Time domain plots of CONF8C: X=15",Y=-9",Z=3"; HP.

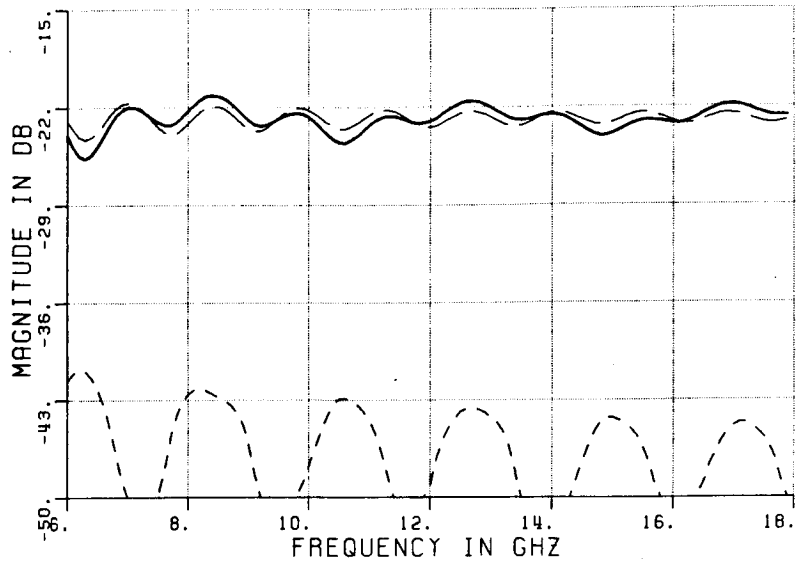

a) calculated result

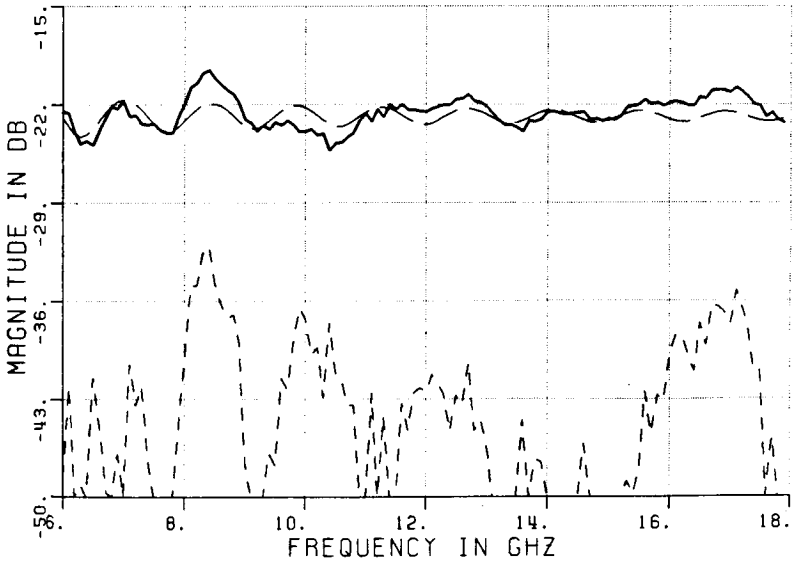

b) measured result

Figure 5.56. Frequency domain plots of CONF8C: X=15",Y=-9",Z=3"; HP.

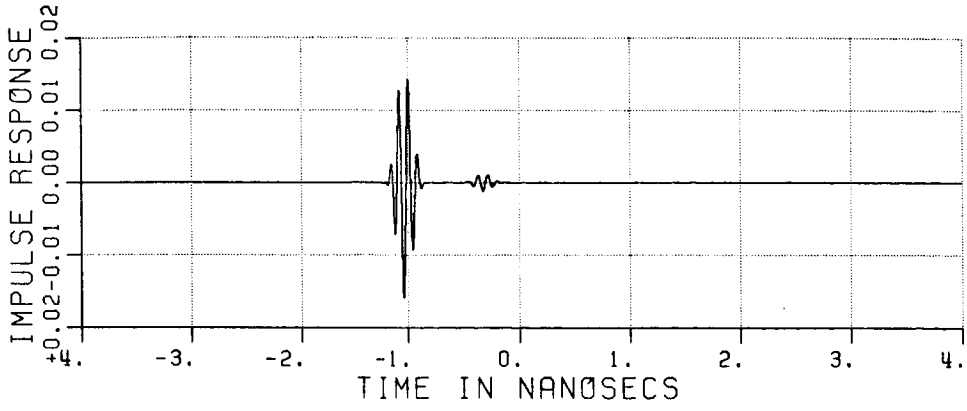

a) Exact sphere

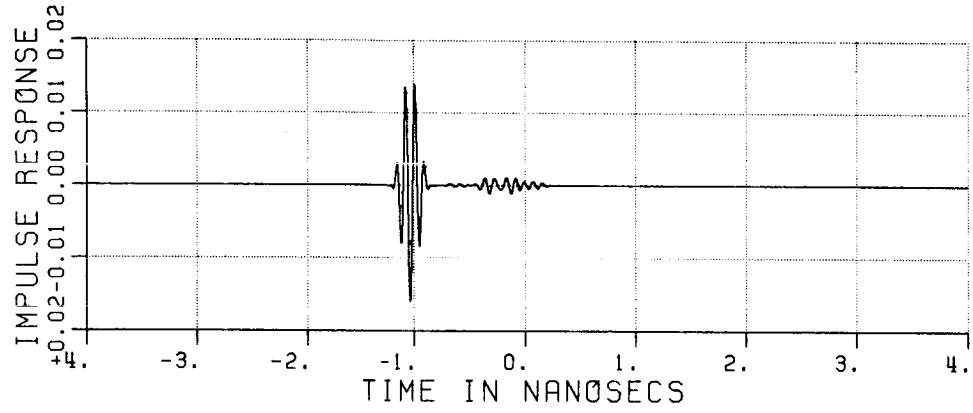

b) Calculated result

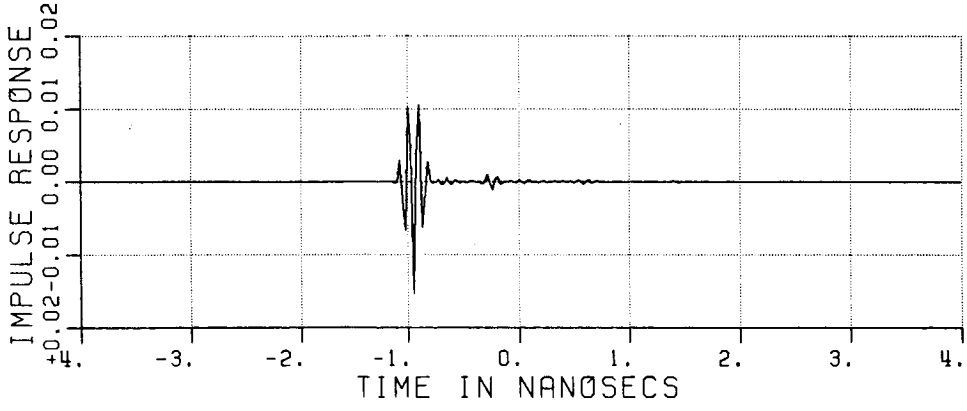

c) Measured result

Figure 5.57. Time domain plots of CONF1D: X=2",Y=0",Z=6"; HP.

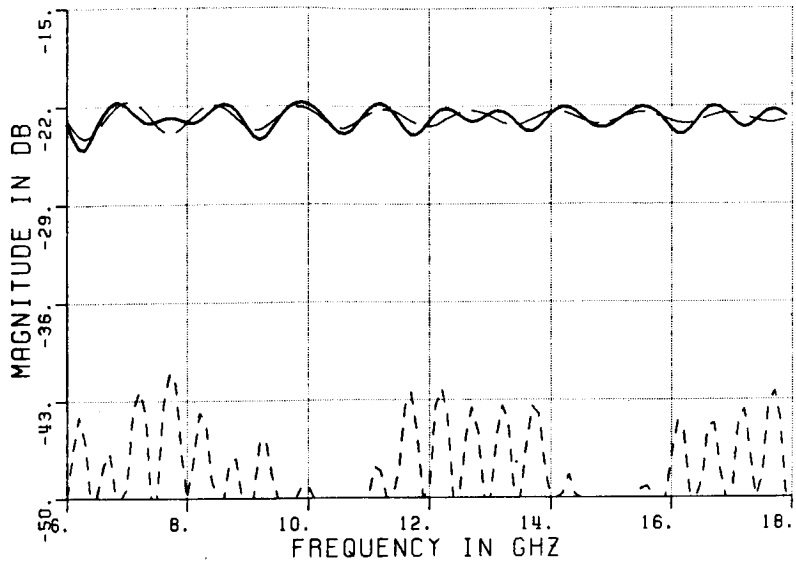

a) calculated result

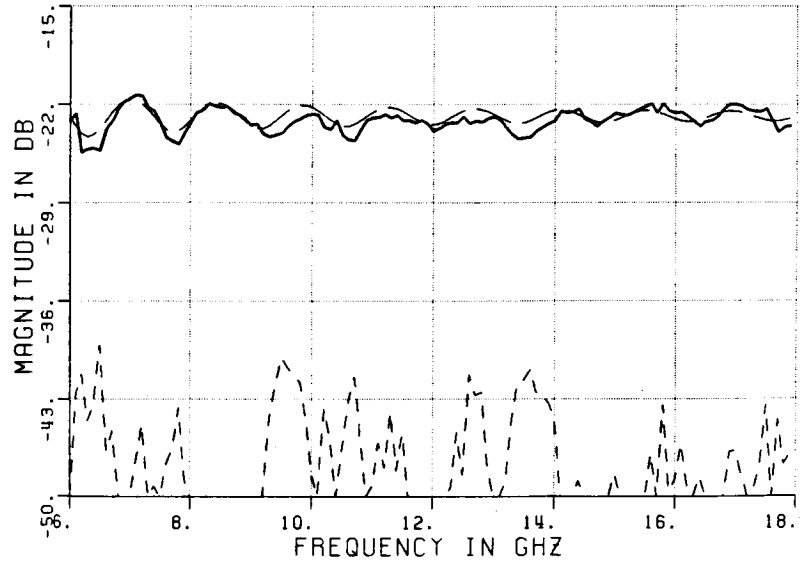

b) measured result

Figure 5.58. Frequency domain plots of CONF1D: X=2",Y=0",Z=6"; HP.

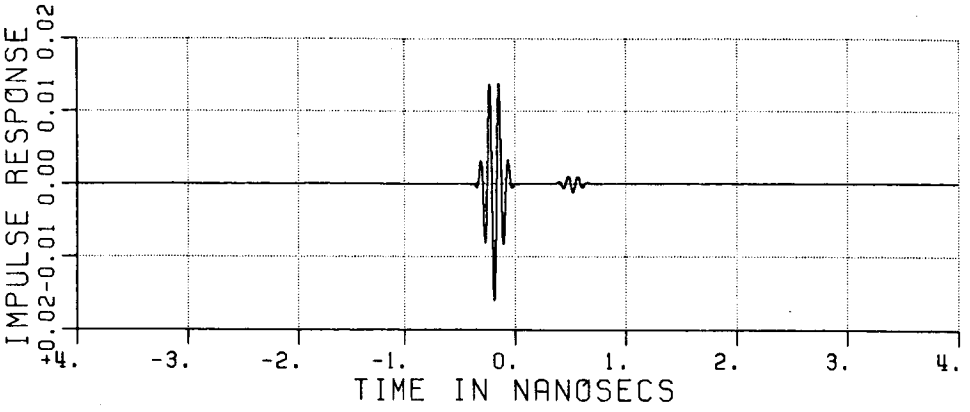

a) Exact sphere

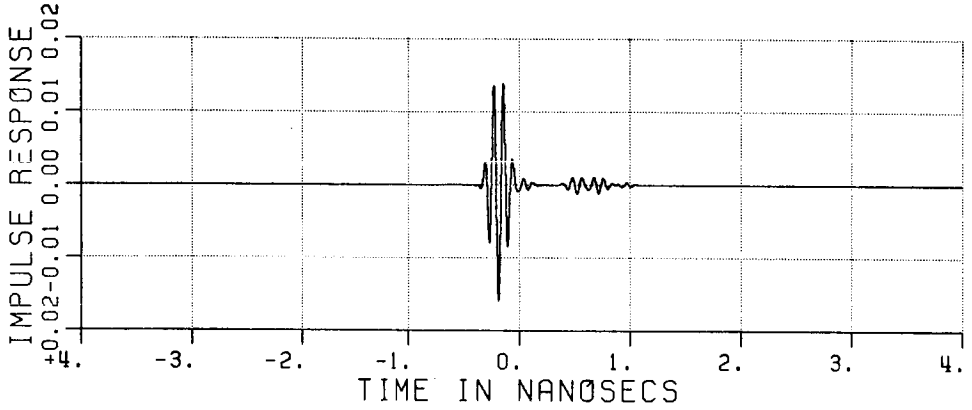

b) Calculated result

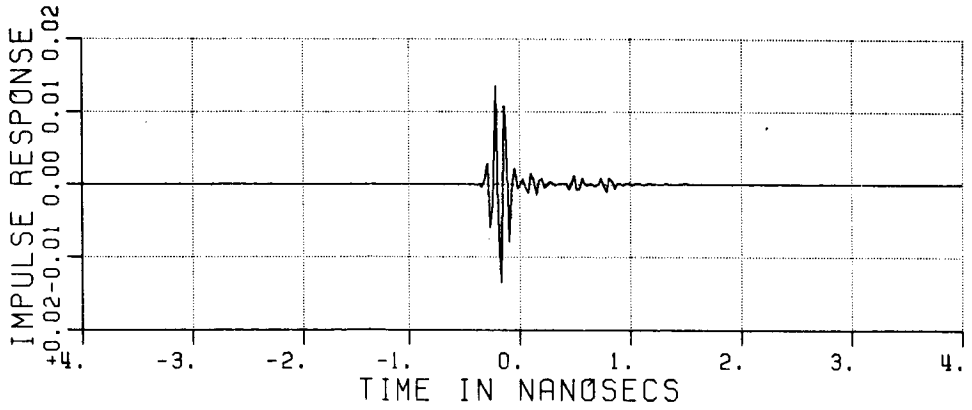

c) Measured result

Figure 5.59. Time domain plots of CONF2D: X=7",Y=0",Z=6"; HP.

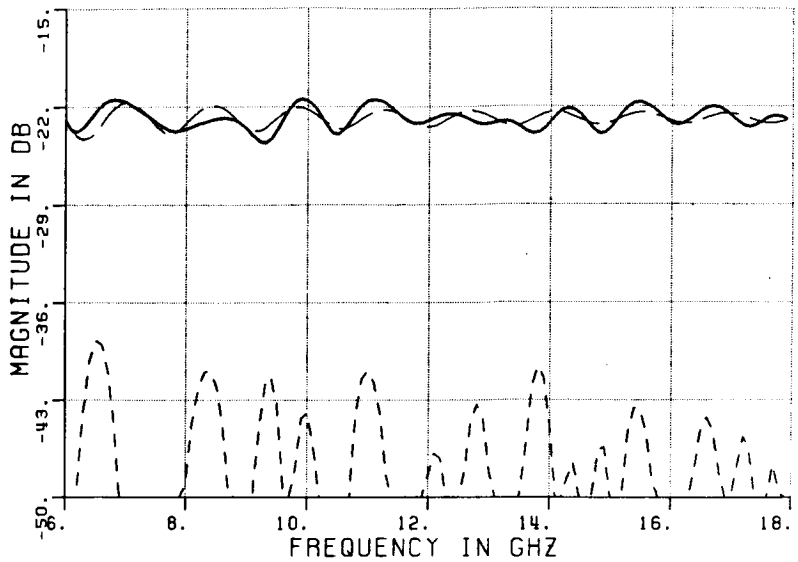

a) calculated result

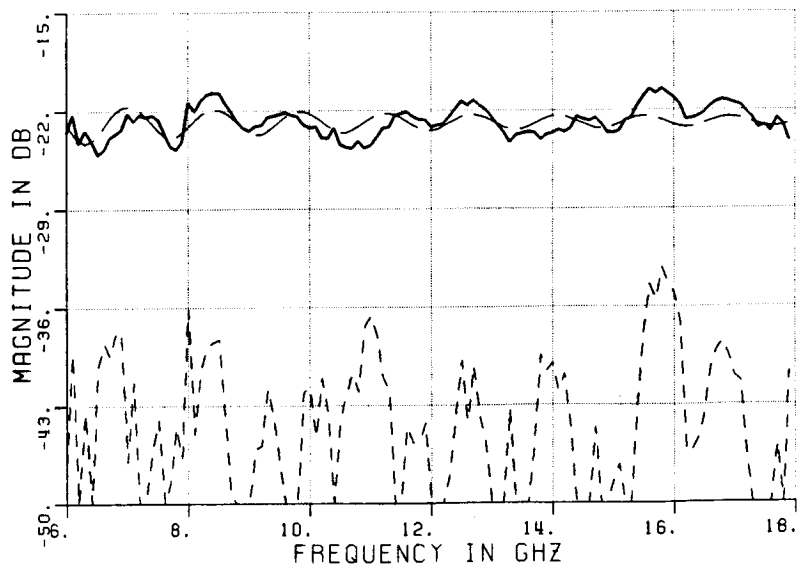

b) measured result

Figure 5.60. Frequency domain plots of CONF2D: X=7",Y=0",Z=6"; HP.

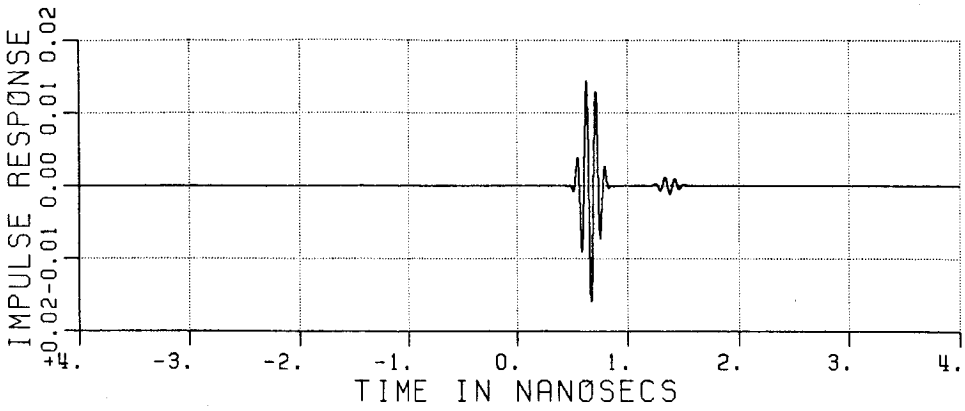

a) Exact sphere

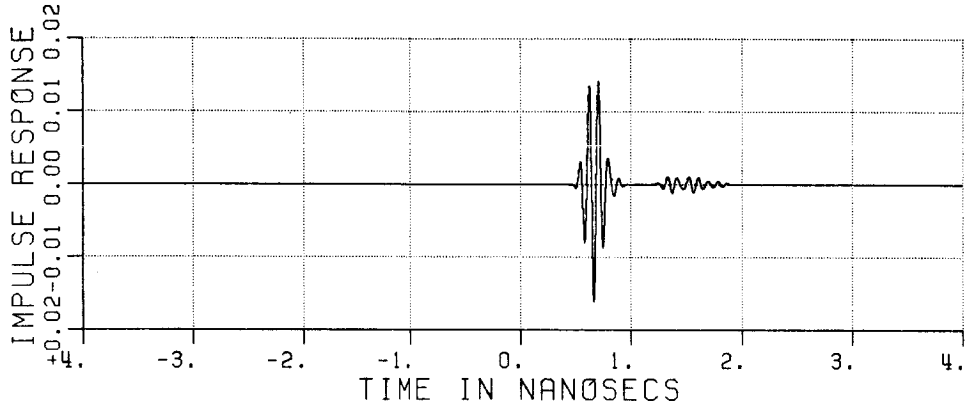

b) Calculated result

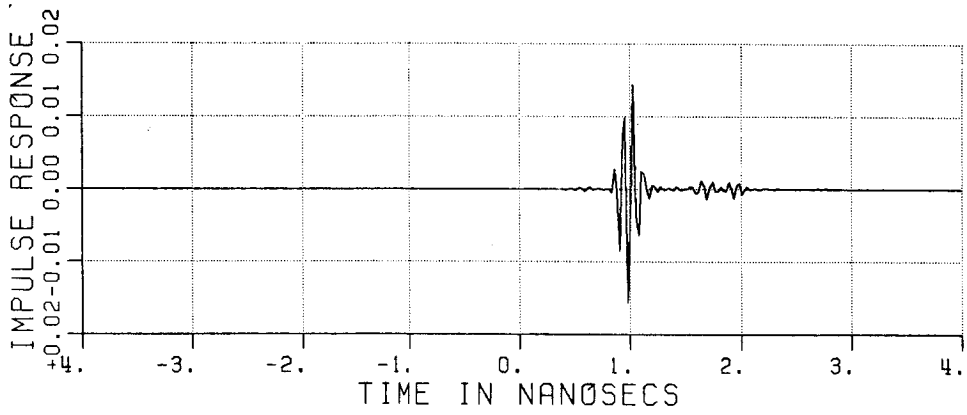

c) Measured result

Figure 5.61. Time domain plots of CONF3D: X=12",Y=0",Z=6"; HP.

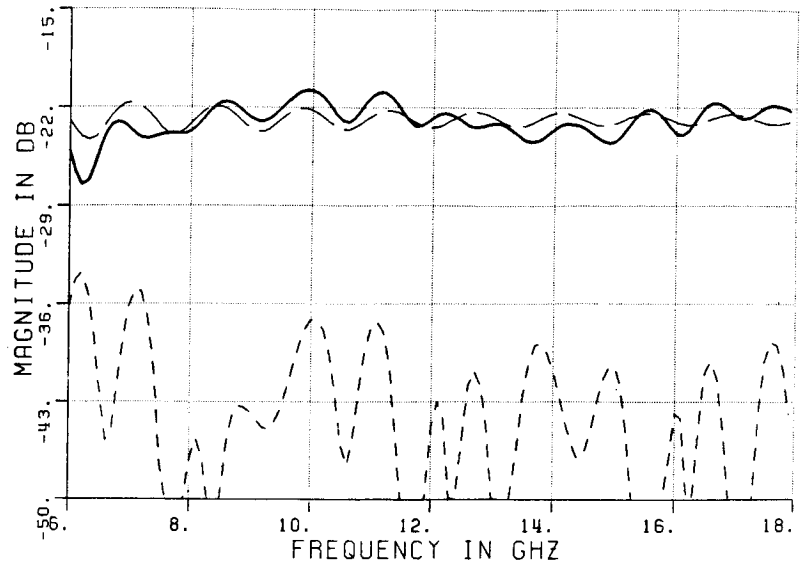

a) calculated result

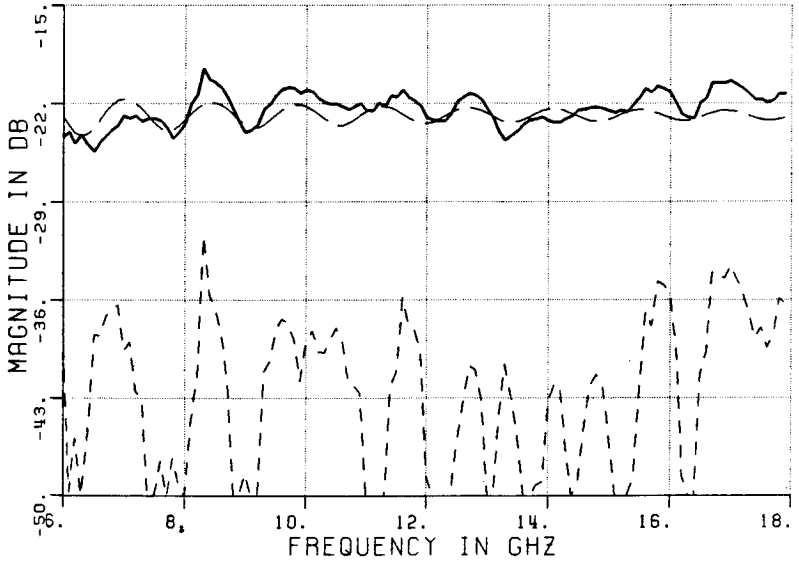

b) measured result

Figure 5.62. Frequency domain plots of CONF3D: X=12",Y=0",Z=6"; HP.

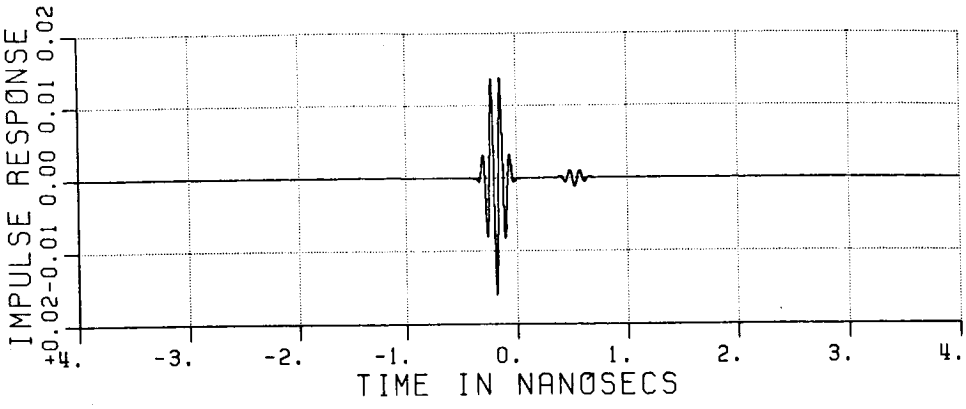

a) Exact sphere

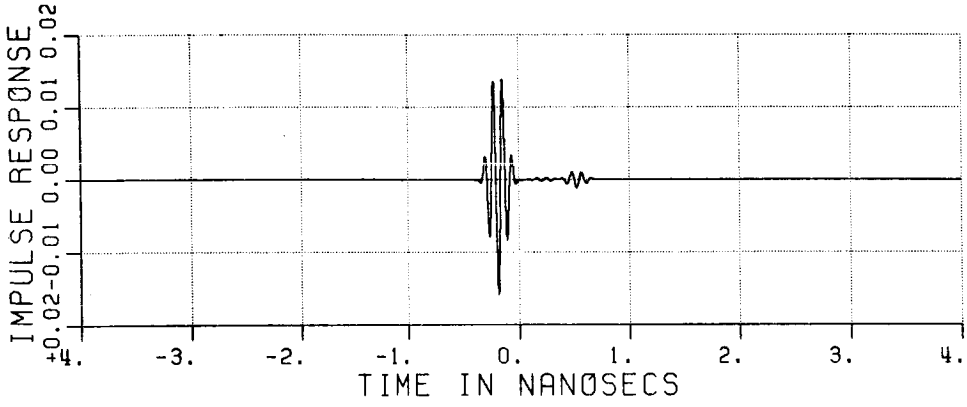

b) Calculated result

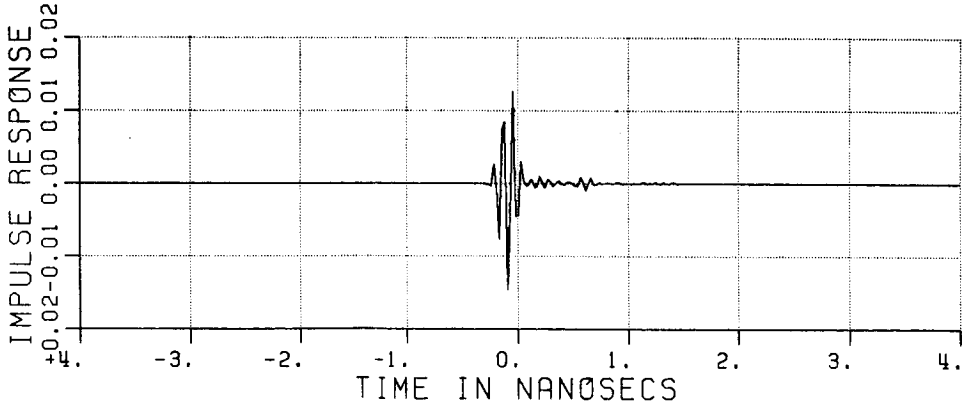

c) Measured result

Figure 5.63. Time domain plots of CONF4D: X=7",Y=-7" ,Z=6"; HP.

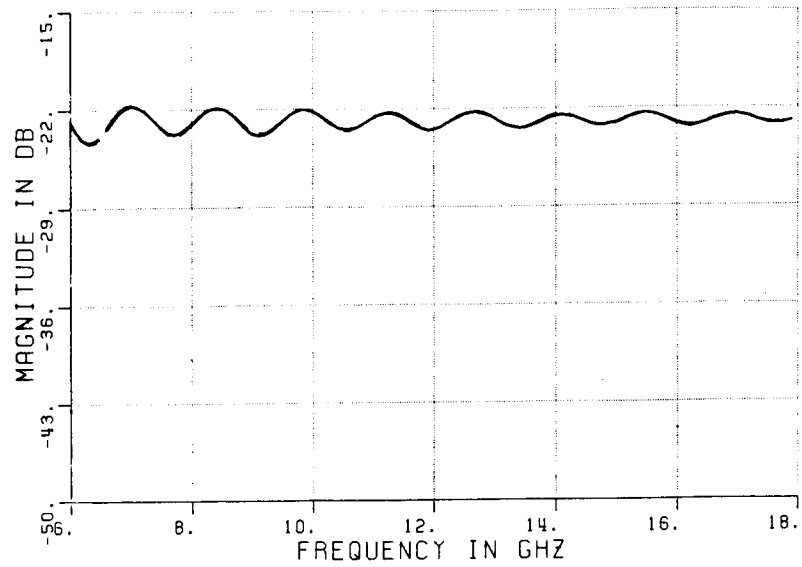

a) calculated result

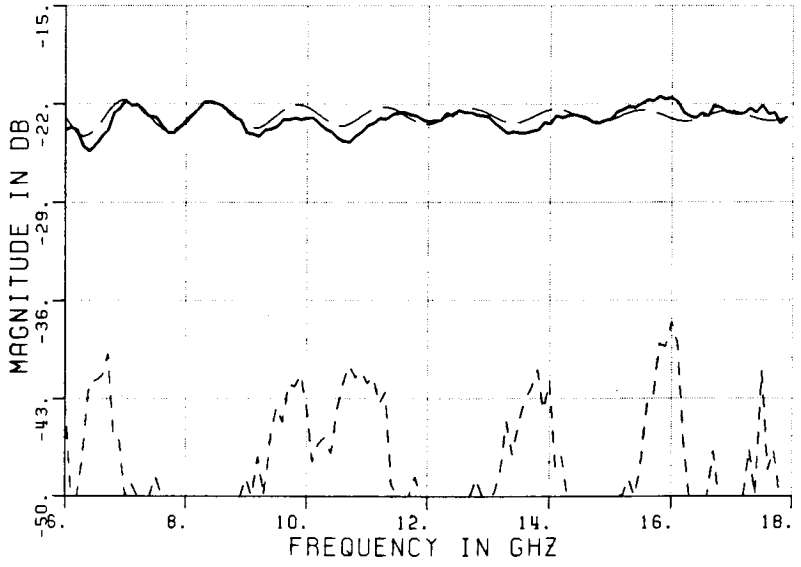

b) measured result

Figure 5.64. Frequency domain plots of CONF4D: X=7",Y=-7",Z=6"; HP.

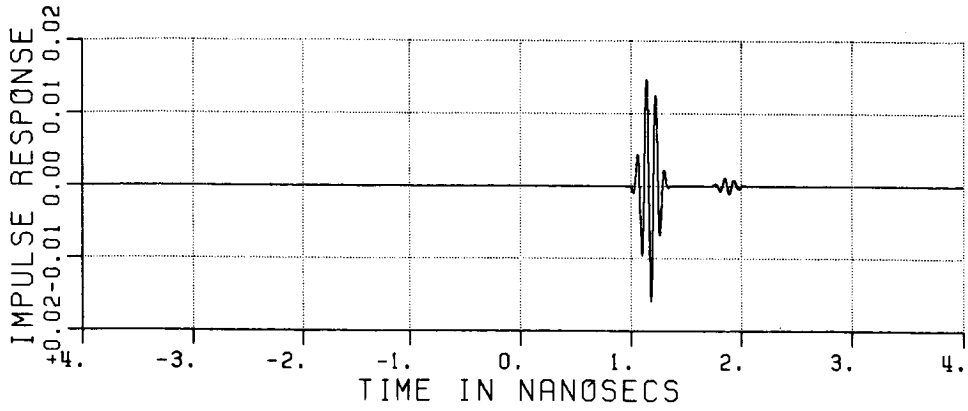

a) Exact sphere

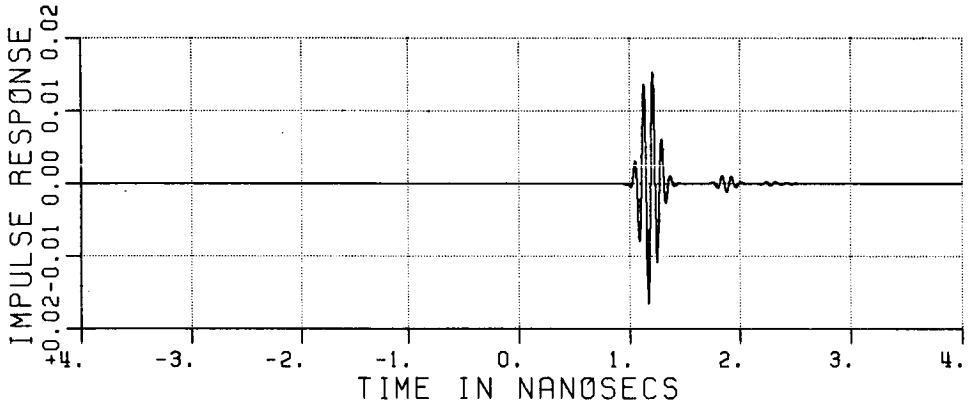

b) Calculated result

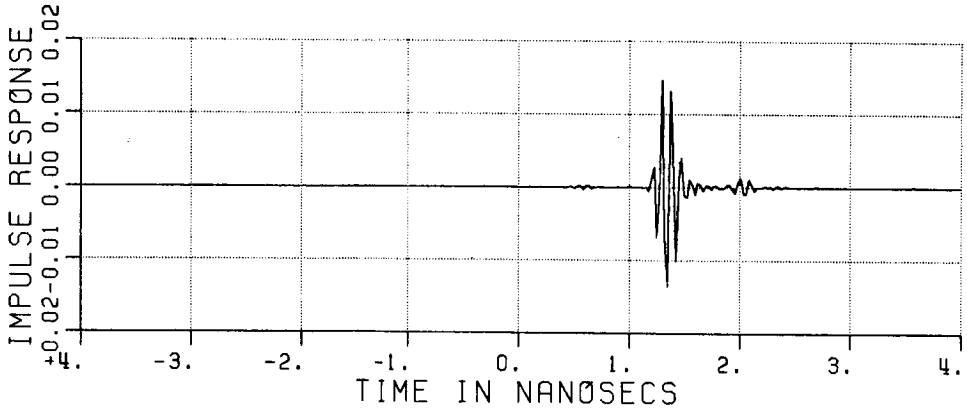

c) Measured result

Figure 5.65. Time domain plots of CONF5D: X=15",Y=0",Z=6"; HP.

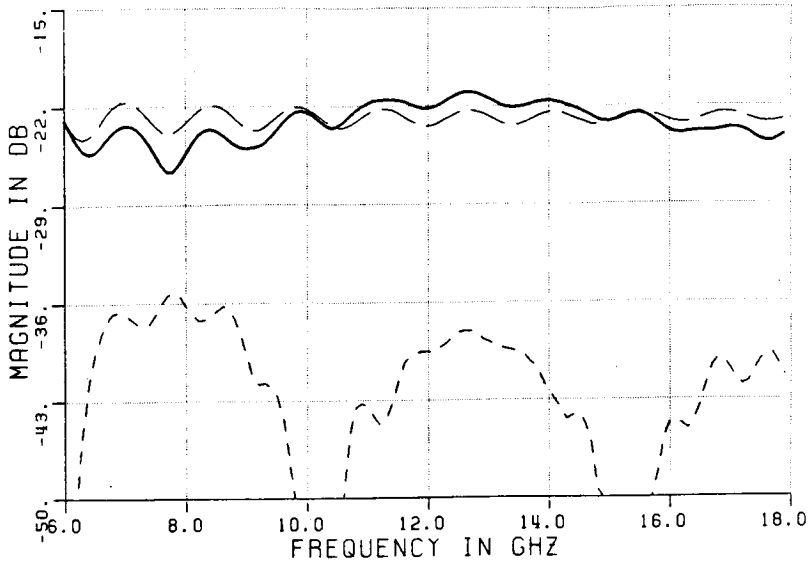

a) calculated result

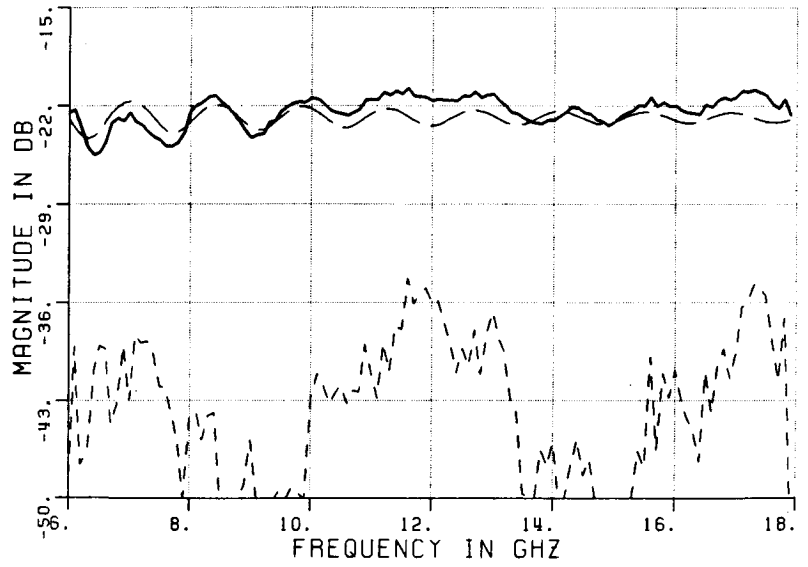

b) measured result

Figure 5.66. Frequency domain plots of CONF5D: X=15",Y=0",Z=6"; HP.

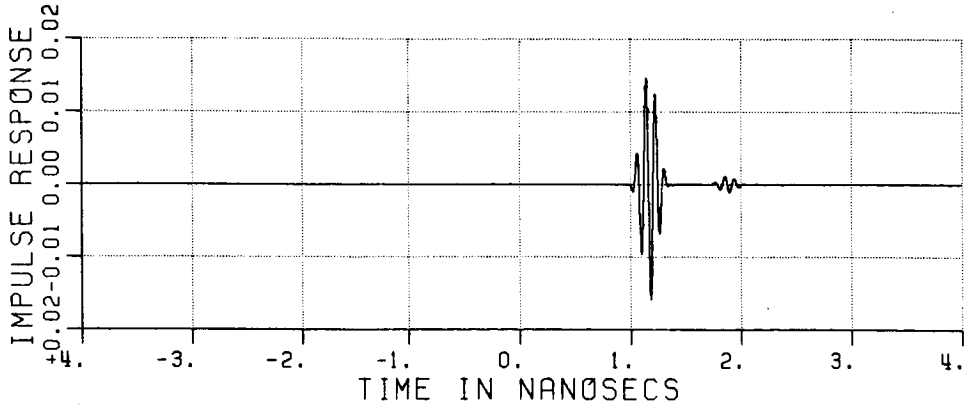

a) Exact sphere

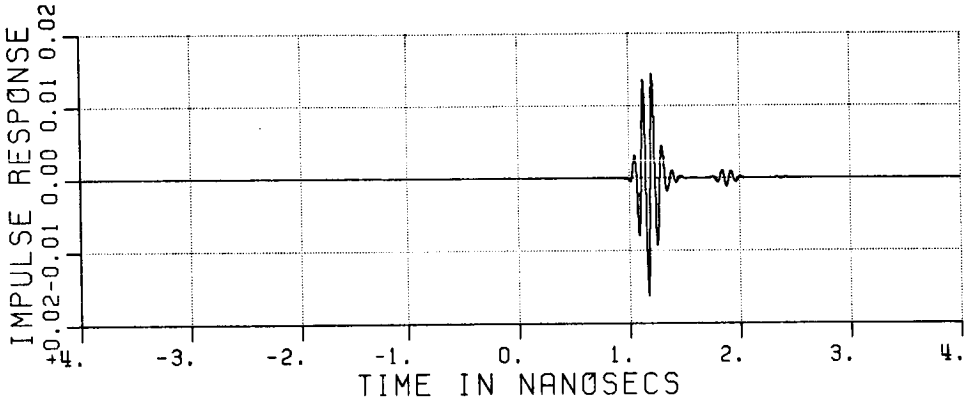

b) Calculated result

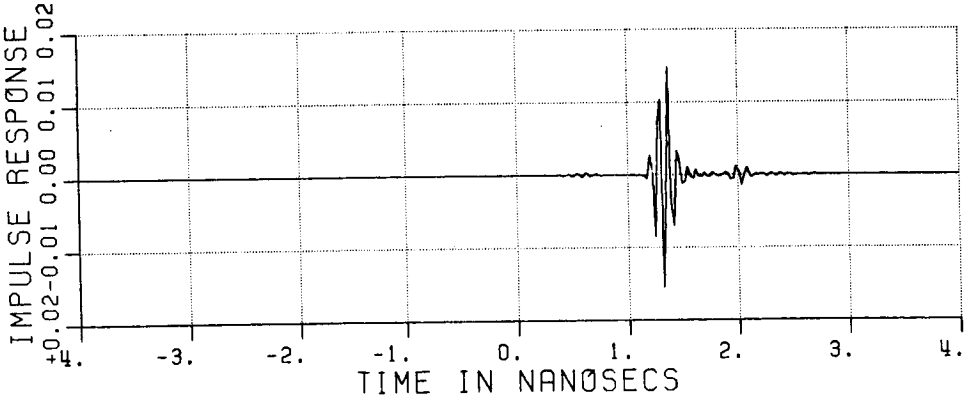

c) Measured result

Figure 5.67. Time domain plots of CONF6D: X=15",Y=-3",Z=6"; HP.

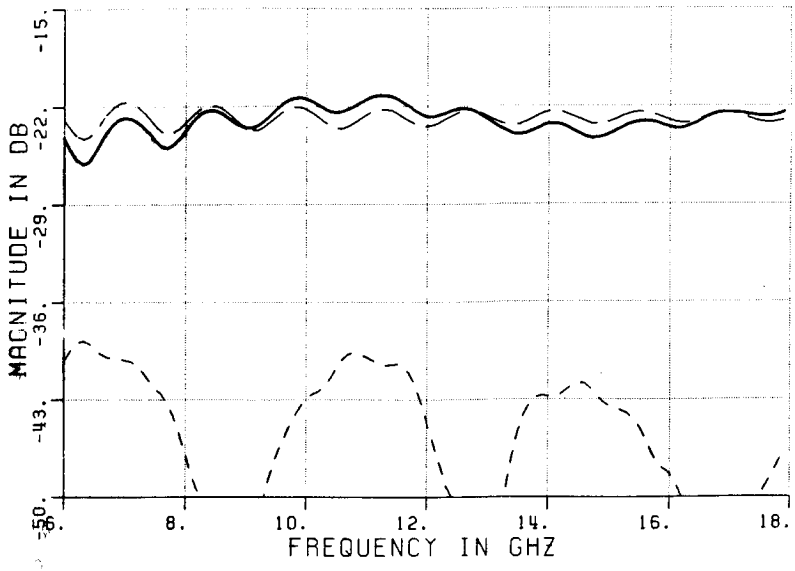

a) calculated result

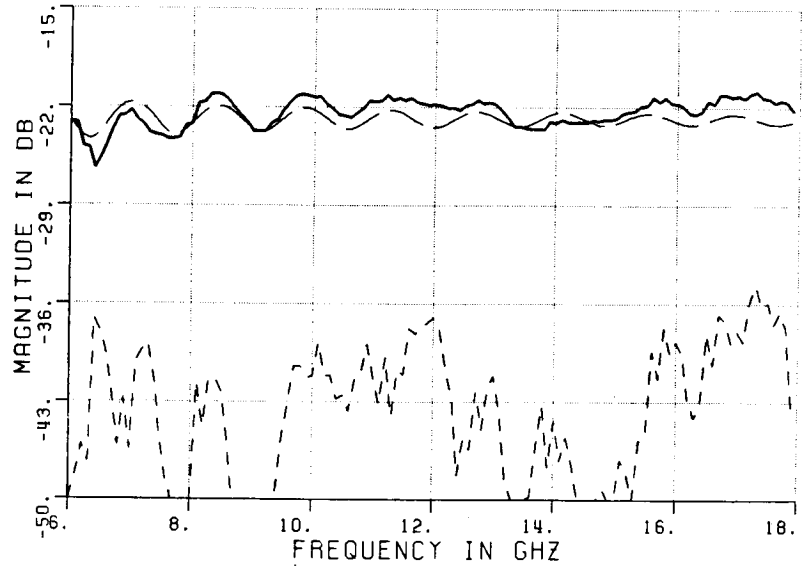

b) measured result

Figure 5.68. Frequency domain plots of CONF6D: X=15",Y=-3",Z=6"; HP.

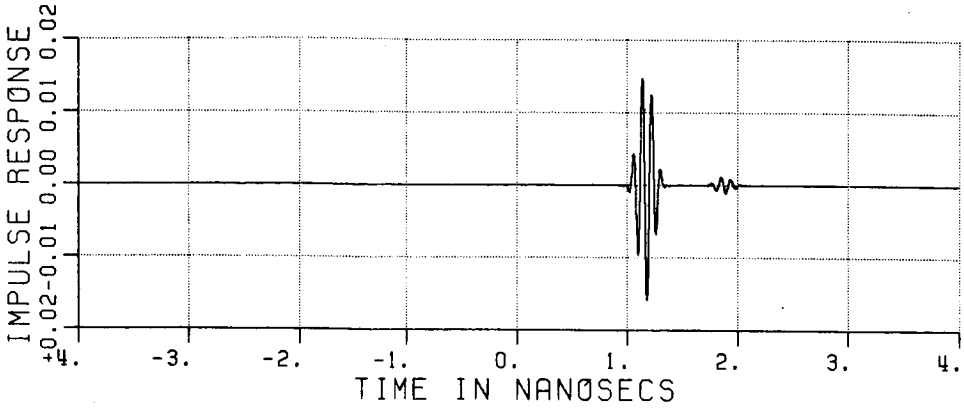

a) Exact sphere

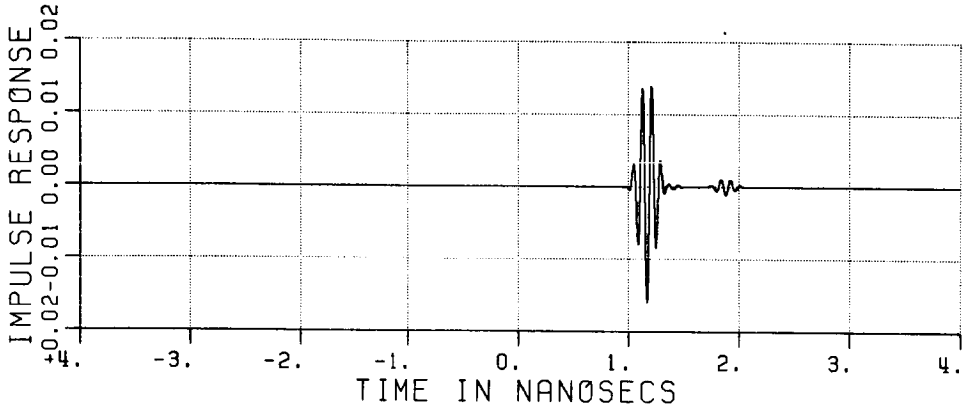

b) Calculated result

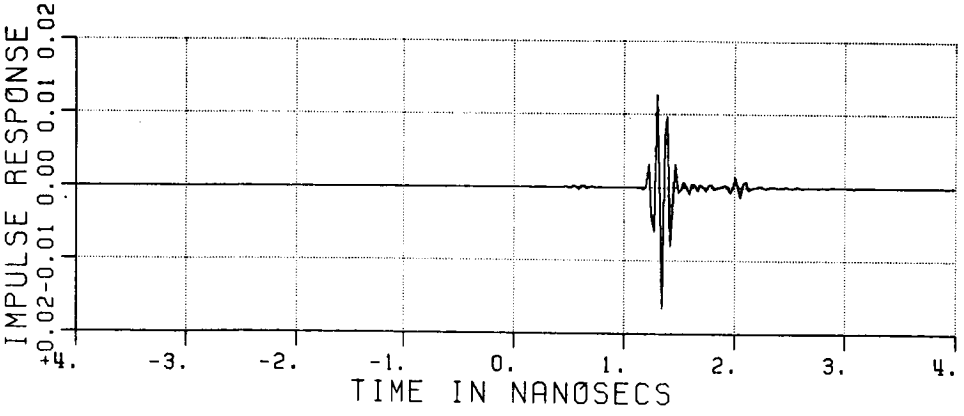

c) Measured result

Figure 5.69. Time domain plots of CONF7D: X=15",Y=-6",Z=6"; HP.

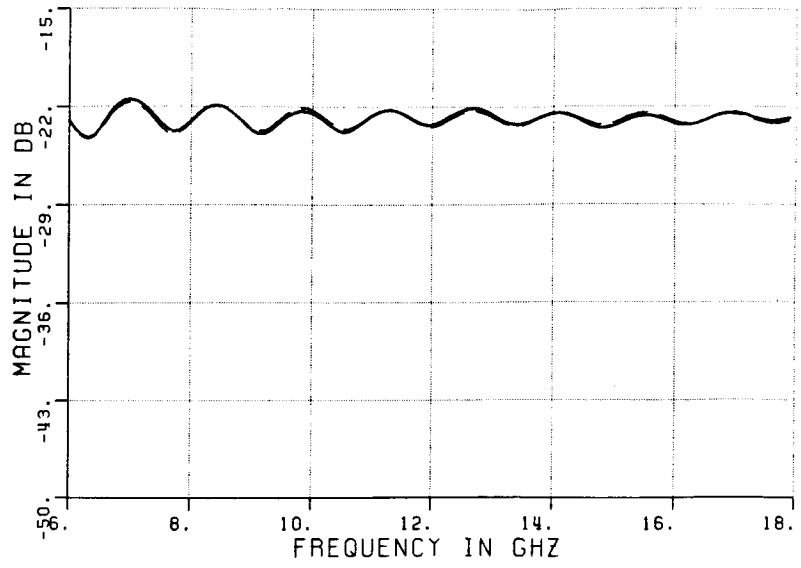

a) calculated result

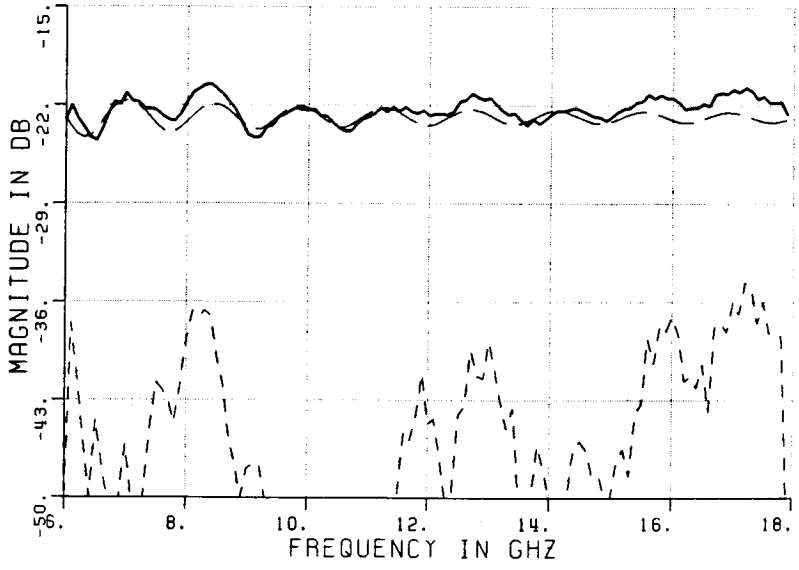

b) measured result

Figure 5.70. Frequency domain plots of CONF7D: X=15",Y=-6",Z=6"; HP.

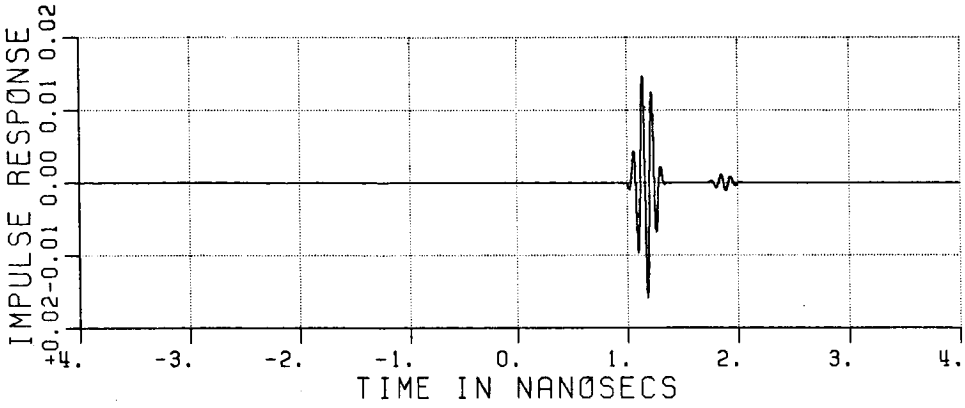

a) Exact sphere

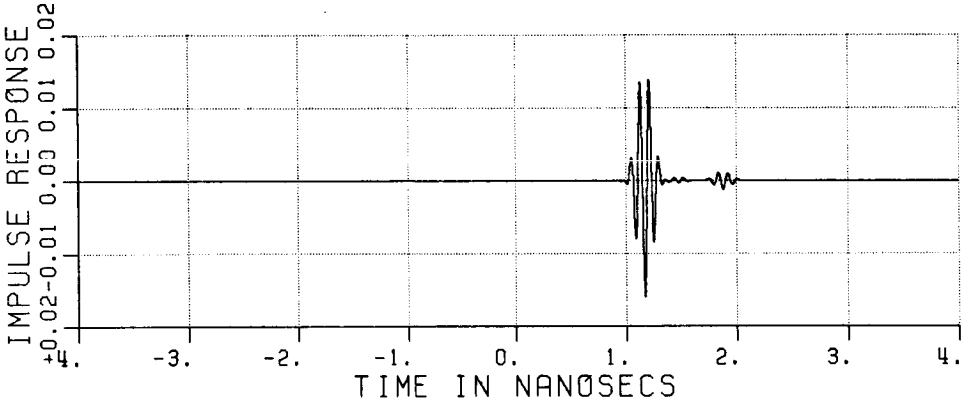

b) Calculated result

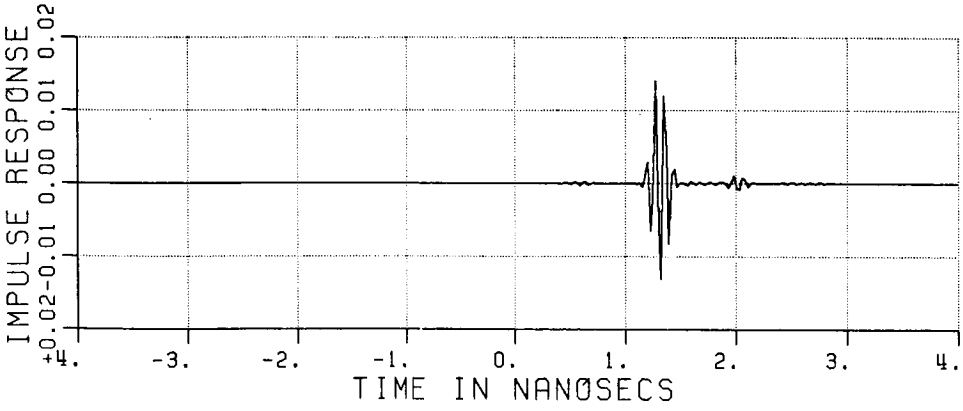

c) Measured result

Figure 5.71. Time domain plots of CONF8D: X=15",Y=-9",Z=6"; HP.

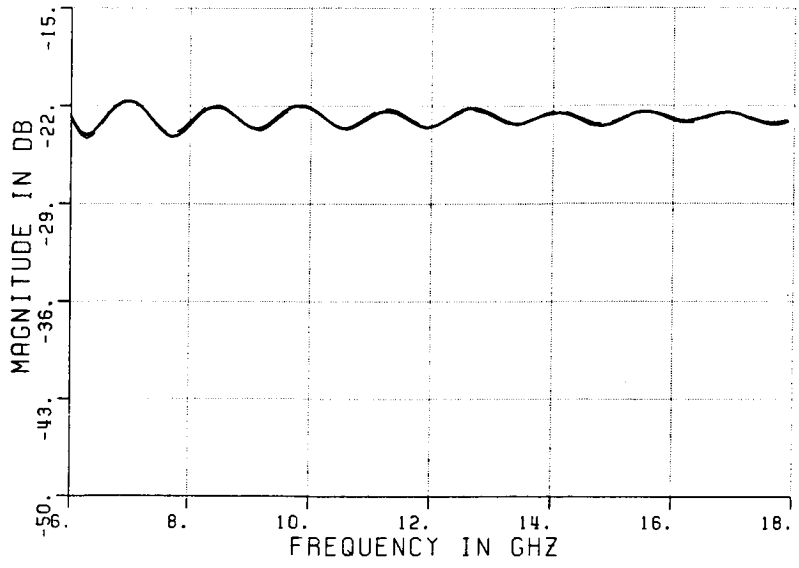

a) calculated result

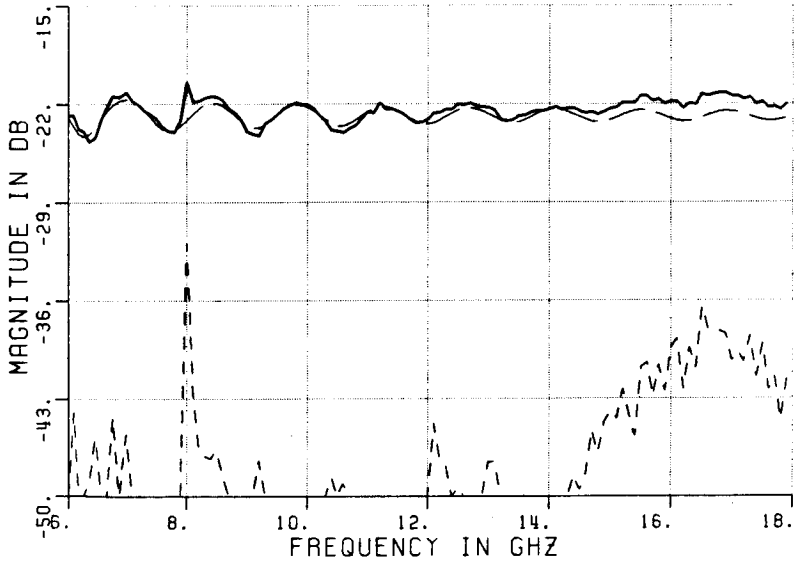

b) measured result

Figure 5.72. Frequency domain plots of CONF8D: X=15",Y=-9",Z=6"; HP.

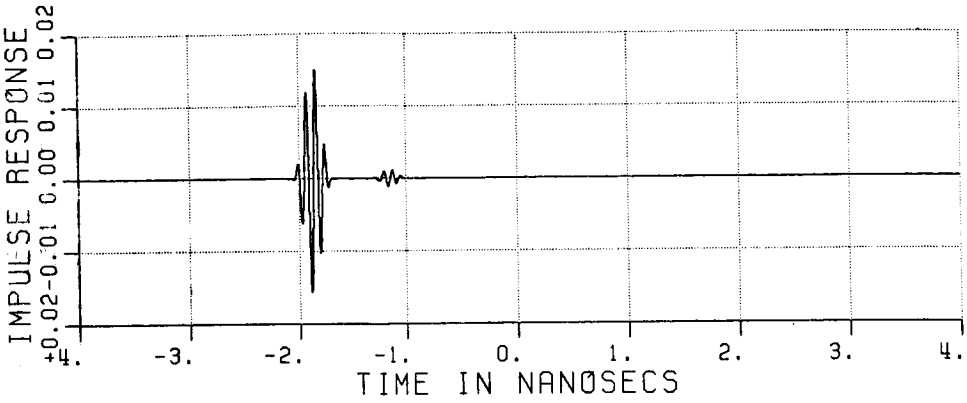

a) Exact sphere

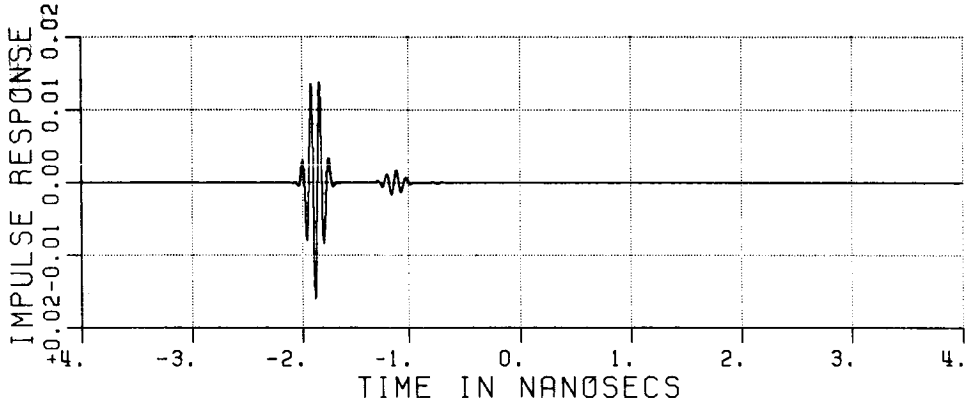

b) Calculated result

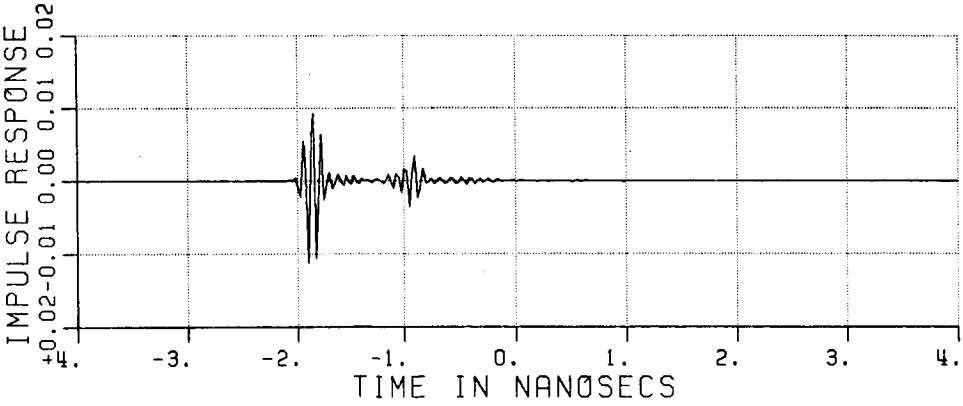

c) Measured result

Figure 5.73. Time domain plots of CONF9E: X=-3",Y=0",Z=-2"; VP.

C-3

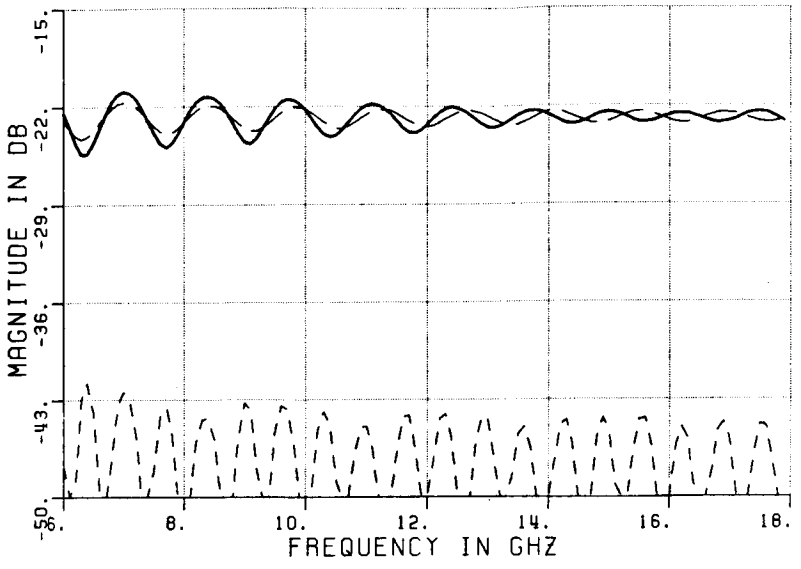

a) calculated result

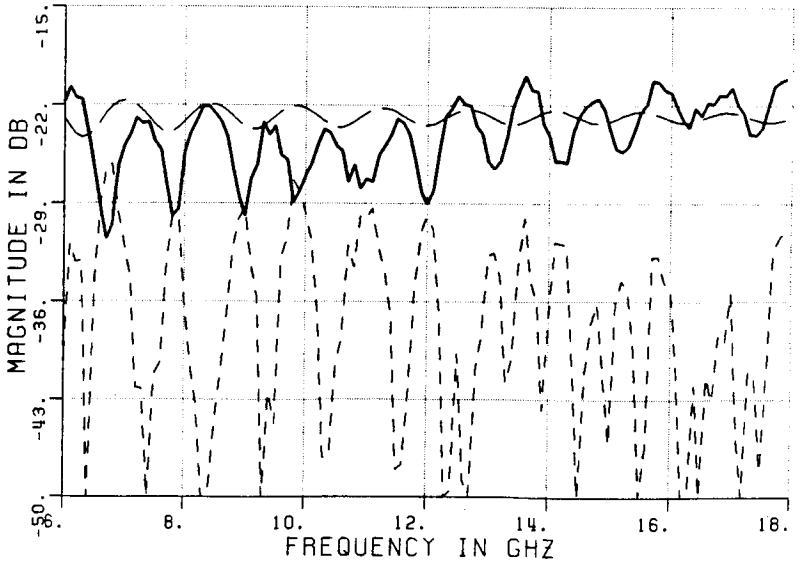

b) measured result

Figure 5.74. Frequency domain plots of CONF9E: X=-3",Y=0",Z=-2"; VP.

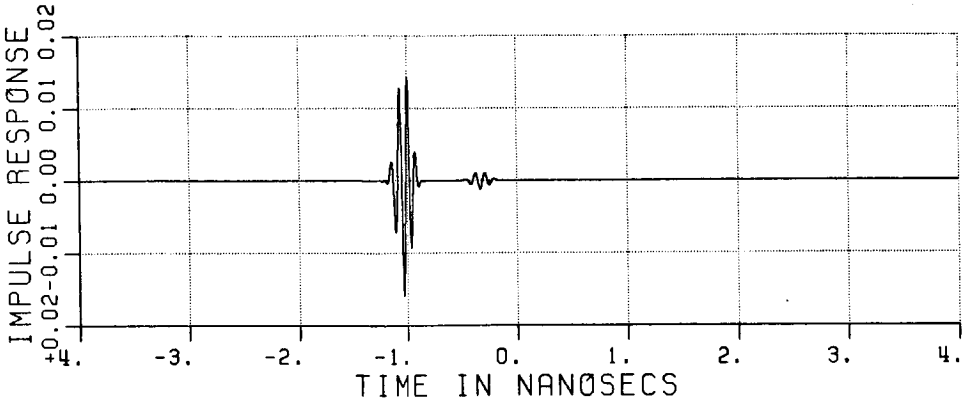

a) Exact sphere

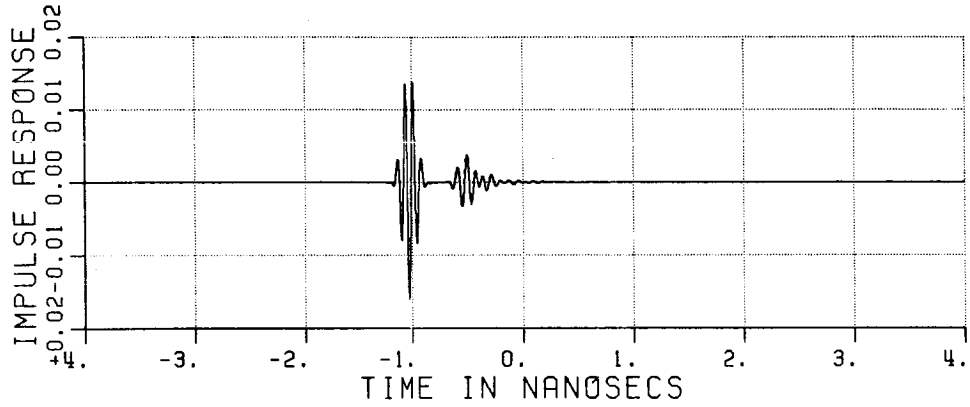

b) Calculated result

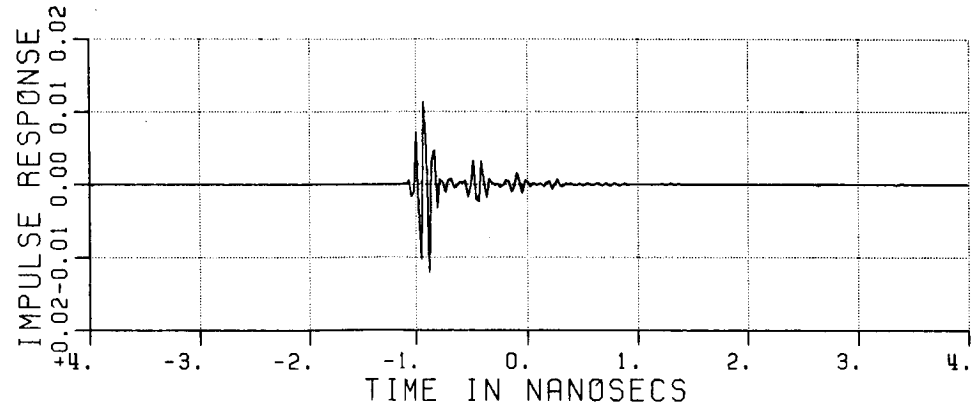

c) Measured result

Figure 5.75. Time domain plots of CONF10E: X=2",Y=-7",Z=-2"; VP.

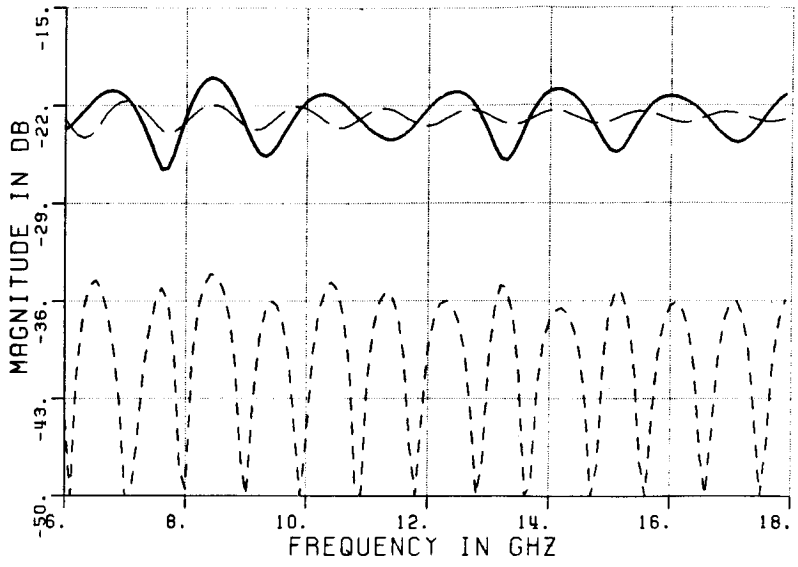

a) calculated result

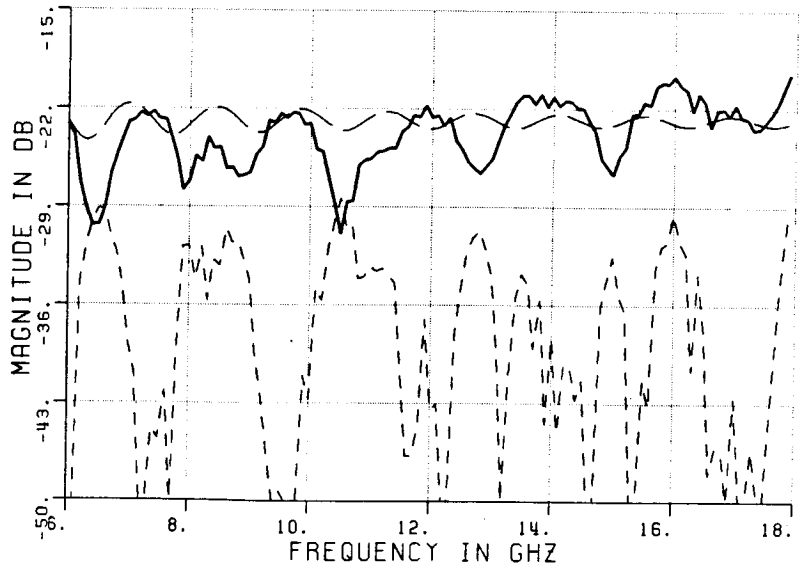

b) measured result

Figure 5.76. Frequency domain plots of CONF10E: X=2",Y=-7",Z=-2"; VP.

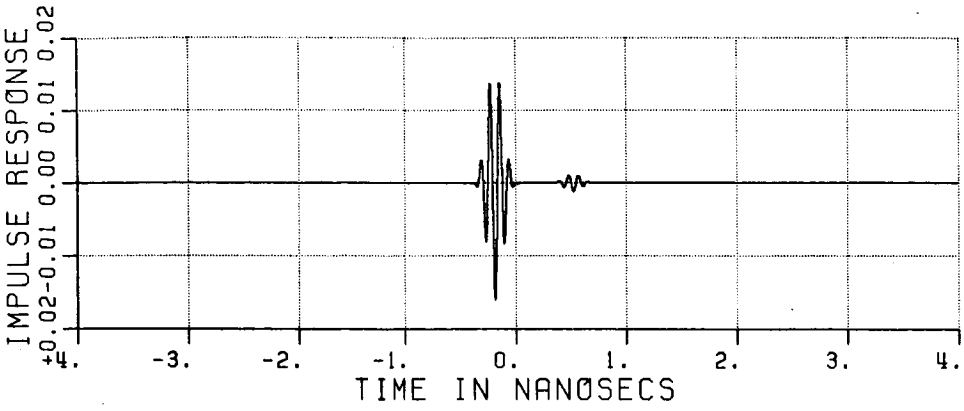

a) Exact sphere

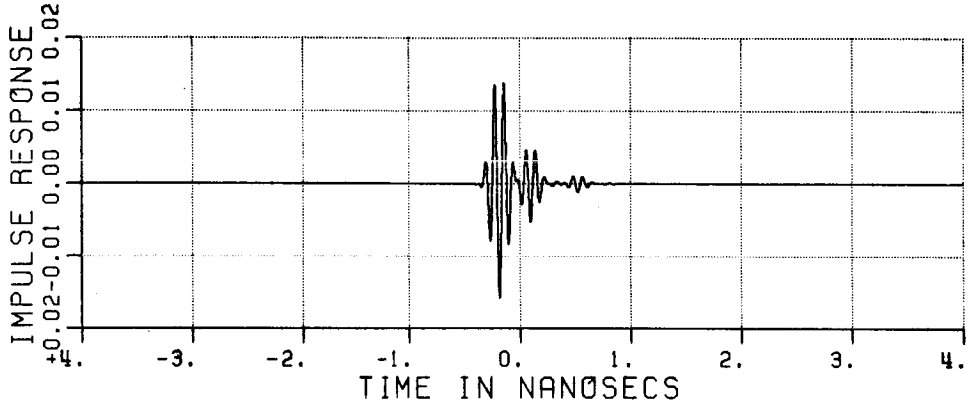

b) Calculated result

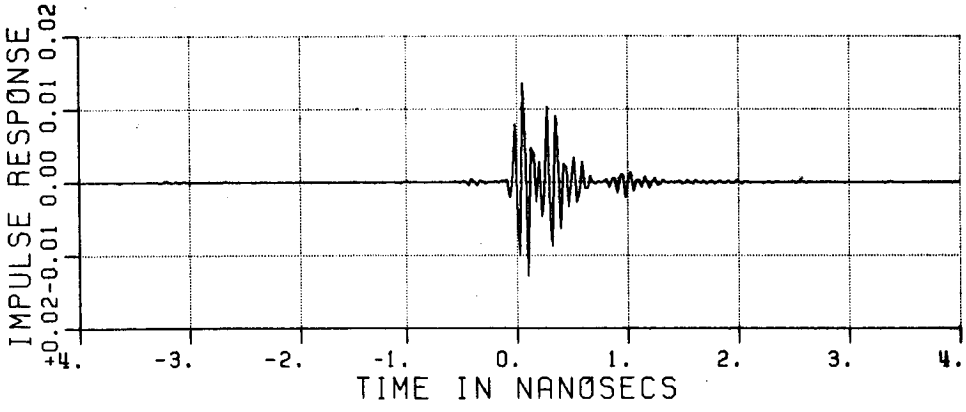

c) Measured result

Figure 5.77. Time domain plots of CONF11E: X=7",Y=-7",Z=-2"; VP.

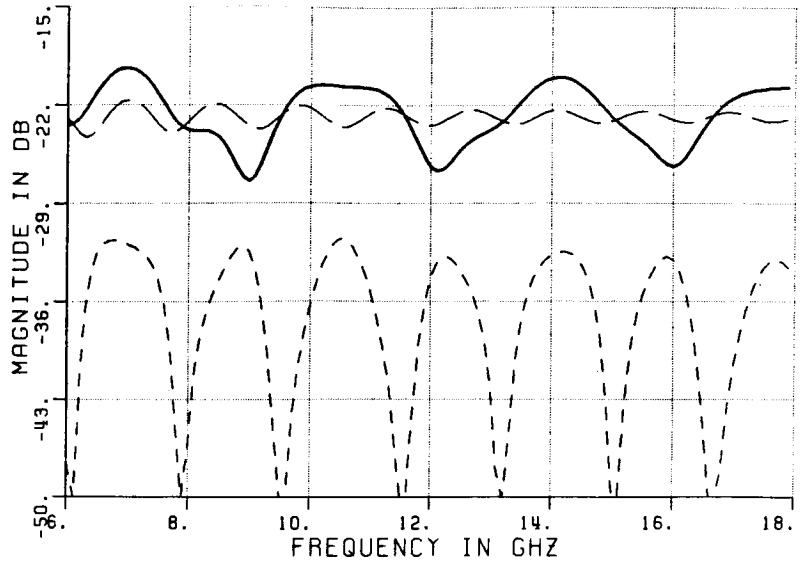

a) calculated result

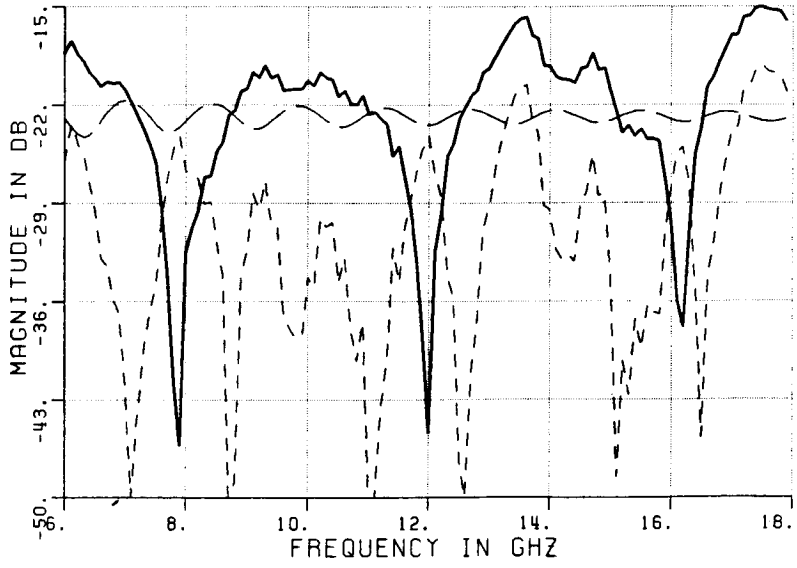

b) measured result

Figure 5.78. Frequency domain plots of CONF11E: X=7",Y=-7",Z=-2"; VP.

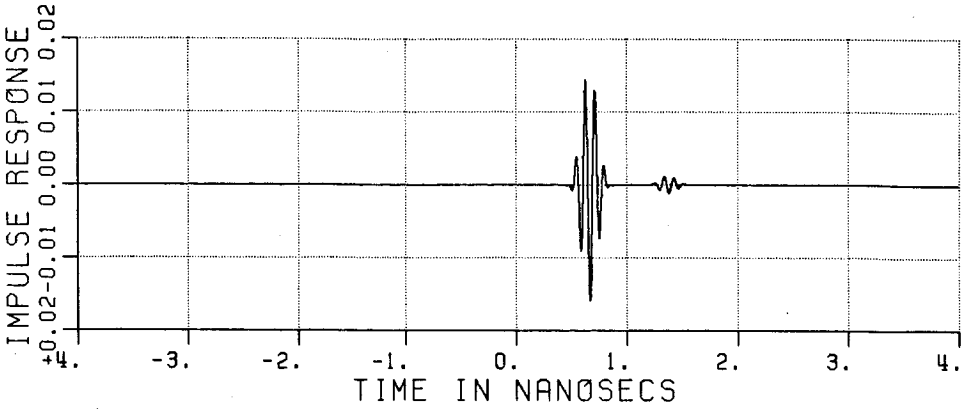

a) Exact sphere

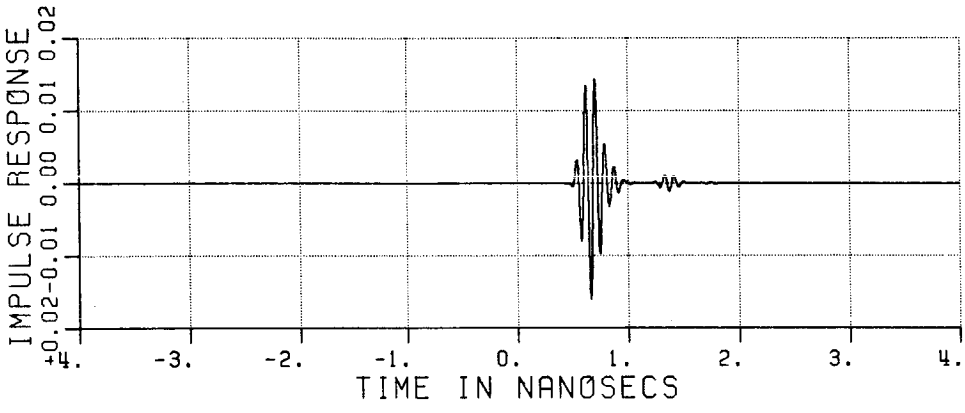

b) Calculated result

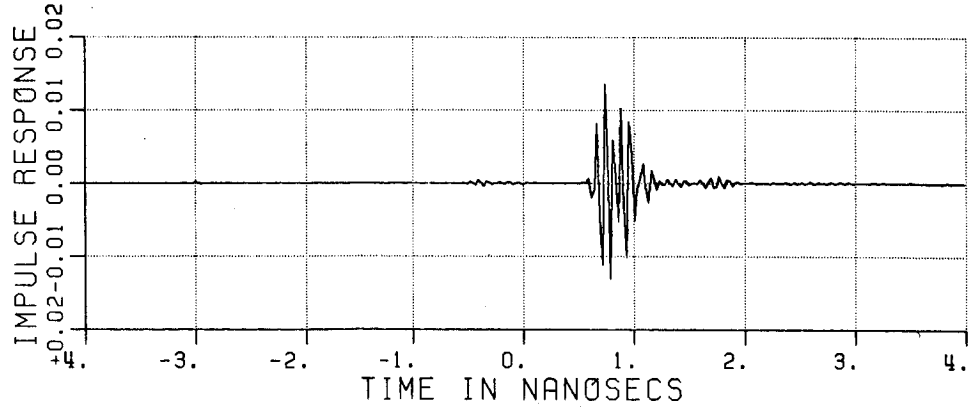

c) Measured result

Figure 5.79. Time domain plots of CONF12E: X=12",Y=-7",Z=-2"; VP.

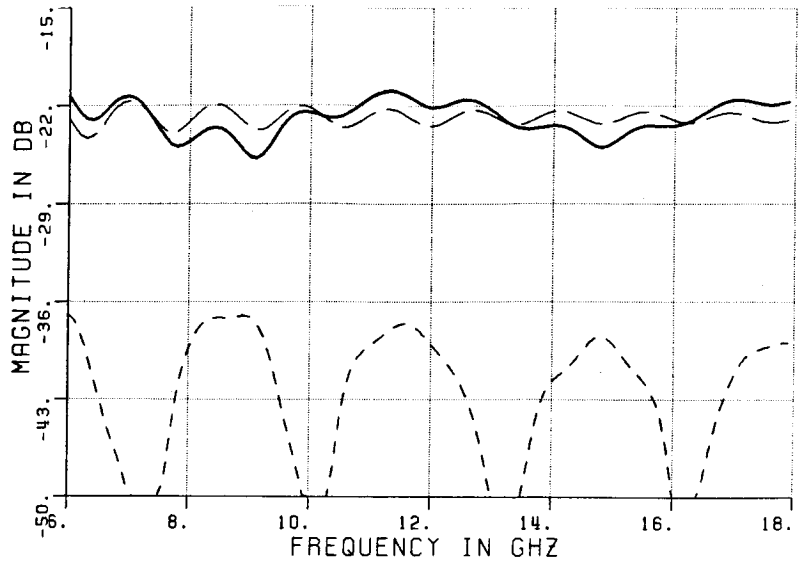

a) calculated result

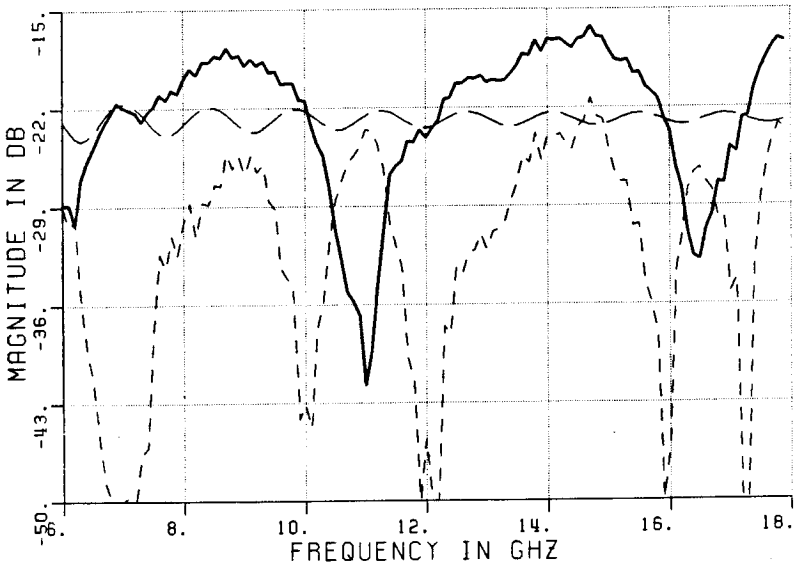

b) measured result

Figure 5.80. Frequency domain plots of CONF12E: X=12",Y=-7",Z=-2"; VP.

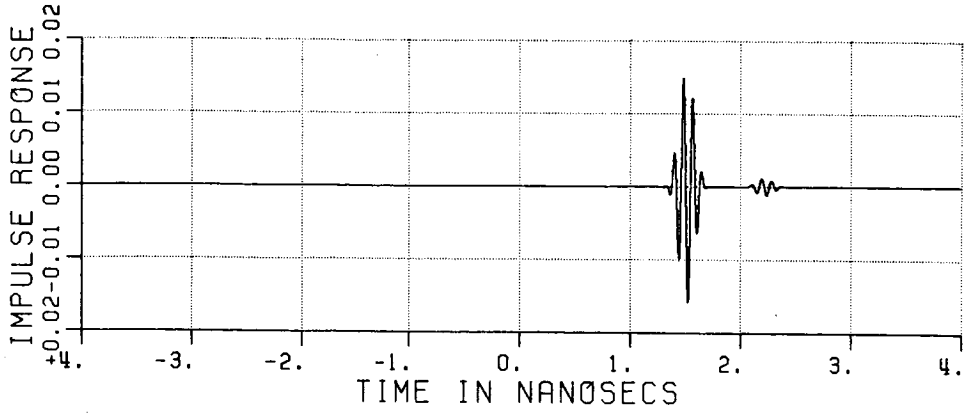

a) Exact sphere

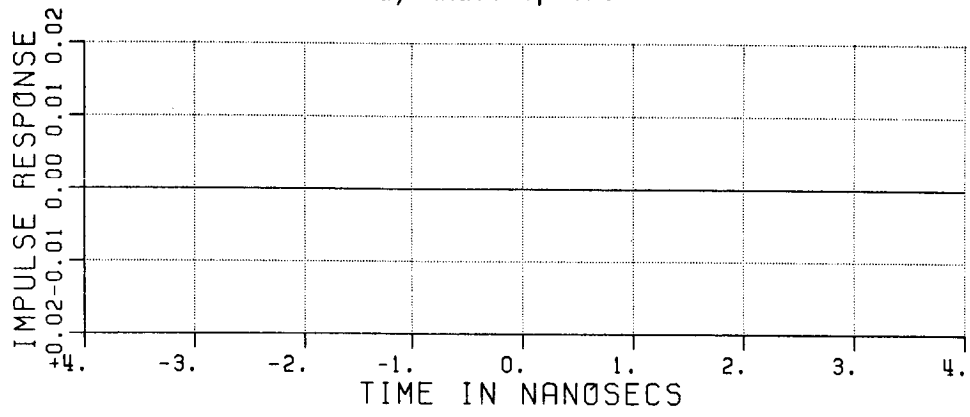

b) Calculated result

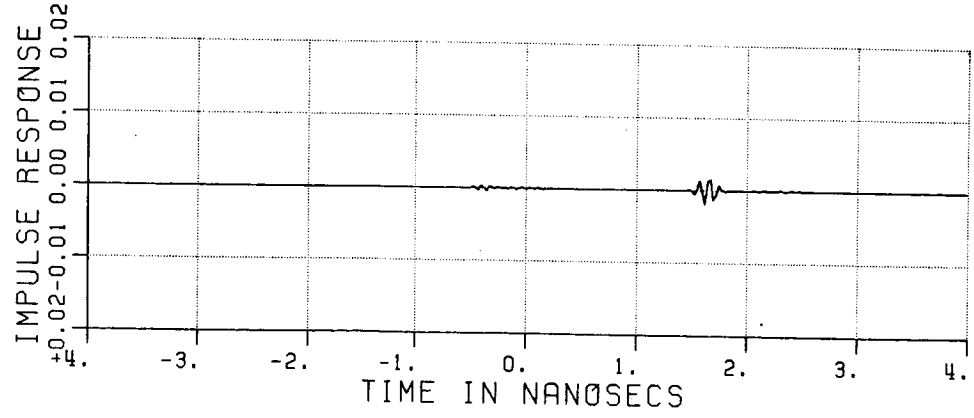

c) Measured result

Figure 5.81. Time domain plots of CONF13E: X=17",Y=0",Z=-2"; VP.

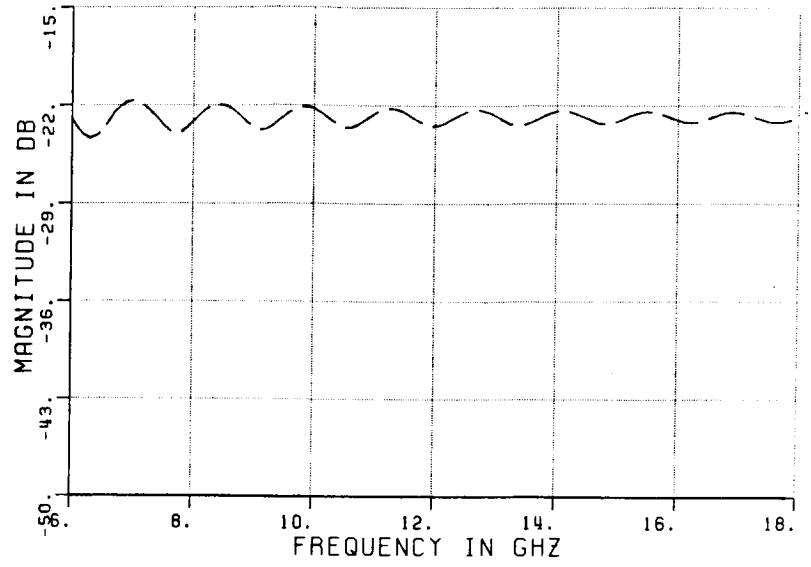

a) calculated result

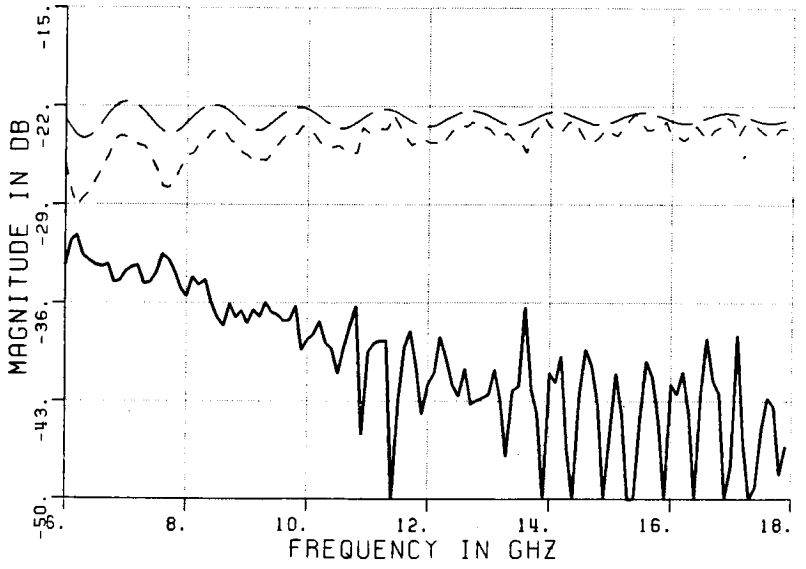

b) measured result

Figure 5.82. Frequency domain plots of CONF13E: X=17",Y=0",Z=-2"; VP.

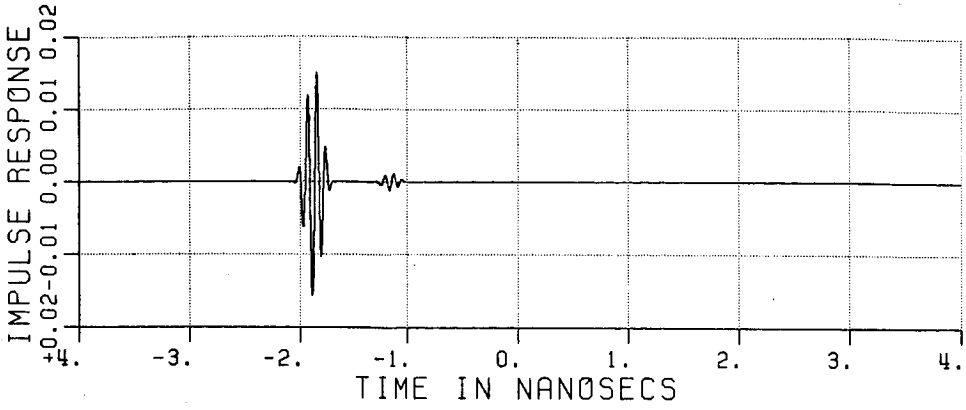

a) Exact sphere

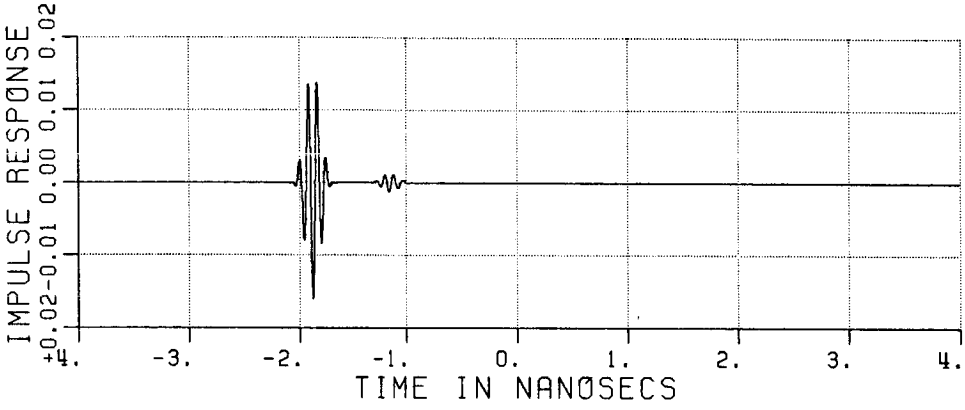

b) Calculated result

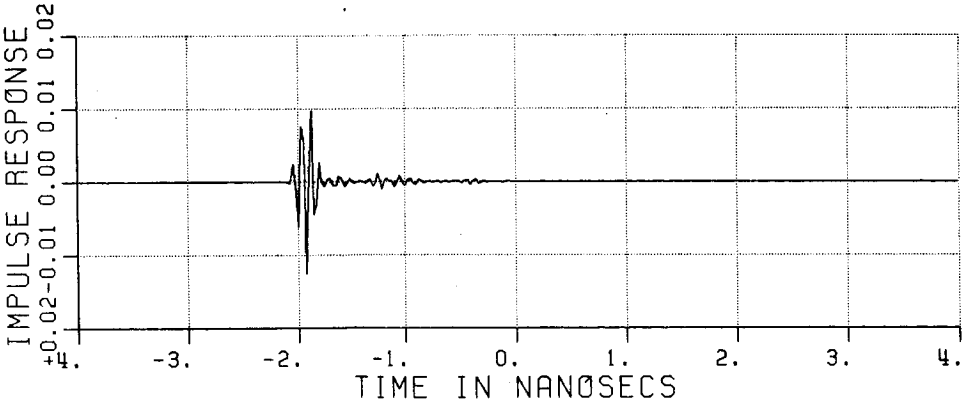

c) Measured result

Figure 5.83. Time domain plots of CONF9F: X=-3",Y=0",Z=-2"; HP.

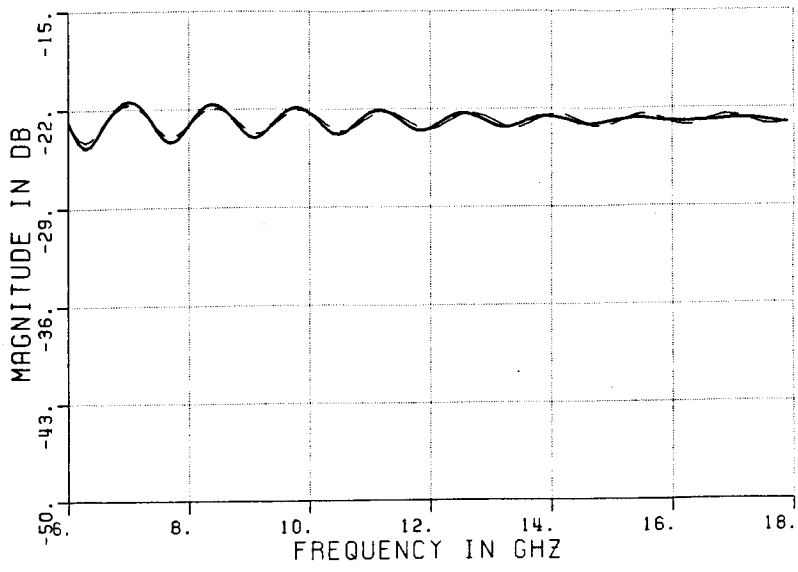

a) calculated result

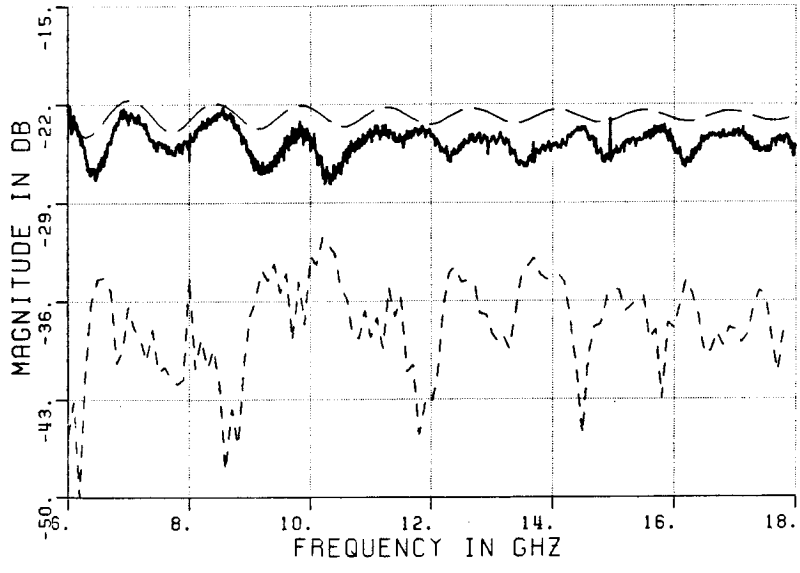

b) measured result

Figure 5.84. Frequency domain plots of CONF9F: X=-3",Y=0",Z=-2"; HP.

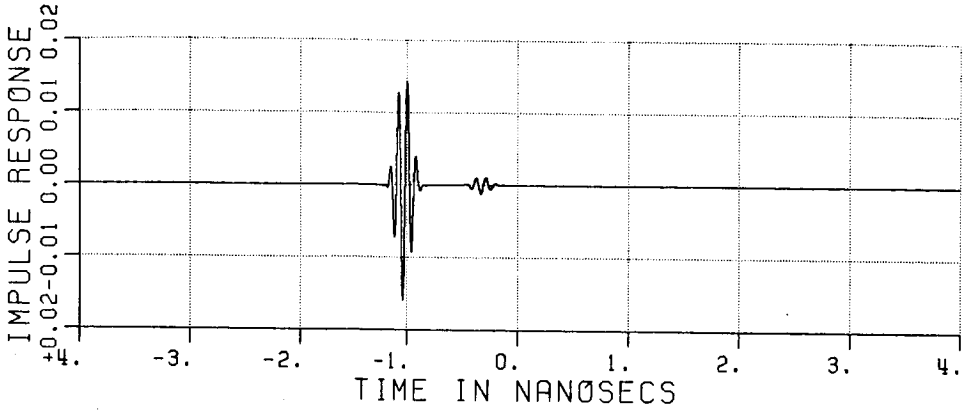

a) Exact sphere

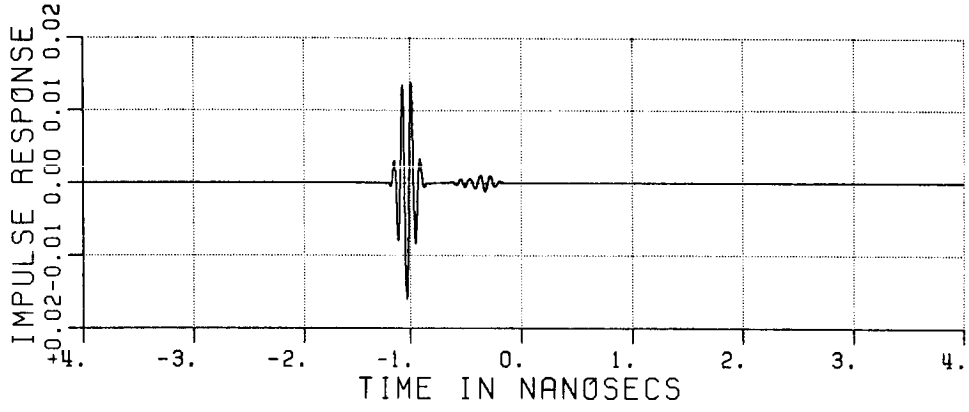

b) Calculated result

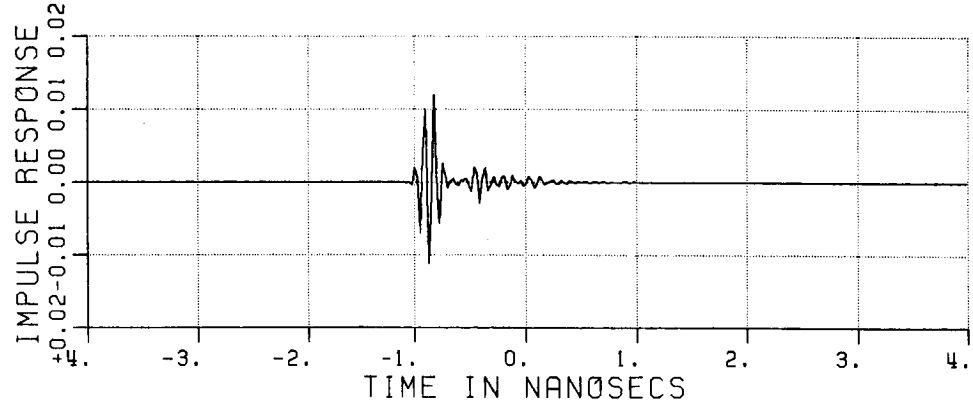

c) Measured result

Figure 5.85. Time domain plots of CONF10F: X=2",Y=-7",Z=-2"; HP.

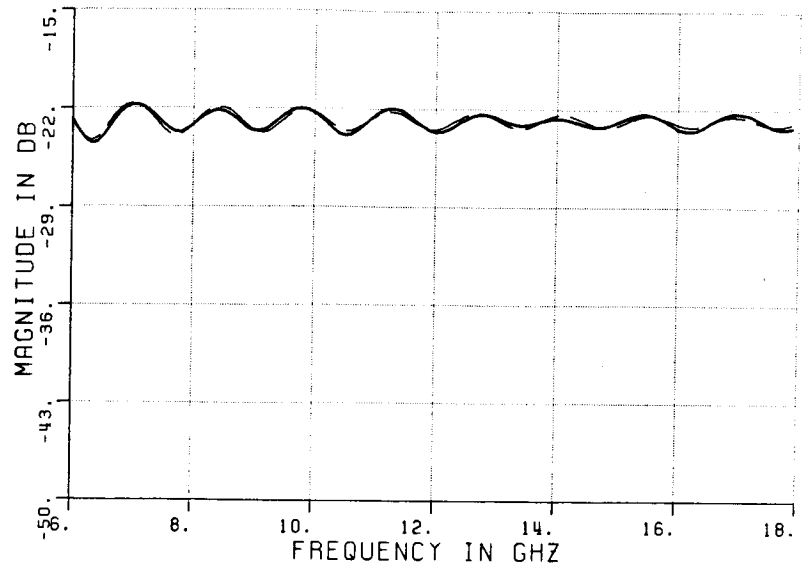

a) calculated result

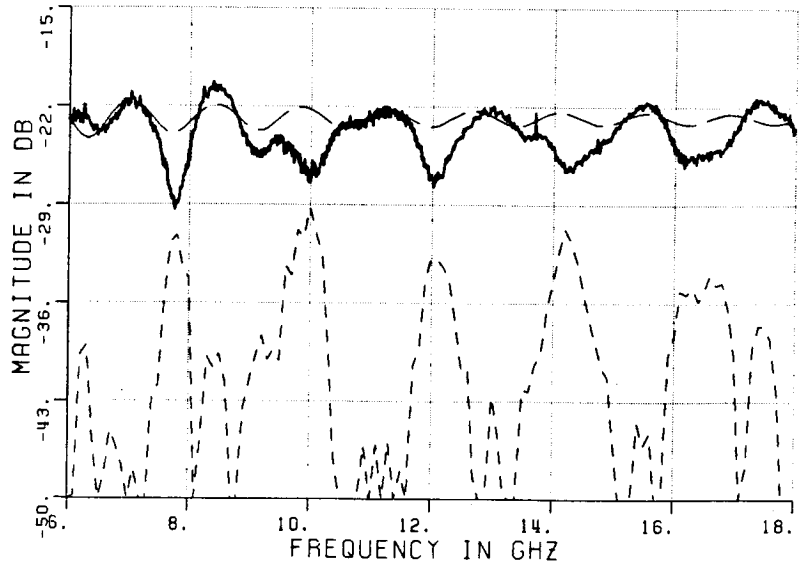

b) measured result

Figure 5.86. Frequency domain plots of CONF10F: X=2",Y=-7",Z=-2"; HP.

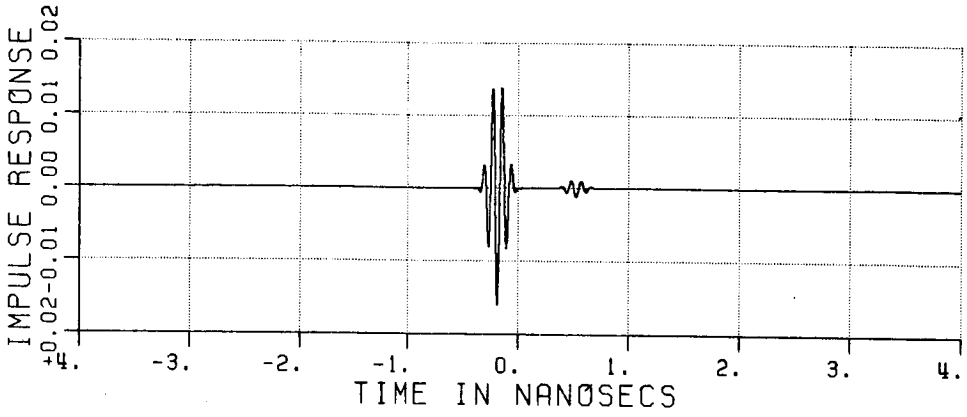

a) Exact sphere

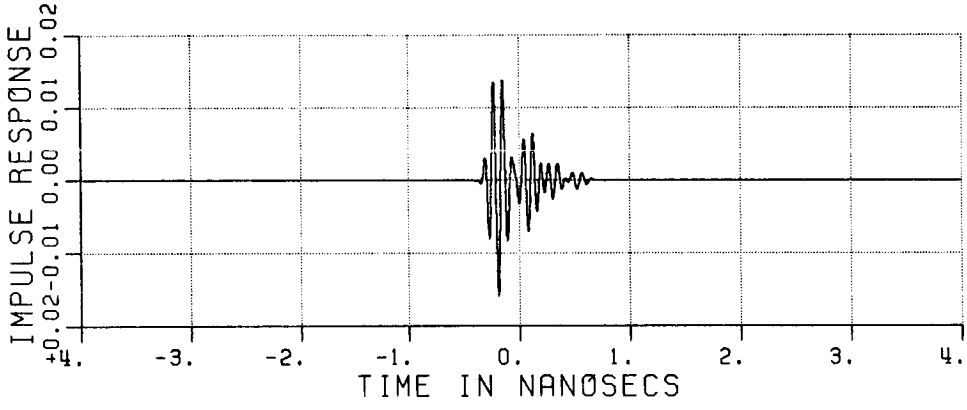

b) Calculated result

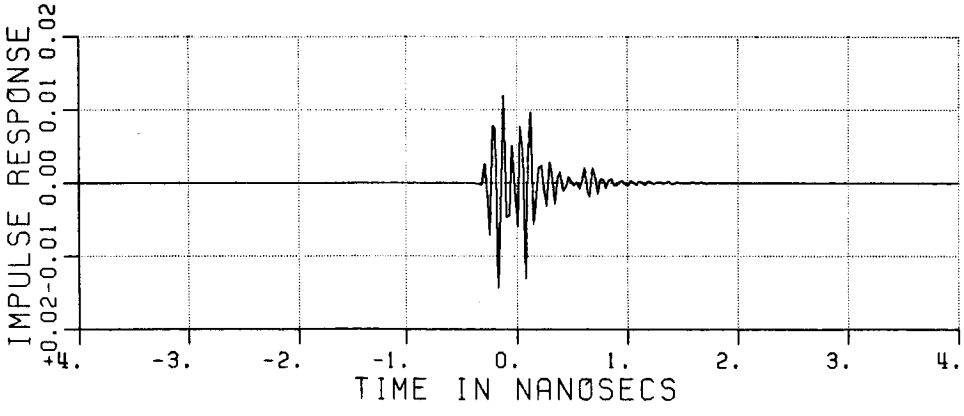

c) Measured result

Figure 5.87. Time domain plots of CONF11F: X=7",Y=-7",Z=-2"; HP.

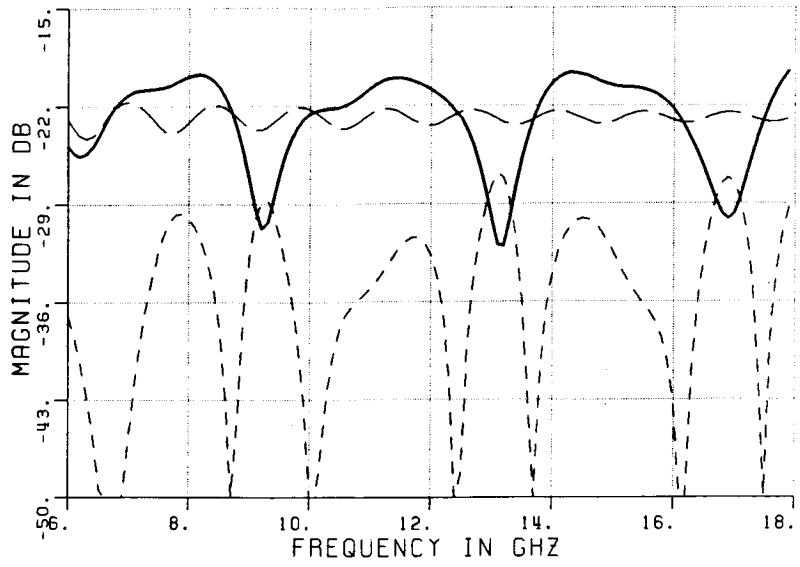

a) calculated result

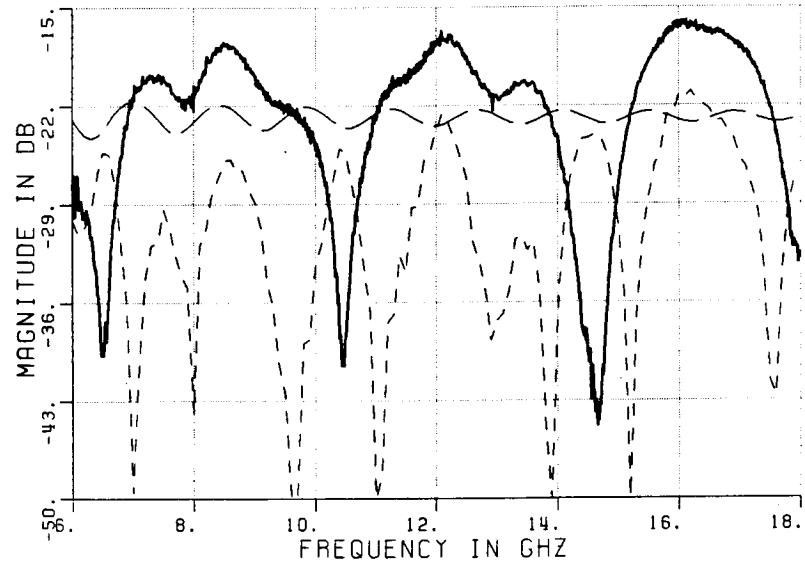

b) measured result

Figure 5.88. Frequency domain plots of CONF11F: X=7",Y=-7",Z=-2"; HP.

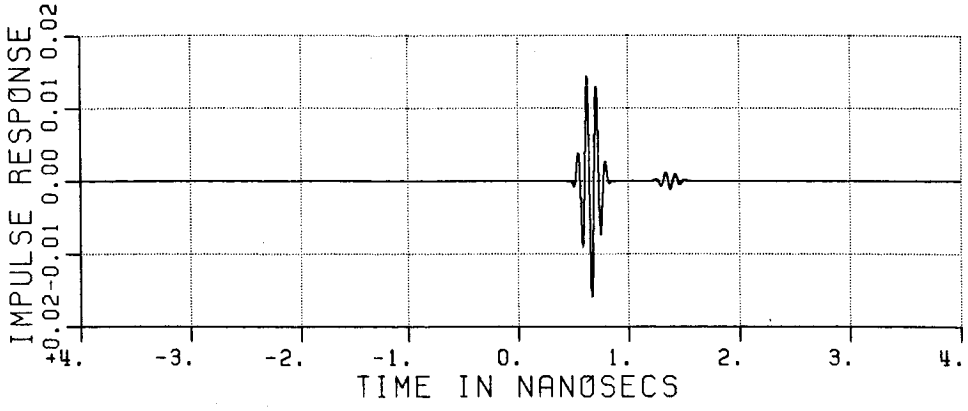

a) Exact sphere

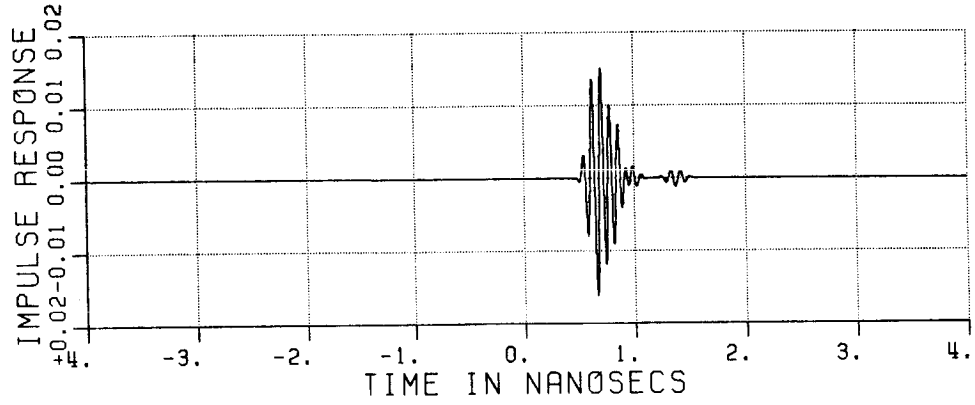

b) Calculated result

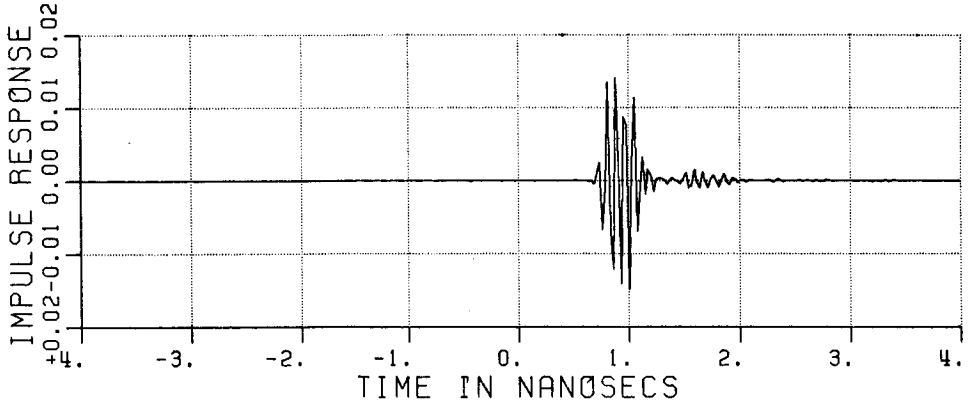

c) Measured result

Figure 5.89. Time domain plots of CONF12F: X=12",Y=-7",Z=-2"; HP.

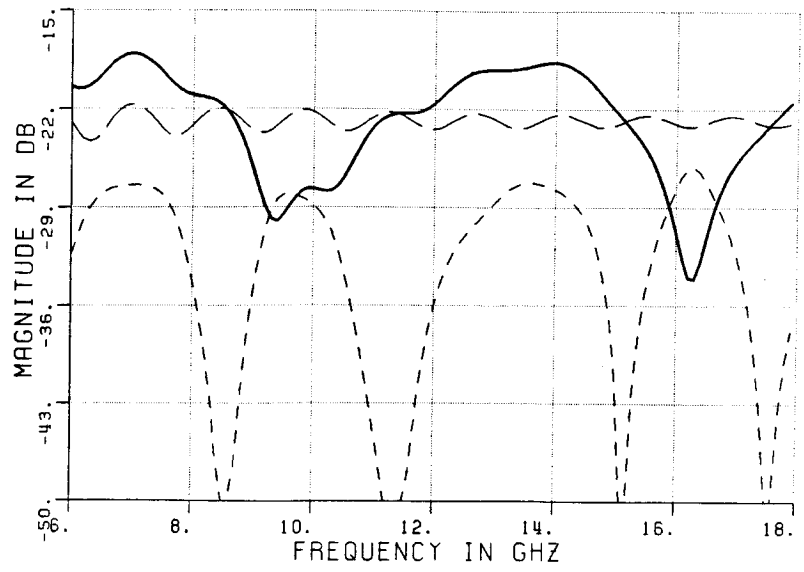

a) calculated result

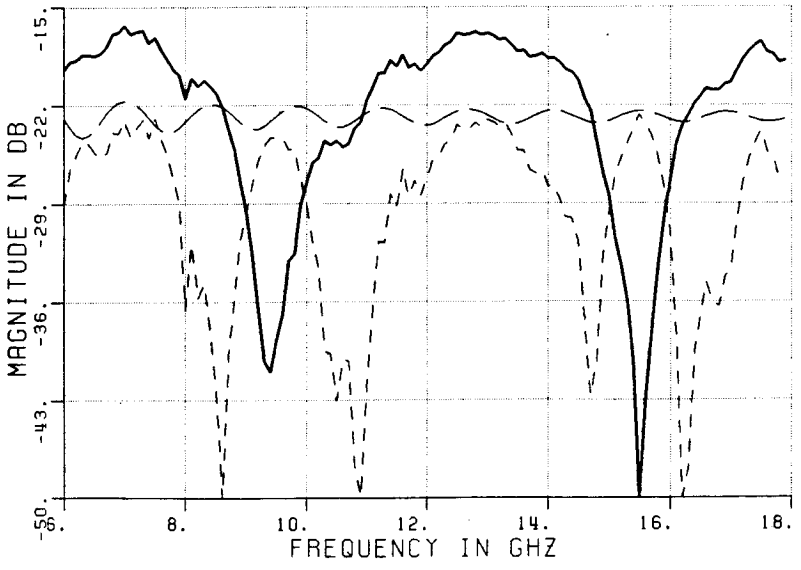

b) measured result

Figure 5.90. Frequency domain plots of CONF12F: X=12",Y=-7",Z=-2"; HP.

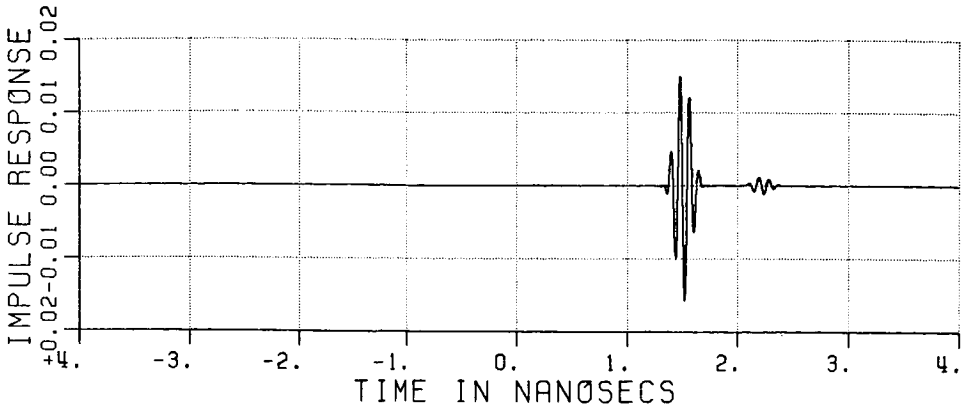

a) Exact sphere

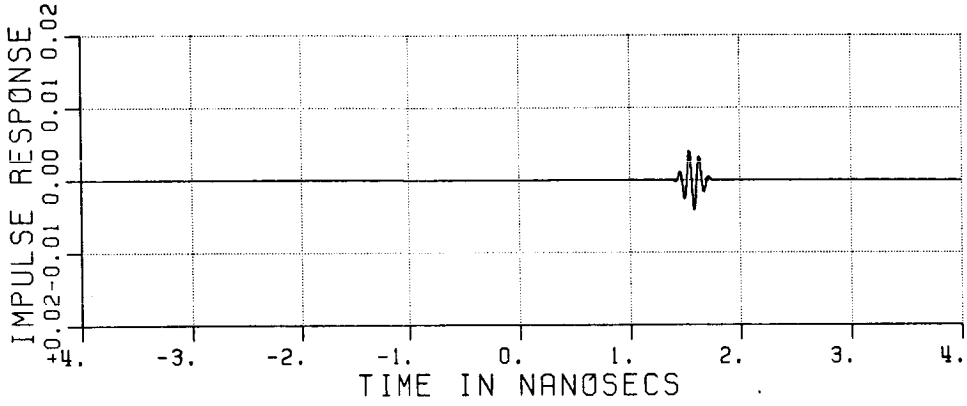

b) Calculated result

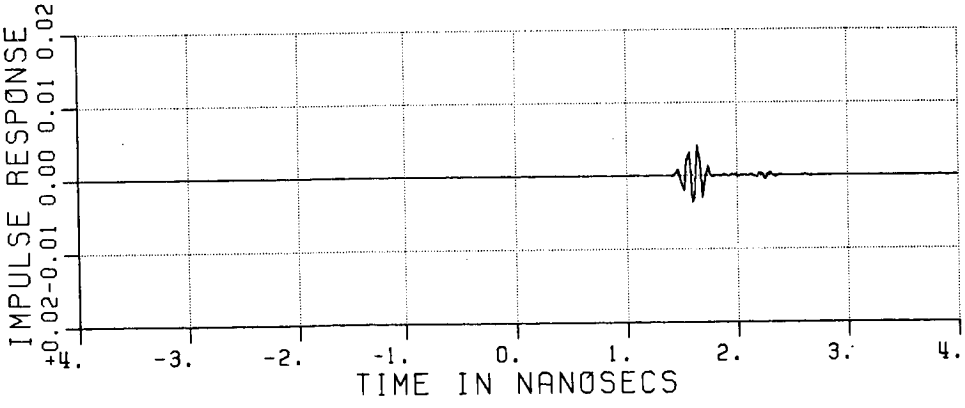

c) Measured result

Figure 5.91. Time domain plots of CONF13F: X=17",Y=0",Z=-2"; HP.

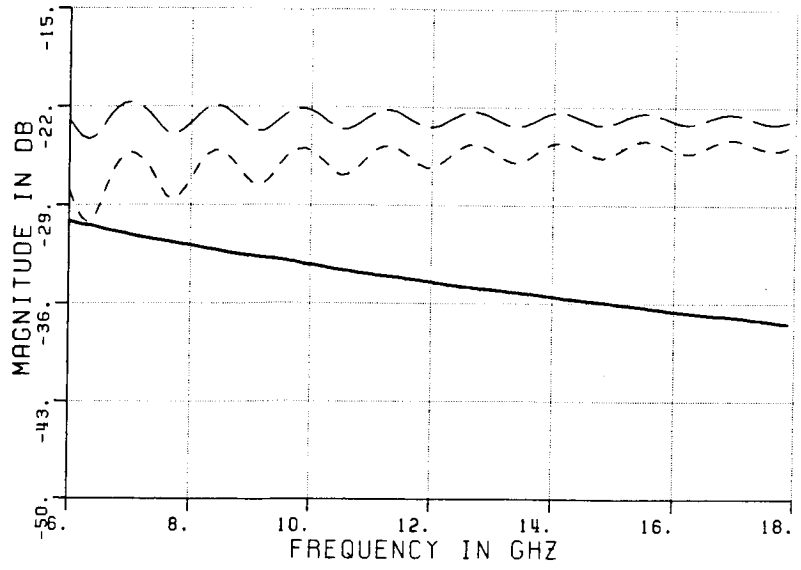

a) calculated result

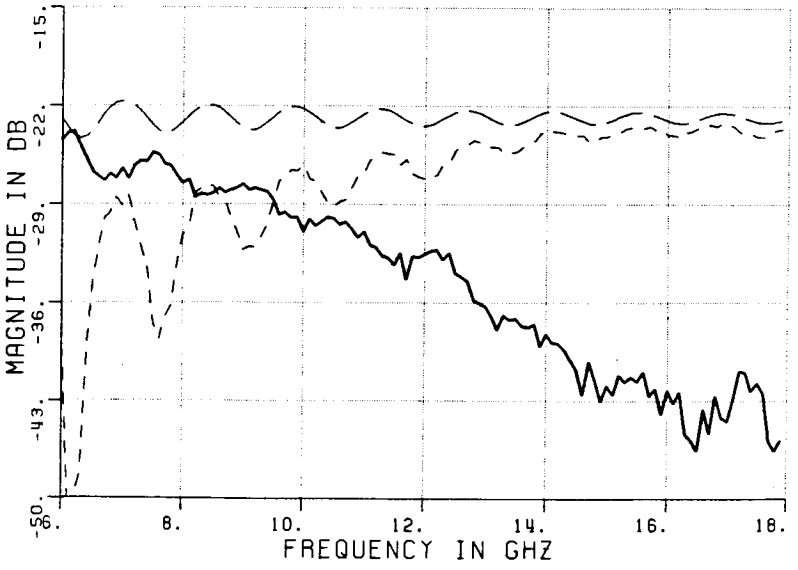

b) measured result

Figure 5.92. Frequency domain plots of CONF13F: X=17",Y=0",Z=-2"; HP.

E. FIELD QUALITY AROUND PEDESTAL

Now that it has been shown that the UTD analysis is reliable enough, let us predict the probed field strength around the pedestal by doing azimuth scans at different levels and frequencies. Azimuth scans around the vertical at a 12" radius for heights of -2", 3", 6" and 9" relative to the top of the pedestal are shown in Figure 5.93 to 5.98, respectively. Note that these results indicate the same conclusions as those obtained in the previous section. Even at 9" above the top of the pedestal, the field variation is about a dB at positions behind the pedestal top.

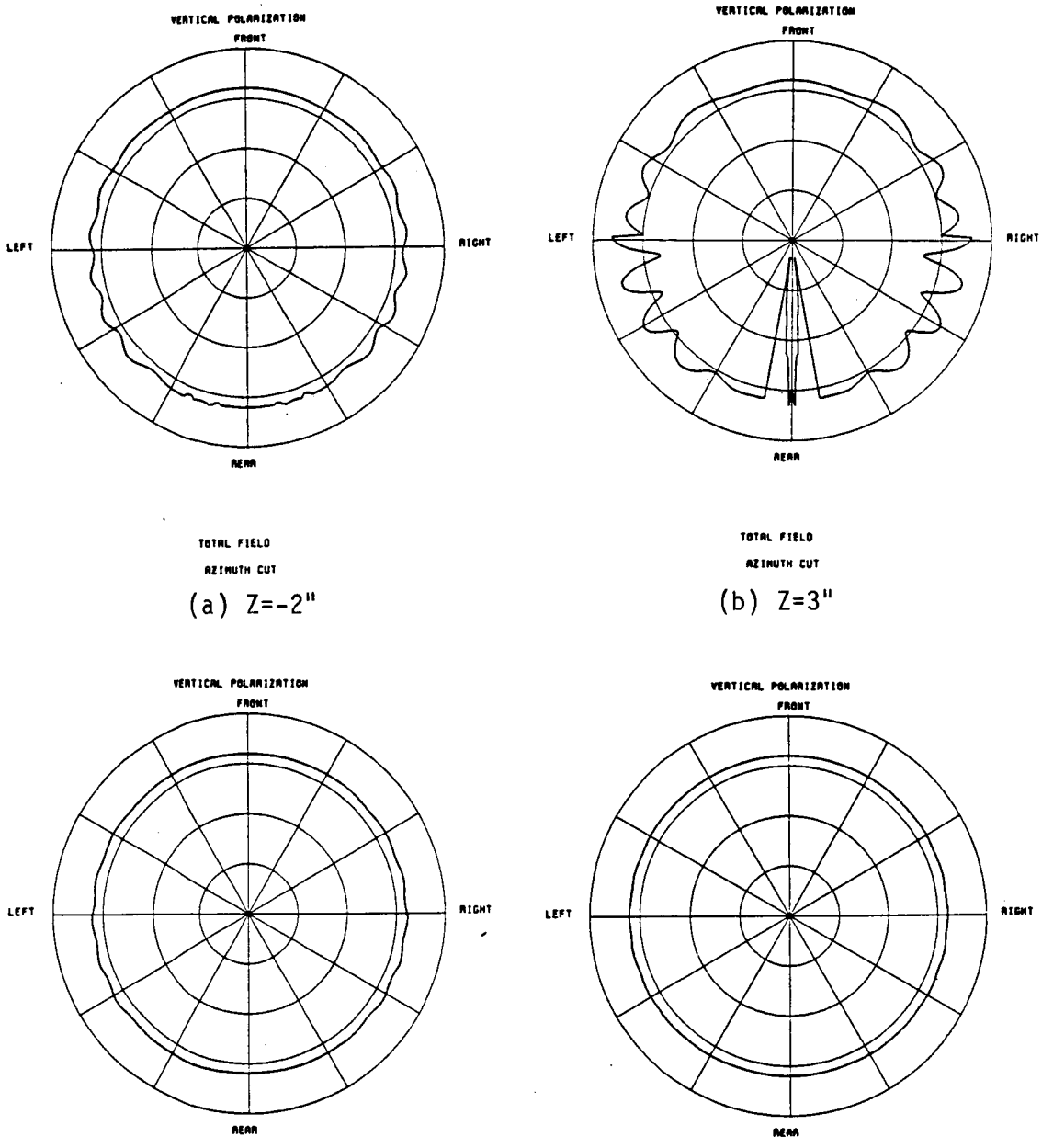

Figure 5.93. Aspect angle scan of backscatter field at 6 GHz, vertical polarization.

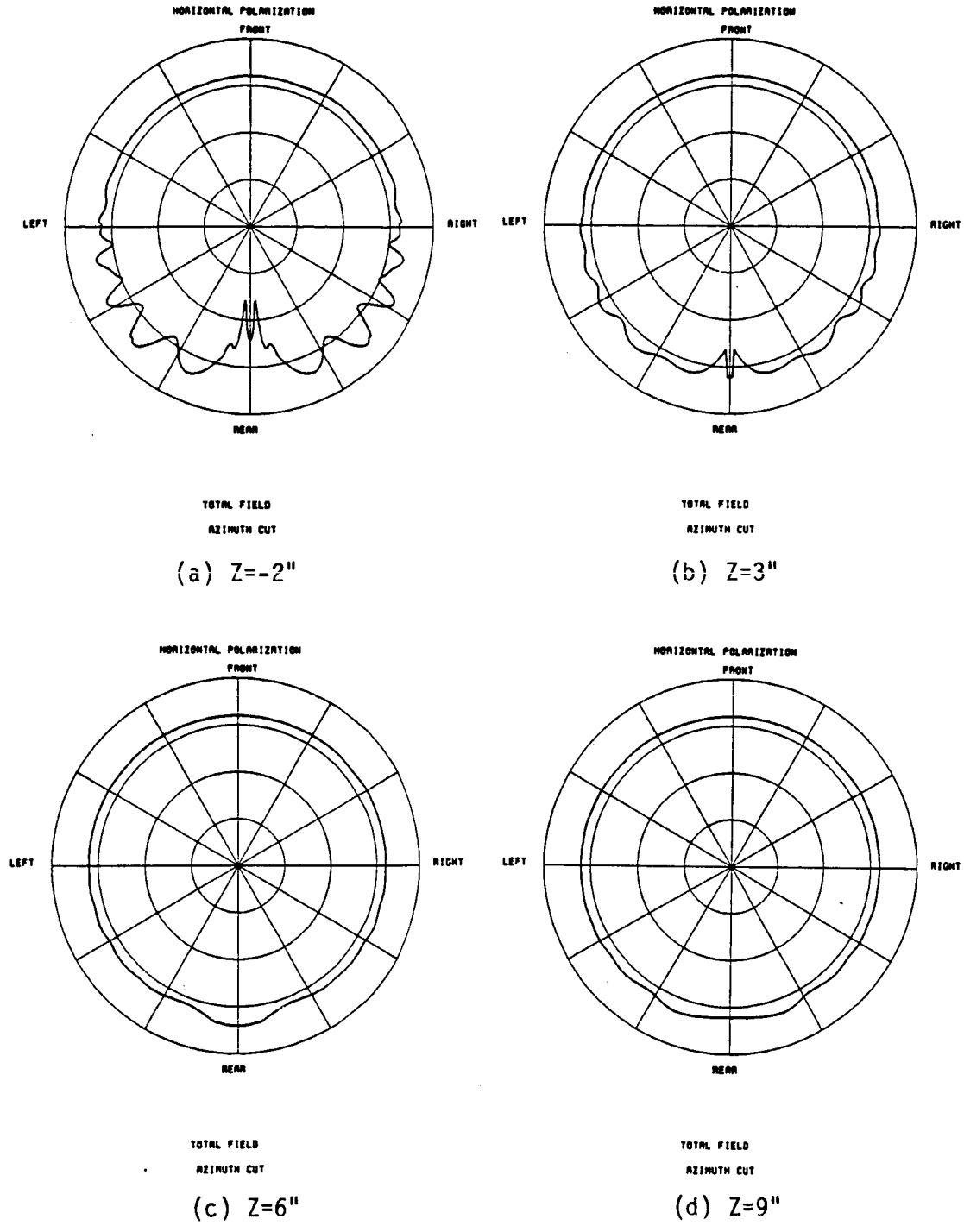

Figure 5.94. Aspect angle scan of backscatter field at 6 GHz, horizontal polarization.

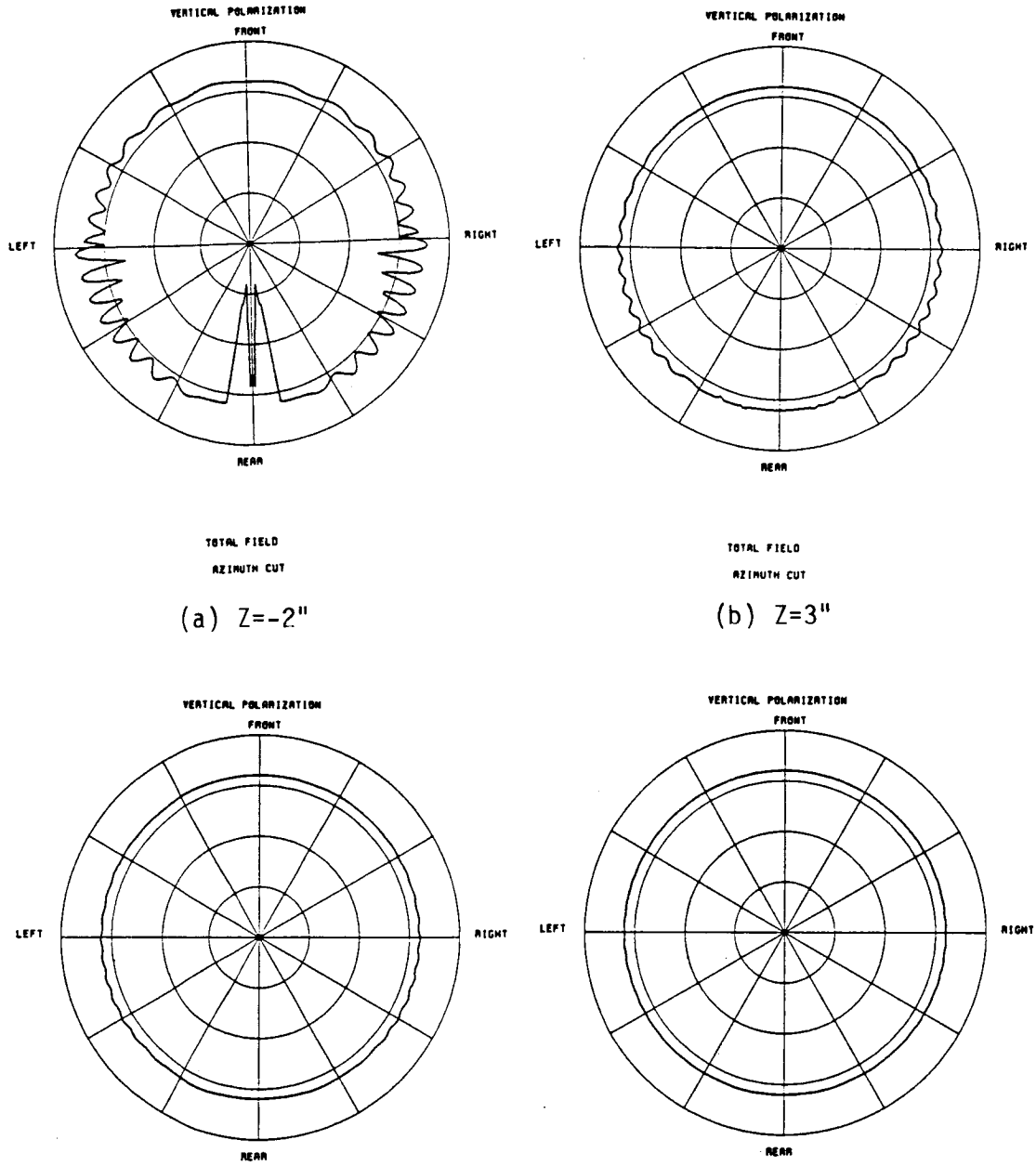

Figure 5.95. Aspect angle scan of backscatter field at 12 GHz, vertical polarization.

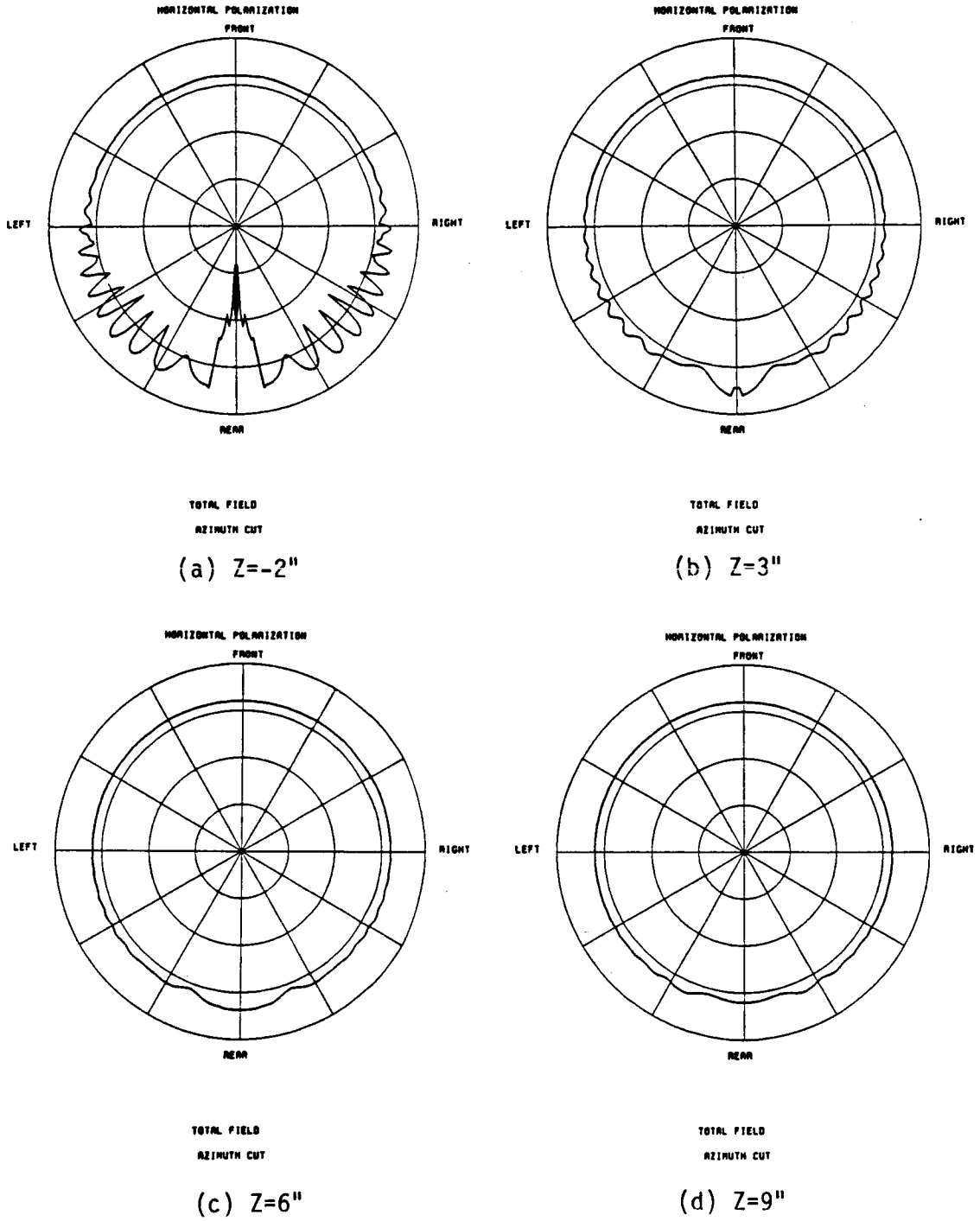

Figure 5.96. Aspect angle scan of backscatter field at 12 GHz, horizontal polarization.

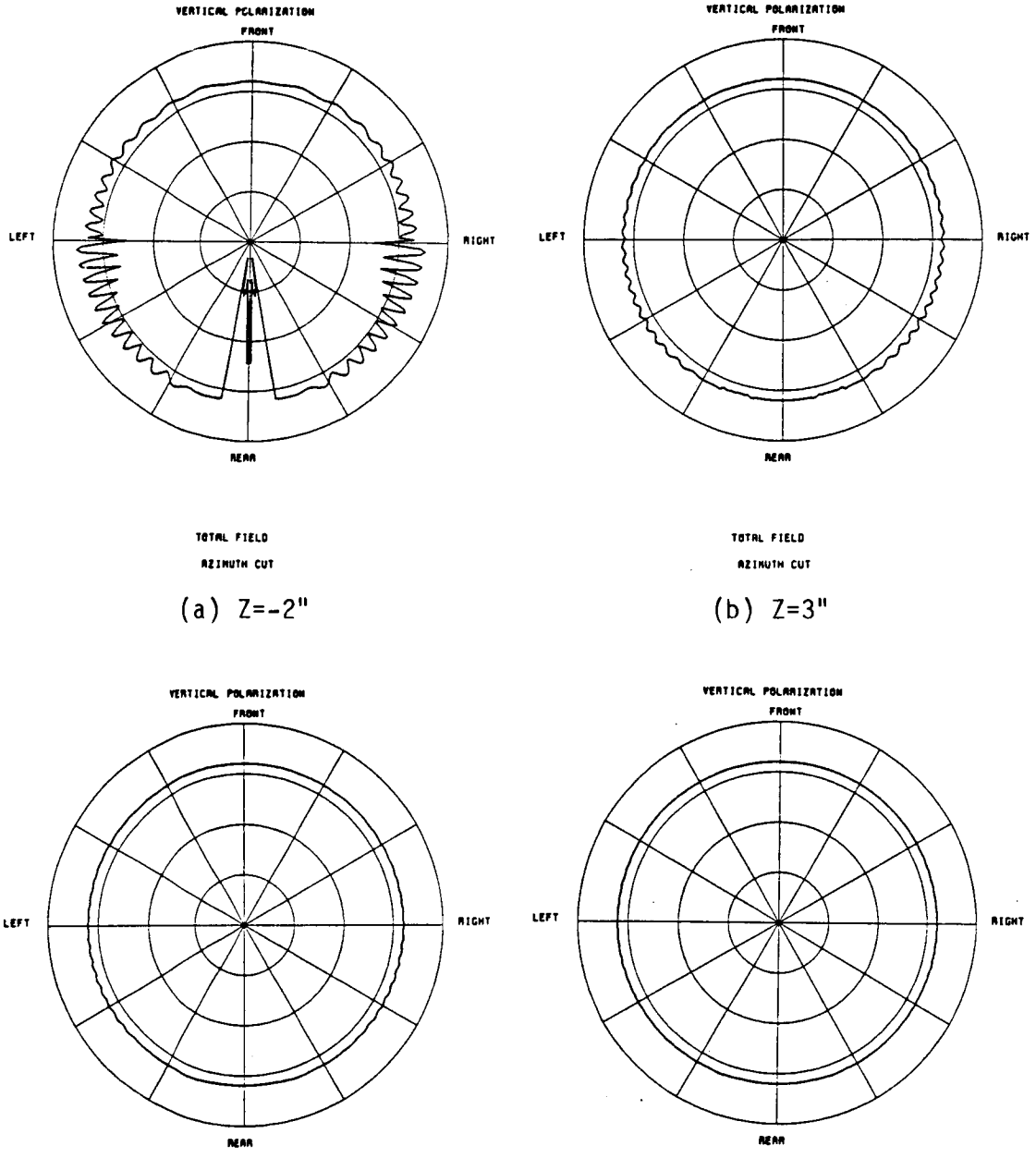

Figure 5.97. Aspect angle scan of backscatter field at 18 GHz, vertical polarization.

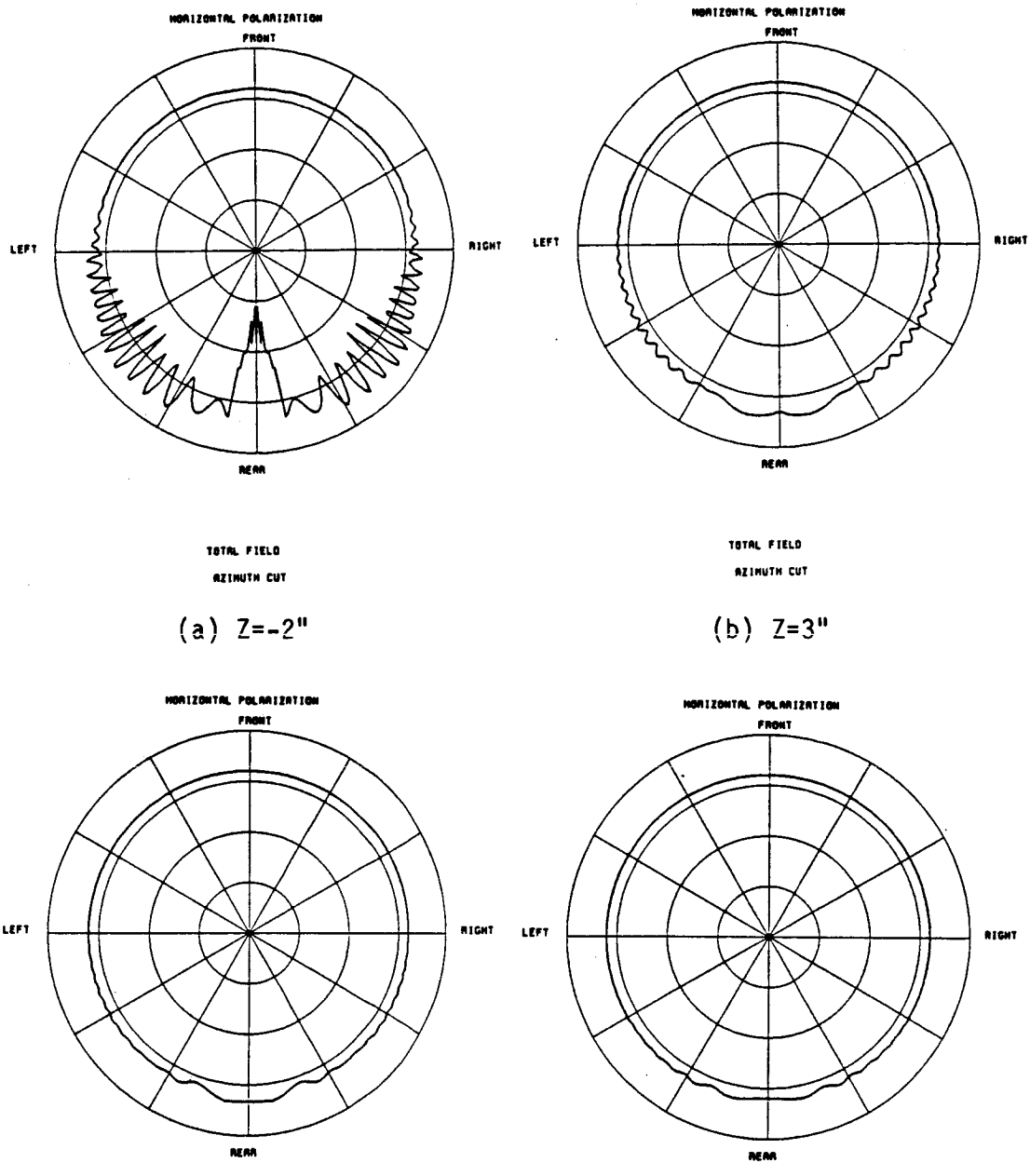

Figure 5.98. Aspect angle scan of backscatter field at 18 GHz, horizontal polarization.

CHAPTER VI

SUMMARY AND CONCLUSIONS

A. SUMMARY

The ogive pedestal scattering was analysed for three cases: direct backscattered field, bistatic scattered field structure, and target/pedestal multiple scattering. This study attempts to evaluate the various ways that the metal conical ogive mount can affect the performance of a high quality RCS measurement system. The second case was a purely theoretical study; however, the first and the last cases are supported by measurements which show very good comparison with the theoretical calculations provided the uniform geometrical theory of diffraction (UTD) solution is valid.

The direct backscatter analysis (Chapter III) showed that the RCS of a pedestal depends on the way the target is mounted (elevated or flush), on the geometry of the pedestal (angle of inclination and wedge angle), and on the frequency of the incoming wave. It was interesting to learn that the pedestal RCS doubled if the target is mounted flush to the top of the pedestal; provided of course, that the target/pedestal junction is directly visible. Based on the UTD analysis, the pedestal RCS can be controlled to some degree by decreasing its inclination angle, decreasing its wedge angle or increasing the frequency.

The bistatic field structure analysis(Chapter IV) showed how the field around the pedestal is affected by various scattering mechanisms. The UTD was used for this analysis; however, limitations of UTD were encountered but judged to be acceptable since they only occurred in a small region at the back of the pedestal. With this in mind, the field structure above the pedestal was calculated at different heights to see how far above the pedestal one needed to go to obtain a nearly uniform plane wave illumination of the target.

The backscatter field structure analysis (Chapter V) compares the calculated backscatter field from a 3.2" test sphere with measurements. Various postions above and below the top of the pedestal were probed to demonstrate the validity of the theoretical approach, which was then used to predict backscatter field at various heights above the pedestal.

From these analyses, it was obvious that any region below and just above the top of the pedestal was not a good place to locate the target. If the target stays below the pedestal, it would encounter an incident field structure such as that shown in Figure 4.17 which is not very desirable. If the target is right on top of the pedestal one has a case of flush mounting which increases the RCS of the pedestal and thus decreases the signal-to-clutter ratio of the whole experimental set-up. If the target is slightly above the pedestal, the interaction between the target and the top of the pedestal is horrible as one can see in Figures 5.93 to 5.98. To avoid all these problems, one should mount the target well above the top of the pedestal if a metal ogive is used. From Figures 4.34 and 4.35 one observes that the bistatic field is

"almost plane" for Z > 6 inches. Also from Figures 5.93 to 5.98, one observes that the target/pedestal interaction is small (lobes less than 1 dB) for Z > 6 inches. Therefore, it is concluded that an elevation of z > 6 inches is necessary for good results provided a completely metal pedestal is used to support the target.

B. RECOMMENDATIONS

Unfortunately, there is one thing that has been neglected all along. How does one hold the target above the pedestal without creating another scattering problem? If a light target is studied, one can use a styrofoam post; however, a metal support is needed for a heavy structure. Although these additional components will further perturb the field, they were not included in our theoretical calculations because such an analysis was beyond the scope of this study. It is clear that more work needs to be done in this whole area, and one must incorporate absorber as part of the solution. Without going into the absorber analysis, it is quite clear that the absorber must be at least 20 dB effective at reducing the reflection coefficient over the whole frequency band of interest. If the absorber is not that effective, certain frequency results will be corrupted by the pedestal scattering. If simultaneously the target has scattering down below the top of the pedestal, these errors could be detrimental. This situation seems very gloomy; however, recent work at OSU has indicated that absorber caps made out of broadband foam absorber can be used to reduce the pedestal and pedestal/target scattering levels.

Since the center issue is to isolate the pedestal from the target so that the pedestal is invisible to the target, one needs an absorber cap on top of the pedestal. To date, one absorber cap that follows the shape of the pedestal was designed by Allen Dominek [6] at OSU as shown in Figure 6.1. It reduces a lot of interaction between the target and the top of the pedestal, but it has two problems. First, the hole at the center where one place the mounting rod allows a wave to go down and reflect back up as shown in Figure 6.2. Second the shape of the cap produces a shadow region behind the absorber structure which masks scattering centers directly behind it. In addition, the absorber structure causes a diffracted field which is still capable of perturbing the field above the pedestal as shown in Figure 6.3. This is contrasted with shadow boundary created by a smooth surface as shown in Figure 6.4. The creeping wave field that smooths out this discontinuity does not affect the field above the pedestal. Recently, another cap is designed by Dennie Burnside [7] at OSU which attempts to correct these problems and also adds many desirable features to the experimental set-up. The cap, as shown in Figure 6.5, is called a Robin's head because it has the shape of a bird's beak. It has six nice features as follows:

1) a high angle of inclination to minimize the radar cross-section of the pedestal.

2) a ridge-type top so that incoming waves would be reflected to the side.

3) a thick top so that downward scattering by the target would be heavily attenuated.

4) a smoothly curved tail so that the discontinuity behind the absorber is corrected by a creeping wave which minimizes the field above the cap.

5) thick side walls so that the target cannot interact with the side edges or faces near the top of the pedestal.

6) the styrofoam mount is loaded at the bottom with a conical absorber load so that any downward reflection from the target into the center hole would be reflected sideway and attenuated by the absorber cap.

A pertinent second step would therefore be the probing of Dominek's absorber cap to verify the existence of the two problems as well as Robin's head to verify the usefulness of the six features suggested above. This will be done in a future study.

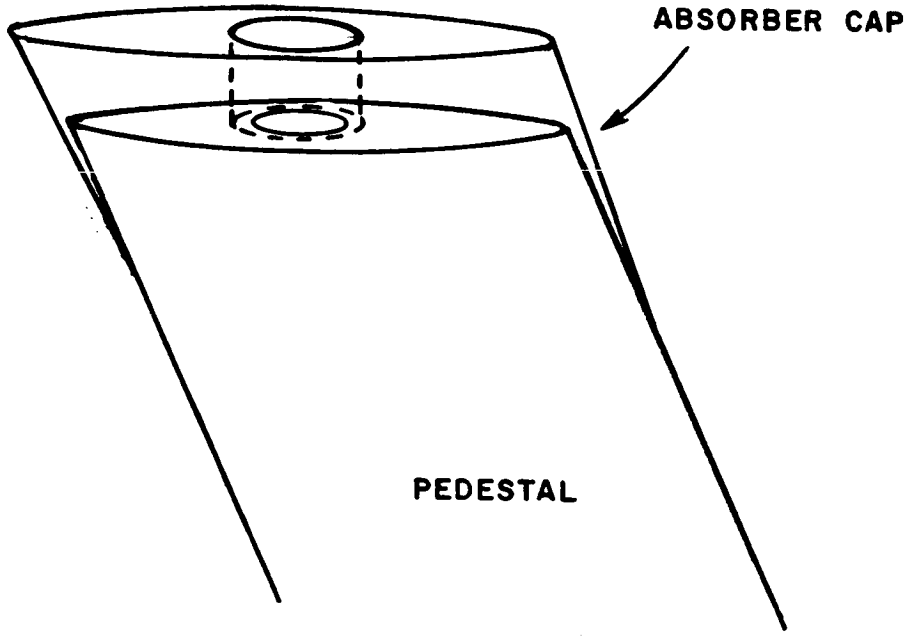

Figure 6.1. Dominek's absorber cap.

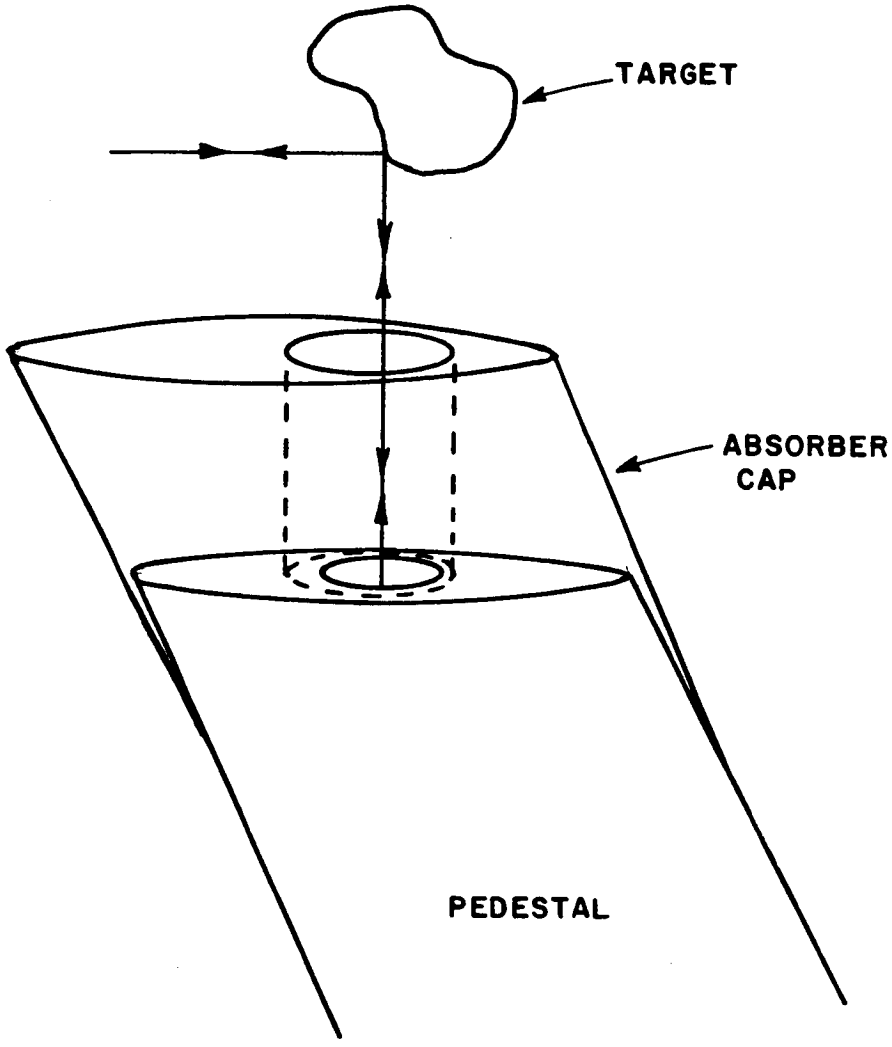

Figure 6.2. Problems with the center hole.

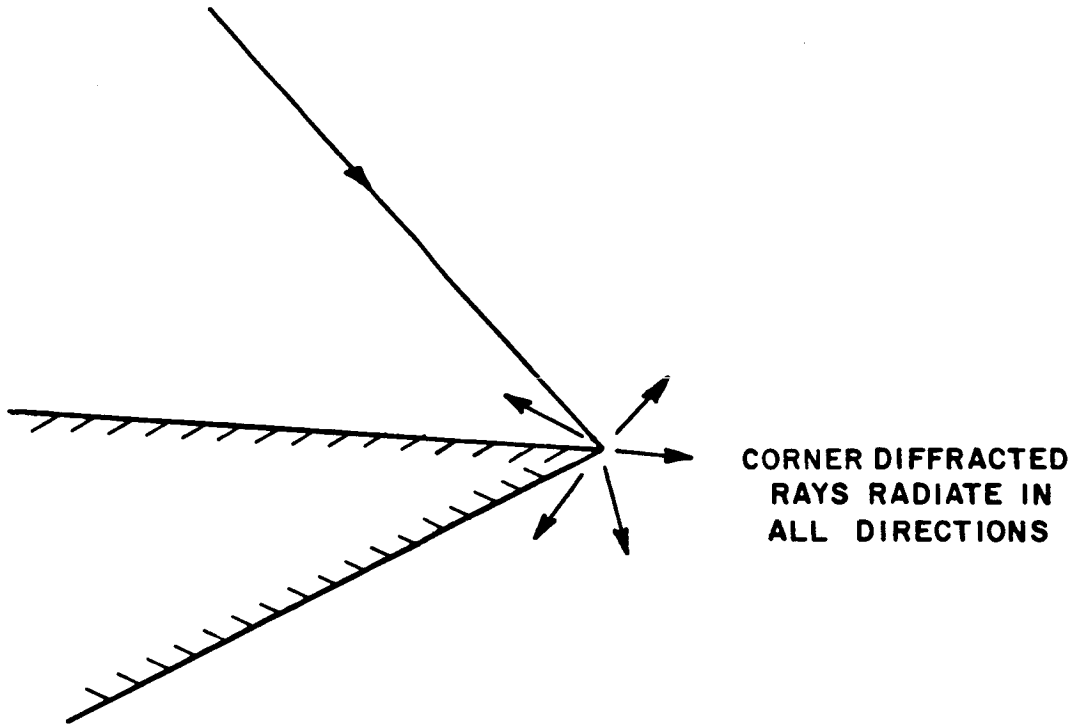

Figure 6.3. Characteristics of shadow boundary created by a corner.

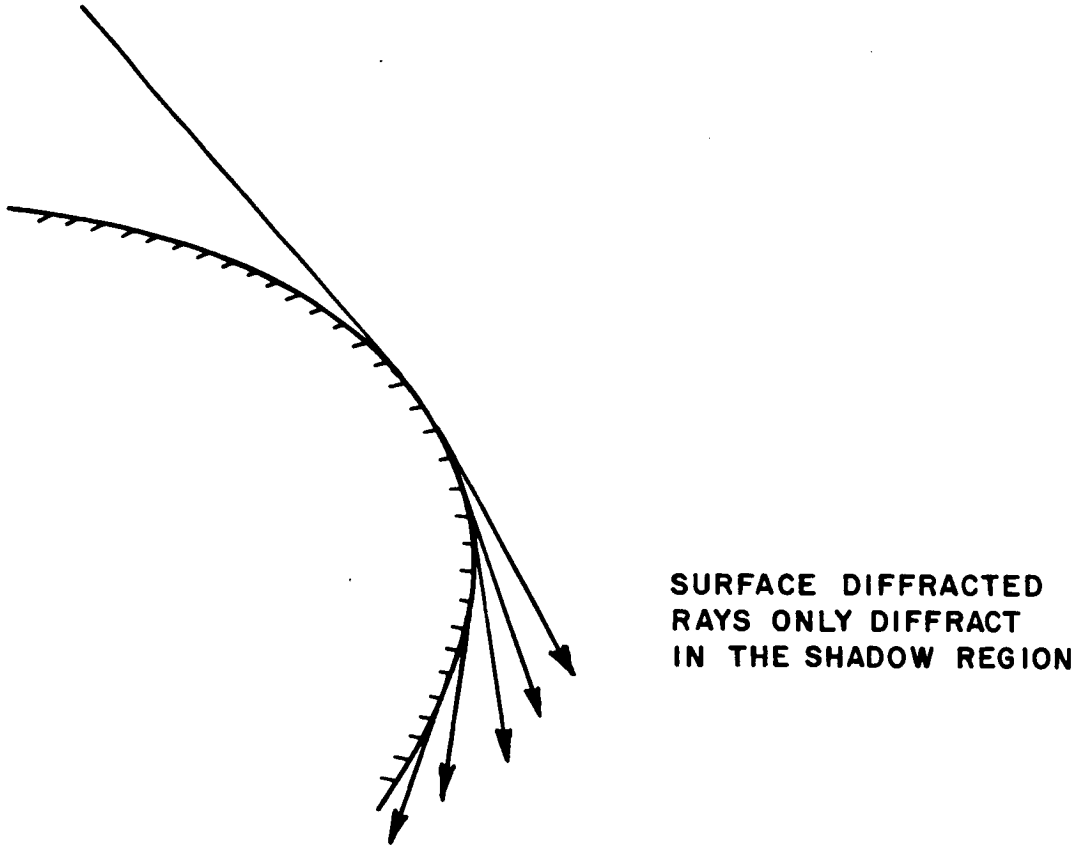

Figure 6.4. Characteristics of shadow boundary created by curve surface.

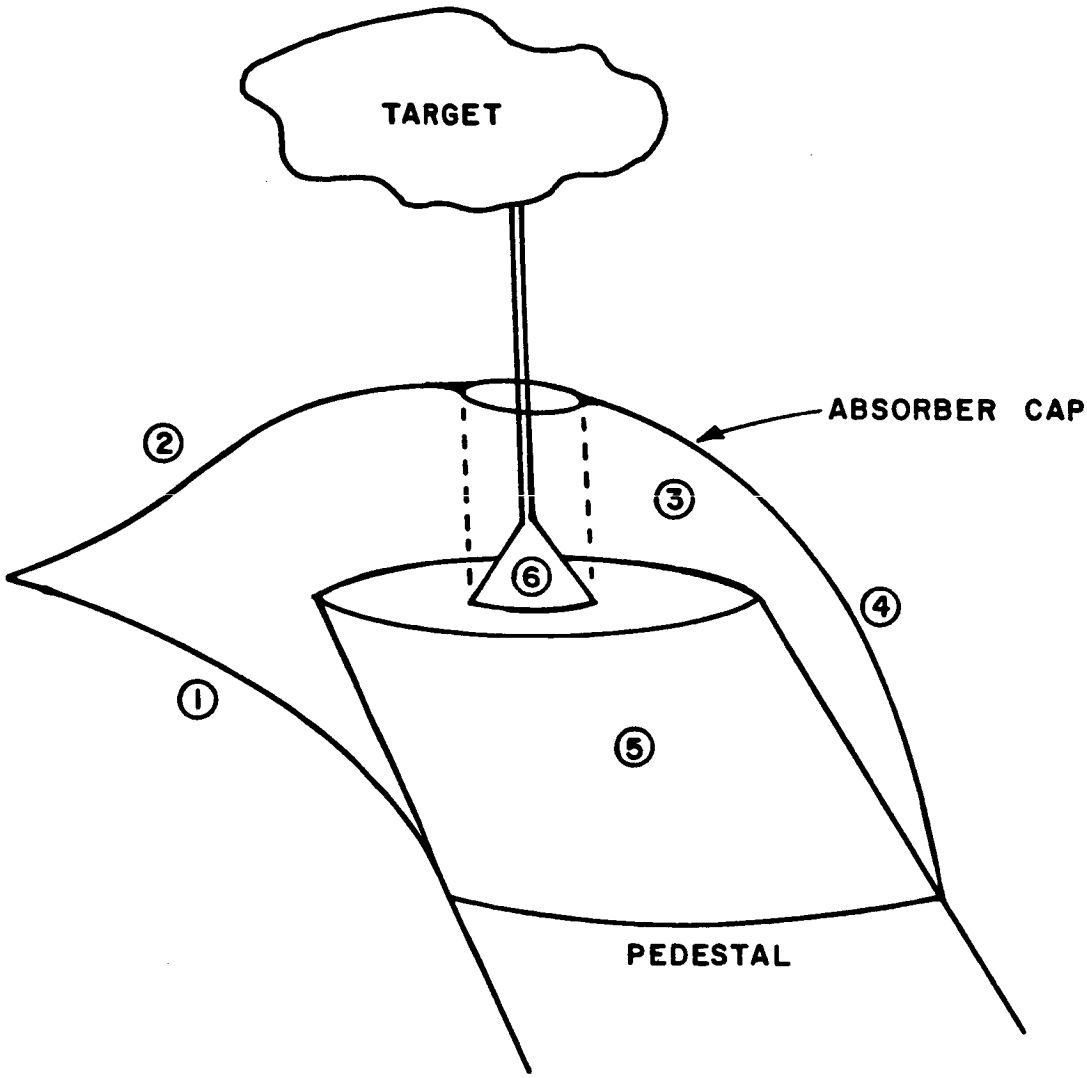

Figure 6.5. Nice features of Robin's head.

REFERENCES

[1] R.G. Kouyoumjian and P.H. Pathak, "A Uniform Geometrical Theory of Diffraction for an Edge in a Perfectly Conducting Surface, Proc. IEEE, Vol. 62 Nov. 1974, pp. 1448-1461.

[2] N.A. Logan, "General Research in Diffraction Theory", Vol. I, LMSD-288087 and Vol. II, LMSD-288088, Missiles and Space Division, Lockheed Aircraft Corporation, December 1959.

[3] W.D. Burnside, N. Wang, and E.L. Pelton, "Near-Field Pattern Analysis of Airborne Antennas", Antenna and Propagation, Vol. AP-28 No.3, May 1980, pp. 318-327.

[4] P.H. Pathak, "An Asymptotic Analysis of the Scattering of Plane Waves by a Smooth Convex Cylinder," Radio Science, Vol. 14, No. 3, May-June 1979, pp. 419-435.

[5] R.C. Rudduck, S.H. Lee and T. Jirapunth, "Radar Cross Section for Standard Cylinder Targets and Target Support", Final Technical Report 784698-1, The Ohio State University ElectroScience Laboratory, Department of Electrical Engineering, generated under Contract No. 0280 for New Mexico State University, Las Cruces, New Mexico 88003, October 1978.

[6] Allen K. Dominek, personal communication at the ElectroScience Laboratory, The Ohio State University, Columbus, Ohio 43212.

[7] W.D. Burnside, personal communication at the ElectroScience Laboratory, The Ohio State University, Columbus, Ohio 43212.